



Multi-scale study of the mechanical behaviour of bearing and bone-bearing bones : towards personalization of FE human models

Xavier Roothaer

► To cite this version:

Xavier Roothaer. Multi-scale study of the mechanical behaviour of bearing and bone-bearing bones : towards personalization of FE human models. Mechanics [physics.med-ph]. Université Polytechnique Hauts-de-France, 2019. English. NNT : 2019UPHF0020 . tel-02966979

HAL Id: tel-02966979

<https://uphf.hal.science/tel-02966979>

Submitted on 14 Oct 2020

HAL is a multi-disciplinary open access archive for the deposit and dissemination of scientific research documents, whether they are published or not. The documents may come from teaching and research institutions in France or abroad, or from public or private research centers.

L'archive ouverte pluridisciplinaire **HAL**, est destinée au dépôt et à la diffusion de documents scientifiques de niveau recherche, publiés ou non, émanant des établissements d'enseignement et de recherche français ou étrangers, des laboratoires publics ou privés.



Distributed under a Creative Commons Attribution - NonCommercial - NoDerivatives 4.0 International License

Thèse de doctorat
Pour obtenir le grade de Docteur de
L'UNIVERSITE POLYTECHNIQUE HAUTS-DE-FRANCE

Discipline, spécialité selon la liste des spécialités pour lesquelles l'École Doctorale est accréditée :

MÉCANIQUE

Présentée et soutenue publiquement par Xavier ROTHAEER

Le 27/11/2019, à Valenciennes

École doctorale: Sciences Pour l'Ingénieur (SPI), Lille Nord-de-France

N° d'ordre: 19/43

Équipe de recherche, Laboratoire: Laboratoire d'Automatique, de Mécanique et d'Informatique Industrielles et Humaines (LAMIH)

**Approche multi-échelle du comportement mécanique des os porteurs
et non porteurs : Vers une personnalisation des modèles numériques
EF de l'être Humain**

JURY

M. Patrick Chabrand , Professeur, Aix-Marseille Université, Marseille	Président du jury
Mme. Hélène Follet , Chargée de Recherche, INSERM, Lyon	Rapporteur
M. Sébastien Laporte , Professeur, ENSAM, Paris	Rapporteur
Mme. Sonia Duprey , Maître de conférence, Université Lyon 1, Lyon	Examineur
M. Rémi Delille , Ingénieur de recherche, UPHF, Valenciennes	Co-encadrant de thèse
M. Hervé Morvan , Ingénieur de recherche, UPHF, Valenciennes	Co-encadrant de thèse
M. Eric Markiewicz , Professeur, UPHF, Valenciennes	Directeur de thèse
M. Christian Fontaine , Professeur, Université Lille 2, Lille	Co-directeur de thèse

This work is licensed under the Creative Commons Attribution International License (CC BY NC ND 2.0 FR). Please find more informations on <https://creativecommons.org/licenses/by-nc-nd/2.0/fr/deed.en>.



Remerciements

Ces travaux de thèse sont le fruit de la collaboration entre le laboratoire LAMIH de l'Université Polytechnique Hauts-de-France et le laboratoire d'Anatomie de l'Université de Lille 2. Sans cette collaboration, ces travaux n'auraient pas pu aboutir à la rédaction de ce mémoire et je souhaite ainsi remercier ces deux institutions pour la confiance accordée pour ce travail de recherche.

Je remercie également les membres de mon jury de thèse, Patrick Chabrand, Hélène Follet, Sébastien Laporte et Sonia Duprey, d'avoir accepté d'évaluer ces travaux avec pédagogie afin d'aboutir à des échanges très constructifs lors de la soutenance.

Je tiens à remercier mes directeurs de thèse, Eric Markiewicz et Christian Fontaine, de m'avoir accordé votre confiance dès le début de cette thèse. Vos remarques tout du long de cette thèse, m'ont permis de prendre du recul à intervalles réguliers et ne pas perdre de vue les objectifs initiaux du projet. Je remercie grandement Rémi Delille et Hervé Morvan, ingénieurs de recherche au LAMIH, de m'avoir partagé leur savoir et de m'avoir accompagné quotidiennement durant ces 3 années de thèse. Cela a toujours été un grand plaisir d'échanger lors de nos différentes réunions et discussions. Votre soutien quotidien, et avec le sourire, m'a permis de persévérer et de réussir à réaliser des choses qui, de premier abord, sont loin d'être évidentes.

De plus, je remercie les différentes personnes qui ont pu intervenir de près comme de loin au cours de ma thèse : Bruno Bennani pour la partie numérique et multi-échelle, Philippe Moreau pour sa connaissance des essais d'indentation et de la machine TriboLab, Jose La Barbera pour son expérience des essais d'indentation, Denis Lesueur pour la préparation des éprouvettes d'indentation, Cédric Hubert pour la reconstruction 3D et simulations numériques DEM, Antoine Vanholder et Fabien Descamps pour la qualité des prélèvements osseux, Sylvain Treutenaere pour ses nombreux conseils avisés sur Python, et enfin Catherine Fourcart et Sabine Guilan-Houvenaghel pour leur aide sur les formalités administratives (très) nombreuses que l'on peut rencontrer au cours de 3 années de thèse. Je souhaite remercier également les différents membres du LAMIH que j'ai eu la chance de cotoyer quotidiennement lors de la thèse : Michel Watremez, Franck Lauro, Delphine Notta-Cuvier, Christophe Maréchal, Fabien Béchet, Anthony Bracq, Jérémy Wouts, Andrés Malo Estepa, Oussama Filali, Camille Bataille, Yassine El Attaoui, Jérémy Sadet, Hugo Carassus et tous ceux que je n'ai pas cités. De par votre convivialité et la bonne ambiance, je me suis senti rapidement intégré au sein du laboratoire.

Je tiens à remercier sincèrement ma famille pour leur soutien sans faille depuis toujours. J'espère que par cette thèse, vous y verrez le fruit de vos nombreux sacrifices qui m'ont permis d'aboutir, aujourd'hui, à la réussite complète dans mes études. Et enfin, je remercie infiniment Iolène pour sa patience et soutien indéniable depuis toutes ces années (je crois savoir maintenant ce qu'est l'os cortical !).

*Une pensée est adressée aux personnes ayant fait don de leur corps à la science sans qui ce travail
n'existerait pas*

Contents

Table of Contents	ix
List of Figures	xi
List of Tables	xiii
List of Acronyms	xv
List of Symbols	xvii
Introduction	1
1 Multi-Scale architectural & Mechanical properties of the cortical bone	5
1.1 Anatomy and histology of long human bone	7
1.1.1 The Human skeleton and different types of bone	7
1.1.2 Trabecular bone	13
1.1.3 Cortical bone	13
1.1.4 Bone remodelling: a throughout life process	20
1.2 Mechanical behaviour of the cortical bone: a multi-scale study	28
1.2.1 Macroscopic and mesoscopic scales	28
1.2.2 Microscopic and submicroscopic scales	35
1.3 Conclusions	38
2 A three dimensional geometric quantification of cortical vascular canals	41
2.1 Introduction	43
2.2 Material and methods	43
2.2.1 Body and sample preparation	43
2.2.2 Micro-CT scanning	47
2.2.3 Algorithm	47
2.2.4 Algorithm validation	60

2.2.5	Statistics	61
2.3	Results and discussion	62
2.3.1	Error and robustness quantification	62
2.3.2	Bearing and non-bearing comparisons	64
2.3.3	Side comparison	78
2.3.4	Inter-parameter relationships	81
2.4	Conclusions	86
3	Mechanical characterisation of human cortical bone	91
3.1	Introduction	93
3.2	Material and methods	94
3.2.1	Sample extraction	94
3.2.2	Macro-mechanical test : quasi-static tensile test	96
3.2.3	Micro-mechanical test : micro-indentation test	100
3.2.4	Statistics and data processing	104
3.3	Results and discussion	105
3.3.1	Bearing and non-bearing bones comparisons	105
3.3.2	Side comparison	112
3.3.3	Multi-scale correlation	114
3.4	Conclusions	119
	Conclusions and outlook	123
	A Illustration of the common symbols	129
	Bibliography	131
	List of publications	148

List of Figures

1.1	Human skeleton	7
1.2	Anatomical planes	8
1.3	Long bone anatomy	9
1.4	Humerus anatomy	10
1.5	Schematic transverse view of human humerus	10
1.6	Femur anatomy	12
1.7	Schematic transverse view of human femur	12
1.8	3D rendering of trabecular bone	13
1.9	Multi-scale architecture of the bone	14
1.10	Cortical bone architecture	15
1.11	Confocal microscopy of cortical bone	16
1.12	Cortical porosity	17
1.13	Collagen fibrils dimensions and orientation	18
1.14	Typical BMU scheme in cortical bone	22
1.15	BMU cells activity	23
1.16	Comparative plot of the cortical bone mechanical behaviour	30
1.17	Tensile stress-strain curve of cortical bone	31
1.18	One dimensional rheological model	33
1.19	Indentation protocol and curve	35
2.1	Morphology plot of the human subjects	44
2.2	Shaft harvest and sample preparation scheme	46
2.3	Optimum 2004V desktop lathe	47
2.4	Global overview of the algorithm	49
2.5	Image thresholding step	50
2.6	Comparison of the image filters efficiency	51
2.7	Canal interpretation	53
2.8	Connectivity scheme	56
2.9	Hierarchy of canals for features computation	57
2.10	BMU closing cone detection	58

2.11	Different BMU profiles and scheme to compute new bone volume	59
2.12	Schematic representation of validation proceeding	60
2.13	General features boxplots and barplots	66
2.14	Canal features boxplots and barplots	70
2.15	Ca.aDm VS Ca.rDm	72
2.16	Connectivity features boxplots and barplots	75
2.17	BMU features boxplots and barplots	77
2.18	Humerus side boxplots and barplots	80
2.19	Polynomial regressions between architectural features (Part 1)	82
2.20	Polynomial regressions between architectural features (Part 2)	83
3.1	Shaft harvest and sample preparation scheme	95
3.2	Set of devices used for tensile tests	95
3.3	Definition of Bone Area (BA) and Total Area (TA)	97
3.4	Side view of a typical specimen during micro-CT scanning	98
3.5	Porosity and area evolution along the scanned length	98
3.6	Typical tensile stress-strain curve	99
3.7	Indentation protocol	100
3.8	Snapshot of a 3x3 array of indents	101
3.9	Indentation curve and interpretation	103
3.10	Machine compliance computation	104
3.11	Mean stress-strain curves bearing and non-bearing bones	106
3.12	Mechanical features boxplots and barplots	109
3.13	Indentation mechanical features boxplots and barplots	111
3.14	Mean stress-strain curves from left and right limbs	112
3.15	Mechanical features from left and right limbs boxplots and barplots	114
3.16	Polynomial regressions between macromechanical features and architecture	118
I	Comparison of an ultrasonic scan and a tomographic one	126

List of Tables

1.1	Review of the different devices used to detect the porosity within the bone	21
1.2	Overview of the cortical porosity assessment	25
1.3	Overview of the human cortical bone mechanical behaviour	29
1.4	Micro and nanoscopic mechanical features reported by indentation.	37
2.1	Global overview of human subjects	45
2.2	Mathematical definition of canals features.	55
2.3	Mathematical definition of connectivity features	56
2.4	Definition of BMU features	59
2.5	Robustness quantification of general features.	62
2.6	Error estimation by comparing theoretical and computing results.	63
2.7	Robustness quantification of canal features	63
2.8	Robustness quantification of connectivity features.	64
2.9	Number of bone samples available for architectural analysis	64
2.10	General features for vascular network	65
2.11	Canal features values	68
2.12	Mean orientation tensor coefficients	69
2.13	Connectivity features values	74
2.14	BMU features values	76
2.15	Left and right humerus comparisons	79
2.16	Architecture inter-parameters polynomial fitting	83
2.17	Prediction error of architectural data	84
3.1	The different types of computed stress	97
3.2	Mechanical features computed for each type of stress	99
3.3	Indentation features computed for each type of bone.	101
3.4	Number of bone samples available for mechanical analysis	105
3.5	Polynomial regressions of mean femur and humerus stress-strain curves	106
3.6	Mechanical features values and bearing and non-bearing comparisons	108
3.7	Indentation mechanical features	110

3.8	Polynomial regressions of mean left and right femurs and humeri stress-strain curves .	112
3.9	Mechanical features values from femurs and side comparisons	113
3.10	Spearman correlation matrix	116
3.11	Coefficients of polynomial regressions between macromechanical features and architecture	117
A.1	Explanations of the symbols commonly used in Chapter 2 and 3 of this manuscript. .	130

List of Acronyms

μ-CT	Micro Computed T omography
BA	B one A rea
BV	B one V olume
BA/TA	Bone surface ratio
BV/TV	Bone volume ratio
BMD	B one M ineral D ensity
BMI	B ody M ass I ndex
BMU	B ase M ulticellular U nit
Ca	C anal
Ca.V/TV	Vascular canals volume porosity
Conn	C onnectivity
CT	C omputed T omography
DVC	D igital V olume C orrelation
DXA	X-Ray absorptiometry
HR-pQCT	H igh R esolution pQCT
LCN	L acunar- C analicular N etwork
MMW	M ann- W hitney- W ilcoxon test
MRI	M agnetic R esonance I maging
NMR	N uclear M agnetic R esonance spectroscopy
Po.V/TV	Vascular canals and LCN volume porosity
pQCT	P eripheral C omputed T omography
SR-μCT	S ynchrotron R adiation C omputed T omography
STD	S tandard D eviation
TA	T otal A rea
TV	T otal V olume
UPHF	U niversit� P olytechnique des H auts-de- F rance

WHO	World Health Organisation
------------	----------------------------------

List of Symbols

α	Opening angle of connectivity [deg]
ϵ	Engineering strain [-]
$\epsilon_{y,X}$	Yield strain limit [-]
ϵ_U	Ultimate strain [-]
ψ	First Eulerian angle [deg]
σ	Engineering stress [MPa]
$\sigma_{y,X}$	Yield stress limit [MPa]
$\sigma_{U,X}$	Ultimate stress [MPa]
θ	Second Eulerian angle [deg]
A_{ii}	Orientation tensor coefficient [-]
aDm	Apparent diameter [μm]
aLe	Apparent length [μm]
$AR2D$	2D aspect ratio [-]
$AR3D$	3D aspect ratio [-]
aS	Apparent surface [μm^2]
BF	Bone Fraction [%]
\bar{BF}	Mean bone Fraction [%]
C	Compliance [mm N^{-1}]
D	Density [mm^{-3}]
E	Macroscopic elastic modulus [GPa]
E_μ	Tissue elastic modulus [GPa]
$fVol$	Volume fraction [%]
H_μ	Tissue hardness [MPa]
p	p-value [-]
rLe	Real length [μm]
rS	Real surface [μm^2]

R^2	Coefficient of determination [-]
$R_{rDm_{(0,12)}}$	Inbound/outbound diameter ratio of connectivity [-]
$R_{rDm_{(1,2)}}$	Outbound diameters ratio of connectivity [-]
rDm	Real diameter [μm]
$U_{l,X}$	Linear toughness [mJ mm^{-3}]
$U_{pl,X}$	Post-linear toughness [mJ mm^{-3}]
$U_{tot,X}$	Total toughness [mJ mm^{-3}]
Vol	Volume [μm^3]
x	Longitudinal angle [deg]
y	Transverse angle [deg]

Introduction

« Emancipate yourselves from mental slavery. None but ourselves can free our mind. »

— REDEMPTION SONG, BOB MARLEY

The human skeleton is the result of a constant transformation throughout the humankind. The main purposes of the skeleton are to serve as brackets for muscles, to protect the internal organs and finally to participate to the locomotor system. Therefore, different types of bone can be distinguished in the skeleton so as to be optimised according to their functions. Although bones have different shapes, they all have similar components. Indeed, to ensure the stiffness of the entire body, the cortical bone is present in every part of the skeleton. The cortical bone keeps adapting itself according to its functions during the life. Albeit it is a hard tissue, bone remains a living one. Indeed, the cortical bone has a within micro-architecture that is specifically designed to provide blood and nutrients required to activate cells. For several decades, many research aimed at observing, describing and understanding the within processes that occur into the bone. Some pioneer works in the second part of the twentieth century named these processes : the bone modelling and remodelling. The first one occurs during the growth up to young adulthood so as to participate to the skeleton development. The second one occurs throughout the life in order to replace the old bone, cure micro-cracks and ensure an optimal bone arrangement according to the bone functions. The bone remodelling consists in an equilibrium between the bone resorption and creation initiated at the cellular level.

With the enhancement of medicine and life quality, human lifespan keeps increasing. As the bone remodelling is complex and depends on many external factors, its activity tends to go wrong in the elderly. Because of the population ageing, bone remodelling defects begin to affect a great part of the worldwide population. This bone disorder is mainly caused by the so-called osteoporosis which affects the cell activities during the bone remodelling process. So as to diagnose it, the World Health Organisation (WHO) provides a method based on DXA (X-Ray absorptiometry) to measure

the mineral part of the bone. Although this method has become the gold-standard for the osteoporosis diagnosis and bone health estimator, this measure often remains local (femoral neck or spine) and is mainly limited to a planar study. By the early 2000s, several techniques have emerged to detect the micro-architecture. Hence, these methods lead to a better understanding of bone remodelling process and the impact of diseases. Unfortunately, due to the resolution, current in-vivo devices aren't able to detect the entire within micro-architecture. Therefore, most of studies, which aim at detecting the cortical architecture, use ex-vivo devices on bone samples harvested from human cadavers. However, mainly due to the very complex shape of the architecture, these studies are limited to an in-plane quantification such as the porous part of the bone. Nevertheless, this porous part has a specific three-dimensional shape that would help to understand the changes within the bone cortex created by the bone remodelling and their impact on the mechanical behaviour at upper scales. Furthermore, the cortical bone remains a very thin layer (a few millimetres thick) that makes bone harvest hard from a human skeleton. As a consequence, many studies are based on animal samples (cow, horse, dog, ...) where the cortical bone is thicker and extrapolate their conclusions to the human cortical bone. Likewise, a great part of studies, which are based on human samples, focuses on the longest bone of the human skeleton : the femur. This unbalance creates a lack of data between the femur and the other bones of the skeleton. As a consequence, architecture of the other bones are poorly investigated and numerical models of the human body are using material data from different studies, some of which can be considered as deprecated, and human subjects. Thereby, individual trends may not be representative of the reality.

The purpose of this thesis is to remedy the lack of data for bearing and non-bearing bones by focusing on the human femur and humerus and comparing their architecture, mechanical behaviour and the impact of the architecture on it. The manuscript begins by reflecting the current state of the art and highlighting its lack in the first chapter. First, the anatomies of the femur and humerus are explained. Then, the cortical bone is depicted at different scales. Likewise, a short section reviews the current devices used to detect the within architecture. Subsequently, the bone remodelling activity is described so as to understand the defects and its impact on the architecture throughout the life.

The second chapter seeks to unravel lacks caused by limitations of in-plane studies of the cortical architecture. An innovative method to analyse tomographic data is described. This method is willing to assess the vascular porosity in 3D where slices from μ -CT are post-processed using the Python language. This algorithm is step-by-step described. Vascular canals, connectivity and Base Multicellular Units (BMUs), cradle of the bone remodelling, are automatically detected. Innovative features, such as orientation, length or the new bone fraction created by BMUs are assessed. The robustness of the script is quantified and proves that it is suitable for such analysis. Then, 77 samples are harvested

from 10 human cadavers in the elderly, provided by the anatomy laboratory of the University of Lille 2. Humerus and femur are compared for each individual so as to extract trends. Similarly, the bias impact on the architecture is also investigated. Finally, an inter-parameter correlation and regression study is performed in order to understand the impact of the new features on the well-known cortical porosity.

The third and final chapter extends the study of the second chapter by assessing the mechanical properties of the cortical bone at two different scales. Indeed, bone samples have been designed so as to fit for macroscopic tensile tests (dumbbell-shape) and a full scan of the gauge length. In addition, indentation samples have also been harvested from a neighbour region to the tensile ones in order to obtain the elastic modulus and hardness of the bone matrix. Similar comparisons, as done in the second chapter, are performed. Finally, the architecture features are correlated with the mechanical ones and regressions are provided in order to lend the possibility of estimating the mechanical health of the bone from an architecture study.

The last section of this manuscript aims at concluding, summing up the main results of the thesis and giving some outlooks and insights for further research.

Chapter 1

Multi-Scale architectural & Mechanical properties of the cortical bone

Contents

1.1	Anatomy and histology of long human bone	7
1.1.1	The Human skeleton and different types of bone	7
1.1.1.1	General description of human skeleton	8
1.1.1.2	Long human bone	8
1.1.2	Trabecular bone	13
1.1.3	Cortical bone	13
1.1.3.1	Up to microscopic scale	14
1.1.3.2	From submicroscopic to nanoscopic scale	16
1.1.3.3	Cortical porosity: devices to detect it	18
1.1.4	Bone remodelling: a throughout life process	20
1.1.4.1	A microscopic process	20
1.1.4.2	The osteoporosis: a bone remodelling defect	23
1.1.4.3	The dynamic turnover assessment of the cortical porosity	24
1.2	Mechanical behaviour of the cortical bone: a multi-scale study	28
1.2.1	Macroscopic and mesoscopic scales	28
1.2.1.1	Experimental characterisation	28
1.2.1.2	Numerical implementation	32
1.2.2	Microscopic and submicroscopic scales	35

1.2.2.1	Experimental methods	35
1.2.2.2	Numerical approaches	37
1.3	Conclusions	38

The first part of this chapter aims at first quickly describing the human skeleton and the different types of bone, the anatomy of long bones with focusing on humerus and femur. Then, the cortical bone is accurately detailed. The multi-scale architecture is depicted. This architecture can be approximated as a tortuous microscopic vascular canal network globally oriented along the longitudinal axis of the long bone. This network is embedded in a bone matrix which also shows an anisotropic organisation (collagen fibrils, osteocytes). Due to the highly tortuous architecture, the mechanical behaviour of the bone is affected. Indeed, recent studies have reported that the detection of the geometry and the amount of the micro-porosity, affected by the continuous bone remodelling, is still a challenge in order to better understand macroscopic phenomena and to "quantify" the bone health.

On the second part of this chapter, the mechanical behaviour of the cortical bone is explained. This description shows the way to characterise the bone tissue at different scales. The mechanical features greatly fluctuate according to the studies. Indeed, due to the complexity to obtain "normative" sample, the extraction of the specimen, the preservation method and the type of mechanical test can impact the results. In addition, the origins of the cadaveric human or animal specimens affect the mechanical behaviour and then have to be considered. A couple of studies correlate the mechanical behaviour of the cortical bone with its architecture, the Bone Mineral Density (BMD), age of the subject, or the morphological parameters of the subject. Numerical studies are also widely used so as to describe complex phenomena such as the crack propagation. However, overall, at a macro and mesoscopic scale, the cortical bone can be considered as a transverse isotropic brittle material with a linear elastic comportment.

1.1 Anatomy and histology of long human bone

1.1.1 The Human skeleton and different types of bone

The human skeleton is constantly evolving from the early life to the young adult age. An adult skeleton has more than 200 bones. As an endoskeleton, the human skeleton has three main functions. The first one is to provide a bracket where muscles can be bound. The second one is to protect the internal organs. And finally, it participates to the locomotor system to provide the movement and stability to the human body. The human skeleton can be divided into the axial skeleton (mainly formed by the skull, rib cage and vertebral column) and the appendicular skeleton. This second part groups the lower and upper limbs, shoulder girdle and pelvic girdle. (Fig. 1.1).

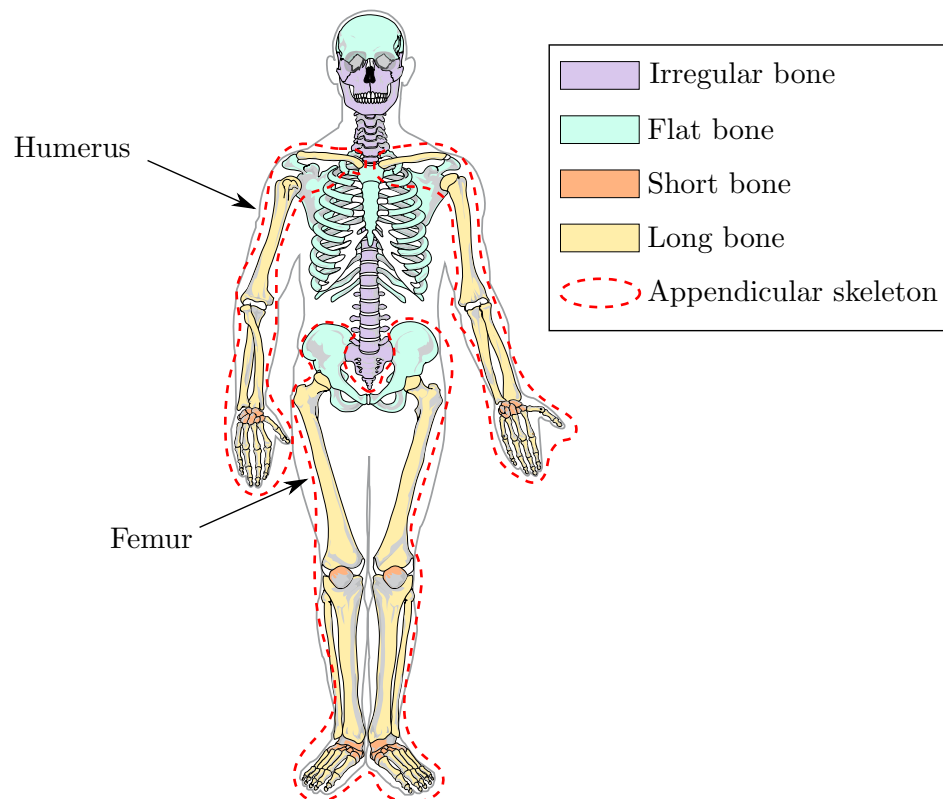


FIGURE 1.1: Human skeleton. The four different types of bone are displayed. Likewise, humerus and femur are highlighted.

As shown by Figure 1.1, four different types of bone can be identified [1]. Long bones can be found in the appendicular skeleton. Their anatomy is described in a subsequent part of this chapter. Flat bones are mainly located in the higher part of the skull, ribs, sternum and ilium. Short bones are located in the hand, foot and knee. Finally, irregular bones can be found in the spinal column and the lower part of the skull. The different shapes of these bones are mainly due to their different functions [2] but they present the same type of structure : the cortical bone and the trabecular bone (also called

cancellous bone or spongy bone). The first one ensures the mechanical stiffness of the structure and protects the trabecular bone which is very porous but guarantees a highly vascular supply. During the childhood and the adolescence, the skeleton is undergoing important changes. This growth is maximum during the pubertal period and can differ according to the sex of the subject [3]. After this peak, the bone accrual keeps increasing until the beginning of the adulthood.

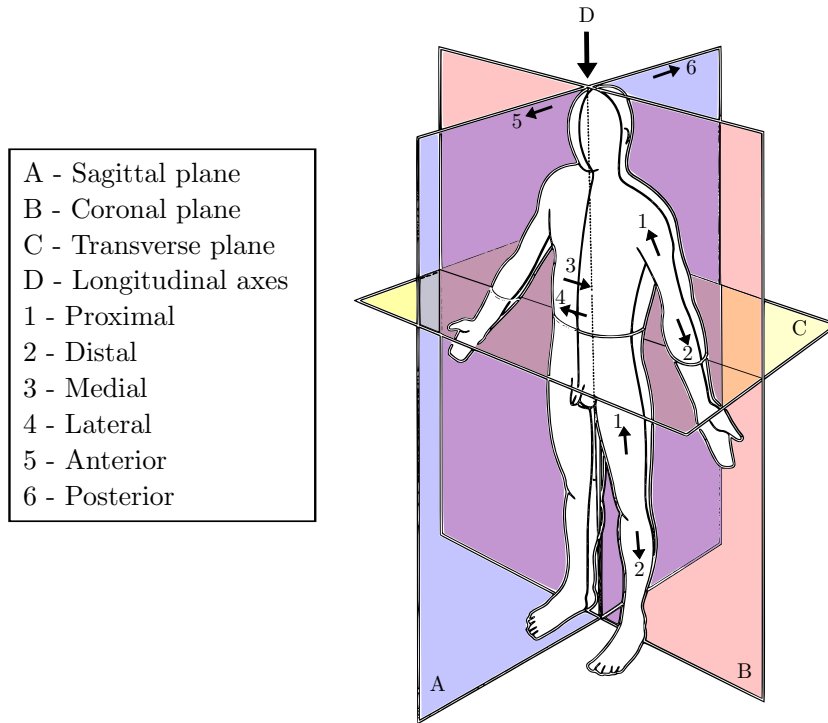


FIGURE 1.2: Human body anatomical planes. Directional terminology is also displayed and will be used to denominate bone samples in this thesis.

In order to facilitate reading the manuscript, Figure 1.2 displays the different anatomical planes and terms of location. For instance, distal and proximal terms are used to define the part of the bone closer and distant to the torso. These terms will be used throughout the manuscript.

1.1.1.1 General description of human skeleton

1.1.1.2 Long human bone

Every long bone is located in the appendicular skeleton. Figure 1.3 shows a typical long bone anatomy. The predominant part of the long bone, called the diaphysis, is the central part of the bone. This shaft is surrounded at each ending by epiphysis. The epiphysis is coated with the articular cartilage. The diaphysis and epiphyses are separated by the epiphyseal line. This part of the bone is where the new bone growth occurs during childhood and adolescence. Composed of cartilaginous components during the growth, this part, also called metaphysis, ossifies at the beginning of the adulthood [4, 5].

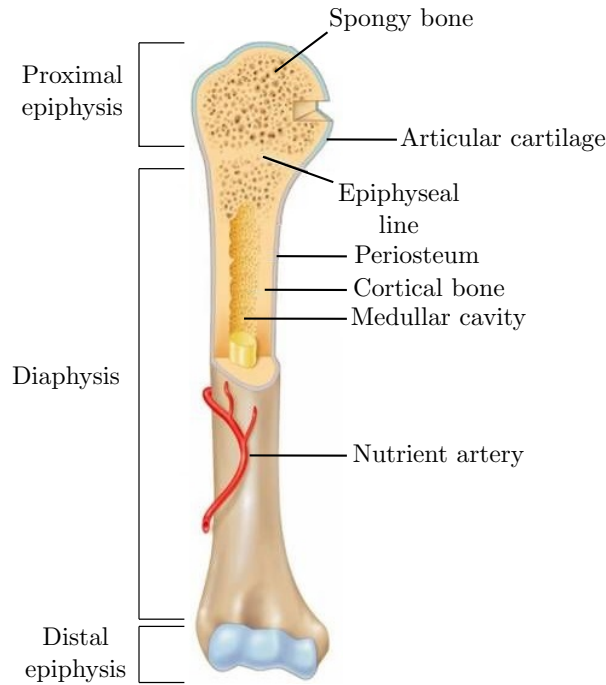


FIGURE 1.3: Partial frontal cutting of a typical long human bone. Humerus is used as an example.

In order to externally distinguish diaphysis from epiphysis, Heim's system of squares is mostly used. This method consists in assuming that epiphysis is contained inside a square whose sides are equal to the widest part of the epiphysis [6].

In diaphysis, several parts can be highlighted. The main part of the diaphysis is the cortical bone, coated by the endosteum on the inner part and by the periosteum on the outer part. At the centre of the shaft, the medullar cavity stores the bone marrow (yellow marrow). The inner surface of the cavity is coated by the thin vascular membrane, called the endosteum. The periosteum, located on the external surface of the cortical bone, excepts at cartilaginous part, can be described as a fibrous connective tissue which supplies blood vessels, nutrients to the bone. The endosteum architecture can be equated to the spongy bone. Both of these coatings contain osteoblasts and osteoclasts cells which ensure the bone remodelling and the widening of the bone during the growth [7]. Furthermore, they strongly contribute to the fracture healing process [8]. As a living tissue, bone requires nutrients and blood vessels also provided by the nutrient artery which penetrates into the bone through the nutrient foramen. Cortical bone architecture is more accurately described in the following parts of the current chapter.

1.1.1.2.1 Humerus

The humeral bone is located in the upper limbs of the human skeleton. The scapula is connected to the proximal humeral epiphysis, whereas the radius and ulna are connected to the distal one. The bone

length is around 30 cm and 33 cm for adults [9, 10]. Figure 1.4 displays the anatomy and the main landmarks. Both epiphysis can easily be defined by Heim's system of squares (red dotted squares).

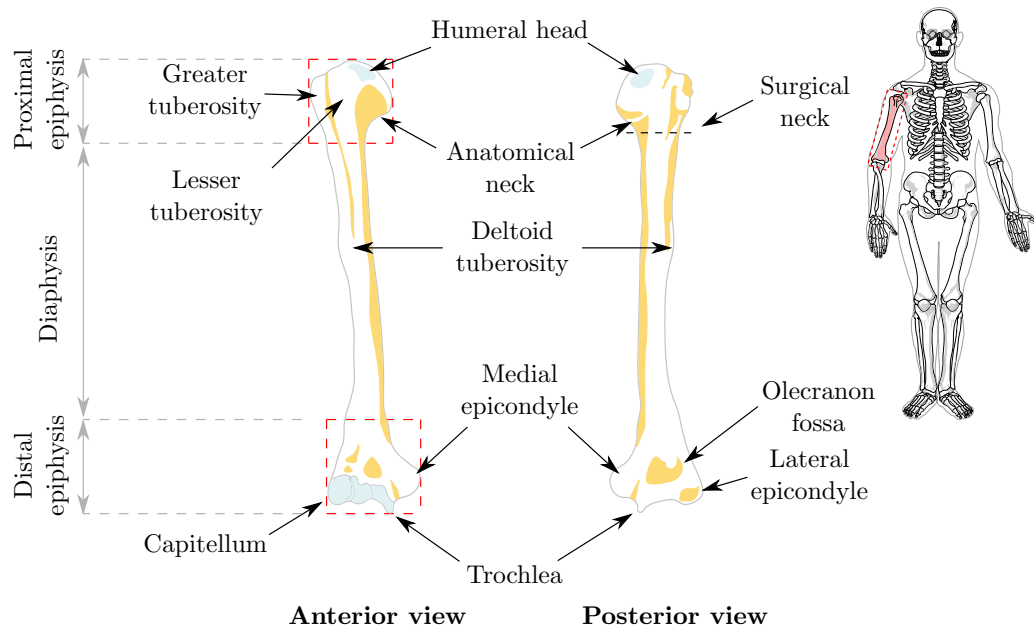


FIGURE 1.4: Humerus anatomy

Humeral head is half-sphere shaped, medially and upwardly facing so as to articulate with the glenoid fossa of the scapula. Greater and lesser tuberosities are located on the lateral part of the humerus. They both serve as attachment site for the rotator cuff muscles. The surgical neck is located behind the humeral head. Due to the orientation of the head, the surgical neck is one of the weakest parts of the proximal sector of the humerus [1, 11]. 70 % of the proximal humerus fractures occur in the region of the surgical neck and of the metaphysis [12]. Lesser and greater tuberosities are separated by the intertubercular groove which extends up to the proximal side of the diaphysis.

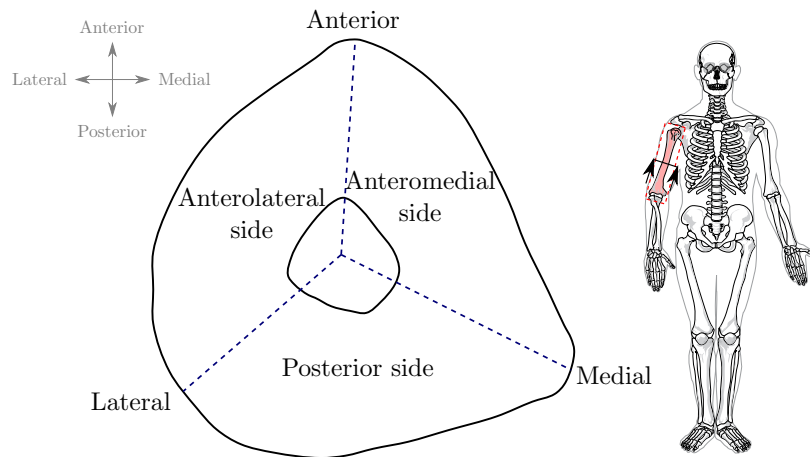


FIGURE 1.5: Schematic transverse view (view from the bottom) of a mid-shaft diaphysis from a right femur.

Figure 1.5 shows the typical transverse shape of the human humerus. The triangular shape of the section enables to define 3 borders and anatomical sides. On the proximal part, the posterior side begins under the surgical neck and runs diagonally down to the deltoid tuberosity. At the mid-shaft, medial ridge is characterised by a roughened area. The cortical bone thickness varies all along the diaphysis. The cortical layer is thicker in the distal side of the diaphysis than the proximal one : Tingart *et al.* [13] reports 4.4 ± 0.1 mm cortical thickness for the proximal part of the diaphysis whereas Diederichs *et al.* [14] reports an over 5 mm thickness for the distal part. However, these values depends on the human subject to the other and a little research report a continuous assessment of same subject. Bry [10] assesses a longitudinal evaluation of the cortical thickness of four different male subjects along the diaphysis on each anatomical ridge (Anterior, lateral and medial). This study reveals that the anterior ridge has the thickest cortical layer (5.8 mm). The lateral and medial borders are thinner with a mean value of 4.9 and 5.3 mm cortical thickness, respectively. Cross-section of the humeral diaphysis changes during the growth and the shape can be asymmetric in the adulthood by comparing left and right humerus of same subject [15].

1.1.1.2.2 Femur

The femur, also called thigh bone, is located in the upper part of lower limbs. The femoral head (proximal epiphysis) forms the hip joint by connecting with acetabulum. The distal end articulates with the kneecap and tibia so as to form the knee joint. This is the longest bone in the human body. The whole length of the femur is about 42 and 45 cm for female and male human subjects, respectively [10, 16]. Figure 1.6 displays the main landmarks of the femur anatomy. Differently than the humerus, only the distal epiphysis can be identified by Heim's system of squares (red dotted squares). To identify the proximal epiphysis, the lowest part of the lesser trochanter is mostly used as a reference (red dotted line).

The femoral head is half-sphere shaped. It is upwardly, medially and slightly forwards directed. The femoral neck has a cylindrical shape and is spatially oriented. The angle with the shaft is about 125° to facilitate the movement. In the transverse plane, the neck forms a 15° angle (anteversion) medially and forward oriented. On the proximal part of the diaphysis, greater and lesser trochanter can be found. The first one has an elongated ridge which runs from the neck to the lateral side of the diaphysis while the second one is medially and backward facing with a conical eminence and runs from the posterior side of the neck to the shaft. They both serve as an attachment site for muscles of the hip. In the skeleton, the femoral shaft is 7° oriented relative to the vertical axis. The posterior border forms a roughened ridge, called the linea aspera. On the way down along the diaphysis, the linea aspera widens. On the distal diaphysis, two large condyles are present on medial and lateral

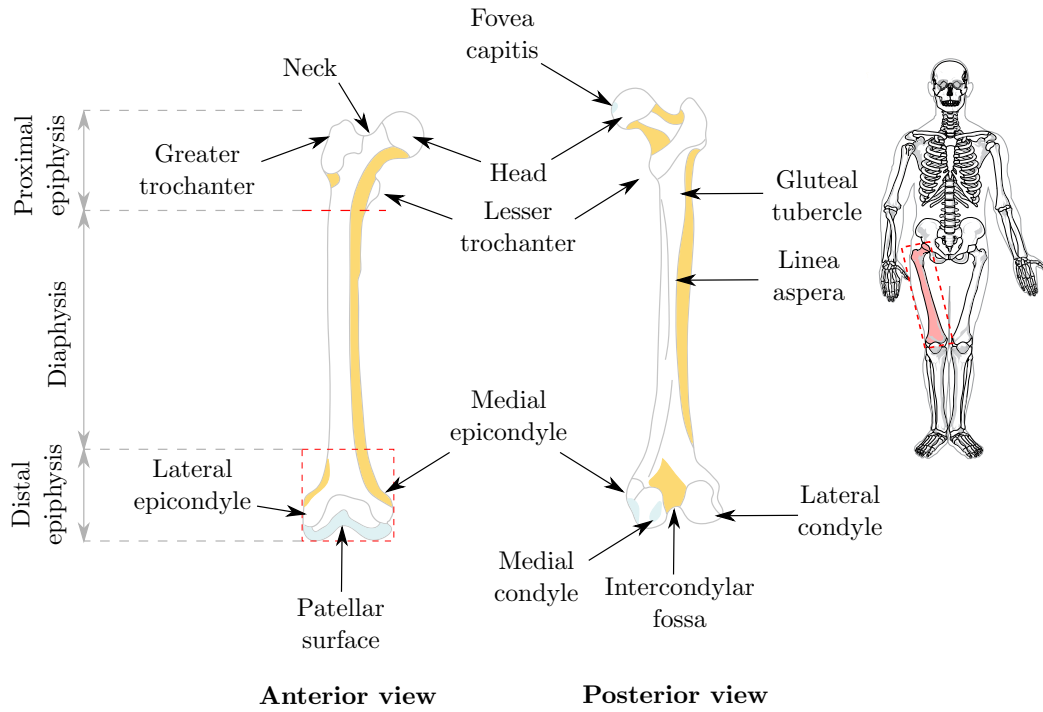


FIGURE 1.6: Femur anatomy.

side. They are posteriorly separated by the intercondylar fossa. The condyles are globally covered by an articular surface. They articulate with the patella and tibia [1, 11].

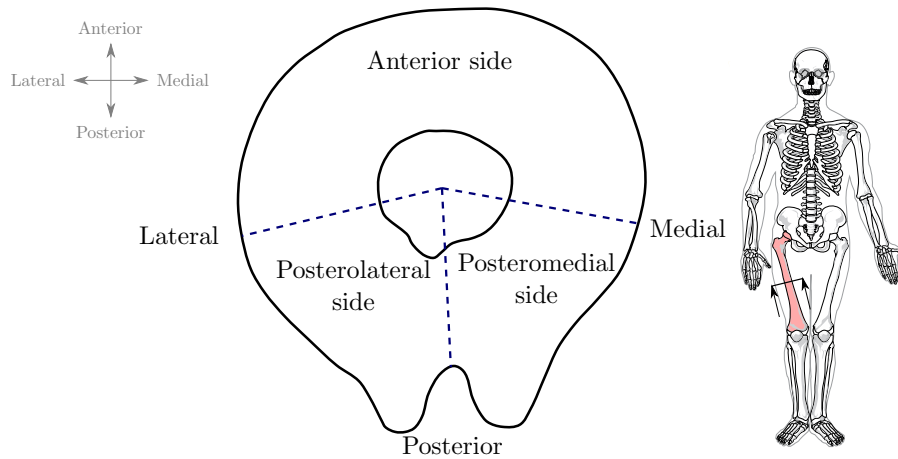


FIGURE 1.7: Schematic transverse view (view from the bottom) of a mid-shaft diaphysis from a right femur.

Figure 1.7 refers to the transverse view of a femoral mid-shaft. 3 borders and anatomical sides are defined. The posterior uses the posterior as reference. Lateral and medial borders are not very marked. The femoral asymmetry of the cross-section increases with age [17]. Overall, the cortical thickness is more important than humerus. Indeed, in most of cases for every border, the cortical thickness is over 6 mm [10, 18]. Bry [10] demonstrates that lateral and medial have almost same cortical thickness (8 and 7.6 mm, respectively). Posterior border has the thickest border with a 9.5 mm cortical thickness.

1.1.2 Trabecular bone

The trabecular bone is present in every part of the skeleton. It can be found at the end of long bone but also wrapped in cortical bone for flat bones. This is a highly porous bone. Fig.1.8 shows a 3D rendering of a typical trabecular bone. The bone is made of trabeculated bone tissue. The trabecular thickness can range from $100\text{ }\mu\text{m}$ to $300\text{ }\mu\text{m}$. The void between trabeculae is filled of bone marrow. The micro-architecture is also dependent on the bone remodelling and is age-related. Mostly evaluated over 70 %, the porosity tends to increase in the elderly (Figure 1.8) [19, 20].

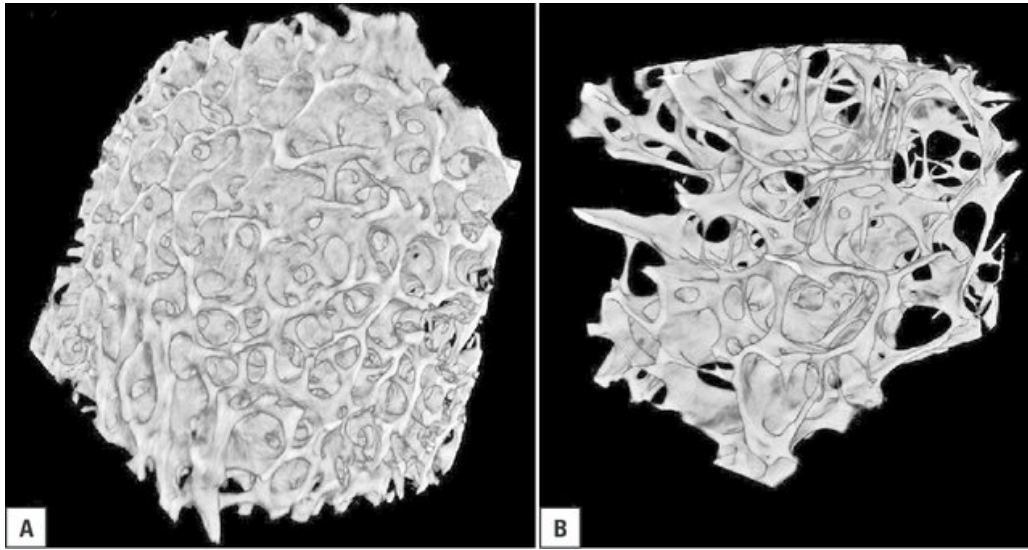


FIGURE 1.8: 3D rendering of trabecular bone obtained from [19]. Both images show a spongy bone of a human lumbar vertebra from a 25-year-old (A) and a 64-year-old human subject (B).

1.1.3 Cortical bone

Cortical bone is the part of the bone which provides the stiffness of the skeleton. Highly spatially arranged, it shows a multi-scale architecture. Figure 1.9 summarises the architecture of the bone at different scales.

From a mechanical point of view, the macroscopic behaviour of the bone is impacted by lower scales architecture. Indeed, the cortical bone is porous. The porosity depends on the subject, gender and is age-related. The porous volume of the bone varies between 5 % and 20 % [22]. So as to have a better understanding of the behaviour, the architecture of the compact bone has to be investigated. In this section, the cortical architecture is described as it should be for a healthy person. Obviously, values depend on numerous external factors such as the age, gender, lifestyle, or disease. The variation of the architecture is studied in part 1.1.4 where bone remodelling is described.

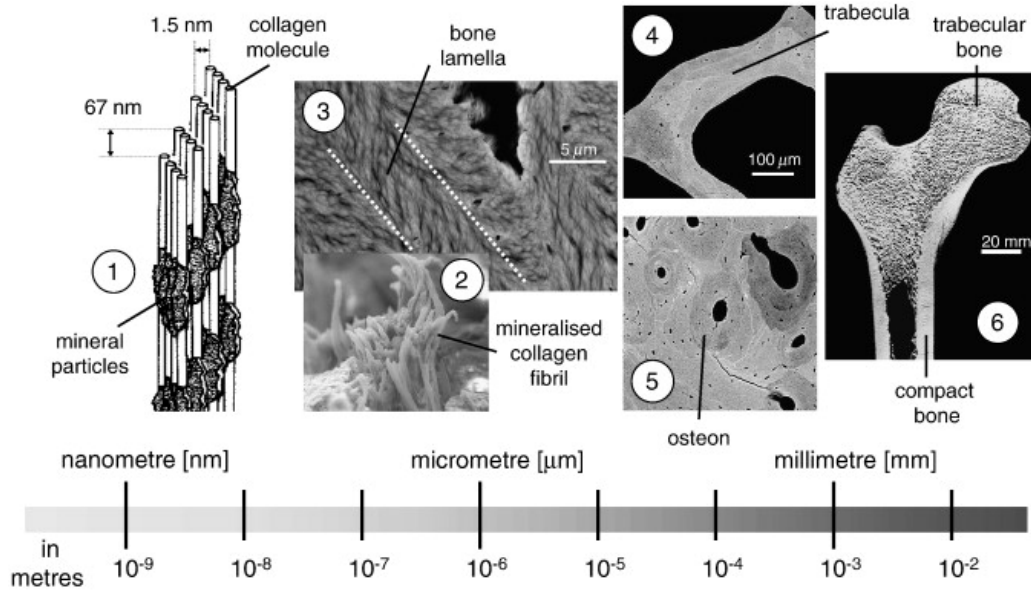


FIGURE 1.9: Multi-scale architecture of the bone adapted from [21]. 1 : At the nanoscopic scale, bone is composed of collagen and mineral particles. 2 : Bone tissue is organised as an oriented mineralised collagen fibrils. 3 : Collagen fibrils create a lamellar arrangement. 4 : Typical view of one trabecula. 5 : Typical view of cortical bone. 6 : Frontal cutting of the proximal side of a femur.

1.1.3.1 Up to microscopic scale

At the microscopic scale (hundreds and tens of micrometres), cortical bone can be considered as a continuous bone tissue crossed by a canal network, called Haversian and Volkmann's canals. This network is formed from vascular canals which provides blood, nutrients and nerve fibres inside the bone. In long bone, they are mainly oriented along the longitudinal axis of the diaphysis (Fig.1.10). This type of canal is surrounded by a lamellar bone, called osteon (or secondary osteons). The osteon is made of several concentric lamellar cylindrical structures. The lamella is less than 5 μm thick. Haversian canal has a diameter over than 50 μm but less than 100 μm while the surrounding osteons has a diameter which mainly ranges from 100 to 300 μm [23]. Qiu *et al.* [24] reveals a positive correlation between Haversian canal area and osteon area in ribs of nine healthy white men: the more canals are large and the greater osteonal diameters are. The authors also show that their size depends on the removed bone during remodelling. Volkmann's canals are defined as vascular canals that are perpendicular to the Haversian network in order to supply them [25]. Their diameters are around 10 μm . However, with the emergence of precise imaging devices, it seems that the vascular network is tortuous which makes hard to distinguish Havers canals from Volkmann's canals [26]. This could explain that Volkmann is poorly investigated. Cooper *et al.* [22] report that the length of the vascular canals is less than 500 μm . Nonetheless, little values are furnished for canal length by the literature due to the complexity of the network.

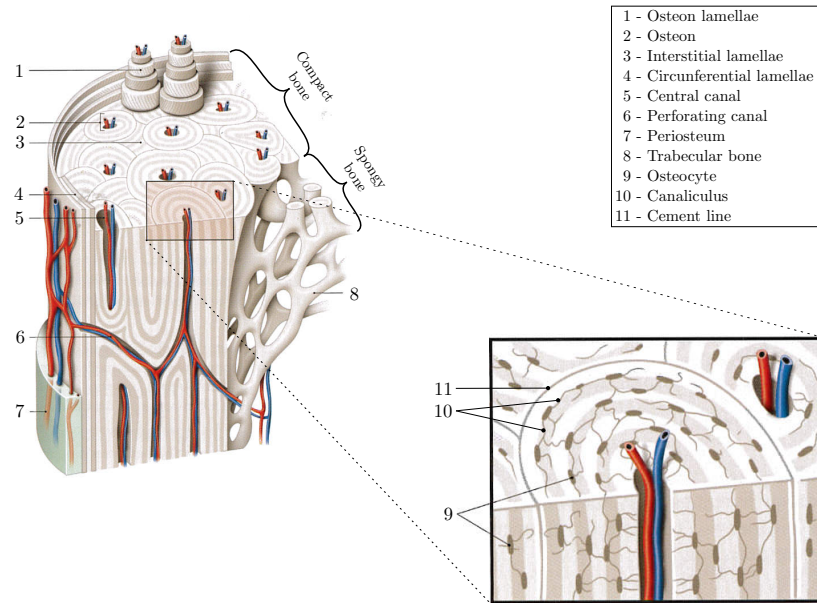


FIGURE 1.10: Cortical bone architecture [1]. Micro-architecture (central canal and perforating canal) and submicroarchitecture (canaliculus, osteocyte) can be found.

The osteon is highly vascularised. A few micrometer size network can be found. Osteocytes are interlinked with the canaliculi. This network is called lacunar-canalicular network (LCN). Figure 1.11 displays a confocal microscopy where LCN can easily be identified. LCN plays a leading role in bone remodelling using a process called mechanotransduction (described in 1.1.4). Some works study the density of LCN, known as bone permeability, and reveal that the length of canaliculi can range from 23 to 50 μm and diameters remain below 0.5 μm [27, 28]. Lacunae have an ellipsoid shape with a volume of about 500 μm^3 [29, 30]. The ellipsoid shape is elongated along the longitudinal axis of bone. The density of osteocytes is over 20 000 mm^{-3} . To ensure vascularisation, osteocytes are linked with several dozen canaliculi [27].

Each osteon is bounded by a very thin layer called cement line. This heterogeneous layer is created during bone remodelling at the interface between bone resorption and formation areas. The thickness is less than 5 μm [23, 32]. The cement line seals the osteon from the outer bone (interstitial bone): the LCN doesn't pass through the line. In spite of the narrow part of the bone matrix, several studies reveal that it has a major role in crack propagation. This mechanical influence is studied in a further part of this manuscript (1.2.2). The bone tissue located outside of the osteons is called interstitial bone (or primary osteon). This tissue shows a similar lamellar structure than the osteonal bone. As a matter of fact, the interstitial bone is a former osteonal bone and is thoroughly replaced by new bone (secondary bone) during remodelling process.

Consequently, the porosity inside the cortical bone can be evaluated at two stages: vascular

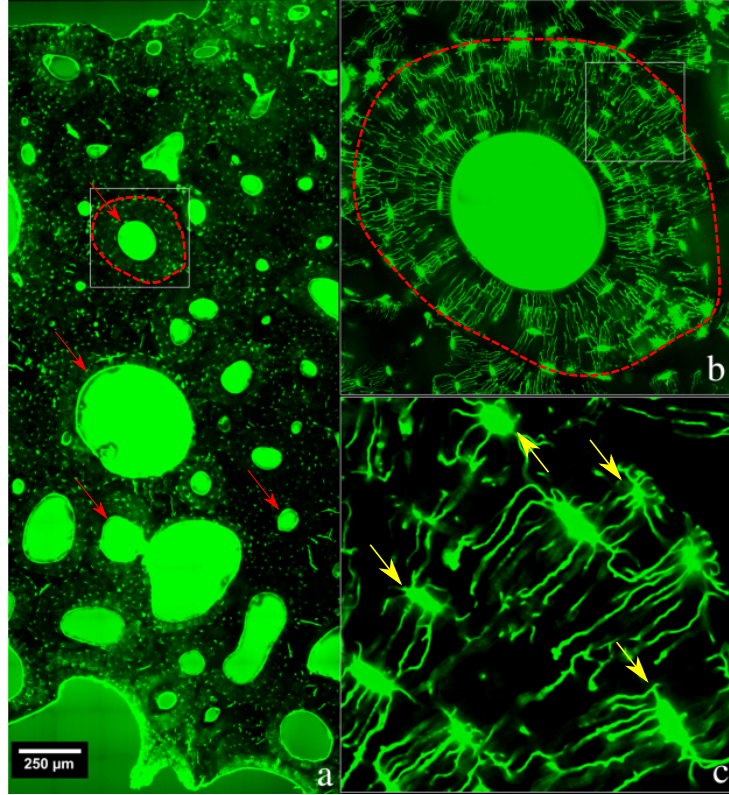


FIGURE 1.11: Confocal microscopy obtained from femoral mid-shaft cross-section of human cortical bone (Anterior femoral, 78 years old female). The figure is adapted from Cooper *et al.* [31] study. The red arrows show some vascular canals surrounded by osteon (red dashed line). The yellow arrows highlight the osteocytes interlinked with the canaliculus network.

porosity (tens at hundred microns), and lacunar-canalicular network (around $1\mu\text{m}$). Figure 1.12 shows the distribution of the global porosity between LCN and vascular network [33]. This plot is quite revealing in several ways. First, even if the density of lacunae is much higher than canals, global porosity is mainly induced by vascular network. Indeed, the lacunae represent about 15 % (and so 85 % for vascular canals) of the total porosity which represents between 2 % and 8 % of porosity in cortical bone, respectively [33, 34]. Second, it exhibits that both types of porosity can be distinguished by their size. Thus, the device used to identify cortical porosity (LCN, vascular canals or both) should be able to give suitable data at the studied scale (see section 1.1.3.3).

1.1.3.2 From submicroscopic to nanoscopic scale

Although the bone matrix seems to be continuous at a microscopic scale, the osteonal bone is composed of $5\mu\text{m}$ thick concentric lamellar structures [35]. These lamellas are formed of collagen fibres which are a stack of collagen fibrils (between 20 and 70 %), mineral crystals (between 65 and 70 %) and water (10 %) [36, 37]. The collagen fibres have a specific three-dimensional arrangement. Indeed, three

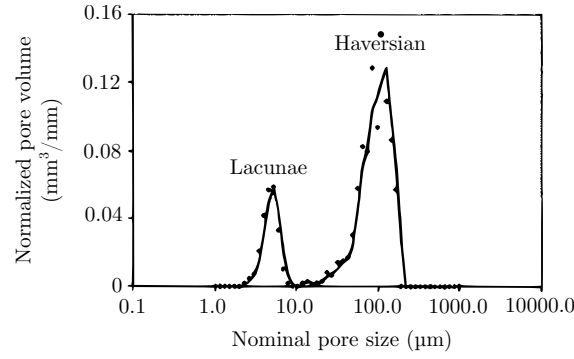


FIGURE 1.12: Graphical distribution of the cortical bone porosity extracted from the study of Wang and Ni [33]. Results are obtained from human cadaver femurs (Age ranges from 16 to 89 years old)

different types of fibre arrangement can be found (as reported in [38–40] and displayed by Figure 1.13):

- type I: Transversal spiral course;
- type II: Alternating transversal and longitudinal spiral course;
- type III: Longitudinal spiral course;

These three types can easily be revealed by using circularly polarised light (CPL) device (Figure 1.13). Indeed, type I arrangement shows a brighter light than the type III arrangement that is nearly dark. Type II can be identified thanks to its hybrid orientation which creates successive brighter and darker lamellae. However, attention should be paid to the osteon orientation which can affect the brightness of it [36]. The arrangement depends on the type of loading applied on the bone. In fact, due to bone remodelling (section 1.1.4), pioneer works, done by Ascenzi and Bonucci [38, 39, 40], showed that an isolated osteon with longitudinal oriented fibres (type I) are more suitable for tensile stress whereas transverse oriented fibres (type III) for compressive ones.

Collagen fibril is a complex repetitive arrangement of amino-acid. The structure is 300 nm long and is triple helical organised [42]. Collagen fibrils are distinguished in more than twenty different types. Indeed, the proteinaceous weight of a mammalian body is essentially made of collagen. Bones are composed of type I collagen fibrils and they are created by osteoblastic cells during remodelling. To assemble collagen molecules together, they overlap each other with a 67 nm periodicity and a 40 nm gap is created so as to join them with a plate-shape mineral crystal [35] (Figure 1.13). The mineral crystals are composed of $\text{Ca}_{10}(\text{PO}_4)_6(\text{OH})_2$. The shape is flat and asymmetric with a privileged direction of growth along the longitudinal axis of collagen fibrils [35, 43]. They are well-known as hydroxyapatite (shortened as HAP). Collagen mineralisation during growth and remodelling is still investigated so far. But it exists several in-vitro processes to synthesise mineralised collagen so as to be used as a

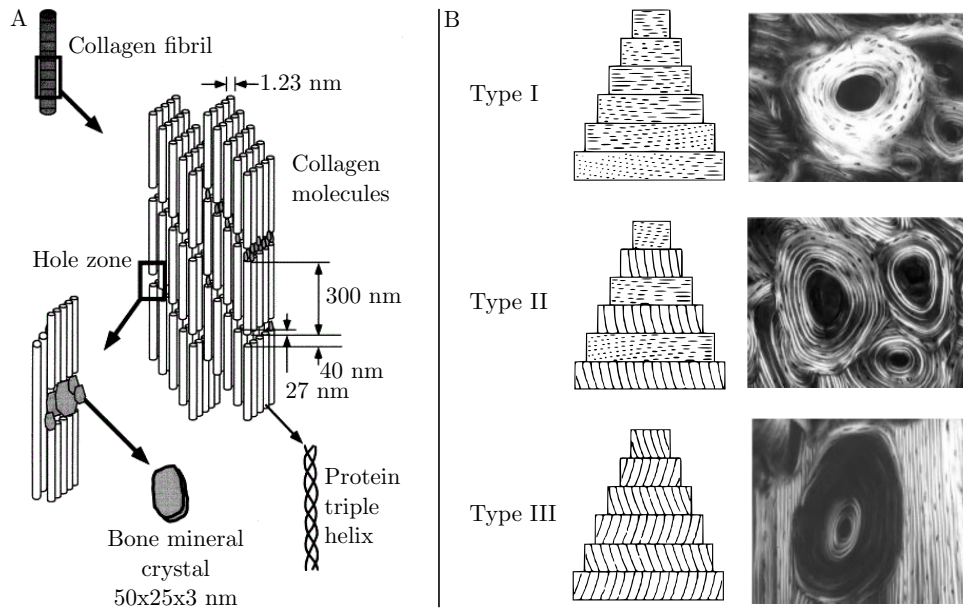


FIGURE 1.13: Collagen fibrils dimensions and orientation inside osteonal bone. A: shows typical dimensions of collagen fibrils (extracted from [35]). B: shows the three types of orientation of collagen fibres and associated circularly polarised light (CPL) images (extracted from [41]).

scaffold for bone implants [37]. This synthetic material facilitates the implant osseointegration with the living bone [44, 45]. Concerning the cement line which surrounds the osteonal bone, its internal composition differs from the adjacent bone. It contains 90% of the phosphorus and calcium of those found in the adjacent regions (osteonal and interstitial bone). In addition, sulphur part in cement lines is higher than those in lamellar bone. The different chemical composition makes the mechanical behaviour of cement lines different.

1.1.3.3 Cortical porosity: devices to detect it (Cooper *et al.* [31])

As shown by the two previous parts of this manuscript, cortical porosity is present at lower microscopic scale: hundreds of microns and below for vascular canal network and LCN (Figure 1.12). This diverse architecture creates voids within the compact bone and has an impact on the mechanical behaviour at higher scale. Hence, for several decades, this architecture is investigated so as to quantify its volume and the global shape of the vascular network. However, it is important to consider what type of architecture, i.e., which scale, has to be measured in order to heuristically chose the adapted device. In 2016, Cooper *et al.* [31] publish a review of the different types of devices to consider in order to detect bone architecture or geometry. This review is summed up in table 1.1 below. The current part reports as it was reviewed by Cooper *et al.* [31].

Nowadays, it remains a major issue to in-vivo detect cortical porosity. Indeed, some devices are used to assess the health of bones. The most common device used is X-Ray absorptiometry, named

DXA. It consists in the assessment of the bone mineral density (BMD) and is mainly measured on the femoral neck or on the spine. From BMD, two factors can be measured: Z-score and T-score. The first one evaluates the deviation of a subject's value by considering age, gender or race. It is used to evaluate healthy growth of children by comparing the score with a similar population (age, gender, region) and even became a standard used by World Health Organization (WHO) [46, 47]. The second score is assessed from comparing subject's value, measured from the femoral neck, with the data available in NHANES (National Health and Nutrition Examination Survey) database and also became a standard factor used by the WHO [48, 49]. T-score is useful to evaluate osteoporosis in femoral neck by comparing with a healthy reference population. However, DXA is restricted to an areal assessment of the BMD (aBMD, g cm^{-2}) with an insufficient resolution to detect cortical porosity. To enhance this measure, Computed Tomography (CT) or Peripheral Computed Tomography (pQCT) can be used in order to obtain a volumetric measure of BMD (vBMD, g cm^{-3}). Unfortunately, both are limited by spatial resolution which is still higher than cortical porosity. High resolution pQCT appeared in 2004 and helps to obtain a resolution below $100\text{ }\mu\text{m}$. Yet, the device can only detect widest canals within the bone ($80\text{ }\mu\text{m}$ isotropic resolution) but can be more accurate when associated with an optimized post-processing method [50]. To enhance spatial resolution for X-ray imaging, radiation dose needs also to be increased (fourth order power relation): this is the main limitation of x-ray imaging. As a consequence, a more recent X-ray scanner has been created and is called EOS [51]. It is based on a high sensitive detector (multi-wire proportional chamber) in order to reduce radiation dose for an acceptable spatial resolution of $250\text{ }\mu\text{m}$ and is half-priced compared to a classic CT scan. One of the numerous advantages of this device is the very low time needed for a whole stand adult body (15sec) and thus it reduces exposure time to radiation. However, this resolution is higher than most of cortical pores that makes this device unsuitable to correctly detect the entire porosity. In order to avoid radiations, Magnetic Resonance Imaging can be used (MRI). It consists in the detection of fluids movement within the bone. Obviously, resolution isn't enough to pick up in vascular network. Merely the marrow cavity and the widest pores in the endosteal side of the cortical bone can be observed. NMR (Nuclear Magnetic Resonance spectroscopy) is an enhancement of MRI. It has a better resolution so as to detect free water in the widest pores wherever they are in the bone cortex. Hence, the cortical porosity is indirectly assessed and consequently underestimated. Furthermore, periosteum isn't clearly distinguished from cortical matrix and can affect results.

Consequently, this review concludes that in-vivo devices are insufficient to directly measure the entire porous network of the cortical bone. So far, only ex-vivo processes can be used to entirely scan cortical architecture. One of the mostly used is the conventional X-ray tubes, also called $\mu\text{-CT}$ (desktop or laboratory $\mu\text{-CT}$). This kind of scanner can easily reach a resolution below $10\text{ }\mu\text{m}$ which

is enough to detect vascular canals. However, only little volumes can be scanned and LCN can't be detected (or only the widest osteocytes). A significant timing scan can be necessary and can affect bone properties by drying it. This device remains accessible for laboratories. To enhance the scan precision, Synchrotron Radiation CT provides slice images with a resolution below 1 μm . It is very useful to detect vascular canals, LCN and microcracks [34]. But this type of process requires important structure and is really expensive. Whatever the type of device, raw data needs to be processed so as to obtain some features such as the porous part of the bone. This process differs from one study to another and is mostly limited to planar assessment (see section 1.1.4.3 for further details).

Obviously, microscopy can be used to identify cortical porosity (as shown by Figure 1.11) but is limited to an external area study from ex-vivo specimens. However, all the previously described devices can't clearly exhibit osteonal bone from interstitial bone. Gray level obtained from X-ray imaging depends on the absorption rate of the matrix. Consequently, the difference between the two types of bone isn't enough to be distinguished. This issue can be solved by preparing the bone sample to stain cement line and osteons (as used by Mirzaali *et al.* [52] with a Von Kossa staining).

1.1.4 Bone remodelling: a throughout life process

In spite of the high rate of mineralisation of bones, this hard tissue remains a living tissue. Thus it has a dynamic process which occurs at a microscopic scale and impacts upper scale. This is the bone remodelling and evolves throughout the life and depends on the gender and the lifestyle. When remodelling fails in the elderly, it strongly disrupts the mechanical behaviour and increases the fracture risk. Moreover, this part aims at proving that cortical porosity can't be limited to a volume that weakens the mechanical behaviour. Indeed, the living porosity can also be considered as a signalling system which transforms mechanical stimuli to chemical ones so as to activate the bone remodelling.

1.1.4.1 A microscopic process

The bone remodelling is a process that closely links bone creation with bone resorption. This phenomenon was revealed in the 60s by two pioneer works done by Frost [53, 54] and is thoroughly investigated so far [55–58]. The phenomenon is named Basic Multicellular Unit (BMU). First, it consists in the resorption of bone organised by osteoclasts cells which acidify and proteolyse collagen fibres and hydroxyapatite crystals (Howship lacunae) [56]. Then, this resorption is followed by a new

Device	Result	Strength	Weakness
X-Ray absorptiometry			
Shortened name DXA	Areal Bone Mineral Density estimation (aBMD)	In-vivo	Under estimates fracture risk
Technology X-ray absorption	Trabecular Bone Score (T-Score) Extension with Hip Structural Analysis (HSA)	High volume scanning Fast	Undirect assessment of cortical porosity Low resolution (100s of microns) Planar study Radiation
Computed tomography			
Shortened name CT or QCT	Volume Bone Mineral Density estimation (vBMD)	In-vivo	Undirect assessment of cortical porosity
Technology X-ray absorption	Trabecular Bone Score (T-Score) Variation of vBMD along a shaft	High volume scanning	Low resolution (100s of microns) Radiation
Peripheral computed tomography			
Shortened name pQCT	Similar principle as QCT but limited to human limbs	In-vivo	Undirect assessment of cortical porosity
Technology X-ray absorption	Volumetric density, moments of inertia, ...	More data than QCT	Low resolution (100s of microns) Radiation
High resolution pQCT			
Shortened name HR-pQCT	Same as pQCT but with better resolution	In-vivo	Under estimation of cortical porosity
Technology X-ray absorption		More data than QCT	Unsuufficient resolution (over 60 μm) Radiation
Magnetic Resonance imaging			
Shortened name MRI	Detection of fluids inside and surrounding bone	In-vivo	Undirect assessment of cortical porosity
Technology Magnetic resonance	Only marrow is detected	No radiation	Limited to large pores near endosteum Periosteal surface not clearly distinguished from cortical bone
Nuclear Magnetic Resonance spectroscopy			
Shortened name NMR	Detection of fluids inside and surrounding bone	In-vivo	Undirect assessment of cortical porosity
Technology Magnetic resonance	Detection of free water in the largest pores	No radiation	Limited to large pores Periosteal surface not clearly distinguished
Conventional X-ray tubes			
Shortened name μ -CT	Creation of slice images uniformly distributed	High resolution (down to 1 μm)	Ex-vivo
Technology X-ray absorption		Direct assessment of cortical porosity	High radiation
			Low volume scanning No or largest LCN porosity detected
Synchrotron Radiation CT			
Shortened name SR- μ CT	Creation of slice images uniformly distributed	Very high resolution (<1 μm)	Ex-vivo
Technology X-ray absorption		Direct assessment of cortical porosity	High radiation
		Assessment of LCN porosity	Low volume scanning

TABLE 1.1: Review of the different devices used to detect the porosity within the bone as reported by Cooper *et al.* [31].

bone matrix created by a cluster of cells called osteoblasts. The entire unit has a similar shape of a vascular canal where the tip is closed by a cone (Figure 1.14).

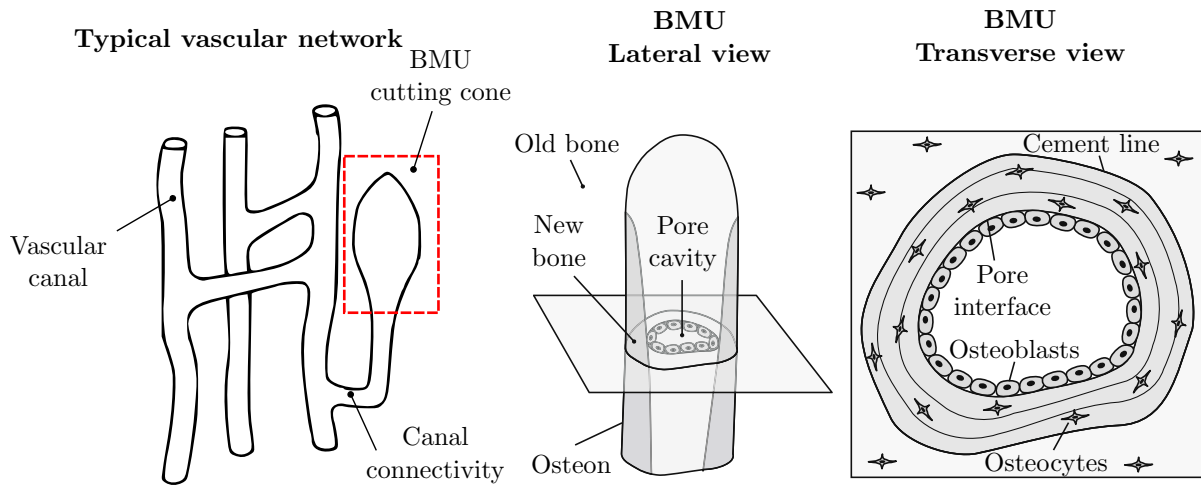


FIGURE 1.14: Typical BMU scheme located in cortical bone. As shown by the left scheme, BMU can be considered as a canal where the tip is closed by a cone (cutting cone) (scheme extracted from [22]). Middle and right schemes display a lateral and transverse view of the BMU architecture associated with the within cell activity, respectively (both extracted from [58]).

Since several years, BMUs are investigated using methods such as mathematical models based on cell activity [57, 58]. Indeed, their detection into the bone matrix remains hard to assess. Therefore, using this type of model, their activity and consequences on the cortical bone can be estimated. However, in 2017, Lassen *et al.* [59] published an original study where the cell activity is directly assessed (See also Figure 1.15). This work is quite revealing in several ways. First, it is the first work where cell densities are directly in vitro quantified. Second, data come from human bones during growth, adulthood and in the elderly. Consequently, it can state available data for healthy and deficient bone turnover. Third, the correlation between cone geometry and cell activity is proved. Three phases can be found in a BMU cone. The first one concerns the Initial Resorption surface (IRs) located on the cone tip where the osteoclasts (primary osteoclasts) erode the bone matrix (cutting cone). It is followed by a reversal-resorption surface (RvRs) where secondary osteoclasts and osteoprogenitors (immature osteoblasts) are sparsely distributed along the surface (Figure 1.15). Through the RvRs, bone keeps being eroded by osteoclasts while osteoprogenitors are continuously recruited. Hence, while IRs elongates the canal, RvRs widens it. 83% of overall resorption occurs in the RvRs phase. Bone resorption is stopped where osteoprogenitors density reaches a threshold value of 39 mm^{-1} along the perimeter. Once this threshold is reached, osteoprogenitors cells become osteoblastic cells and bone formation begins. Consequently, the length of the RvRs directly derives from the osteoprogenitors recruitment rate. A longer RvRs will also create a wider canal which will be more porous. Likewise, a longer RvRs means a higher temporary bone lack during the bone remodelling cycle and consequently a more porous cortical matrix.

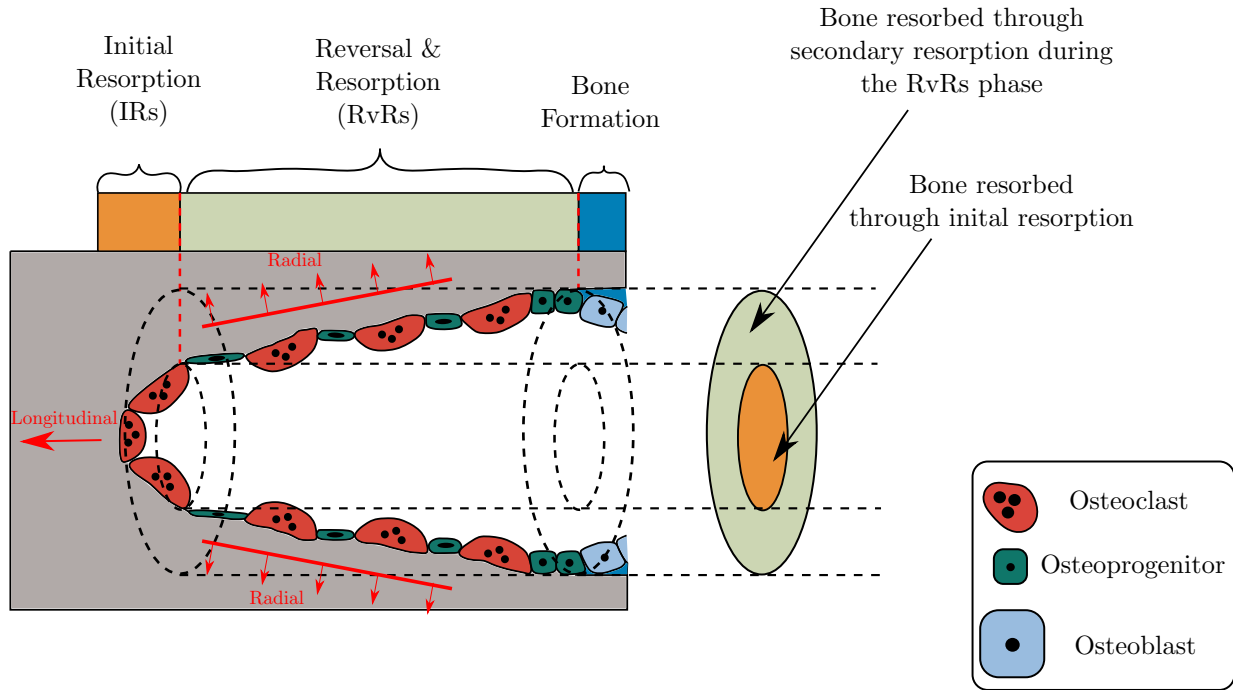


FIGURE 1.15: BMU cell activity (scheme extracted from [59]). The cutting cone has a complex cell activity where three steps can be highlighted: Initial resorption (IRs), Reversal & Resorption (RvRs) and bone formation. It shows the impact of the cell activity on the shape of the canal.

The osteoblasts keep forming new bone until being trapped within the bone matrix and subsequently become osteocytes with canaliculi [56]. Osteocytes remain an active cell by recruiting osteoclasts and create new Howship lacunae where it is required. These cells are mechanosensitive and are able to signal and transport molecules and nutrients within the bone. They convert strain energy into electrical and biochemical signals [60]. This phenomenon is called mechanotransduction and remains fairly obscure. Fluids inside LCN are squeezed and produce shear stresses at the osteocytes (canalicular fluid flow hypothesis) [60]. Overall, LCN has a major role in osteocyte metabolism which acts on the bone remodelling activity [27].

1.1.4.2 The osteoporosis: a bone remodelling defect

As previously shown, the bone remodelling is a complex dynamic process which acts throughout the life. The efficiency of this process depends on numerous factors and can easily be disordered. The most common bone disorder is the osteoporosis. About 200 million peoples worldwide are affected by this disease [61]. Men and women are both concerned especially in the elderly. Indeed, about one third of the European and American population are osteoporotic with a continuously growing risk of fractures into late adulthood and elderly [61, 62]. With the population ageing, it becomes a societal interest to diagnose it. However, it remains hard to detect it and is often found when the patient suffers a fractured bone. The WHO proposes a diagnosis process coupled with DXA (X-Ray absorptiometry)

so as to measure BMD and compute T-score (see section 1.1.3.3 for more details). T-score below -2.5 means that osteoporosis is present. Low bone mass, named osteopenia, can be diagnosed with a T-score between -1 and -2.5 [48]. However this factor is one of many. Indeed, osteoporosis can be classified into two groups called primary and secondary osteoporosis, respectively. The first one concerns the osteoporosis caused by hormone deficiency (mainly postmenopausal women) and ageing. The secondary osteoporosis concerns bone mass reduction induced by other diseases (AIDS, depression, ...), lifestyle (lack of vitamin D, smoking, alcohol, ...) or medication (anticoagulants, glucocorticoids, ...) [63, 64].

Defects of the bone remodelling affect the osteoblastic activity. The Receptor activator of nuclear factor $\kappa - \beta$ ligand (RANKL) and osteoprotegerin (OPG) are physiologic mediators which strike the function of osteoclasts. The ratio OPG/RANKL expresses the delicate balance of the bone remodelling: a high ratio will result bone disease such as primary osteoporosis [65]. Different medical treatments exist so as to restore bone remodelling equilibrium. Biphosphonates (antiresorptive agents) seem to be the most commonly used for osteoporosis. Calcium, vitamin D or selective oestrogen receptor modulators can also be recommended. However, these treatments remain heavy medication (several years of treatment) with side effects and osteoporosis type should be considered so as to personalise for each subject [61, 62, 65].

1.1.4.3 The dynamic turnover assessment of the cortical porosity

Cortical bone has a dynamic turnover which evolves according external factors (age, lifestyle, ...). As described in the section 1.1.4, bone remodelling affects the cortical porosity so as to adapt the within architecture to the mechanical stress applied on it. Thus, the cortical porosity needs to be investigated in order to analyse its impact on the mechanical behaviour. All the values (porosity, diameter, ...) reported in this part are mostly obtained from studies where devices allow the direct measurement of the cortical (μ -CT, SR- μ CT, or microscopy) in order to avoid underestimation of the architecture (vascular canals or LCN). However, limited by current device resolution, it mainly concerns ex-vivo samples (see section 1.1.3.3 for more details concerning the device limitations). Table 1.2 stores some data obtained from bibliography.

To assess the architecture of the cortical bone, several features are commonly used. The first one is the porosity and can be noted Po.V/TV. This is the most usual computed feature from cortical architecture. Its computation remains easy: this is the ratio between pores and bone matrix. It requires a pre-treatment of the slice images: the image threshold. This method differs from a study to another because the sample shape, devices and image artefacts have to be considered and there is

	Device	Type of porosity	N	Age	Gender	Bone	Po.V/TV (%)	Ca.Dm (μm)	Canal density	Lc.Dm or Lc.Li (μm)	Lacunae density
Ashique <i>et al.</i> [66]	Confocal laser scanning microscopy	Vascular and LCN	5	20-23	Female	Femur	4.8 \pm 0.5	-	-	7.6 \pm 3.3	695 \pm 79 mm^{-2}
			6	70-86	Pooled	Femur	15.4 \pm 9.8	-	-	7.7 \pm 3.4	546 \pm 79 mm^{-2}
Bousson <i>et al.</i> [26]	SR-pCT	Vascular	19	72-103	Female	Femur	15.9 \pm 9.9	102 \pm 72	-	-	-
Carter <i>et al.</i> [67]	SR-pCT	Vascular and LCN	30	20-86	Female	Femur	-	59 \pm 30	-	11.7 \pm 2.4, 3.3 \pm 0.6, 1.5 \pm 0.5	23942 \pm 2529 mm^{-3}
Cooper <i>et al.</i> [68]	pCT	Vascular	77	18-92	Pooled	Femur	7.3 \pm 6.9	117 \pm 90	12.3 \pm 2.4 mm^{-2}	-	-
			27	20-87	Female	Femur	9.8 \pm 9.2	150 \pm 119	11.5 \pm 2.5 mm^{-2}	-	-
			77	18-92	Male	Femur	5.9 \pm 5.0	99 \pm 63	12.7 \pm 2.2 mm^{-2}	-	-
Gauthier <i>et al.</i> [34]	SR-pCT	Vascular and LCN	8	50-91	Female	Femur	8.5 \pm 2.8	73 \pm 30	-	22.7 \pm 1.0, 11.7 \pm 0.5, 5.4 \pm 0.6	21617 \pm 3622 mm^{-3}
			8	50-91	Female	Radius	4.3 \pm 2.5	63 \pm 19	-	25.7 \pm 2.2, 10.8 \pm 0.7, 5.4 \pm 0.3	21191 \pm 1480 mm^{-3}
Hunter and Agnew [69]	Virtual slide microscope	Vascular and LCN	30	49-100	Pooled	Femur	13.2 \pm 1.0	-	-	-	940 \pm 178 mm^{-2}
			30	49-100	Pooled	Radius	12.2 \pm 1.1	-	-	-	1074 \pm 137 mm^{-2}
			39	46-99	Pooled	Femur	6.0 \pm 4.0	-	-	-	-
Mirzaali <i>et al.</i> [52]	pCT	Vascular	18	44-64	Pooled	Femur	3.4 \pm 3.0	-	-	-	-
Neil Dong and Edward Guo [70]	Transmitted light microscope	Vascular	17	60-93	Pooled	Radius	6.2 \pm 3.3	207 \pm 40	-	-	-
Tjong <i>et al.</i> [71]	pCT	Vascular and LCN	19	16-89	Pooled	Femur	6.2 \pm 3.3	57 \pm 13	-	3.9 \pm 0.4	-
Wang and Ni [33]	Custom built image acquisition	Vascular and LCN	12	16-89	Male	Femur	11.0 \pm 3.2	56 \pm 10	-	3.8 \pm 0.3	-
			7	21-84	Female	Femur	15.3 \pm 5.3	62 \pm 19	-	3.9 \pm 0.6	-
Bry [10]	pCT	Vascular	11	64-77	Male	Femur	5.7 \pm 1.2	-	-	-	-
			11	64-77	Male	Humerus	5.0 \pm 1.3	-	-	-	-
Bala <i>et al.</i> [72]	pCT	Vascular	13	6-18	Pooled	Fibula	10.3 \pm 6.5	139 \pm 62	-	-	-
			16	50-91	Pooled	Fibula	15.9 \pm 10.3	144 \pm 69	-	-	-

TABLE 1.2: Overview of the cortical porosity assessment. Only studies with direct measurement of the porosity from human bone was considered. Consequently, ex-vivo values are reported. N is the number of samples. Age is reported as min-max of the set of samples. Po.V/TV is the cortical porosity (Vascular canals and LCN porosity). Ca.Dm and Lc.Dm express the diameter of the vascular canals and lacunae (considered as spheroid), respectively. Lc.Li is the 3 main axis length computed from the lacunae which is considered as ellipsoid. Density for canals and lacunae can be computed by both ways: as an areal value (mm^{-2}) and as a volume value (mm^{-3}).

no existing gold-standard method. It has a great impact on the results and can be combined with additional filters [66]. However, global fixed threshold method seems to be the most common one [26, 66–68, 72]. Hence, pores and bone matrix can be distinguished from white and black pixels. Due to ex-vivo studies (imposed by devices limitations), many studies concern samples from late adulthood or elderly age. However, several works get data for young people but remains limited. Cortical porosity seems to increase with age [66, 68, 72]. This rise is the result of three possible micro-architecture changes: pores enlargement [68, 73], density of canals [72] or both [74]. As a matter of fact, these changes differ from the region of interest. For instance, Perilli *et al.* [74] have shown that in the femoral bone, in the endosteum part, pores coalesced to create giant pores which leads to a trabecularisation and a thinning of the cortical cortex in the elderly (Anterior, Medial and Lateral regions). Consequently, the mean in-plane spacing between pores decreased with age. Bala *et al.* [72] suggest that the higher porosity, in the periosteum region, results from a denser canal network. Po.V/TV values reported in Table 1.2 are highly dispersive. These differences are explained by the restrictive volume of interest, the different types of bone, gender or subject. Indeed, as explained in the section 1.1.4, the bone remodelling is age, gender, lifestyle dependant and mechanical sensitive. Thus, bearing and non-bearing bone architectures should be investigated from bone harvested on similar subjects. This type of study requires a heavy experimental protocol (harvest, number of available cadavers) and is consequently poorly investigated. Moreover, human cortical bone remains thin (less than 10 mm) even in the longest bone of the skeleton (femur) [10, 18]. Therefore, bearing-bones (especially femur) are the most reported bones in human studies while the others are overlooked (Table 1.2). Still, works done by Bry [10] report tomographic results obtained from four adult males where 9 humeral and 11 femoral samples were extracted from right members. Pore diameters are slightly larger in femur than humerus. As a result, femoral samples are more porous than humeral ones. The conclusion reveals that the femur is a bearing bone which carries more strain and requires a more active mechanotransduction process to supply and activate bone remodelling. Gauthier [30] observed the same trend by comparing the radius and femur and concluded that the non-bearing bone is less mechanosensitive than the bearing one. Indeed, the radius receives less damages and requires less mechanosensors, i.e. osteocytes. Recently, osteocytes shape and orientation are investigated so as to understand the link with microdamages. Osteocytes have an ellipsoid shape and are spatially oriented [34, 67]. However, some studies report a diameter to quantify the osteocyte shape because they are limited to a planar study (microscopy) [33, 66]. The shape is highly related with the mechanosensitivity of the osteocytes. A circular shaped osteocyte is reported as more sensitive than a flatter one [75, 76]. Carter *et al.* [67] reports a lacunar volume reduction in older women. However, osteocytes are reported as flatter and more elongated for women below 50 years old than women over 50 years old. Moreover, lacunae are orientated to the longitudinal axis of the femur and is age-independent. The density

of lacunae decreases in the elderly. Flat shape osteocytes are observed in radius whereas rounder osteocytes are found in the femur [34]. These changes impact the vascularisation inside LCN and make bone less mechanosensitive with age [67].

Even though the vascular canal network has wider dimensions and is easier to be observed than LCN, it is very tortuous, spatially arranged and interconnected. Consequently, little research report 3D geometrical analysis of the bone architecture with a clear definition of canals. So a great part of studies are limited to planar study. For example, the canal length is poorly investigated while it is very useful for numerical approach of the cortical bone multi-scale behaviour (see section 1.2.1.2). Likewise, the vascular canal network is often restricted to a longitudinal canal network (Haversian canals) transversally crossed by a thinner one (Volkmann's canals) without being clearly defined (orientation, length). This simplified view begins to be qualitatively refuted with the emergence of accurate 3D scanning devices [26, 68]. To three-dimensionally investigate the vascular network, a skeletonisation algorithm seems to be the most common technique [22, 71, 77]. This method preserves the topology by successively thinning a set of voxels and is adapted for tubular architecture assessed by tomography [78]. However, a few geometrical features can be computed and are limited to the orientation or length of the canals. Cooper *et al.* [22] studied the vascular network by skeletonising it and reports a mean canal length of 385 μm from only two human femoral samples. Nevertheless, the authors specified that the smallest channels were lost due to the resolution (10 μm) and didn't specify how canals are defined. Two studies where orientation of canals are reported were found. However, while the first one concerns only two animal samples [77], the second one used an important resolution size (18 μm) which can affect network topology [71] and only one angle is computed. Yet, vascular network orientation is oblique in human bone (47.7°) and differences were found between two species which means that it is highly bone turnover dependant. Likewise, BMU cutting cones are found in the vascular network (see Figure 1.14) and are the witness of the bone remodelling. The BMU shape is complex and requires 3D analysis. No study where BMUs are automatically detected from tomographic data or 3D assessed was found.

Osteons can't be exhibited by conventional tomographic devices. Indeed, the contrast between osteonal and interstitial bones is weak because both have similar composition and makes similar attenuation contrast [30]. Hence, it is essential to use microscopy devices associated with a stained technique to measure osteon and cement line dimensions. In the cortical bone, the osteon size highly fluctuates [24]. This variation can be explained by the fact that osteon is the result of BMU bone creation. This bone creation can be activated by micro damages. To replace old damaged bone, Howship cavity is created with a size close to, or larger than, the zone to replace. Canal and osteonal areas are positively correlated [24]. Recently, two studies distinguished two types of osteon

[79, 80]. The first type is created from a penetrative resorption which doesn't overlap the pore of an existing osteon. The second one overlaps at least one existing canal. The type 1 osteon embodies the first remodelling in bone matrix. Their number decrease with age and make bone more porous. The type 2 osteon is the result of a subsequent bone turnover and contributes to pore enlargement and are more numerous in the elderly. Moreover, many studies, which don't distinguish the different types of osteon, show that osteonal area tends to decrease with age [81–83]. The different studies agree with the fact that the reasons of these changes remain unclear so far.

1.2 Mechanical behaviour of the cortical bone: a multi-scale study

The bone remodelling affects the cortical architecture by adjusting the within topology. Obviously, the mechanical behaviour is impacted. A considerable amount of literature has been published on the mechanical characterisation of the cortical bone. These studies used different types of method and device so as to obtain the mechanical features. However, the complex arrangement of the cortical bone makes the mechanical test tricky to assess. Moreover, cortical bone is nearly always harvested from cadavers and the preservation method has received considerable attention. The aim of this part is to have an overview of the mechanical behaviour of the human cortical bone so as to infer the mainstream features in spite of the diversity of methods and tested samples.

1.2.1 Macroscopic and mesoscopic scales

1.2.1.1 Experimental characterisation

The cortical bone has a complex macromechanical behaviour. Due to the spatial arrangement of bone matrix (mineralised collagen fibres), LCN (ellipsoid shaped osteocytes) and vascular canals network (mainly oriented along the longitudinal axis of bone), different conjectures regarding the mechanical behaviour can be made.

First, cortical bone can be considered as a transverse isotropic material. Indeed, several studies reveal that the elastic properties are predominant along the main axis of bone and are similar for both radial and tangential axis (transverse plane axis) [72, 84, 88]. The transverse isotropy is mainly ruled by the mineral crystals orientations in collagen fibres whereas orthotropy is affected by the within porosity [89]. The ratio between longitudinal and transverse stiffness is about 1.5 [70, 84, 90]. Outside of the natural solicitation axis (longitudinal axis), ultimate strain and stress are dramatically reduced (Figure 1.16) [10, 90, 91].

	Mechanical test	N	Age	Gender	Bone	E (GPa)	C ₃₃ (GPa)	σ _y (MPa)	σ _u (MPa)	ε _u (%)
Mirzaali <i>et al.</i> [52]	Tensile	32	46-99	Pooled	Femur	18.16 ± 1.88	-	71.56 ± 10.19	92.95 ± 10.07	1.9 ± 0.6
	Compression	32	46-99	Pooled	Femur	18.97 ± 1.84	-	115.06 ± 16.36	153.59 ± 21.63	1.3 ± 0.3
	Torsion	32	46-99	Pooled	Femur	6.07 ± 0.57	-	31.62 ± 4.00	46.31 ± 5.82	-
Lefevre <i>et al.</i> [84]	Ultrasound	14	1-18	Pooled	Fibula	-	24.00 ± 5.15	-	-	-
		7	1-15	Pooled	Femur	-	19.00 ± 5.50	-	-	-
		16	50-95	Pooled	Fibula	-	28.00 ± 3.71	-	-	-
Bry [10]	Tensile	11	64-77	Male	Femur	15.8 ± 5.4	-	-	133.0 ± 30.6	1.6 ± 1.0
		9	64-77	Male	Humerus	23.8 ± 4.6	-	-	113.3 ± 26.4	0.7 ± 0.2
Evans [85]	Tensile	35	41.5	Male	Femur	14.6	-	-	100	1.32
		35	71	Male	Femur	13.3	-	-	67	1.07
		67	41.5	Male	Tibia	18.5	-	-	103	1.76
		34	71	Male	Tibia	15.9	-	-	82	1.56
		20	33	Male	Fibula	18.8	-	-	98	2.10
		16	59	Male	Fibula	14.9	-	-	78	1.19
		17	44-64	Pooled	Femur	16.61 ± 1.83	-	-	-	-
Neil Dong and Edward Guo [70]	3 point bending	48	69.3 ± 5.1	Pooled	Femur	17.85 ± 1.01	-	-	183.76 ± 15.11	1.79 ± 0.26
		74	54-85	Pooled	Femur	19.9 ± 1.8	-	107.9 ± 12.3	-	-

TABLE 1.3: Overview of the human cortical bone mechanical behaviour. Values are obtained from quasi-static tests. E and C_{33} means the longitudinal elastic modulus and the longitudinal elastic coefficient of the stiffness tensor, respectively. For torsional tests, E is the shear modulus. σ_y is the yield stress. σ_u and ϵ_u represents the strength and strain at the fracture.

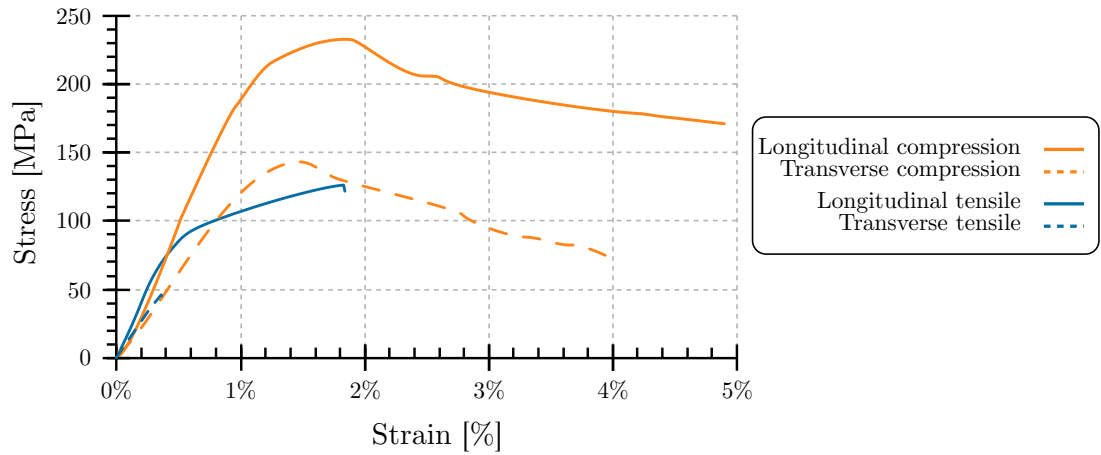


FIGURE 1.16: Comparative plot of the cortical bone mechanical behaviour extracted from [90] (Stress and strains are reported as absolute values to make comparison compression and tensile curves easier). It is apparent from this plot that in the transverse direction, mechanical properties are heavily reduced (especially for tensile ones). It is important to notice that these curves were obtained from bovine femurs.

Second, the cortical bone compressive properties differ from tensile ones. Indeed, the yield limits and ultimate stress are higher for compression loadings (longitudinal axis). However, the elastic modulus is similar for both loadings [10, 52, 90–92]. As a matter of fact, during the compression, the voids close whereas they expand during tensile tests. It could explain why yield modulus is less affected than the other features. Figure 1.16 displays a typical compressive and tensile behaviour of the cortical bone in both transverse and longitudinal axis obtained from bovine femurs [90]. This figure is quite revealing in several ways. First, it confirms that the overall compressive behaviour outstrips the tensile one. Second, it shows the complete behaviour of the cortical bone in both transverse and longitudinal axis. It clearly highlights the orthotropy of the cortical bone. Compressive behaviour is less impacted by loading direction. When transversally tensile tested, mechanical features are dramatically reduced. At failure, stress and strain don't exceed 50 MPa and 0.5 %, respectively [10, 90]. It suggests that bone adapts itself in order to better perform along the main axis of the long bone diaphysis. Third, it points out that cortical bone remains a brittle material whatever the direction or loading.

Some studies use three-point bending tests to perform cortical bone mechanical tests [86, 93, 94]. This mechanical test requires specimens shape easier to harvest, whereas dumbbell-shaped samples are required for tensile tests. However, for example, to compute the elastic modulus, assumptions need to be done to apply the beam theory. Moreover, bending tests material in both compression (upper side) and tensile (bottom side) but is particularly adapted for crack propagation and toughness assessment [95].

Figure 1.17 displays a typical tensile curve where common features are shown. Stress is computed from the ratio between load measurement (N) and the specimen area (m^2). The type of surface used

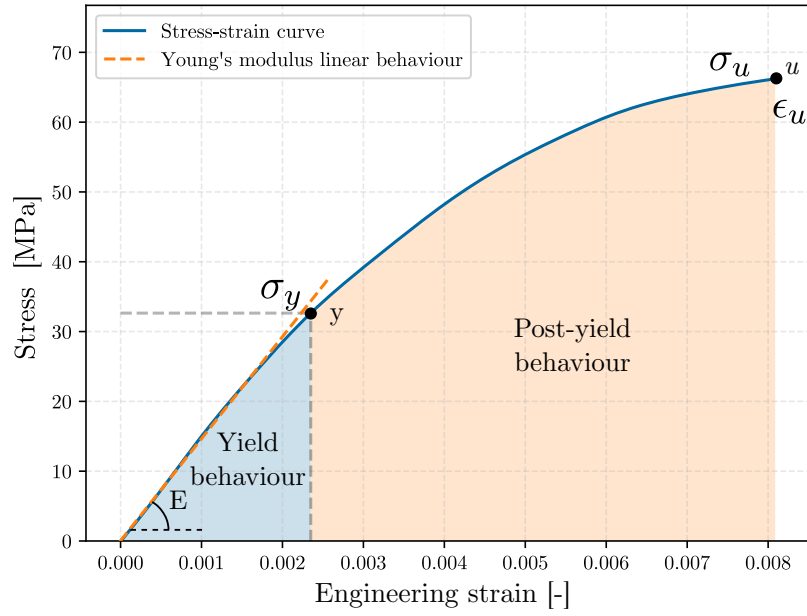


FIGURE 1.17: Tensile stress-strain curve of cortical bone. The elastic and post-elastic behaviour are not clearly exhibited. Different methods exist to extract yield features. y is the yield point and u is the fracture one. Tensile toughness can be computed as the area below the curve. Some of these features are reported in Table 1.3.

to compute stress is not clearly specified. Indeed, when coupled with tomography, it is possible to choose either total surface with or without the porosity. Displacements are mainly measured using strain gauge extensometers [52, 90–92, 96]. Strain is computed as the ratio between displacements and the initial length. The elastic modulus can be obtained by several ways: by computing the initial slope of the curve [90], or using two end cycle points (for cyclic tests) [10, 91] or by linear regression at low strains value [52, 92]. Elastic modulus obtained from ultrasound studies are computed by multiplying the density with the square value of the wave velocity [72, 84]. The yield point (y on Figure 1.17) is mainly assessed using a 0.05 or 0.2 % offset criterion [52, 87, 92]. For cyclic tests, yield point is defined when residual strains are obtained [91]. Strain and stress at failure, commonly called ultimate point, are assessed as maximum strain and its corresponding stress. Toughness is the area under stress-strain curve (J m^{-3}). Most of these features are reported in Table 1.3. Concerning the elasticity of the cortical bone, ultrasound devices offer a complete assessment of it. Indeed, the entire elastic tensor can be computed (C_{ii} coefficients) [72, 84, 88].

The stiffness of the cortical bone evolves throughout the life. Indeed, during the growth and puberty, the bone stiffness increases with age up to reach an adult value (between 8 and 22 % of increase) [72, 84, 85, 88]. On the other hand, the stiffness decreases in the elderly [52, 72, 84]. The reason of this evolvement can be explained by changes in the cortical architecture. The different studies converge to demonstrate the negative correlation between bone stiffness and cortical porosity. Hence, the growth porosity decrease and elderly increase aim at increasing and decreasing of stiffness,

respectively. However, shear properties are not clearly linked with porosity and opinion differ between studies. Similar negative correlations with porous volume are found for yield and ultimate limits [52, 70, 72, 84, 85, 87, 88]. Correlation with others architectural features were found. For instance, Bala *et al.* [72] reveals that the mean separation value between vascular pores is positively correlated with stiffness: more pores are distant, stiffer is the bone. However, the authors suggest that vascular network should be deeper investigated and further compared with elasticity. Mirzaali *et al.* [52] demonstrates that macromechanical features are poorly gender-dependent. As shown by Table 1.3, many studies concern human femur assessment. Non-bearing bone are poorly investigated. Bry [10] study reports the tensile test of human femur and humerus bone harvested from 4 old males. Humerus has a higher longitudinal elastic modulus (23.8 ± 4.6 GPa) than the femur (15.8 ± 5.4 GPa). No differences were found for transverse loading. Femur tends to have a higher ultimate strain than the humerus (1.6 ± 1.0 % versus 0.7 ± 0.2 %). However, flat specimens without reduced section were used for tensile tests. This creates a heterogeneous strain field in the measured area and can consequently affect failure behaviour.

Damages can also be assessed. To characterise the damage evolution, cyclic tests are commonly used [10, 91, 92]. It consists to sequentially load and unload. Each new cycle reach an upper strain value to the former one. Damages accumulation is associated with bone modulus loss. Thus, a modulus is computed for each cycle and damage is reported as the ratio between the cycle modulus and the initial modulus (first or preconditioning cycles). In bearing-bones, no significant differences were found for damage accumulation rate between tension and compression [91]. However, accumulated damages in compression strongly impact elastic tensile properties but not vice versa. These differences can be explained by previous accumulated microcracks opening and closing in tension and compression, respectively [92]. By comparing humerus and femur bones, it seems that damage accumulation rate is higher and occurs later for the bearing bone. Bry [10] grants these variations to the architecture differences. A denser osteonal bone network in the humerus is found and delays the crack propagation thanks to the numerous cement lines.

1.2.1.2 Numerical implementation

Since several decades with the computing enhancement, multiple human Finite Element Models (FEM) have emerged [97]. Many of them aim at predicting the global body behaviour during car crash tests so as to avoid the expensive use of a physical dummy model. Hence, several of them were created by car manufacturers. Indeed, THUMS human body was developed in the early 2000s by Toyota Motor Corporation [98] and is thoroughly enhanced [99]. HUMOS was developed by the

European Commission IMT and the LAB (Peugeot Citroën Renault) [100]. Both these human models are based on a 50th percentile male. Other 50th percentile male models are available and called GHBM (Global Human Body Models Consortium) [101, 102] and HUByx (specifically designed for ballistic prediction) [103]. More recently, CHARM model has been developed so as to account body differences between a 10 (CHARM-10) and a 70 year old (CHARM-70) female [104]. All these models focus on the geometrical assessment of the human body. For instance, to obtain a representative 50th percentile body, the personalisation is limited to the thickness or the length of bones. No variation of material law is implemented. Moreover, attention is particularly paid to the rib cage so as to predict injuries for internal organs. Overall, the cortical bone behaviour is considered as an elastic-plastic material associated with a failure criterion based on a maximum strain value. The material properties of long bones are mainly issued from Yamada *et al.* [105] (1970) which is one of the few studies which reports material data for the humerus. For instance, HUByx uses a bone modulus of 11 GPa and 17 GPa for humerus and femur, respectively. Same trend is used by the CHARM-70 model: the humerus has a lower elastic modulus (14 GPa) than the femur (17 GPa). This trend is in contrast with values recently reported by Bry [10]. Moreover, the material is considered as isotropic with a compressive behaviour similar to the tensile one.

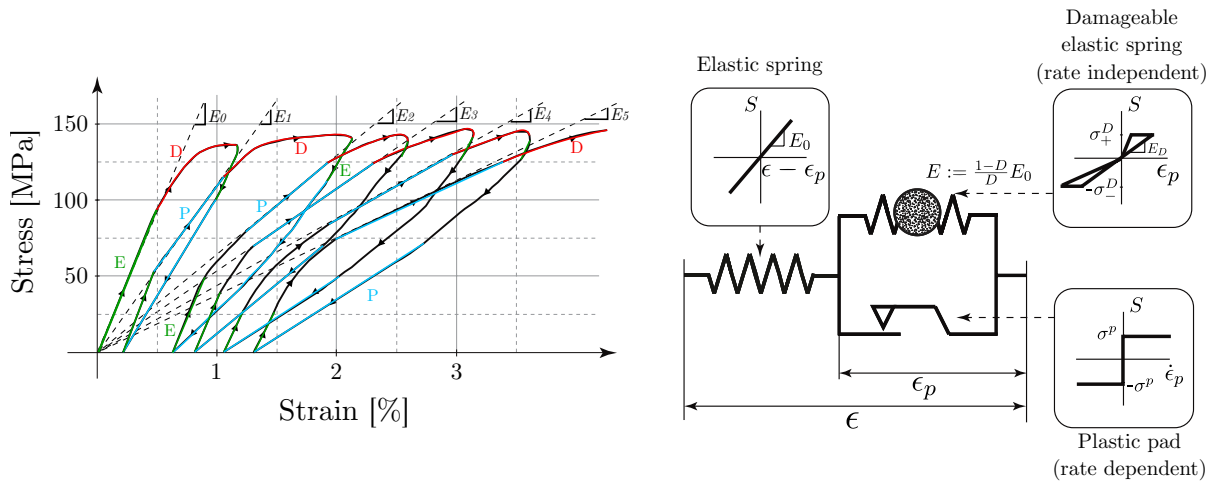


FIGURE 1.18: One dimensional rheological model used by Garcia [106]. On the left figure is a cyclic tensile test where within mechanical behaviour of the bone are described. E means the linear elasticity. D is the damaging mode. P is the plastic Mode. On the right figure is an associated 1D rheological model used to describe the mechanical behaviour (Figure extracted from Garcia [106]).

Hence, one of the most common ways to characterise the macromechanical behaviour of cortical bone is the use of a constitutive law based on a 1D rheological model [92, 106, 107]. Garcia [106] described the mechanical behaviour by splitting it in three consecutive modes: the intact linear elasticity, the damaging mode and the plastic mode (illustrated by Figure 1.18). The first mode is found at both the beginning of loading and unloading phases and is explained by the bone cohesion.

The second mode appears at the end of each cycle and consists in the creation of microcracks that leads to permanent strains and energy dissipation. This damage is computed from the reduction of bone modulus. The last mode embodies the sliding of previously created microcracks. Consequently, it can be found on both loading and unloading curves. Regarding the rheological setup, an elastic spring is used to characterise the intact linear elasticity (E on left figure 1.18). It is included in series with a damageable elastic spring in parallel with a rate dependent plastic pad so as to characterise the damaging (D on left figure 1.18) and the plastic mode (P on left figure 1.18), respectively.

However, although the high influence of the within architecture, this type of model does not consider it. Due to the multiscale architecture, it can not be easily meshed and computation time would be extremely high. To overcome this lack, multiscale models are used. One of the most famous multiscale models uses the Mori-Tanaka scheme [108]. This scheme is an expanded version of the Eshelby scheme [109, 110] by considering an unbounded medium crossed by N ellipsoids phases where between phases interactions are considered. Thus, this model aims at using an equivalent homogeneous model of the heterogeneous material to describe. Consequently, it requires to know the shape and the orientation of the microscopic architecture and the local mechanical features. The shape of inclusions is described by the ratio, named the aspect ratio, between the length and the diameter of the inclusion. Therefore, an elongated shape inclusion has a high aspect ratio value (over 1). Several studies use this scheme for cortical bone [111–115]. Hamed *et al.* [113] describes a transverse isotropic bone matrix (interstitial bone) crossed by a different transverse isotropic porous phase (osteonal bone with 4% of void). To compute stiffness of both phases, the authors reviewed different mineral, collagen and water volume fractions, elastic moduli and orientations. Hence, the interstitial bone is stiffer than the osteonal bone (23.15 GPa vs 18.87 GPa for longitudinal stiffness coefficient). However, the aspect ratio is not reported. Other studies [111, 114], that use a Mori-Tanaka scheme so as to describe the mechanical behaviour, deem the aspect ratio. The conclusion was an aspect ratio over 10 has low-impact on the stiffness coefficients. Both of these studies use an aspect ratio over 20 by justifying that an osteon has a length of several millimetres [114] or by a low error value [111]. No direct assessment of the vascular canals aspect ratio was found due to a lack of 3D data for the vascular network (see section 1.1.4.3).

Recently, FFT (Fast Fourier Transform) homogenisation has been used for cortical bone assessment [116]. This meshless method requires less computation costs than classical FEM model. μ -CT images can be used as inputs so as to consider within architecture. This recent method is still currently in process and several open-source toolboxes are available [117]. Cai *et al.* [116] studied 55 samples harvested from human femoral diaphysis. The high number of samples reflects that this process requires much less computation time than it should be necessary for FEM models. Interestingly, the

authors reveal that the bone architecture is enough to explain the macroscopic stiffness changes in the cortical bone.

1.2.2 Microscopic and submicroscopic scales

The previously reported mechanical tests concern macroscopic and mesoscopic mechanical tests. Therefore, the architecture impacts the results. And thus, these tests can be regarded as structural tests instead of material tests. In order to solve this issue, some mechanical tests exist and aim at characterising the bone matrix without the architecture. In addition, some micro FEM models are also assessed so as to investigate, for instance, the crack propagation inside the bone matrix.

1.2.2.1 Experimental methods

At micro and nanoscopic scales, the gold-standard protocol to characterise bone matrix is the indentation test. It consists in the penetration of a hard tip on the surface of a material. Load and depth can be measured (indentation test) or not (hardness test) (Figure 1.19). In both cases, the impacted area needs to be evaluated so as to obtain mechanical features. Several types of tip exist [118]. Circular cones and spherical shapes are well designed for soft material: local stress depends on the penetration depth. They are also used for wear testing. Three-sided pyramidal shapes (Berkovich and cube-corner) have the advantage to have only one point contact with material. Berkovich tip has a flat shape with low curvature radius which allows to test thin layers. Four-sided pyramidal shapes (Vickers and Knoop) are also available. Vickers is the most common tip used. It has an angle of 65.27° and can be used for both nano and micro-indentation. Tips are used to be in diamond because of the very high material stiffness.

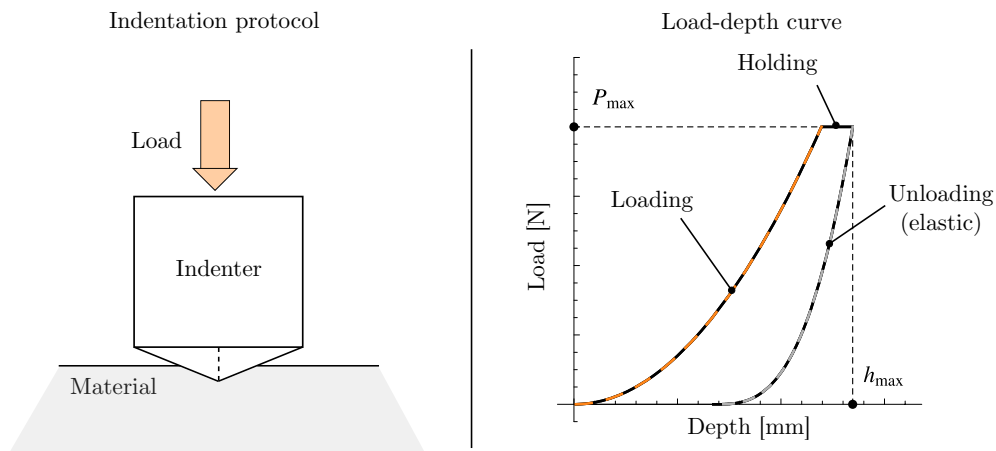


FIGURE 1.19: Indentation protocol and curve.

A typical indentation test begins by a linear loading ramp, followed by a holding period and an unloading ramp (Figure 1.19) [119]. When no load or depth measurement is provided, the area dimensions are measured using an optical device and only material hardness can be computed. Indentation devices provide load and depth measurements where several features can be assessed from it. These features are commonly computed from the theory explained in the pioneer work of Oliver and Pharr [120] based on the well-known Hertz contact theory. The material elastic modulus (E_f) and hardness (H) can be computed using equations 1.1 and 1.2.

$$\frac{1}{E_r} = \frac{1 - \nu_f^2}{E_f} + \frac{1 - \nu_i^2}{E_i} \quad (1.1)$$

$$H = \frac{P_{max}}{A_p(h_{c_{max}})} \quad (1.2)$$

E_r is the reduced modulus. It is the first modulus to be obtained by Oliver and Pharr [120] theory. However, it is a global modulus and depends on the tip features (ν_i and E_i) and the material features (ν_f and E_f). To obtain the reduced modulus, the global and machine compliances (C and C_m , respectively) and tip shape features have to be considered (equation 1.3).

$$C = \frac{1}{S} = \frac{1}{\left(\frac{dP}{dh}\right)_{h=h_{max}}} = C_m + \frac{\sqrt{\pi}}{2\beta\sqrt{A_p(h_{c_{max}})}} \frac{1}{E_r} \quad (1.3)$$

β is a shape correction factor and depends on the tip shape. A_p is the projected area of the footprint when $h = h_{c_{max}}$. $h_{c_{max}}$ is the contact depth between the tip and material surface when $h = h_{max}$. $\left(\frac{dP}{dh}\right)_{h=h_{max}}$ is the slope of the unloading tangent at $h = h_{max}$. C_m is a factor which considers the compliance of the machine during the test. It needs to be considered and previously determined. Oliver and Pharr [120] suggests a power law relation so as to fit to the unloading part of the curve as following (equation 1.4):

$$P = b(h - h_f)^m \quad (1.4)$$

h_f is the final depth after complete unloading. b and m are the fitting parameters.

The indentation test is widely used to determine the bone tissue modulus [119] and some results are reported in Table 1.4. Several conclusions can be made. First, even at the lamellar level, the anisotropy of bone is revealed. Indeed, transverse values (elastic modulus and hardness) are lower

	N	Direction	Age	Gender	Bone	Matrix	E (GPa)	H (MPa)
Vandenbulcke [111]	85	Longitudinal	64-77	Male	Humerus	Pooled	18.3 ± 1.1	450 ± 40
	<85	Longitudinal	64-77	Male	Humerus	Osteon	16.5 ± 1.2	393 ± 33
	<85	Longitudinal	64-77	Male	Humerus	Interstitial	19.4 ± 1.9	468 ± 47
	37	Transverse	64-77	Male	Humerus	-	18.6 ± 2.8	457 ± 57
Lefevre [121]	15	Longitudinal	4-18	Pooled	Fibulae	Osteon	24.4 ± 1.9	1040 ± 70
						Interstitial	25.8 ± 1.9	1106 ± 19
	16	Longitudinal	50-95	Pooled	Fibulae	Osteon	26.1 ± 1.9	1065 ± 86
						Interstitial	26.6 ± 1.1	1226 ± 72
Wu <i>et al.</i> [122]	10	Longitudinal	58-89	Pooled	Femur	Osteon	16.5 ± 3.5	-
						Interstitial	20.2 ± 3.5	-
Mirzaali <i>et al.</i> [52]	38	Longitudinal	46-99	Pooled	Femur	Pooled	19.1 ± 1.8	455 ± 78
						Osteon	18.1 ± 1.7	408 ± 69
						Interstitial	20.1 ± 1.2	503 ± 56
		Transverse	46-99	Pooled	Femur	-	13.1 ± 1.9	395 ± 89

TABLE 1.4: Micro and nanoscopic mechanical features reported by indentation tests. Matrix means the type of bone which has been tested (osteon or interstitial bones). E and H are the bone elastic modulus and the bone hardness, respectively.

than axial ones [52, 111]. This could be explained by the anisotropic arrangement of collagen fibres and mineralised crystals in the bone matrix. However, the degree of anisotropy remains lower than the macroscopic one. Second, osteonal bone seems to be softer than interstitial bone in the adulthood [52, 111]. This trend is not clearly exhibited during the growth due to the presence of primary bone [121]. Third, bone matrix features are age-related during the growth [121]. Both elastic modulus and hardness increase with age due the continuous decrease of primary bone. Finally, no significant differences were clearly found between male and female samples [52, 122].

1.2.2.2 Numerical approaches

Numerical tools can be used so as to understand the crack propagation mechanism inside the bone matrix. They aim at studying the impact of the architecture or local bone mechanical features on the crack propagation. They are often based on experimental data (tests, scans, microscopy) and use X-FEM (extended finite element method) approach.

Demirtas *et al.* [123] used seven transverse microscopy slices (1 mm^2) of mid-diaphysis harvested for mid-shaft tibiae cortical bone. They were numerically extruded in order to obtain a 1 mm^3 cubic sample and placed in a compact tension (CT) test sample. Osteon and interstitial bone are exhibited. The impact of the mechanical features distribution inside bone is studied. Indeed, the authors explain that long-term osteoporotic treatment using bisphosphonate can lead to a reduction of the heterogeneity of mechanical features in bone matrix. Results show that the crack unhindered propagates in

a homogeneous bone matrix. The authors suggest that bone optimises the within mechanical heterogeneity so as to maximise crack propagation resistance. The cement line (which surrounds osteons) deflects the crack path. Hence, interstitial bone is more easily damaged than osteons. Similar trends were concluded from analogous studies [124, 125].

However, these studies are limited to planar studies. Mullins *et al.* [126] reports the impact of the 3D architecture on the strain repartition in the bone by regarding a 3D REV (Representative Element Volume). It consists in the modelling of one longitudinal Haversian canal transversally crossed by two Volkmann's canals. No experimental data are used for orientation of vascular canals and REV is consequently lightened to the classical Haversian-Volkmann vascular network. It was shown that orientation of the Haversian canal has a significant effect on the global mechanical behaviour of the VER. Moreover, maximum stress was found near intersections that would suggest that the angle of canal connectivity can strongly affect the bone fracture.

1.3 Conclusions

This chapter reviews the current knowledge on the cortical bone for a bearing and a non-bearing bones by focusing on humerus and femur. These two bones are considered as long bones and are located in the appendicular human skeleton. The cortical bone is a thin layer which stiffens the entire skeleton. The first part of this chapter highlights that the cortical bone thickness varies according to the human subject, the anatomical faces and through the shaft. It remains thicker in femur than humerus. The second part shows that the cortical bone has a multiscale architecture with various shapes. A tortuous vascular network, called Haversian or Volkmann's canals, ensures the blood vessels and nutrients supply within the bone. A smaller network, the lacunar-canalicular network, also performs the nutrients supply. Both of these networks take part into bone remodelling. The bone tissue has also a spatial arrangement which is made of collagen fibres and hydroxyapatite. All of these features contribute to the anisotropy of bone. A short review, based on the Cooper *et al.* [31] study, points out that, currently, to directly assess the cortical porosity, X-ray imaging (tomography) is the only adapted device. However, mainly due to radiation, it inflicts ex-vivo studies.

Subsequently, to replace old bone or microcracks, a dynamic process is described and occurs throughout the life: the bone remodelling. This turnover affects the architecture according to the applied stress. This process is activated by mechanosensors, called the osteocytes, located in lacunae of LCN. They are mechanosensitive by converting mechanical energy into electrical and biochemical signals: this is the mechanotransduction. The Bone Multicellular Unit (BMU) is the phenomenon

which initiates the bone resorption and creation. BMUs are found in the vascular network as closing canals. However, they are only studied in 2D and no automatic detection criterion was found so as to assess a complete quantification.

Several studies were reported on the cortical porosity assessment in order to determine the impact of external factors, such age or gender, on the architecture. The porous volume, also noted $Po.V/TV$, tends to increase in the elderly due to pores enlargement and denser canal network [66, 68, 72–74]. $Po.V/TV$ and canal diameters are the most reported features but are only studied in 2D. Only two studies which analyses the 3D arrangement and shape of the vascular network were found. The first one concerns only two animal samples [77] and the second is limited to the computation of one mean angle of canals. However, qualitative analysis of the vascular network aims at proving that the cortical network is very tortuous. On the contrary, 3D assessment of LCN proves that lacunae have an ellipsoid shape with directional bias along the longitudinal axis of bone [30]. Their density tends to decrease in the elderly. They also become rounder which is the witness of the mechanosensitivity decrease. A few studies report the porosity assessment of both bearing and non-bearing from same human subject. Femur is more porous than the humerus [10]. Likewise, osteocytes are flatter in non-bearing bone [30]. These differences are explained by the fact that bearing bone requires more supplies (blood or nutrient) and a more active turnover than non-bearing ones.

Due to its complex spatial arrangement, the cortical bone can be considered as a brittle transverse isotropic material [72, 84, 88]. Compressive features (stress and strain) are higher than tensile ones [90]. Cortical bone adapts itself so as to better perform its mechanical behaviour along the axial direction rather than transverse direction [90, 96]. As the porosity grows in the elderly, mechanical features decrease [52, 72, 84]. Bry [10] shows that humerus is stiffer than femur with lower strain at failure. However, only 20 samples from 4 male subjects were studied and samples had not reduced section (tensile tests). Consequently, cortical bone is mostly reported as an elastic-plastic with damage material. Some numerical human models are reviewed and reveal that implemented material laws for humerus and femur are in contrast with reported values (i.e. Bry [10]), and the personalisation of human models only concerns geometry of bones. Mori-Tanaka numerical scheme considers the within multiscale architecture of material and is often used for cortical bone [111, 112, 114]. Therefore, an important shape factor, the aspect ratio, is used as inputs of this kind of model and no study directly assesses this factor (from architecture analysis). To understand the macromechanical behaviour, indentation tests can be used to measure bone matrix stiffness. It is based on the Oliver and Pharr [120] study. The interstitial bone is stiffer than the osteons [52, 121, 122]. The elastic modulus is age-related in the growth and doesn't differ between male and female samples [52, 122].

Hence, the following chapters attempts to clarify and overcome some lacks that are thoroughly reported and highlighted in this chapter. First, the second chapter of this manuscript aims at providing an innovative method, coupled with the use of a μ -CT device, so as to quantify 3D features from the vascular architecture of the cortical bone. This method requires to clearly define the vascular canals so as to quantify them. Actually, connectivity are also automatically detected and some features are also measured. Another novelty, and not the least, is the automatic detection of BMUs, cradle of the bone remodelling. Due to the lack of gold-standard method, attention is paid to the image processing of the tomographic slices. The entire Python script is step-by-step described and its robustness is quantified. This method is applied on 77 human samples harvested from 10 cadavers. Humeral and femoral samples are compared so as to exhibit significant differences between these two bones. Bias impact on the architecture is also investigated. A correlation study is performed to find some relationships between the numerous architectural features.

Chapter 2

A three dimensional geometric quantification of cortical vascular canals

Contents

2.1	Introduction	43
2.2	Material and methods	43
2.2.1	Body and sample preparation	43
2.2.1.1	Human individuals	43
2.2.1.2	Shaft harvest and sample preparation	45
2.2.2	Micro-CT scanning	47
2.2.3	Algorithm	47
2.2.3.1	Python version	48
2.2.3.2	Image processing	48
2.2.3.3	3D link detection and canals construction	50
2.2.3.4	3D connectivity detection	52
2.2.3.5	3D canals smoothing	52
2.2.3.6	3D canals and connectivity features	52
2.2.3.7	BMU detection and features computations	56
2.2.4	Algorithm validation	60
2.2.4.1	Error quantification	60

2.2.4.2	Robustness quantification	61
2.2.5	Statistics	61
2.3	Results and discussion	62
2.3.1	Error and robustness quantification	62
2.3.1.1	Error quantification	62
2.3.1.2	Robustness quantification	62
2.3.1.3	Conclusions	64
2.3.2	Bearing and non-bearing comparisons	64
2.3.2.1	General features	65
2.3.2.2	Canal features	67
2.3.2.3	Connectivity features	74
2.3.2.4	BMU features	76
2.3.3	Side comparison	78
2.3.4	Inter-parameter relationships	81
2.4	Conclusions	86

2.1 Introduction

As reviewed by the first chapter of this manuscript, the cortical porosity has a great influence on the macromechanical behaviour. It is formed of two types of porosity. The first one concerns the lacunar-canalicular network (LCN). The second one is formed by the vascular canals often called Havers and Volkmann canals. As the LCN has recently been studied in 3D [30], the vascular network never has been. Actually, some 3D rendering are provided by studies [22, 72, 74] and reveal that the vascular network is very tortuous. This spatial arrangement makes complex to assess this network in 3D. Yet, this complex architecture has a great influence on the macromechanical behaviour as reported by planar studies and the previous chapter.

The purpose of this chapter is to describe a novel method which is able to detect and quantify the 3D geometrical features of the vascular network. This method requires the use of a μ -CT device with a 2.94 μm resolution. The novelty of this method lies in the fact that canals are detected by seeking a 3D link between two pores located on subsequent images. To obtain representative data, connectivity are detected. Hence, vascular canals are clearly defined as voids which range from connectivity to another one. Another novelty, and not the least of them, is also the automatic detection of BMUs. 17 three-dimensional features are computed for each canal, connectivity and BMU. The algorithm is step-by-step described. Due to the novelty of this method, an error and robustness quantification are described and performed. Then, this method is applied on 77 human samples harvested from both left and right humeri and femurs of 10 human cadavers. Thus, comparison study is performed by comparing the bearing with the non-bearing bone, but also by comparing left and right limbs of each type of bone.

This method has been subject to one publication in an international journal [127] and one international conference paper [128].

2.2 Material and methods

2.2.1 Body and sample preparation

2.2.1.1 Human individuals

This study is based on the harvest of paired humeri and femurs from 10 cadaveric human subjects (7 males, 3 females) provided by the body donation bank Anatomy Laboratory (Faculty of Medicine,

University of Lille 2). No known bone disease was reported. Upper limb side bias is unknown. Care was taken to reduce bone drying by using a body embalming procedure (methanol, distilled water, glycering and phenol solution) injected in the carotid artery two days maximum post-mortem [10]. Figure 2.1 and Table 2.1 store information of the human subjects. Height and weight were recorded prior to the autopsy. The Body Mass Index (BMI) is obtained by dividing the weight by the square of the body height. It highlights that the study concerns peoples in the elderly (age: 65-96 years old). The left femur of 0014 wasn't available because of the presence of a hip prosthesis in the femoral shaft which made impossible to extract the cortical bone. Weight and height of 0017 weren't provided by hospital and remain unknown. However, this subject can be qualitatively reported to the SmallF group (see further for explanations of morphology groups).

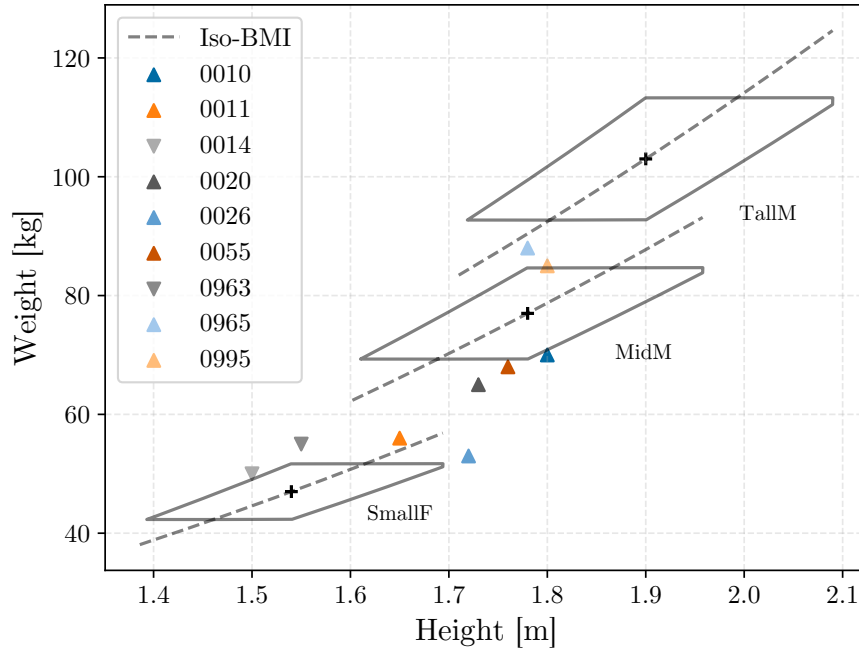


FIGURE 2.1: Morphology plot of the human subjects. Males and females are displayed with triangles up and down, respectively. This plot was introduced by Bertrand [129] for morphology analysis. Dotted lines show the iso-BMI line for each group. Subject 0017 isn't displayed due to missing information.

To easily compare the morphology of individuals, a weight-height plot is used (Figure 2.1). In order to identify morphology, three morphotypes obtained from Bertrand [129] are displayed :

- TallM: 95 percentile European male subject (Height: 1.90 m, Weight: 103 kg);
- MidM: 50 percentile European male subject (Height: 1.78 m, Weight: 77 kg);
- SmallF: 5 percentile European female subject (Height: 1.54 m, Weight: 47 kg);

Subject number	Gender	Age	Weight [kg]	Height [cm]	BMI [kg m ⁻²]	Morphotype	Length [cm]			
							Femur		Humerus	
							Left	Right	Left	Right
0010	Male	65	70	180	21.6	MidM	43	43.5	35	34
0011	Male	86	56	165	20.6	SmallF	40	40	33	33
0014*	Female	96	50	150	22.2	SmallF	42	42	28	28
0017**	Female	96	-	-	-	SmallF	40	40	30	30
0020	Male	80	65	173	21.7	MidM	43	43	31	31
0026	Male	75	53	172	17.9	SmallF	42	42	32	32
0055	Male	68	68	176	22.0	MidM	39	39	28	29
0963	Female	87	55	155	22.9	SmallF	38	40	30	30
0965	Male	77	88	178	27.8	MidM	42	42	34	34
0995	Male	87	85	180	26.2	MidM	43	43	30	30

TABLE 2.1: Global overview of human subjects. 7 males and 3 females subjects were obtained. BMI is the Bone Mass Index. Morphotype is the closest morphology group to the human subject used by Bertrand [129] (See Figure 2.1). Lengths of femurs and humeri were externally measured on the cadaver. (*): The left femur of subject 0014 wasn't available due to a hip prosthesis in the shaft. (**): Weight and height were unknown for subject 0017. However its morphology seemed to be close to the SmallF group.

Groups are plotted using a factor of $\pm 10\%$ from the reference weight, height and BMI. As shown by Figure 2.1 and contrary to expectations, none of individuals are located in any groups. A possible explanation for this is that morphotypes were established from a range of healthy peoples in the adulthood. In this study, weight and height are reported by hospital. It suggests that the subjects were unhealthy and probably bedridden for a while. Hence, the physical activity is highly reduced and then can affect the body weight (i.e. loss of muscle mass). For this reason, it can explain that subjects 0011 and 0026 (males) are close to the SmallF group. A hypothetical loss of mass suggests that subjects 0010, 0011, 0020, 0055 and 0965 are former MidM subjects. Likewise, 0965 and 0995 can also be considered as former TallM individuals.

2.2.1.2 Shaft harvest and sample preparation

On each body, a 100 mm mid-diaphysis was sectioned on left and right femurs and humeri (See Table 2.1 for details). Particular attention was paid to the extraction site. Indeed, the highest distal point and the trochlea are used to measure the length of the two bones (Table 2.1). Furthermore, these two points are also used to identify the mid-diaphysis line of bones. From this line, the 100 mm section is cut in order to be centred on the diaphysis. Figure 2.2 depicts the protocol used to obtain cortical bone samples.

Anatomical quadrants (Anterior, Medial, Posterior, Lateral) were easily identified on the femurs (linea aspera on the posterior side) so as to obtain a parallelepipedic sample from the lateral side

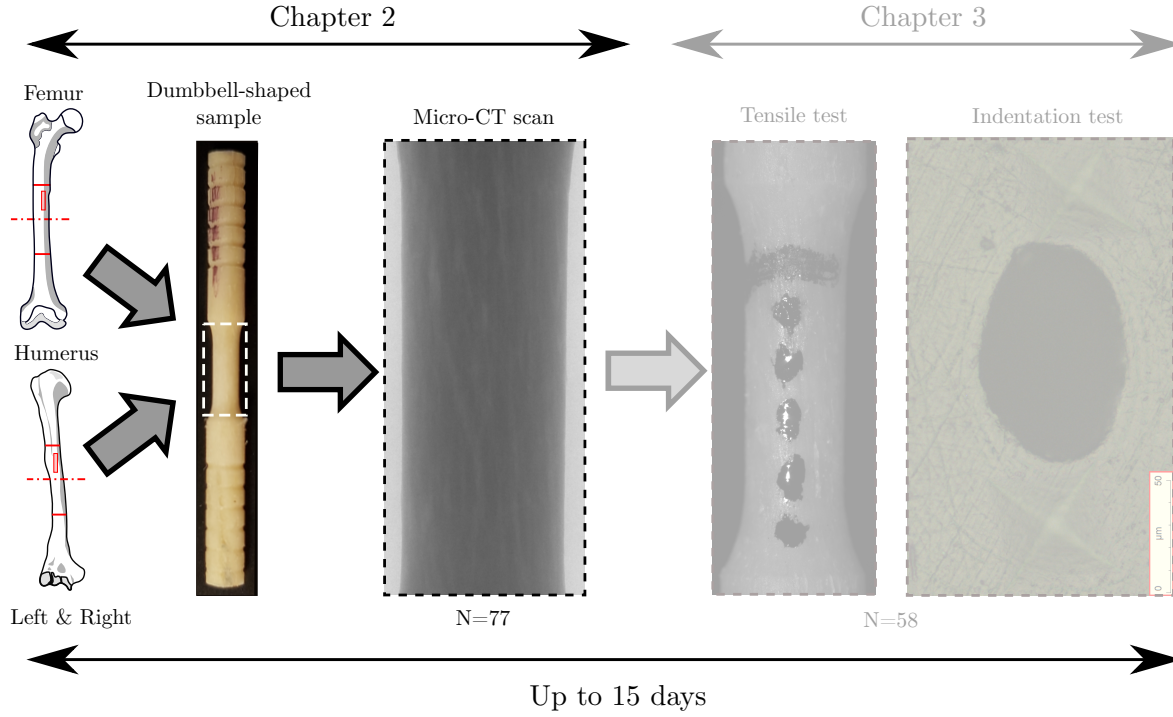


FIGURE 2.2: Shaft harvest and sample preparation scheme. The first step aims at harvesting a 100 mm piece of mid-diaphysis. Then, two parallelepipedal shape piece of cortical bone is extracted and lathed so as to obtain a dumbbell-shaped sample. Finally, the reduced section (targeted diameter = 2.5 mm, length = 6 mm) is fully scanned at a $2.94\mu\text{m}$ isotropic resolution. Following steps (tensile and indentation tests) are described in Chapter 3. Bone samples were stored in distilled water at 4°C up to 15 days after the shaft harvest.

using a surgical saw (CONMED, Hall Micropower). Humeral quadrants weren't identified due to the lack of a prominent border. In addition, the transverse shape of the humerus differed from one subject to another which adds complications to extract from the same location. This trend is confirmed by Perchalski *et al.* [15] that demonstrates the humerus pattern highly depends on the subject lifestyle. Therefore, and because of the thin cortical shell in humerus shaft, parallelepipedic samples were extracted on the thicker region. Specimens were cut through the cortical thickness and along the longitudinal axis of the shaft (50 mm) in the distal part of the sectioned shaft.

Parallelepipedic samples were subsequently machined using a desktop lathe (Optimum TU 2004V). First, the parallelepipedic samples were reduced to a cylinder with a 3.5 mm diameter. Then, the reduced section is centrally machined to attain a diameter of 2.5 mm along a gauge length of 6 mm with an inlet radius of 4 mm. Hence, a 50 mm long dumbbell-shaped sample is finally obtained. This shape is optimised in order to fully scan the gauge length and further tensile tests (described in chapter 3). Small grooves were also machined so as to reduce slippage risk during tensile test. Prior attention was paid to ensure the most perfect alignment as possible between each section of the sample.

Throughout the extraction and machining protocol and up to mechanical tests (Figure 2.2), bone

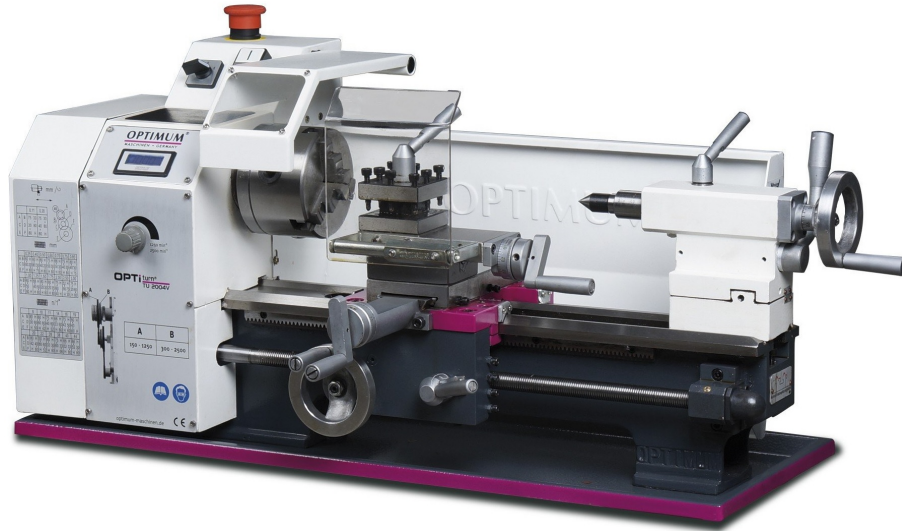


FIGURE 2.3: Optimum 2004V desktop lathe

was preserved in distilled water and stored at 4°C so as to avoid bone drying. Stefan *et al.* [86] reports that fresh-frozen bone preservation method (saline water at -20°C) is currently the best method to reduce effects on bone. However, recently, impacts of fresh frozen method on the cortical bone has been proved after a couple of days [93]. That's why, in this study, samples weren't frozen and a 15-day deadline after bone harvest was established.

2.2.2 Micro-CT scanning

All samples were scanned using SkyScan 1172 high resolution desktop micro-CT (80 kV, 100 μA , 180° , rotation step : 0.25°) at $2.94\mu\text{m}$ isotropic voxel size. All micro-CT slices images are reconstructed using Nrecon 1.7.04 software. About 90 min scan times per sample were necessary to obtain about 2300 slice images along the longitudinal axis. Hence, about 6.7 mm is scanned. The VOI corresponds to the reduced section volume of the dumbbell-shaped specimens. 77 samples were scanned. They are split into 36 and 41 femoral and humeral samples, respectively.

2.2.3 Algorithm

In this section, the algorithm is step by step described in the same order as the processing. First, the image processing and contours detection are detailed, especially the threshold method. The image processing was initially developed so as to automatically apply an adaptive threshold on different types of transverse shape. On parallelepipedic shape, beam hardening strongly affects the image and brightness isn't constant in the slice. This makes image processing more complex than a circular shape. Hence, in order to have the most generic image processing, parallelepipedic samples were

considered. However, the method can also be applied to cylindrical specimens. Second, the 3D link detection and canal construction are explained. Third, connectivity are detected and each canal is split at each intersection. Canals are subsequently smoothed in order to compute more realistic canal and connectivity features. Finally, BMU are automatically detected and some geometrical features are computed. So as to ease reading, the following newly defined symbols are summarised and illustrated in Appendix A. Please also refer to the lists of acronyms and symbols at the beginning of this manuscript.

2.2.3.1 Python version

The algorithm was carried out using Python 3.7 with OpenCV 3.2 [130] for image processing and contours detection. Statistical data were obtained using Scipy 0.19 [131], Numpy 1.13 [132] and Pandas 0.20.1 libraries and plotted via Matplotlib 2.0.0 [133].

2.2.3.2 Image processing

The first step of the algorithm is to read the slice images using OpenCV library and convert them into greyscale images (Figure 2.4). In order to minimise noise effects, an adaptive threshold method was developed and coupled with several filters. A bilateral filter is first applied to the raw picture. This filter is based on a blur algorithm but has the advantage to preserve edges of an image [134]. Because of brightness difference due to parallelepipedical shape of the sample (beam hardening artefacts), a global thresholding method can't be used. The customised threshold method is based on the Otsu threshold algorithm [135]. It consists in splitting each image along the brightness difference axis and independently processes and thresholds inner and outer portions (Figure 2.5). The number of portions is a user-specified input parameter and has to be chosen according width dimensions of the sample. A short sensitivity study has shown that 5 portions is a suitable value in most cases. Indeed, the brightness of each kind of portions can be adjusted using a global gamma correction (Equation 2.1).

$$P_{x_{corrected}} = 255 * \left(\frac{P_x}{255}\right)^{\left(\frac{1}{\gamma}\right)} \quad (2.1)$$

As shown by figures 2.5 and 2.6, it is essential to apply additional filters to the thresholded image. Actually, dummy pixels are still visible out of bone matrix and near pores. These dummy pixels are created from local brightness differences which affect the threshold result. To reduce noise, morphological filter followed by a hierarchical filter are applied. The first one consists in removing isolated pixels [136] on the thresholded image, and the second one is applied after edge detection

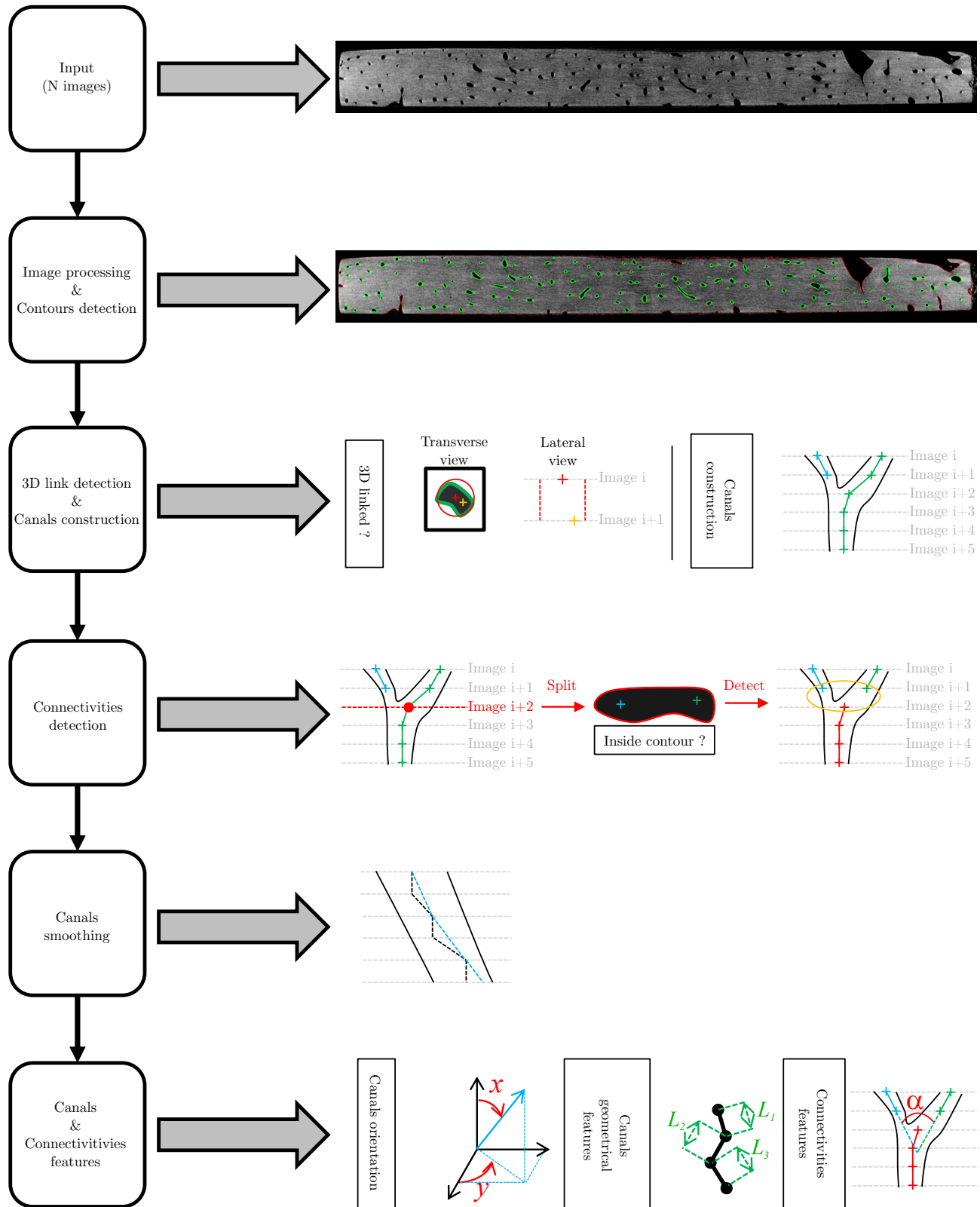


FIGURE 2.4: Global overview of the algorithm

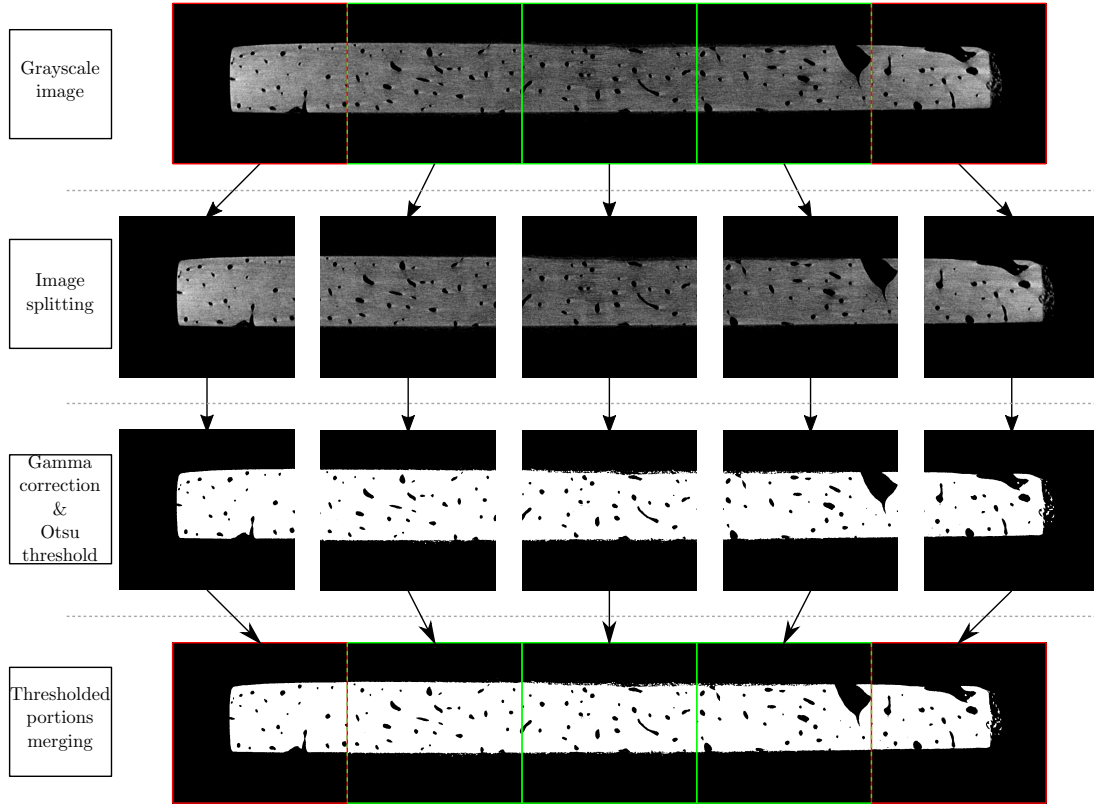


FIGURE 2.5: Image thresholding step. This step follows the bilateral filter but precedes the morphological filter. The figure shows the example with five portions along the width of the sample with 0.5 gamma correction on inner portions (no gamma correction on outer portions). Inner and outer portions are green and red surrounded, respectively. This figure was generated from the raw image, without applying any filter so as to note threshold efficiency.

and keeps only contours which the parent is the sample contour (Figure 2.6). Contours are sorted according their area value. Therefore, it is possible easily identify the sample contour from pore contours (Figure 2.6). One advantage of the above-described process is that it avoids the use of a qualitative global threshold value and generic values can be set : five portions per image applied with 0.5 gamma correction on inner portions give the best results.

2.2.3.3 3D link detection and canals construction

Previous studies have reported a 3D interpretation of the cortical porosity using the skeletonisation algorithm [22, 77]. However, these results focus only on few geometric features (orientation or length). In this chapter, a new 3D interpretation is proposed. The next step of the algorithm is the 3D link detection step between consecutive images (Figure 2.4). Indeed, from the detected contours, moments [130] are computed in order to obtain the area value of the contours (M_{00} moment), and to obtain the contour centroid coordinates (Equation 2.2).

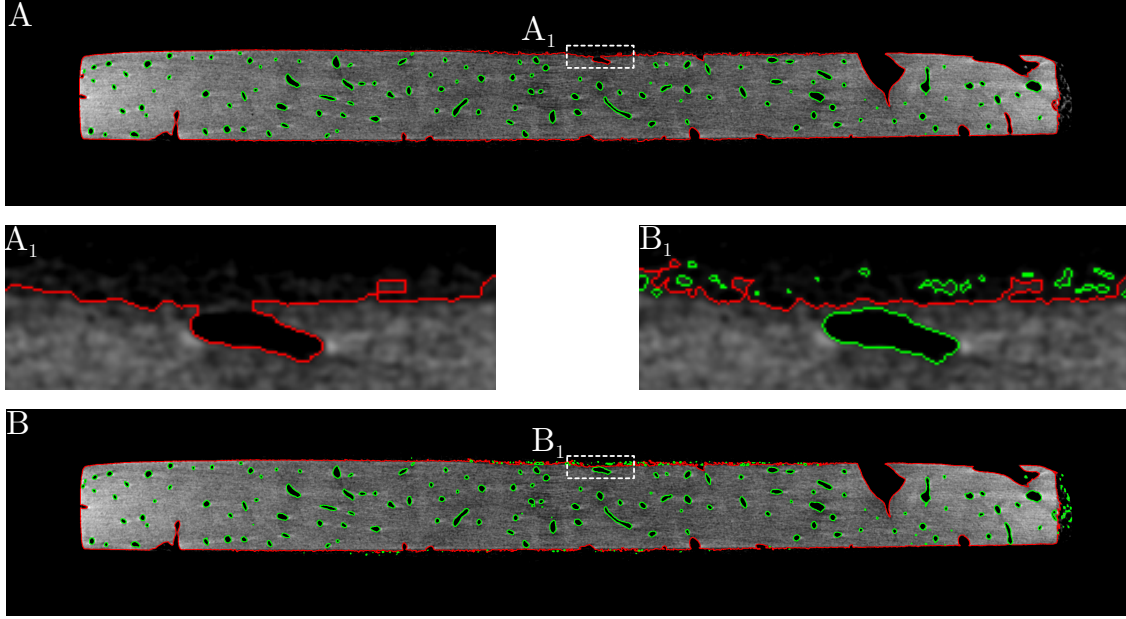


FIGURE 2.6: Comparison between contours from the filtered image (Image A) and contours from the raw image (Image B). Same threshold parameters are set (5 portions with 0.5 gamma correction on inner portions). Sample contour is highlighted in red. Images A and B have 126 and 248 contours, respectively.

$$\begin{pmatrix} ctd_x \\ ctd_y \\ ctd_z \end{pmatrix} = \begin{pmatrix} \frac{M_{10}}{M_{00}} \\ \frac{M_{01}}{M_{00}} \\ -i \end{pmatrix} \quad (2.2)$$

Centroid coordinates are written ctd_x , ctd_y , and ctd_z for x, y and z axes, respectively. Equation 2.2 shows that ctd_x and ctd_y are computed from contour moments. z coordinate is induced by longitudinal scanning. Hence, from these data, the contour's equivalent diameter can be computed. So as to create a 3D link between inter-slice contours, condition specified by Equation 2.3 should be reached.

$$\sqrt{(ctd_{i,j_1x} - ctd_{i+k,j_2x})^2 + (ctd_{i,j_1y} - ctd_{i+k,j_2y})^2} \leq Dm_{i,j_1} \quad (2.3)$$

In other words, this condition means that the projected distance between contour j_1 from the i^{th} image and contour j_2 from the $(i+k)^{th}$ image (left term on Equation 2.3) must be less than the equivalent diameter computed from the upstream contour, Dm_{i,j_1} , to be considered as a 3D link (see Figure 2.4 for schematic interpretation). k is a user-specified parameter which represents the number of images to compare until link detection. Isolated contours are not considered further. Due to high resolution scanning, only canals with over five segments are considered (To reduce residual noise and edge-effects).

2.2.3.4 3D connectivity detection

Previous works done by Cooper *et al.* [22] have shown that the cortical bone has a highly connected architecture. However, it is important to consider connectivity in order to obtain representative statistical values. Therefore, in this study, canals have to be split at each connectivity. At this stage in the proceeding, a set of canals is available (Figure 2.7a). Nevertheless, these canals aren't necessarily split at each connectivity and can pass through several connectivity (see Figure 2.4). Thus, an automated script is used to detect connectivity. Firstly, it consists in iterating each contour from each canal in order to detect the end of another canal inside the contour. If the end of a canal is inside the contour, the first canal is split at this point (Figure 2.4). This first iteration split all the canals at connectivity by detecting the end of another canal inside the contour. Then a second iteration performs the same test for each canal's end in order to detect connectivity.

2.2.3.5 3D canals smoothing

In order to reduce the occurrence of jaggies on wire centroid line, canals are smoothed. Indeed, oriented canal can be perceived as a set of longitudinal segments with occasionally oriented segments (see Figure 2.4, black wire line on Canals Smoothing scheme). To reduce this phenomenon, the algorithm detects the first point of every longitudinal segment so as to create a new wire line. This new wire line (Figure 2.4, blue wire line on Canals Smoothing scheme) goes through on previously detected point. Other points are in-plane projected on the new wire line in order to keep z coordinate.

2.2.3.6 3D canals and connectivity features

Thanks to numerous available data, considerable features can be computed. In order to standardise these features, a standard nomenclature (partially inspired by Parfitt [137]) is employed. As a matter of fact, segment and canal features are preceded by Seg and Ca, respectively. According to the wire interpretation, each canal is considered as a set of segments which link two consecutive contours (see Figures 2.7a and 2.7b). Hence, each feature is first computed from segments. Then, from segment features, canals characteristics are computed (Table 2.2).

Orientation

Orientation is derived in two stages. The first stage consists in considering 3D orientation using Euler angles. It comprises two consecutive rotations from the image plane (Figure 2.7c). The first rotation, Theta (θ), represents the rotation about \vec{y} axis. The second rotation, Psi (ψ), represents the rotation

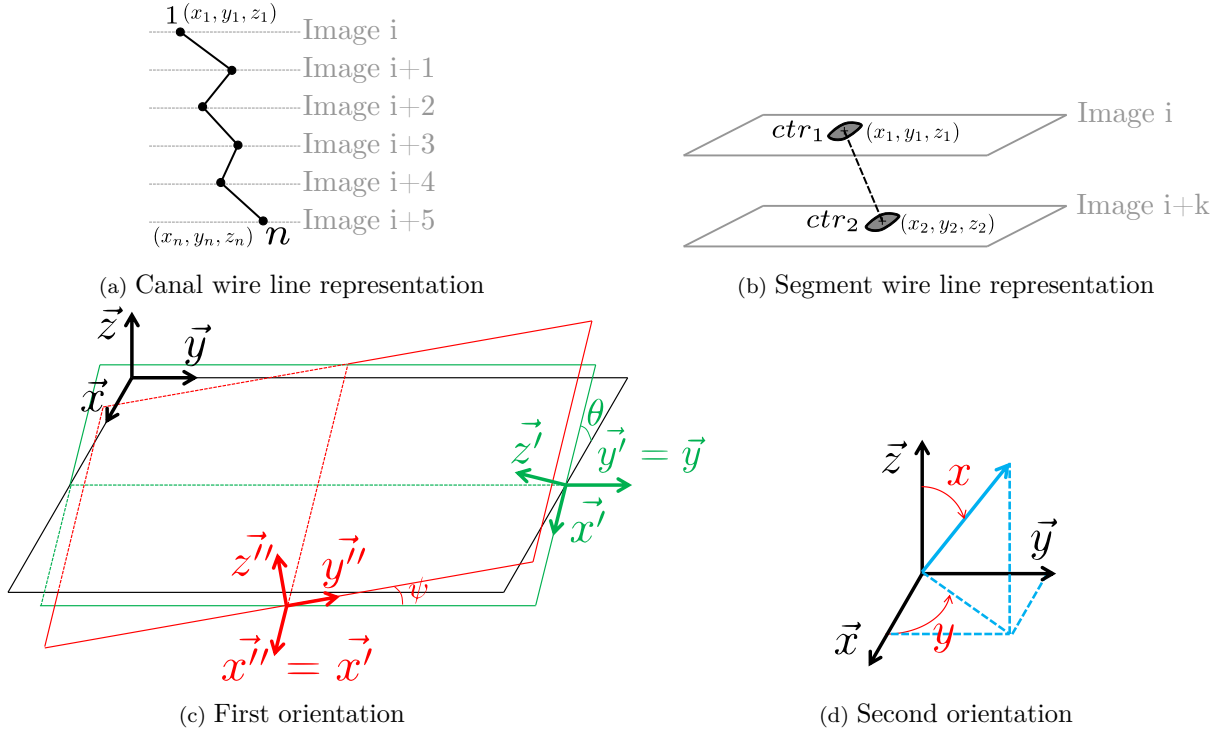


FIGURE 2.7: Canal interpretation. The canal wire line is a set of segments which link 2 inter-frame contours. Figure (a) : the canal wire-line connects each canal centroid indexed from 1 to n ($n-1$ segments). Figure (b) : This figure shows that each segment can link 2 contours (written ctr) spaced from k images. k is a user specified parameter (see Equation 2.3 and explanations for more details). Figure (c) : The orientation is computed from Eulerian angles (θ and ψ). Black colour is set for image plane. Green and red colours are set for intermediate plane and transverse plane of the canal, respectively. Hence, the normal to the red plane represents the orientation of the canal. Figure (d) : A second orientation is computed from Eulerian angles (Table 2.2). This orientation is reduced to a longitudinal (x angle) and transverse orientation (y angle) relative to image plane coordinate system.

about \vec{x}' . In addition, considering cylindrical porosity, the normal of the red plane is collinear to the longitudinal axis of the cylinder (Figure 2.7c). From this Euler angles, a second orientation system can be set (Figure 2.7d). The main advantage of this orientation over the Euler's one is only one angle is useful to describe either the longitudinal orientation (angle x) or transverse orientation (angle y). Thereby, according to its mathematical formula (see Table 2.2), x ranges from 0 deg (longitudinal orientation) to 90 deg (transverse orientation). Likewise, y ranges from ± 90 deg (collinear with \vec{y}) to 0 deg (collinear with \vec{x}).

Length

Concerning length, two different features are computed : real and apparent length. The first one represents the centroid wire line length by summing all the segments length and the second one represents the height difference between segments ends for segment features (*Seg.aLe*) and distance between first and last point of canals for canal features (*Ca.aLe*) (See Appendix A for schemes).

Segment apparent length is useful to compute segment volume whereas canal apparent length is used for canal 3D aspect ratio computing.

Surface and equivalent diameter

As specified above, surface value is obtained from contour moments using M_{00} moment. Therefore, equivalent diameter can be computed using Equation 2.4. Segment features are obtained by averaging contour values (Figure 2.7b and Table 2.2) and canal assessment is the average of segments characteristics.

$$Dm_{eq} = \sqrt{\frac{4 * M_{00}}{\pi}} \quad (2.4)$$

The novelty of this methodology is that it takes into account 3D orientation. Actually, assuming oriented cylindrical porosity, apparent surfaces perceived by slice images (elliptical shape) are larger than cylindrical transverse surfaces (circular shape) (See Appendix A for schemes). Please also refer to the lists of acronyms and symbols at the beginning of this manuscript.). Consequently, directly computing equivalent diameter from slice images leads to biased results. Hence, apparent and real surfaces are related according Equation 2.5.

$$\frac{\text{Real Surface}}{\text{Apparent Surface}} = \cos(x) \quad (2.5)$$

Volume and Volume Fraction

In order to obtain the global volume fraction of the sample, usually called $Ca.V/TV$, segment volume is computed from multiplication between apparent length and surface (Table 2.2). Then, each segment volume is summed to obtain canal volume. $Ca.V/TV$ is computed from the ratio between total canal volume and sample volume.

$$Ca.V/TV = \frac{\sum_{i=1}^N Ca_i.Vol}{\text{Sample volume}} \quad (2.6)$$

2D & 3D aspect ratio

Two types of aspect ratio are computed for this purpose. 2D aspect ratio is obtained by dividing the width and length from bounding rotated rectangle of contour. In case of oriented cylindrical canals, 2D aspect ratio equals to $\cos(x)$. Thus, it would be of interest to investigate this correlation between 2D and 3D features. 3D aspect ratio provides the general shape of the canal. Indeed, based on the

Features	Notation	Segment features	Canal features
ψ	ψ	$Seg.\psi = \tan^{-1}\left(\frac{y_2-y_1}{z_1-z_2}\right)$	$Ca.\psi = \frac{1}{N} \sum_{i=0}^{N-1} Seg_i.\psi$
θ	θ	$Seg.\theta = \tan^{-1}\left(\frac{x_1-x_2}{z_1-z_2}\right)$	$Ca.\theta = \frac{1}{N} \sum_{i=0}^{N-1} Seg_i.\theta$
x	x	$Seg.x = \cos^{-1}(\cos(\psi) * \cos(\theta))$	$Ca.x = \frac{1}{N} \sum_{i=0}^{N-1} Seg_i.x$
y	y	$Seg.y = \tan^{-1}\left(\frac{-\sin(\psi)}{\cos(\psi) * \sin(\theta)}\right)$	$Ca.y = \frac{1}{N} \sum_{i=0}^{N-1} Seg_i.y$
Real Length	rLe	$Seg.rLe = \sqrt{(x_2 - x_1)^2 + (y_2 - y_1)^2 + (z_2 - z_1)^2}$	$Ca.rLe = \sum_{i=0}^{N-1} Seg_i.rLe$
Apparent Length	aLe	$Seg.aLe = z_2 - z_1$	$Ca.aLe = \sqrt{(x_n - x_1)^2 + (y_n - y_1)^2 + (z_n - z_1)^2}$
Apparent Surface	aS	$Seg.aS = \frac{ctr_1.S + ctr_2.S}{2}$	$Ca.aS = \frac{1}{N} \sum_{i=0}^{N-1} Seg_i.aS$
Real Surface	rS	$Seg.rS = Seg.aS * \cos(Seg.x)$	$Ca.rS = \frac{1}{N} \sum_{i=0}^{N-1} Seg_i.rS$
Apparent Diameter	aDm	$Seg.aDm = \sqrt{\frac{4}{\pi} * Seg.aS}$	$Ca.aDm = \frac{1}{N} \sum_{i=0}^{N-1} Seg_i.aDm$
Real Diameter	rDm	$Seg.rDm = \sqrt{\frac{4}{\pi} * Seg.rS}$	$Ca.rDm = \frac{1}{N} \sum_{i=0}^{N-1} Seg_i.rDm$
Volume	Vol	$Seg.Vol = Seg.aL * Seg.aS$	$Ca.Vol = \sum_{i=0}^{N-1} Seg_i.Vol$
Volume Fraction	$fVol$	$Seg.fVol = \frac{Seg.Vol}{Sample.Vol}$	$Ca.fVol = \sum_{i=0}^{N-1} Seg_i.fVol$
2D Aspect Ratio	$AR2D$	$Seg.AR2D = \frac{1}{2}(ctr_1.AR2D + ctr_2.AR2D)$	$Ca.AR2D = \frac{1}{N} \sum_{i=0}^{N-1} Seg_i.AR2D$
3D Aspect Ratio	$AR3D$	-	$Ca.AR3D = \frac{Ca.aLe}{Ca.rDm}$

TABLE 2.2: Mathematical definition of canals features. Seg and Ca prefixes are related to Segment and Canal, respectively. All canal features are computed from segment features except for the apparent length and 3D aspect ratio which have either a different definition or aren't defined. Sample volume is obtained using the same formula for canal volume applied to contours of each slice which have the highest area value. See Appendix A for additional schemes.

straight cylindrical shape assumption for canals, this quantitative relation distinguishes flat shape porosity (<1) from rod-like shape porosity (>1) (See Appendix A for schemes).

Connectivity features

Connectivity detection provides possibilities for computing features. Actually, three geometric characteristics are carried out for canal intersections which links three canals at most (Table 2.3). The first feature, called opening angle, stands for the angle between linear fitting vector of outgoing canals (Figure 2.8). The aim of this measure is to determine the statistical distribution in order to potentially link stress concentration with tight connectivity. Second and third features lend morphological information to intersections. $R_{rDm(0,12)}$ expresses the ratio between outgoing canals diameter sum and incoming canal diameter. If the ratio equals to 1, this means that the entire of the incoming canal diameter is split into 2 canals. Similarly, $R_{rDm(1,2)}$ expresses the diameter fraction between outgoing canals. If the ratio equals to 1, canals have the same diameter.

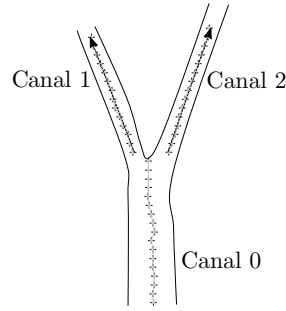


FIGURE 2.8: Connectivity scheme. Arrows represent canals mean vectors \vec{U}_i

Features	Connectivity features
α	$Conn.\alpha = \cos^{-1}(\frac{\vec{U}_1 \cdot \vec{U}_2}{\ \vec{U}_1\ \cdot \ \vec{U}_2\ }) $
$R_{rDm(0,12)}$	$Conn.R_{rDm(0,12)} = \frac{Ca_1.rDm + Ca_2.rDm}{Ca_0.rDm}$
$R_{rDm(1,2)}$	$Conn.R_{rDm(1,2)} = \frac{\max(Ca_1.rDm, Ca_2.rDm)}{\min(Ca_1.rDm, Ca_2.rDm)}$

TABLE 2.3: Mathematical definition of connectivity features. Conn prefix is used for each characteristic. \vec{U}_i is obtained from the linear fitting of centroid wire line of the i^{th} canal.

2.2.3.7 BMU detection and features computations

At this step of the algorithm, canals can be classified into various types (Figure 2.9). First, unconnected canals are not considered for further computation. As a matter of fact, they are mainly composed of residual noises that the algorithm considers as short canals with small volume. Therefore residual noises are numerous, they aren't considered for the canal density. However, $Ca.V/TV$ is computed from all canals because some unbounded canals aren't connected but affect the porous volume. A short study has shown that residual noises poorly affect porosity. Then, connected canals are split

into boundary and within canals. Boundary canals are associated with unbounded ones. It means that the canal was cut during sample preparation. Consequently, their topology are affected and can not be considered for the feature computation. Interestingly, as shown in Chapter 1, several studies have explained that BMU (Bone Multicellular Unit) are part of the vascular network. Thanks to the novel 3D assessment, BMUs can be defined as a void which begins by connectivity on one side and they close (cutting cone) on the other side (see Figure 1.14 on page 22, Chapter 1). Thus, one-side bounded canals are exhibited so as to detect a closing cone on the other side. A python script was developed intended to display canal wire lines and canals contours as cloud points using FreeCAD 0.16 macro workbench.

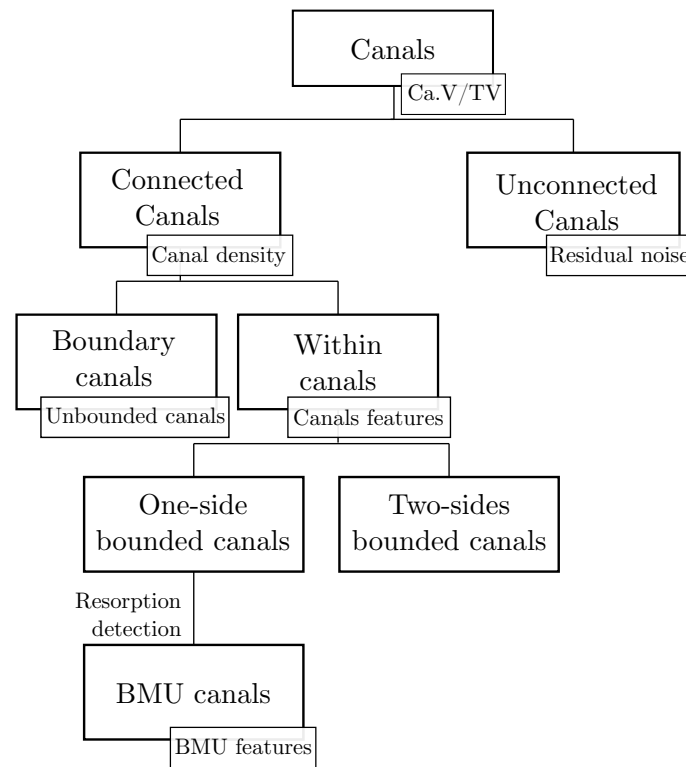


FIGURE 2.9: Hierarchy of canals for feature computation. $Ca.V/TV$ is computed from all canals. The canal density is computed from connected canals. Unbounded canals aren't considered for canal features computation.

To detect the closing cone, the evolution of the real diameter through the canal is investigated. If along the last measurements, a drop in the value of the diameter below $15\mu m$ is detected (threshold derivative criteria), then the canal is considered as a BMU closing cone (Figure 2.10).

BMU has a major impact on the bone turnover. The shape of the BMU is closely linked with the cellular activity [79]. The first phase consists in a bone resorption which is followed by a bone refilling phase (see Figure 1.15 on page 23, Chapter 1). Assuming this type of process, the groove behind the maximum diameter fits with the new bone created. Hence, the assessment of this volume can lead to the quantification of the new-created bone. To compute these features, canals are assumed to have

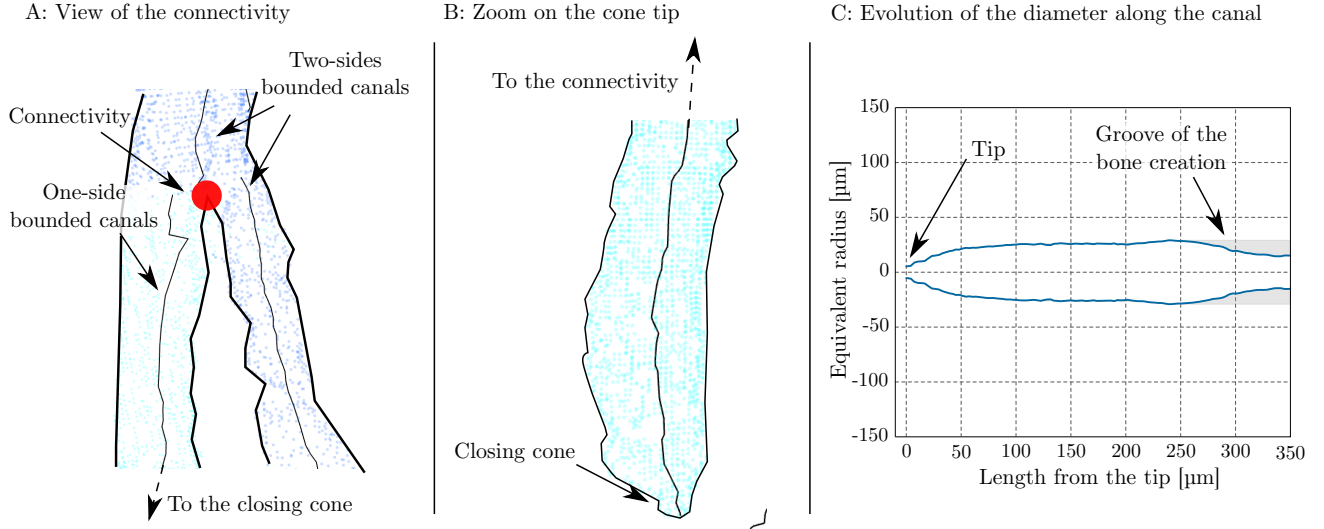


FIGURE 2.10: BMU closing cone detection. The detection of BMU closing cones begins by classifying one-side bounded canals. Then a derivative criterion is applied on the diameter evolution along the canal. Canals are classified as BMU if a drop in the value of the diameter is detected below $15\mu\text{m}$. Views A and B are obtained from FreeCAD snapshot where wire lines and canal contours (cloud points) are displayed. Two and one side bounded canals are shown in blue and cyan, respectively.

a cylindrical shape. An analysis of the geometry of BMUs using a radius-length plot (as shown by Figures 2.10 and 2.11) reveals that the global shape of BMUs highly differs from one to another, even in the same VOI. Indeed, as shown by Figure 2.11, several types of BMU shape can be found. On this figure two types are shown. The first one (orange) has a closing cone which is easy to identify thanks to a diameter that quickly grows and followed by a diameter decrease. The second one (blue) is tricky to analyse : the diameter keeps growing up to the connectivity. Therefore, several very small grooves are created and can be viewed thanks to red crosses (centroids of grooves).

Consequently, an algorithm is developed so as to be able to compute the new bone volume whatever the shape of the BMU. Hence, local peaks on the equivalent radius-length curve are detected. From these peaks, the groove of the new bone is detected until a possible diameter increase or the end of the BMU (Figure 2.11). The groove areas are computed using the classical trapezoidal integration method between the BMU profile and the groove profile (continuous and dotted lines on Figure 2.11, respectively). The centroid of each area is computed in order to obtain the new bone volume using the Guldinus theorem (Equation 2.7) :

$$V = \alpha * \|OH\| * A \quad (2.7)$$

α is the revolution angle and equals to 2π . A is the area of the groove. $\|OH\|$ is the distance between the centroid of the area O and its orthogonal projection H on the revolution axis. Due to

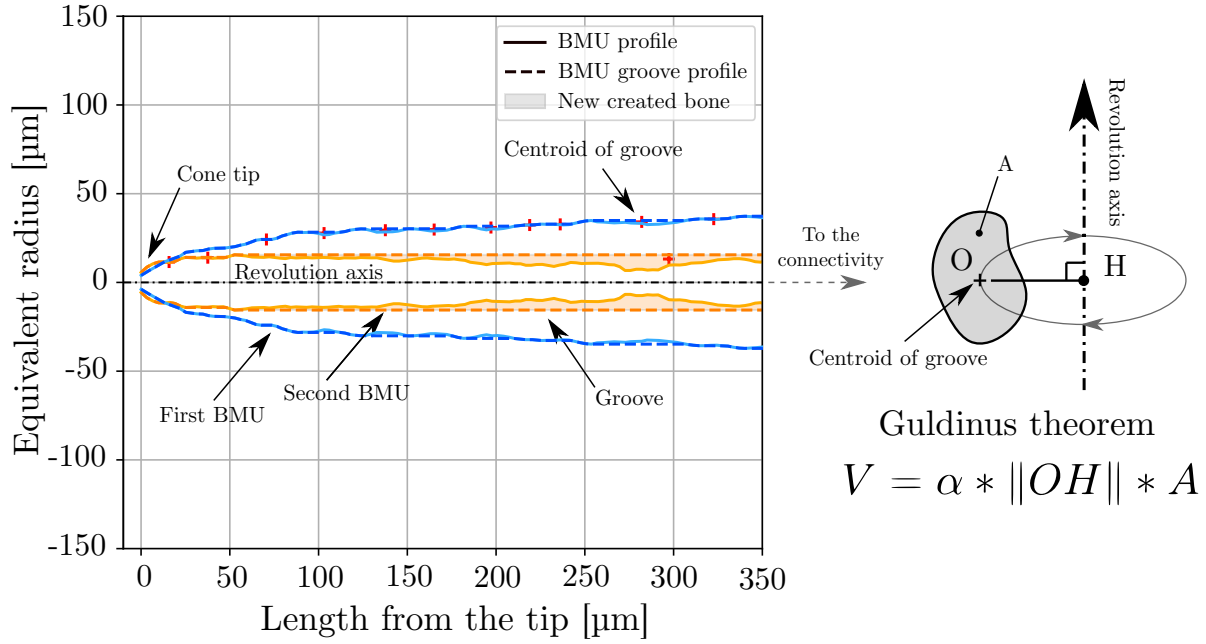


FIGURE 2.11: Different BMU profiles and schemes to compute new bone volume. Two types of profiles are plotted (Blue and orange). Both are extracted from the same sample. The blue one shows a low bone creation, whereas the orange one has a more important bone volume created. Red crosses are the centroid of each groove. The bone volume is computed by using the Guldinus theorem where $\alpha = 2\pi$ and OH the distance between centroid and revolution axis.

the presence of several grooves (N on Equation 2.8) on the BMU profile, each groove volume has to be summed in order to obtain the new bone volume created by the BMU (Equation 2.7).

$$\text{New bone volume} = \sum_{i=0}^N 2\pi \|OH\|_i A_i \quad (2.8)$$

Consequently, two BMU features can be computed (Table 2.4) The first one is the new bone fraction, noted BF . It is obtained by dividing the new bone volume by the total volume (TV) and is expressed in percent. Subsequently, the mean new bone fraction (noted \bar{BF}) can be computed from the ratio of BF and the number of BMU. This second feature can be considered as an efficiency quantification of the BMU bone creation. Real diameter and length are recorded from canal features.

Features	BMU features
rDm	$BMU.rDm = Ca.rDm$
rLe	$BMU.rLe = Ca.rLe$
BF	$BMU.BF = \frac{\text{New bone volume}}{TV}$
\bar{BF}	$BMU.\bar{BF} = \frac{BMU.BF}{Nb \text{ BMU}}$

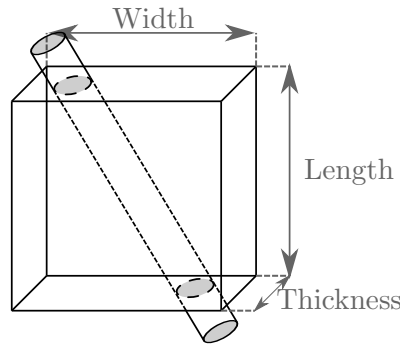
TABLE 2.4: Definition of BMU features. BMU diameter and length are those computed for canals. $BMU.BF$ is the new bone fraction created by the grooves of BMUs. $BMU.\bar{BF}$ is the mean bone fraction. It quantifies the BMU efficiency. See Appendix A for schemes.

2.2.4 Algorithm validation

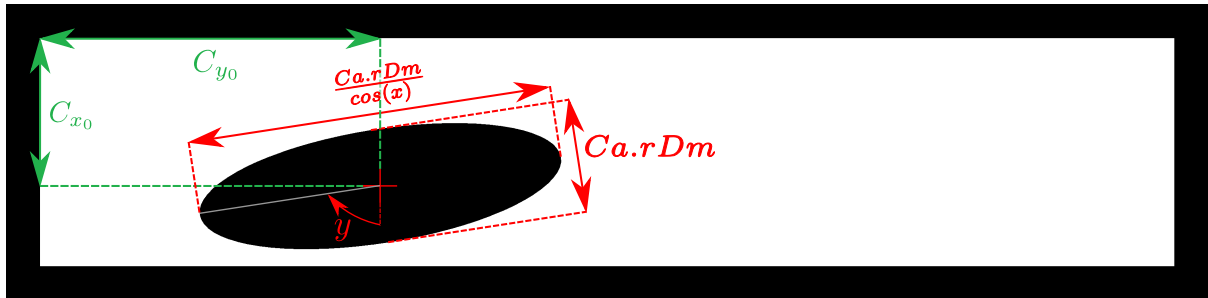
2.2.4.1 Error quantification: creation of dummy images

Due to original 3D interpretation of cortical porosity, an error estimating is required. For this purpose, a Python script was carried out by creating dummy slice images based on geometrical inputs using OpenCV library. Indeed, this algorithm assumes a parallelepipedic sample crossed by a user-specified number of oriented cylinder (Figure 2.12). Orientation is specified by Euler angles. Cylinder diameter and position on the first slice image are indicated (Figure 2.12b). The number of images depends on the resolution required by user and sample length. Ellipse position on the i^{th} image is determined from Equation 2.9.

$$\begin{cases} x_i = x_0 - i * \tan(\theta) \\ y_i = y_0 + i * \frac{\tan(\psi)}{\cos(\theta)} \end{cases} \quad (2.9)$$



(a) Overview of sample dimensions



(b) First slice image

FIGURE 2.12: Schematic representation of validation proceeding. The image on this figure was generated using the same input parameters as those used to obtain results outlined in Table2.6.

2.2.4.2 Robustness quantification: multiple scans of one sample

On the previous part, only the computing error is quantified. However, the experimental protocol is not considered. Indeed, in order to scan the specimen, the sample needs to be accurately placed so as to be as close as possible to the rotational axis of the scanner. Moreover, due to high spatial resolution, vibrations caused by rotations during the scan can also affect the slices (blurring). The effect of all of these factors have to be quantified. Therefore, one bone cylindrical sample (similar shape as described in section 2.2.1) was subsequently scanned four times. 2094 slices were obtained for each scan (6.22 mm). A $2.94\mu\text{m}$ isotropic voxel size was obtained. The Python script was executed on all scans with similar inputs shown in 2.2.3.2. Between two subsequent scans, the sample was completely removed from the $\mu\text{-CT}$ and its bracket and then replaced inside as it should be done for a new scan.

2.2.5 Statistics

Data are thoroughly reported as mean \pm standard deviation. Femur and humerus were compared on the pooled population (gender, side, ...) unless other specified. Then, limbs side bias was investigated by separating the humerus and femur. Statistical results were performed thanks to several Python libraries. Scipy and statsmodels libraries are used for correlation and significant differences tests. A Shapiro-Wilk test reveals that many of features have not a normal distribution. Therefore, non-parametric tests were chosen. Significant differences were investigated using the non-parametric Mann–Whitney–Wilcoxon (MWW) test. Two features are defined as significantly different if the obtained p-value is below 5%. Outlier values are defined as 1.5 times of the inter-quartile (IQR) under the first quartile (Q_1) and below the third quartile (Q_3) ($1.5 * IQR \pm Q_i$). Spearman correlation test was performed so as to find a correlation between features. Outliers points are removed prior to correlation tests. Confidence intervals are computed from a bootstrapping method using 1000 resamples.

2.3 Results and discussion

2.3.1 Error and robustness quantification

2.3.1.1 Error quantification: creation of dummy images

In order to validate the algorithm processing, a set of images was generated. Sample length, width and thickness were 1.5, 10 and 2 mm, respectively. A $2.94\mu\text{m}$ resolution was chosen to obtain 510 images. One cylindrical porosity with a diameter of 1.0 mm goes through the sample oriented along $\psi=70^\circ$ and $\theta = 25^\circ$ Eulerian angles. Results are summed up in Table 2.6. This table is quite revealing in several ways. First, although the highly oriented canal, process is able to detect and predict its geometric features with an acceptable average error of 2.04 %. Second, Ca.V/TV can accurately be predicted from the canal volume fraction. Highest errors are obtained from the real surface, real diameter and 3D aspect ratio. These differences can be explained by the fact that these features accumulate inaccuracy from other characteristics. Indeed, for instance, real surface is obtained from the product of the apparent surface and $\cos(x)$. Therefore, real surface cumulates errors of both features. One of the possibilities to reduce inaccuracy is to decrease scan resolution in order to have better edge description or to directly compute these features from raw images.

Global features	Ca.V/TV [%]	Ca.D [μm^{-3}]	Po.D [μm^{-2}]	Conn.D [μm^{-3}]	BMU.D [μm^{-3}]
Mean	7.02	93.03	20.12	44.02	7.56
Standard deviation σ	0.07	2.02	0.22	1.57	0.27
Standard error : $\frac{\sigma}{\sqrt{n}}$	0.04	1.01	0.11	0.78	0.13

TABLE 2.5: Robustness quantification of general features. These results were obtained from 4 successive scans of a femoral bone sample. Same parameters were set so as to obtain the slices. The protocol is described in section 2.2.4.2.

2.3.1.2 Robustness quantification: multiple scans of one sample

The results of this analysis are displayed in tables 2.7, 2.5 and 2.8 for canal , global and connectivity features, respectively. For canal and connectivity features, only mean values were compared. The standard error $\frac{\sigma}{\sqrt{n}}$ is computed. Overall, these tables reveal that the standard deviation and standard error reflect that the results are poorly dispersive between the four scans. The ratio between mean and standard error reveals a less than 1 % dispersion. Moreover, it also highlights that the μ -CT scan does not affect the architecture topology.

Canal features	$Ca.\psi$ [deg]	$Ca.\theta$ [deg]	$Ca.x$ [deg]	$Ca.y$ [deg]	$Ca.Vol$ [mm ³]	$Ca.fVol$ [%]	$Ca.rLe$ [mm]	$Ca.aLe$ [mm]	$Ca.aS$ [mm ²]	$Ca.rS$ [mm ²]	$Ca.aDm$ [mm]	$Ca.rDm$ [mm]	$Ca.AR2D$ -	$Ca.AR3D$ -
Theoretical values	70.0	25.0	71.9	-81.3	3.8	12.6	4.8	4.8	2.5	0.8	1.8	1.0	0.3	4.8
Computational values	71.7	24.4	73.6	-82.3	3.8	12.7	4.8	4.8	2.5	.7	1.8	0.96	0.3	5.0
Absolute error	2.47 %	2.36 %	2.29 %	2.55 %	1.06 %	1.35 %	0.09 %	0.24 %	0.51 %	8.43 %	0.26 %	4.37 %	0.73 %	4.32 %

TABLE 2.6: Error estimation by comparing theoretical and computing results. Absolute error is computed from the ratio of the computational value and the theoretical value. These results are obtained from a dummy sample crossed by an oriented cylindrical porosity (diameter: 1.0 mm, $\psi=75^\circ$, $\theta=25^\circ$).

Canal features	$Ca.\psi$ [deg]	$Ca.\theta$ [deg]	$Ca.x$ [deg]	$Ca.y$ [deg]	$Ca.Vol$ [μm ³]	$Ca.fVol$ [%]	$Ca.rLe$ [μm]	$Ca.aLe$ [μm]	$Ca.aS$ [μm ²]	$Ca.rS$ [μm ²]	$Ca.aDm$ [μm]	$Ca.rDm$ [μm]	$Ca.AR2D$ -	$Ca.AR3D$ -
Mean	2,31	1,11	25,06	-1,08	8,91E+05	2,66E-03	244,62	233,26	8069,62	6866,83	82,67	76,01	0,63	4,99
Standard deviation σ	0,22	1,81	0,23	0,38	2,05E+04	6,00E-05	3,81	3,71	109,21	104,73	0,76	0,79	0,00	0,07
Standard error : $\frac{\sigma}{\sqrt{n}}$	0,11	0,91	0,12	0,19	1,03E+04	3,00E-05	1,90	1,85	54,60	52,36	0,38	0,39	0,00	0,03

TABLE 2.7: Robustness quantification on canal features. These results were obtained from 4 successive scans of a femoral bone sample. Same parameters were set so as to obtain the slices. Only mean values were compared. The protocol is described in section 2.2.4.2

Connectivity features	$Conn.\alpha$ [deg]	$Conn.R_{rDm(0,12)}$ [-]	$Conn.R_{rDm(1,2)}$ [-]
Mean	33.30	0.84	2.18
Standard deviation σ	0.23	0.00	0.02
Standard error : $\frac{\sigma}{\sqrt{n}}$	0.11	0.00	0.01

TABLE 2.8: Robustness quantification of connectivity features. These results were obtained from 4 successive scans of a femoral bone sample. Same parameters were set so as to obtain the slices. Only mean values were compared. The protocol is described in section 2.2.4.2.

2.3.1.3 Conclusions

These results are very encouraging and reflect that the Python algorithm can doubtless be applied on bone samples. First, an algorithm which creates dummy slices, where architecture topology is known, was assessed. From this study, the error can be valued at 2.04 %. Second, the protocol robustness is studied. Four successively scans were carried out on one bone sample. Results are poorly dispersive (less than 1 %). This study confirms that the obtained results are robust and the protocol has a low impact on results. Consequently, the scanning protocol is suitable to the vascular network assessment.

2.3.2 Bearing and non-bearing comparisons

Subject number	Age	Gender	Femur		Humerus		Total
			Left	Right	Left	Right	
0010	65	Male	2	2	2	2	8
0011	86	Male	2	2	4	2	10
0014	96	Female	0*	2	2	1	5
0017	96	Female	2	2	2	2	8
0020	80	Male	2	2	2	2	8
0026	75	Male	2	2	2	2	8
0055	68	Male	2	2	2	2	8
0963	87	Female	2	2	2	2	8
0965	77	Male	2	2	2	2	8
0995	87	Male	1	1	3	1	6
Total			17	19	23	18	77

TABLE 2.9: Number of bone samples available for architectural analysis. *No samples are available for this femur due to a hip prosthesis.

77 samples were scanned (36 Femur, 41 Humerus) (Table 2.9). 17 features are computed for each canal. General features refer to those where only one value per sample is computed (such as the density or porosity) and are reported in Table 2.10. Tables 2.11, 2.13 and 2.14 report the statistical values obtained by comparing bearing and non-bearing bones. For each sample, only the mean value of each feature is considered. The mean VOI size is $31.1 \pm 6.8 \text{ mm}^3$. The VOI is slightly smaller in

humeral samples because of the very thin cortical layer available that made samples hard to harvest ($34.9 \pm 5.0 \text{ mm}^3$, $27.8 \pm 6.4 \text{ mm}^3$ for femur and humerus respectively). So as to ease reading, most of the following symbols are summarised and illustrated in Appendix A. Please also refer to the lists of acronyms and symbols at the beginning of this manuscript.

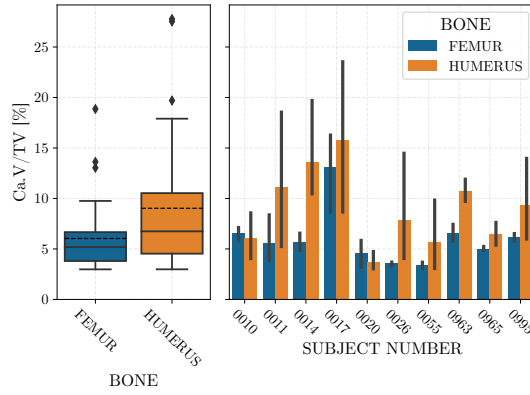
2.3.2.1 General features

	Bone	Mean \pm Std	Median	Min	Max	Q1	Q3	p-value
Ca.V/TV [%]	Pooled	7.63 ± 5.24	5.76	2.98	16.34	4.22	9.47	0.019
	Femur	6.04 ± 3.24	5.18	2.98	9.75	3.80	6.66	
	Humerus	9.03 ± 6.17	6.74	2.98	17.90	4.53	10.53	
Ca.D [mm^{-3}]	Pooled	90.84 ± 31.81	78.85	48.58	132.66	69.89	95.95	0.317
	Femur	93.62 ± 34.22	82.41	53.20	132.66	71.74	99.45	
	Humerus	88.40 ± 29.32	78.81	48.58	126.42	69.21	95.77	
Po.D [mm^{-2}]	Pooled	14.81 ± 2.80	14.64	8.87	21.61	12.80	16.58	0.002
	Femur	15.91 ± 2.83	15.35	11.13	21.61	14.13	17.59	
	Humerus	13.84 ± 2.38	13.61	8.87	18.99	12.50	15.75	
Conn.D [mm^{-3}]	Pooled	28.31 ± 10.91	25.34	10.21	44.93	21.01	31.12	0.206
	Femur	29.23 ± 10.97	25.42	17.39	36.20	22.44	31.11	
	Humerus	27.50 ± 10.79	25.34	10.21	48.90	20.57	33.05	
BMU.D [mm^{-3}]	Pooled	8.44 ± 2.68	8.11	4.31	14.36	6.54	9.88	0.004
	Femur	9.36 ± 2.91	9.08	5.29	15.21	6.96	10.90	
	Humerus	7.63 ± 2.16	7.29	4.31	12.64	5.94	8.69	

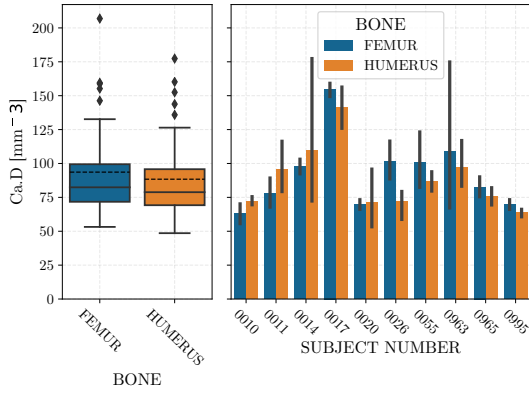
TABLE 2.10: General features for vascular network. Ca.V/TV is the vascular porosity. D suffix means density for each type (Ca: Canal; Po: Pore; Conn: Connectivity; BMU: BMU). Minimum and maximum values are reported without considering outliers (by groups). Q1 and Q3 are the first and third quartile, respectively. p-value is the result of significant differences, assessed by Mann-Whitney-Wilcoxon (MWW) test, between each bone. Bold values are those below 0.05 (which means that groups are significantly different).

Table 2.10 is quite revealing in several ways. First, significant differences were found between humerus and femur for the porosity, pore and BMU densities. Second, even if the way of Ca.V/TV assessment differs (3D computation), porosity remains in the same order as reported by the literature (see Table 1.2 on page 25, Chapter 1, for references). No comparative values were found so as to compare the different densities. However, the pore density (number of pores per slices divided by the sliced bone area), noted Po.D, is also measured and is close to those reported by Cooper *et al.* [68] ($12.3 \pm 2.4 \text{ mm}^{-2}$). Humerus seems to be more porous than the femur. This trend is enforced by individual comparisons as depicted by Figure 2.13a. Overall, all the subjects have a more porous humerus than femur (56 % higher). An exception is made for subjects 0010 and 0020 where femur is slightly more porous than the humerus. This finding is in contrast with those reported by Bry [10] and Gauthier [30]. However, Bry [10] study is based on only 4 male subjects and similar contrasts are found by individual comparisons. The opposite trend found in this study can also be explained

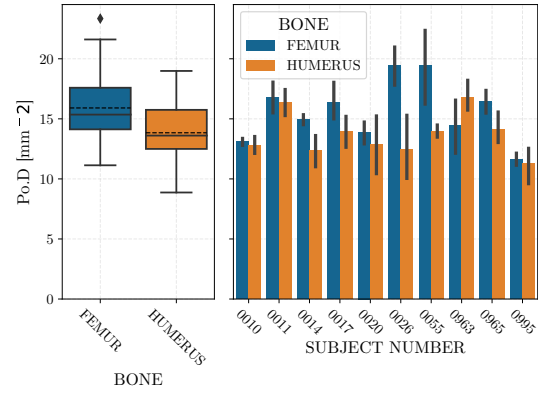
by the fact that the subject history is unknown. Indeed, due to its functions, bearing bones need a higher rate of vascularisation than non-bearing ones [10, 30]. However, a prolonged bed rest affects the bone remodelling and can lead to an architectural change. In addition, the current VOI size is overall higher than other studies (Gauthier [30]: 0.225 mm^3 , Cooper *et al.* [68]: 21.2 mm^3). These two differences could explain the opposite trend with other studies.



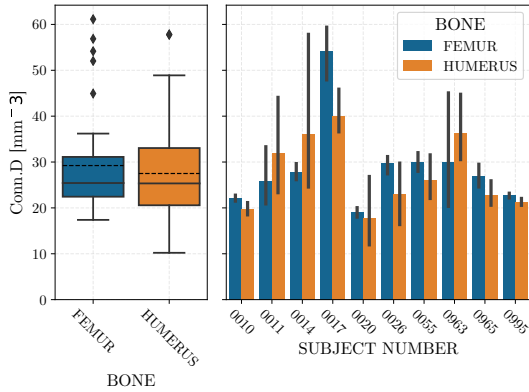
(a) Ca.V/TV boxplots and barplots



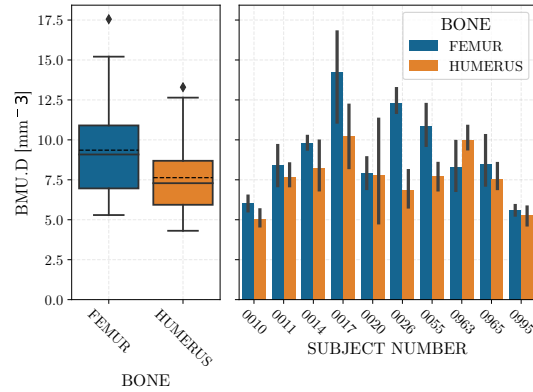
(b) Ca.D boxplots and barplots



(c) Po.D boxplots and barplots



(d) Conn.D boxplots and barplots



(e) BMU.D boxplots and barplots

FIGURE 2.13: General features boxplots and barplots. Barplots display the mean value. The vertical black line is the 95 % confidence interval for each group. Left plot shows boxplot for all grouped femoral and humeral samples. Dotted and straight horizontal lines are the mean and median values, respectively. Outliers are displayed by diamond markers. On the right, features are individually highlighted.

As shown by Table 2.10, the pore density is significantly different whereas canal and connectivity densities aren't. This counter-intuitive conclusion indicates that to assess the density of the canal network, a three-dimensional assessment is required. The higher pore density of the femur can facilitate blood and nutrients supplies within the cortex. Even though humeral samples are more porous than femoral ones, no differences are found for the canal density. Consequently, this result shows that the canal shape differs between the two bones and needs to be investigated so as to understand these differences. Interestingly, the BMU cone density differs between the two bones. Indeed, BMU cones are denser in the femoral cortex. Similar trend is found for each human subject (Figure 2.13e). It highlights a different bone remodelling which occurs in the two bones. This confirms that the bone remodelling depends on the type of bone. BMUs are further investigated where all the features are displayed (Section 2.3.2.4).

Overall, by comparing the general features, some significant differences were found. Actually, humeri are more porous than femurs. This porosity seems to be poorly dependent of the canal density. Hence, it is recommended to deeper investigate the canal network so as to understand the reasons of the different porosities. In addition, different BMU densities are found which suggests different bone turnovers. So as to explain these features, canal, connectivity and BMU shapes are investigated in the following sections of this manuscript.

2.3.2.2 Canal features

In the previous section, general features are exhibited and some differences are found. However, to understand these differences, the canal shape is investigated through 12 features and are reported in Table 2.11.

In this table, orientation of canals are reported. x angle is the longitudinal angle. Hence, it ranges from 0° (longitudinal orientation) to 90° (transverse orientation). It is somewhat surprising that the overall orientation is angled. Indeed, whatever the bone or the human subject, the angle remains more than 25° (Figure 2.14a). The y angle, which is the transverse angle, is highly dispersive (Figure 2.14b). It means that the canal network has no privileged transverse direction of orientation. These two angles contradict with the common view of the cortical architecture as a longitudinal vascular network. Hence, the cortical architecture is a very complex network where the orientation slightly differs from a bone to another. Actually, the MWW test reveals a significant difference between humerus and femur. The humerus vascular network is slightly more oblique. A possible explanation for this result may be the diaphysis of femur takes more longitudinal stress due to its bearing function.

	Bone	Mean \pm Std	Median	Min	Max	Q1	Q3	p-value
Ca. ψ [deg]	Pooled	0.63 ± 3.34	0.33	-7.67	7.67	-1.72	2.55	0.111
	Femur	1.08 ± 2.50	1.02	-2.71	5.91	-1.20	2.84	
	Humerus	0.23 ± 3.89	0.15	-8.16	7.67	-1.99	2.28	
Ca. θ [deg]	Pooled	0.20 ± 3.01	0.13	-7.44	6.69	-1.79	2.44	0.268
	Femur	0.37 ± 3.02	0.65	-7.44	6.20	-1.84	2.55	
	Humerus	0.04 ± 2.99	-0.49	-5.06	6.69	-1.79	2.41	
Ca. x [deg]	Pooled	28.02 ± 2.10	27.93	23.62	32.48	26.73	29.08	0.001
	Femur	27.24 ± 1.62	27.02	23.62	30.82	26.05	28.30	
	Humerus	28.70 ± 2.23	28.76	23.75	33.98	27.24	30.02	
Ca. y [deg]	Pooled	-0.54 ± 5.33	-0.51	-11.53	10.78	-3.29	2.79	0.279
	Femur	-0.71 ± 4.43	-0.88	-8.93	8.24	-2.74	1.79	
	Humerus	-0.38 ± 6.00	0.11	-11.53	10.78	-3.71	3.44	
Ca.rLe [μm]	Pooled	228.91 ± 56.43	240.87	117.59	316.97	203.98	265.11	0.047
	Femur	237.67 ± 50.96	246.61	164.19	303.27	228.66	272.20	
	Humerus	221.21 ± 59.79	231.91	87.95	316.97	186.44	256.41	
Ca.aS [$10^3 \mu\text{m}^2$]	Pooled	11.99 ± 12.05	7.19	2.59	20.00	5.06	11.27	0.008
	Femur	8.32 ± 6.57	6.29	2.59	15.35	4.45	9.34	
	Humerus	15.21 ± 14.58	9.28	3.21	38.13	5.66	19.55	
Ca.rS [$10^3 \mu\text{m}^2$]	Pooled	10.17 ± 10.18	6.09	2.18	17.31	4.31	9.80	0.008
	Femur	7.05 ± 5.40	5.33	2.18	13.39	3.72	8.13	
	Humerus	12.92 ± 12.37	8.09	2.60	30.45	4.83	16.15	
Ca.aDm [μm]	Pooled	84.69 ± 28.43	75.81	49.79	121.93	65.61	93.28	0.016
	Femur	76.36 ± 20.34	71.82	49.79	118.24	61.38	87.14	
	Humerus	92.01 ± 32.25	77.62	52.85	158.70	66.32	103.97	
Ca.rDm [μm]	Pooled	77.01 ± 25.53	68.33	45.65	111.85	58.31	85.71	0.020
	Femur	69.70 ± 18.17	65.82	45.65	105.11	56.09	79.56	
	Humerus	83.42 ± 29.10	70.79	47.24	146.24	59.91	94.78	
Ca.Vol [$10^6 \mu\text{m}^3$]	Pooled	1.30 ± 0.65	1.18	0.42	2.74	0.85	1.62	0.001
	Femur	1.04 ± 0.40	0.92	0.46	2.02	0.70	1.31	
	Humerus	1.53 ± 0.74	1.36	0.42	2.74	1.07	1.87	
Ca.AR2D [-]	Pooled	0.62 ± 0.03	0.63	0.55	0.67	0.60	0.64	0.006
	Femur	0.63 ± 0.03	0.63	0.58	0.67	0.61	0.65	
	Humerus	0.61 ± 0.03	0.62	0.55	0.65	0.60	0.63	
Ca.AR3D [-]	Pooled	4.48 ± 1.41	4.46	1.45	7.41	3.65	5.38	0.015
	Femur	4.83 ± 1.35	5.14	1.90	7.11	3.86	5.89	
	Humerus	4.17 ± 1.38	4.20	1.45	7.41	3.10	5.16	

TABLE 2.11: Canal features values. See Table 2.2 for abbreviations. Minimum and maximum values are reported without considering outliers (by groups). Q1 and Q3 are the first and third quartile, respectively. p-value is the result of significant differences, assessed by Mann-Whitney-Wilcoxon (MWW) test, between each bone. Bold values are those below 0.05 (which means that groups are significantly different).

	A_{11}	A_{12}	A_{13}	A_{22}	A_{23}	A_{33}
Pooled	0.084205	-0.000764	0.002541	0.085805	-0.008599	0.829990
Humerus	0.090362	-0.000800	0.000272	0.091759	-0.002592	0.817880
Femur	0.077193	-0.000724	0.005124	0.079025	-0.015440	0.843782

TABLE 2.12: Mean orientation tensor coefficients. Bold values highlight significant differences between humerus and femur using MWW test ($p < 0.05$). Axis 3 is the longitudinal one. Axes 1 and 2 are those in the transverse plane.

Humerus, as a non-bearing bone, is subjected to more complex stresses. For this possible reason, the canal network optimised itself so as to perform blood and nutrients supplies as best as possible.

Another way to compute the overall orientation of canals is the oriented distribution function (ODF) [138]. It is a symmetric 3 by 3 second-order tensor, noted A obtained from the orientation vector \vec{a} of canals. It is computed from the tensor product between \vec{a} and itself (Eq. 2.10) :

$$A = a \otimes a \quad (2.10)$$

Hence, A can be computed for each canal from the mean orientation vector \vec{a} . The global ODF tensor is obtained by averaging all canal ODF tensors. It is a very useful parameter for Mori-Tanaka homogenisation so as to describe the global orientation of a set of inclusions. Interestingly, the diagonal terms of the tensor can be interpreted as the probability of the inclusion orientation along each axis. Consequently, the sum of the diagonal terms always equals to one. For instance, for an architecture oriented along the axis 3, the coefficient A_{33} equals to one whereas the others are null.

This tensor is assessed for each sample, and mean values are available in Table 2.12. This table confirms that the global orientation of vascular canals is mainly longitudinal (0.83). However, it remains fairly oblique with about 17 % along the transverse axes. Remarkably, significant differences (at a $p = 0.05$ level) are found along the longitudinal and transverse axes using MWW test. Nevertheless, transverse differences can't be interpreted because radial and circumferential axes were not recorded during harvest and information were lost during machining (asymmetrical shape). Overall, it confirms that vascular canals adapt their orientation according to the functions of the bone.

Two shapes factor are assessed and noted $Ca.AR2D$ and $Ca.AR3D$, respectively. The first one depicts the transverse shape of the pores, whereas the second one concerns the 3D shape of canals. $Ca.AR2D$ highlights that pores are mainly elliptically shaped. It suggests that canals would be considered as a cylindrical shape with a elliptic cross-section. In the current study, canals are considered as classical cylinders with a circular cross-section. Hence only one value of the diameter is assessed. This transverse asymmetrical shape can be explained by a possible asymmetric need of blood and

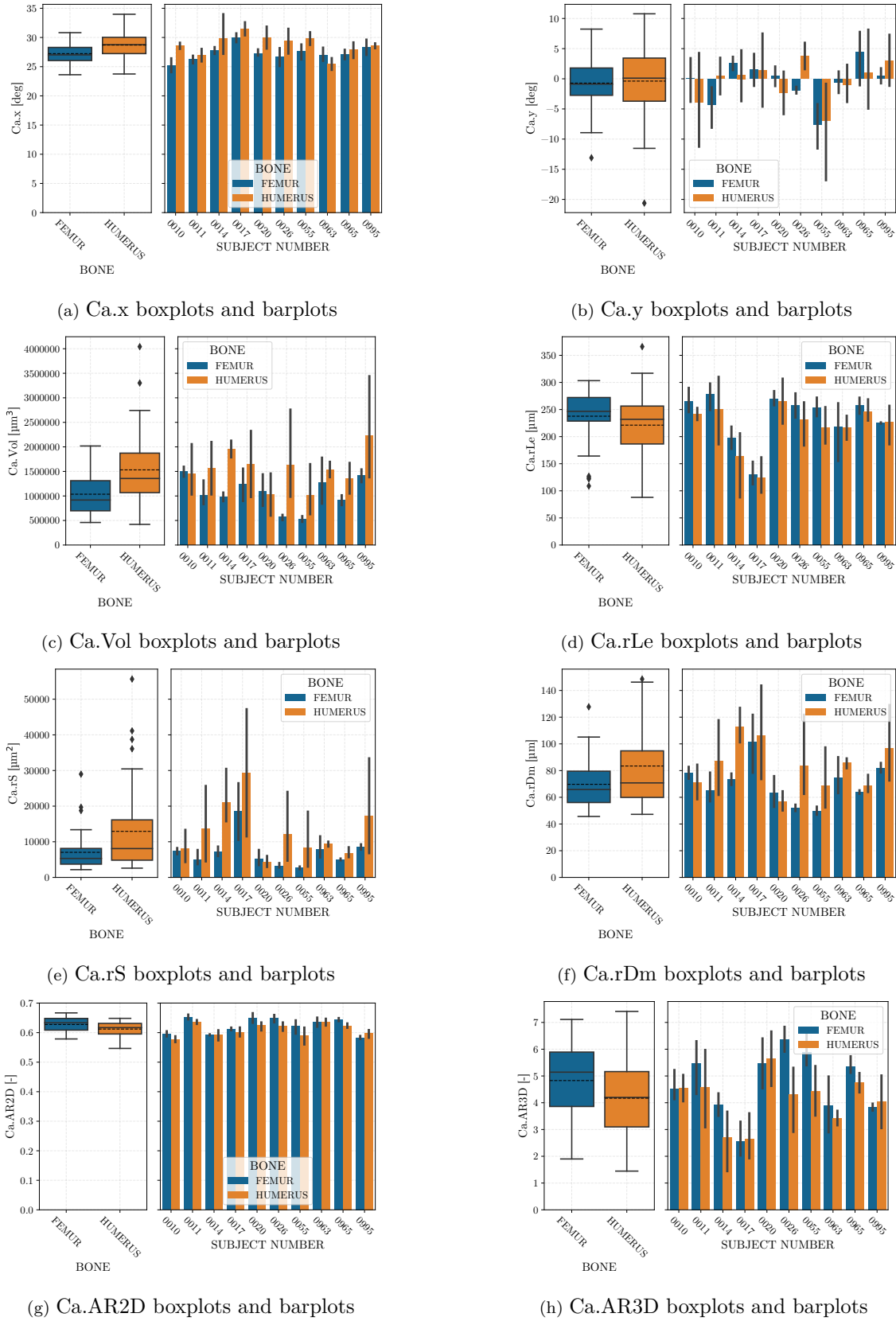


FIGURE 2.14: Canal features boxplots and barplots. Barplots display the mean value. The vertical black line is the 95% confidence interval for each group. Left plot shows boxplot for all grouped femoral and humeral samples. Dotted and straight horizontal lines are the mean and median values, respectively. Outliers are displayed by diamond markers. On the right, features are individually highlighted.

nutrients supply in a privileged direction (radial or circumferential). Unfortunately, as mentioned above, transverse directions couldn't be recorded during harvest and this hypothesis can't be currently verified. Moreover, as it is not the purpose of this study, it would be interesting to compare this transverse asymmetry with the radial and transverse axes or compare it with preferred canaliculi orientation as previously reported by Repp *et al.* [139]. The 3D shape factor, $Ca.AR3D$, aims at describing the global shape (flat or elongated) of each canal. Hence, a ratio over 1 means that the shape is elongated whereas below 1, the shape is flat. This ratio was previously used in some studies using the Mori-Tanaka homogenisation so as to describe the global shape of inclusions (voids in the case of the cortical bone) [111, 114]. However, they didn't report direct measurement of this factor (see Chapter 1 section 1.2.2, page 35). They finally chose an elongated shape by justifying that an osteon has a length which can range up to several millimetres or that the numerical error is reduced using a very elongated shape (over 20). Numerical approaches aim at proving that the aspect ratio impact stagnates over 10. Although, by studying the distribution of this feature on every scan, an average of $87 \pm 6\%$ of all canals is found with an aspect ratio below 10. This difference can be explained by the fact that a clear definition of the canal as a void which ranges from connectivity to another has been established. Consequently, this result points out that aspect ratio should be thoroughly measured prior to this type of numerical approach.

Although for both of these features the values for the humerus and femur remain close to each other, significant differences between them are found. Humerus canals seem to have a slightly more elliptic transverse shape (0.61 vs 0.63) and flatter 3D shape (4.17 vs 4.83). These differences can be explained, as previously mentioned, by a hypothetical optimisation of the shape of canals. Indeed, the different functions of these two bones lead to different applied strains which finally bring different bone remodelling activities. Hence, blood and nutrient needs within the bone differ. Therefore, bone remodelling adapts the architecture so as to perform this supply as best as possible. The 3D shape differences can come from several features. Actually, this factor is computed from the ratio between the length of the canal and its diameter. For this reason, these two features need to be investigated so as to understand the shape differences.

Regarding the length of canals, it is apparent from Table 2.11 and Figure 2.14d that the mean length of canals is much smaller than the values justified for Mori-Tanaka studies [114]. Only two comparative values were found and reported by Cooper *et al.* [22] : 329.3 and 441.1 μm . Values obtained in this study are smaller (228.91 μm). One possible explanation for this might be that the definition of canals differs from Cooper *et al.* [22] study where they aren't clearly depicted. As the canal may not be split on connectivity (not specified), it would explain why current values are smaller. Mean length of canals is significantly shorter in the humerus (221.21 vs 237.7 μm). Interestingly, a

similar trend is found by individually compare humerus with femur for each subject. It means that whatever the subject history (physical activity, bone disease), humerus tends to have a shorter canal network than the femoral one. However, this difference remains slight. The standard-deviation is higher than the difference between the two groups and MWW p-value is close to 0.05. Although, this slight difference could be explained by a different bone turnover. Furthermore, femurs are longer than humeri. Hence, in the femoral diaphysis, canals need to be longer in order to better provide needs to the bone matrix.

Canal diameter is widely computed because it doesn't require a complex study of the architecture. Only a transverse study is sufficient. Nonetheless, the error quantification with dummy images proves that the canal 3D orientation should be considered so as to avoid over-estimation of the real diameter. Moreover, the ratio between the real diameter of the canal (which considers the orientation of the canal) and the apparent diameter (in-plane diameter, directly measured from slices) reveals that a direct measurement of the diameter overestimates it by 13 %. Somehow, it proves that a 3D assessment is required so as to correctly measured canal diameter. Otherwise, a linear regression was performed so as to be used to correctly quantify diameter for 2D studies. Both of these features are strongly correlated ($R^2 = 0.99$) (Figure 2.15) :

$$Ca.rDm = 0.914 * Ca.aDm \quad (2.11)$$

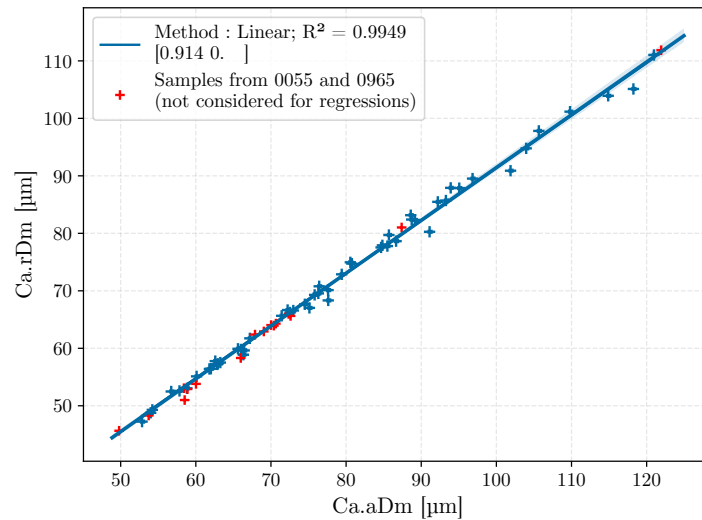


FIGURE 2.15: Ca.aDm VS Ca.rDm. This regression might be useful for further in-plane studies so as to avoid overestimation of the canal diameter.

Mean diameter remains in the same magnitude as the literature. A significant difference is found by comparing the bearing bone with the non-bearing bone. As a matter of fact, canals are larger in the

humerus than femur. Although, this finding differs from some published studies [10, 30]. Gauthier [30] compared radius samples with femoral ones and concluded that canal diameters were slightly larger in the bearing bone. Same trend is found by Bry [10] by a similar comparison between humerus and femur. Current opposite finding can be explained by several reasons. First, in the Gauthier [30] study, SR- μ CT was used on very small VOI (less than 1 mm^3). Therefore, the VOI shouldn't be representative to the entire bearing bone. Second, in the Bry [10] study, only 21 samples were harvested from 4 male subjects. By individually comparing diameter distributions from humeral and femoral samples, two subjects have a larger humeral pore diameter distribution whereas for the two others the opposite trend was found. It proves that, an overall trend is hard to obtain, and many human subjects are needed so as to conclude. In the current study, larger canal diameters are found in the humerus for 8 subjects (Figure 2.14f). This may due to the old age of the human subjects. Indeed, osteoporosis constantly acts in the elderly. Perilli *et al.* [74] proved that, in the elderly, canals enlarge and coalesce between themselves so as to create giant canals. This phenomenon is called trabecularisation and can be found in every bone of the skeleton. It begins in the endosteum part of the cortical shell and grows with age towards the periosteum one. The medullary cavity expands at the expense of the cortical shell by thinning it [140]. Humerus cortical bone is thinner than the femoral one (less than 5 mm [10, 13, 14] vs more than 6 mm [10, 18]). Therefore, the trabecularisation easier impacts humerus than femur. Consequently, it may explain why canals are larger in the humerus cortical shell than the femur one.

Regarding the two human subjects who highlight the opposite trend (0010 and 0020), i.e. a mean diameter which is larger for femur than humerus, it would suggest that the trabecularisation is absent or is at a primitive step. Consequently, it can be assumed that these two subjects were poorly impacted by osteoporosis or had a better physical activity prior to death or both. As a consequence, humerus is less porous than the femur (Figure 2.13a). This tendency is commonly justified by the fact that the femur, as a bearing bone, is more frequently damaged, which requires a more active bone turnover. Hence, so as to more activate bone remodelling, more supplies are needed. Canals with a large diameter are then more suitable [10]. However, this is in contrast with conclusions from Lassen *et al.* [59] study. Indeed, the bone matrix is remodelled thanks to the complex activity of BMU. In BMU, both of the bone resorption and creation occur. At the tip of a BMU, the old bone is resorbed by osteoclast cells. This resorption keeps eroding walls of this newly created canal up to reach a certain threshold density of reversal/osteoprogenitor cells. When this threshold is reached, the new bone is created and forms the new osteon. As shown by the authors of this study, osteoclast cells keep eroding even if the minimum density isn't reached. Therefore, a deficiency of recruiting osteoprogenitor leads to a canal enlargement without creating new bone. This conclusion justifies why mean canal

length remains shorter in the humerus whatever the human subjects (because the deficiency doesn't impact length of canals) and also why 8 human subjects have a larger canal network in the humerus. Moreover, trabecularisation is one of the consequences of osteoporosis and bone creation defect [141]. Subsequently, the 3D shape is affected (Figure 2.14h) as well as the mean volume of canals.

The mean canal volume is significantly more important (48 %) in the humeral cortical cortex (Table 2.11). This trend is found for every subject except for 0010 and 0020 human subjects. It points out that the canal diameter strongly impacts shape and volume of canals which leads to various porous cortical cortices. Correlations between architectural features are investigated in a further section of this manuscript (Section 2.3.4).

2.3.2.3 Connectivity features

Thanks to the novel technique of the 3D assessment of the vascular network within the cortical bone, connectivity are not only automatically detected, but some features are also measured. Table 2.13 and Figure 2.16 store the features which are computed for every connectivity.

		Bone	Mean \pm Std	Median	Min	Max	Q1	Q3	p-value
Conn. α	[deg]	Pooled	34.91 ± 3.50	34.75	26.65	43.39	32.11	37.23	0.145
		Femur	34.46 ± 2.68	34.34	29.37	40.34	32.92	35.98	
		Humerus	35.31 ± 4.04	34.97	26.65	46.02	32.11	38.21	
Conn. $R_{rDm_{(0,12)}}$	[-]	Pooled	0.88 ± 0.02	0.88	0.83	0.93	0.86	0.89	0.206
		Femur	0.88 ± 0.03	0.88	0.83	0.93	0.87	0.90	
		Humerus	0.88 ± 0.02	0.88	0.83	0.91	0.86	0.89	
Conn. $R_{rDm_{(1,2)}}$	[-]	Pooled	2.66 ± 0.86	2.38	1.70	3.88	2.07	2.81	0.006
		Femur	2.41 ± 0.59	2.28	1.70	3.17	1.98	2.57	
		Humerus	2.88 ± 0.99	2.57	1.89	4.44	2.25	3.21	

TABLE 2.13: Connectivity features values. See Table 2.3 for abbreviations. Minimum and maximum values are reported without considering outliers (by groups). Q1 and Q3 are the first and third quartile, respectively. p-value is the result of significant differences, assessed by Mann-Whitney-Wilcoxon (MWW) test, between each bone. Bold values are those below 0.05 (which means that groups are significantly different).

The angle between two connected canals is assessed. This angle aims at quantifying the opening of the connectivity. Higher the angle is, wider the opening of the connectivity is. Statistics prove that the mean angle poorly differs between bone groups. A histogram analysis (not displayed), by comparing the humerus and femur on each subject, confirms that whatever the bone, distribution is similar for both bones : maximum of histograms is reached in $Conn.\alpha \in [10, 30]$ range. It means that this angle doesn't depend on the bone remodelling and the optimised shape is the same for a bearing and a non-bearing bone. However, it would be interesting to further compare this feature with

mechanical features. Indeed, a small angle means a narrowed space between two connected canals. This narrowed space could lead to some stress concentration during a mechanical loading.

$Conn.R_{rDm(0,12)}$, which is the ratio between the sum of outgoing canal diameters and the incoming canal diameter, is close to 1 but remains below 1. It means that the incoming canal is slightly larger than the combination of the two outgoing canals. The second ratio, $Conn.R_{rDm(1,2)}$, that is the ratio between the two outgoing canal diameters, suggests that outgoing canals have different shapes. Indeed, the mean value is over 2.66 ± 0.86 . It means that the largest outgoing canal is 2.66 times larger than the second one. Hence, this value suggests that canals interconnect between themselves whatever their diameter. Interestingly, this ratio is significantly higher for humeral samples. This trend is confirmed by comparing femoral and humeral samples on each subject (Figure 2.16c). However, histograms of this ratio (not displayed) show that in all samples, $Conn.R_{rDm(1,2)}$ peak distribution is reached in the range $[1, 1.5]$ which means that most of connectivity (37%) have $Conn.R_{rDm(1,2)}$ have a value below 1.5. Hence, 37% of connectivity have similar outgoing canals. The significant differences can be explained by more decreasing distributions of $Conn.R_{rDm(1,2)}$ in humeral samples.

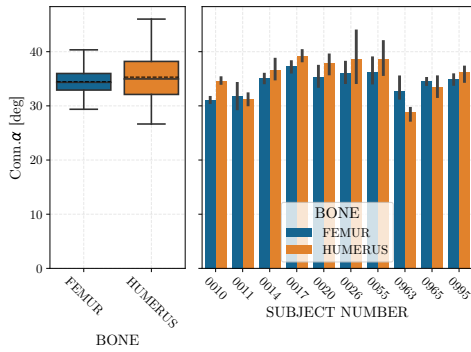
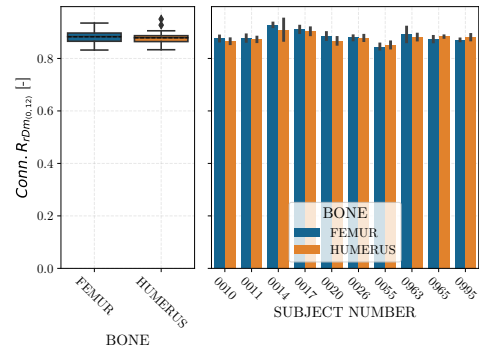
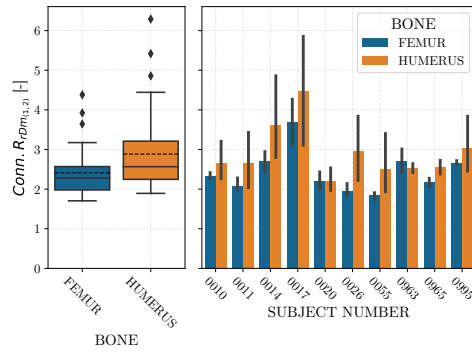
(a) $Conn.\alpha$ boxplots and barplots(b) $Conn.R_{rDm(0,12)}$ boxplots and barplots(c) $Conn.R_{rDm(1,2)}$ boxplots and barplots

FIGURE 2.16: Connectivity features boxplots and barplots. Barplots display the mean value. The vertical black line is the 95% confidence interval for each group. Left plot shows boxplot for all grouped femoral and humeral samples. Dotted and straight horizontal lines are the mean and median values, respectively. Outliers are displayed by diamond markers. On the right, features are individually highlighted.

All of these results show that canals are interconnected with a privileged opening angle whatever the diameter in both bearing and non-bearing bones. This conclusion confirms the qualitative analysis made by Bousson *et al.* [26].

2.3.2.4 BMU features

Previous sections have shown that some differences exist between a bearing and a non-bearing bone. These differences are mainly justified by the bone remodelling which differently acts on each bone. The bone remodelling is activated by osteoblast and osteoclast cells and can be found in BMU canals. Hence, investigating BMU canals would be an interesting way so as to understand the architectural differences between the two types of bone. Besides automatic detection of canals and connectivity, BMU are also automatically detected.

In total, 4 features are computed for each BMU detected. Mean values and barplots are shown in Table 2.14 and Figure 2.17.

	Bone	Mean \pm Std	Median	Min	Max	Q1	Q3	p-value
<i>BMU.rDm</i> [μm]	Pooled	55.52 \pm 18.95	49.30	32.95	96.87	42.21	64.32	0.031
	Femur	50.27 \pm 13.82	46.73	32.95	77.81	41.26	57.82	
	Humerus	60.12 \pm 21.49	51.57	36.34	102.05	43.77	72.64	
<i>BMU.rLe</i> [μm]	Pooled	176.08 \pm 41.42	183.83	93.62	260.19	156.95	205.07	0.020
	Femur	184.65 \pm 41.37	190.82	103.97	260.19	167.25	213.73	
	Humerus	168.56 \pm 39.97	172.67	99.75	235.95	156.61	195.45	
<i>BMU.BF</i> [%]	Pooled	0.12 \pm 0.05	0.12	0.03	0.25	0.08	0.16	0.045
	Femur	0.13 \pm 0.04	0.13	0.04	0.24	0.10	0.17	
	Humerus	0.12 \pm 0.06	0.10	0.03	0.25	0.08	0.16	
<i>BMU.BF</i> [%]	Pooled	5.25E-04 \pm 2.86E-04	4.45E-04	1.26E-04	1.08E-03	3.41E-04	6.45E-04	0.024
	Femur	4.32E-04 \pm 1.45E-04	4.18E-04	1.26E-04	7.05E-04	3.29E-04	5.08E-04	
	Humerus	6.06E-04 \pm 3.47E-04	5.36E-04	1.53E-04	1.20E-03	3.71E-04	7.25E-04	

TABLE 2.14: BMU features values. See Table 2.4 for abbreviations. Minimum and maximum values are reported without considering outliers (by groups). Q1 and Q3 are the first and third quartile, respectively. p-value is the result of significant differences, assessed by Mann-Whitney-Wilcoxon (MWW) test, between each bone. Bold values are those below 0.05 (which means that groups are significantly different).

Table 2.14 is interesting in several ways. First, as found for canal diameter (section 2.3.2.2), mean diameters of BMUs are significantly different (MWW p-value < 0.05). Indeed, diameters are 20 % higher in the humerus than femur. As suggested in section 2.3.2.2, BMU deficiency lies in the osteoprogenitors recruitment rate which delays the bone creation process for the benefit of an excessive bone resorption which enlarges newly formed canals and makes bone more porous [59]. Interestingly, 0010 and 0020 subjects keep the opposite trend even for the BMU diameter. Overall, the BMU diameter remains below to the diameter of the other canals. It suggests that the canal expansion is

in process and needs to keep enlarging so as to reach the number of osteoprogenitors needed to begin bone creation [59].

Second, BMUs are shorter than classical canals (176 vs 229 μm). This result makes sense because canals with a BMU cone tip are expanding up to connect to another canal. Interestingly, BMUs are significantly longer in femur than in the humerus. It would suggest that a different canal expanding speed is effective. Indeed, the bone resorption is assessed at two levels : the first one is located on the tip of the cone so as to expand the length of the BMU, and the second one is located on the wall of the cavity so as to enlarge it [59]. Smith *et al.* [142] highlights that the bone turnover is maintained by two balancing processes in order to control the progression speed (faster or lower). These processes can lead to a ceasing of the BMU expansion. Consequently, the significant difference found in BMU length between humerus and femur would suggest that a different expansion speed occurs. However, in current study, only one scan is assessed on a post-mortem human sample. It would be interesting to assess this kind of study on a living tissue so as to follow the expansion of BMUs. Nonetheless, current in-vivo scan devices are limited due to their resolutions that are not suitable to fully detect vascular canals (over 80 μm , see section 1.1.3.3 on page 18).

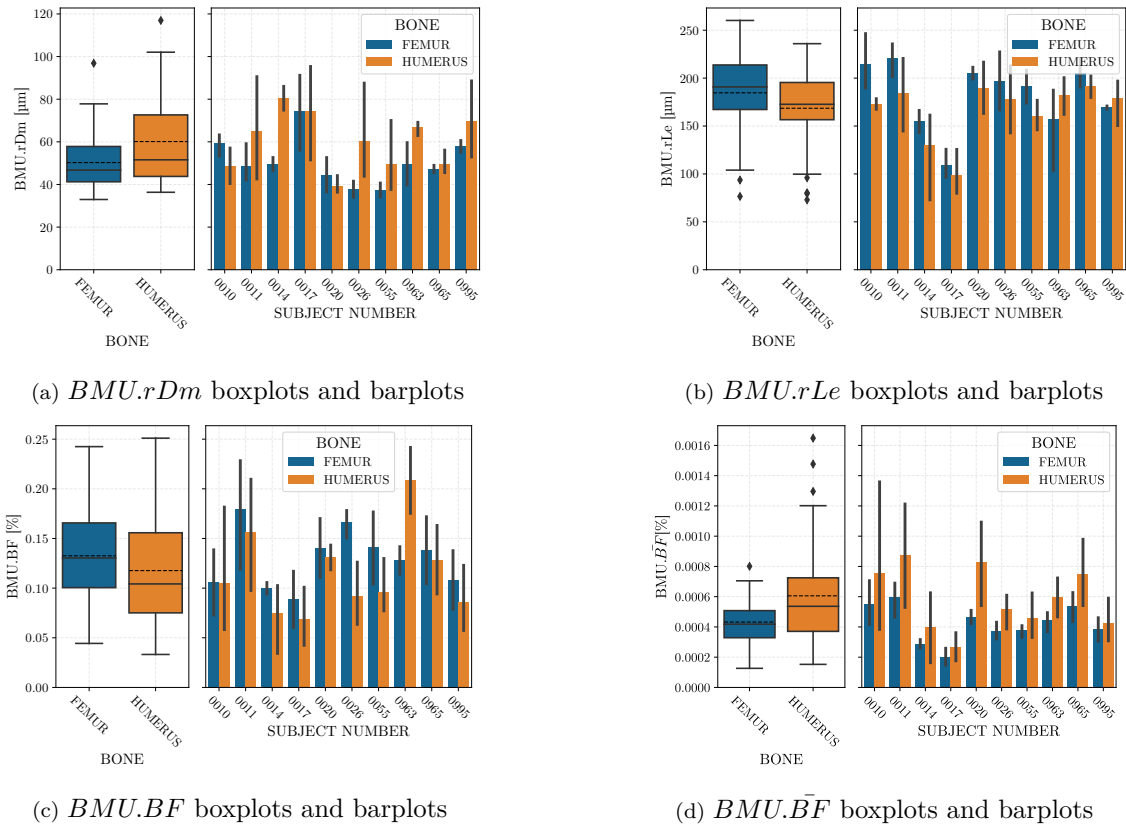


FIGURE 2.17: BMU features boxplots and barplots. Barplots display the mean value. The vertical black line is the 95 % confidence interval for each group. Left plot shows boxplot for all grouped femoral and humeral samples. Dotted and straight horizontal lines are the mean and median values, respectively. Outliers are displayed by diamond markers. On the right, features are individually highlighted.

Third, new created bone fraction is assessed ($BMU.BF$). This feature is the ratio between the new bone volume and the total volume of the sample. Due to the numerous processing steps needed to compute this feature, this value shouldn't be quantitatively considered. That's why, it will only be used for comparisons. More remodelled bones are found in the femur than in the humerus. It hints at the bearing bone is more active so as to create new bone. However, the efficiency of BMUs, $BMU.BF$ is assessed by dividing the new created bone fraction by the number of BMUs in the sample. Surprisingly, this feature is more important for the humerus. It implies that even if more bones are remodelled in the femur, BMUs remain more effective in the humerus. Moreover, even though many more bones are remodelled in 0963 humeral samples (Figure 2.17c), BMU efficiency is similar to the other subjects (Figure 2.17d).

These results highlight that BMUs differently infer in the cortical cortex and is bone dependant. Indeed, significant differences between the femur and humerus are found for all BMU features. Their efficiency seems to have similar trends (Humerus > Femur) whatever the human subject that would suggest that the new bone created by BMUs depends on the type of bone. However, more new bones are created in the femur which highlights that the bearing bone needs to more actively replace old bone. Hence, a significant denser BMU network occurs in the bearing bone (Figure 2.13e). To initiate new BMUs (Howship lacunas), osteocytes need to convert strain energy into electrical and biochemical signals (mechanotransduction) [60]. Thus, a homogeneous strain field, would lead to a denser BMU network. That would be the reason why the BMU network and the new-created bone volume is more important in the femur than in the humerus. In the case of the humerus, the strain field should be more heterogeneous with high local strains which create less BMUs but with a bigger local volume to replace. Obviously, these hypotheses needs to be verified in further studies by performing a similar architectural study on in-vivo samples. By comparing individuals, 0014 and 0017 (female), which are the oldest human subjects in the database (96 years old), have new bone fraction and BMU efficiency that remain lower to all the other human subjects. Due to the very old age of these two subjects, osteoporosis can be considered as advanced in bone. Hence, it highlights that the osteoporosis impacts the BMU activity by reducing the new created bone and consequently its efficiency.

2.3.3 Side comparison

On the previous section, samples were compared so as to exhibit differences between the bearing and the non-bearing bone (See Table 2.9 on page 64 to obtain the number of samples). However, on each human subject, samples were extracted from both left and right limbs. The laterality of the samples are recorded. So far, no study on the comparison of the cortical architecture between left and right

limbs were found. Recently, Perchalski *et al.* [15] provided a study so as to investigate global bone shape asymmetry of paired humeri. This study reveals that the global shapes of left and right humeri differ in the late of growth. Hence, a similar study is performed on the cortical architecture so as to exhibit directional asymmetry. So as to avoid data redundancies, only features with significant differences between left and right of the corresponding limbs are displayed by Table 2.15 and Figure 2.18.

	Humerus side	Mean \pm Std	Median	Min	Max	Q1	Q3	p-value
Ca.V/TV [%]	Right	7.71 \pm 6.08	5.35	2.98	10.52	4.22	9.37	0.038
	Left	10.06 \pm 6.05	8.28	3.07	19.70	5.66	12.24	
Ca.rLe [μ m]	Right	237.18 \pm 61.20	242.63	206.03	296.73	221.87	262.50	0.043
	Left	208.72 \pm 55.55	203.98	87.95	316.97	180.36	249.93	
BMU. $\bar{B}\bar{F}$ [%]	Right	7.42E-04 \pm 3.91E-04	6.57E-04	2.00E-04	7.79E-04	5.02E-04	7.65E-04	0.015
	Left	4.99E-04 \pm 2.63E-04	3.97E-04	1.53E-04	1.08E-03	3.25E-04	6.41E-04	

TABLE 2.15: Left and right humerus comparisons. See Tables 2.2, 2.3 and 2.4 for abbreviations. Only features with significant differences between left ($N = 23$) and right ($N = 18$) humeri are shown. All the other features are similar for both sides. p-value is the result of significant differences, assessed by Mann-Whitney-Wilcoxon (MWW) test, between each side. Bold values are those below 0.05 (which means that groups are significantly different).

A similar protocol is used to compare paired left and right limbs. Interestingly, MWW test didn't reveal any significant difference ($p < 0.05$) between left and right femurs whatever the architectural feature. This result makes sense because bearing bones are mainly used for locomotion. No asymmetric use of lower limbs is exhibited during a healthy walking. As a consequence, bone remodelling acts similarly for both sides. Hence, similar architecture network is found in left and right femurs. No comparative work that studies and compare cortical micro-architecture of left and right human femurs was found. However some studies, where the femur geometry or aBMD is assessed, report that very small differences remain between two paired of femur [143–145]. These studies mainly use in-vivo devices (DXA, CT or HR-pQCT). Therefore, due to the limitations of this type of device, micro-architecture of cortical bone can't be detected.

Three architectural features are statistically different by comparing left and right humeral samples. Interestingly, one of the most important architectural features, Ca.V/TV shows that left humeral samples tend to be significantly more porous than the right ones (10.06 % vs 7.71 %). Barplots on Figure 2.18a shows that this trend is verified on 8 human subjects. Similarly, canals are longer in left humerus than in the right one (208 μ m vs 237 μ m). Remarkably, the BMU efficiency (BMU. $\bar{B}\bar{F}$) is more important in the right humeral samples.

All of these results highlight that femur has a similar within architecture whatever the side. No significant differences were found for the 17 computed features. However, the cortical bone of humeri shows a significant asymmetry for 3 architectural features, particularly the cortical porosity. These

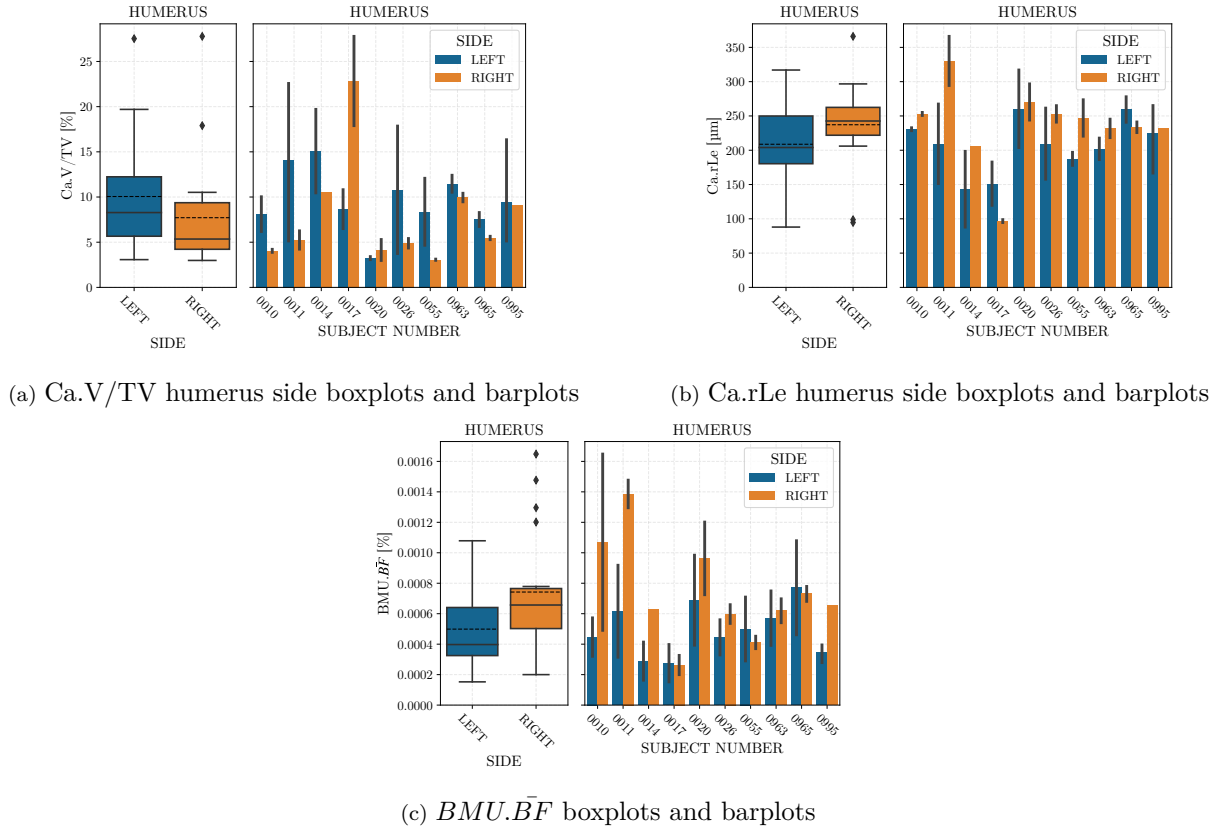


FIGURE 2.18: Humerus side boxplots and barplots. Barplots display the mean value. The vertical black line is the 95 % confidence interval for each group. Left plot shows boxplot for all grouped left and right humeral samples. Dotted and straight horizontal lines are the mean and median values, respectively. Outliers are displayed by diamond markers. On the right, features are individually highlighted.

differences point out that the human humerus asymmetry needs to be considered. It also highlights that the bone remodelling acts differently and creates different architectures. It makes sense because the bone remodelling highly depends on the mechanical strains applied on it. Hence, different functions of the bone will lead to different bone remodelling. As most of peoples, a privileged arm is used to complete everyday tasks. This creates an asymmetry in bones. In the current study, all the humans are the elderly category. It means that osteoporosis is present and has already impacted the cortical bone for a while. Particularly, in the 0017 human subject (Female), which is the oldest subject in the database, an important porosity difference is found between left and right humeri. It shows that the bone remodelling deficiency can also create an asymmetry in upper limbs. This large asymmetry in porosity isn't found for the canal length. It would suggest, as shown in a previous section, that the porosity poorly depends on the canal length. Interestingly, for the two oldest female subjects (0014 and 0017), BMU efficiency remains lower than all the other subjects whatever the humeral side. It can state that the BMU efficiency is impacted by advanced osteoporosis, and trabecularise the cortical bone by making it more porous and enhance asymmetry of humeri.

2.3.4 Inter-parameter relationships

In the previous sections, it was shown that the cortical porosity highly differs between a bearing and a non-bearing bone. It was also shown that bearing bones are asymmetric due to different bone remodelling. However, so as to compute these features, a 3D assessment is required. Hence, it would be interesting to provide some regressions between 2D, which are more accessible, and 3D features. For instance, the porosity is widely computed in the literature. The dispersion of the porosity is the result of various canal networks with different canal shapes. At the same time, providing these regressions will help to understand what is the impact of 3D features, such as canal length or diameter, on the global features, such as the porosity.

Therefore, regressions are performed using non-linear least squares method (Scipy python library). A linear and quadratic polynomial functions are used in order to fit two parameters together. Squared R value (R^2) is used to define a more or less good fit. Linear regression is privileged if the squared R from quadratic isn't enhanced of at least 5%. Outlier values are not considered so as to don't affect regressions. Plots that show the most relevant regressions are displayed in Figures 2.19 and 2.20. Blue area on these plots displays the 95 % confidence interval of regressions after bootstrapping ($N = 1000$). Regression coefficients are stored in Table 2.16. So as to validate these regressions, two human subjects are not considered for regressions (0055 and 0965). Hence, samples from these two subjects are used to validate regressions. Error is computed by dividing the absolute difference between the predicted and measured values by the measured value. Mean and median error for each feature are shown in Table 2.17. Thus, 61 and 16 samples are used to define and validate regressions, respectively.

As expected, Ca.V/TV is correlated with many canal features. However, it is poorly correlated with the different densities. It means that porosity mainly depends more on the canal shapes instead of the vascular network density. Regarding the regressions, mean canal length, diameter, volume and 3D aspect ratio can be more or less properly predicted.

Squared R remains low for the canal length (0.45). Hence, from the two subjects which are not considered, about 9 % of deviation is found. It would suggest that the canal length has a low impact on the cortical porosity. However, contrary to expectations, a negative trend is found between these two features : more porous the bone is, less elongated canals are. It means that due to the trabecularisation of the cortical bone during osteoporosis, canals are shortened. This conclusion makes sense because canals enlarge during trabecularisation and coalesced. According to the fact that canals are defined as a void which ranges between two subsequent connectivity, canals shorten due to the

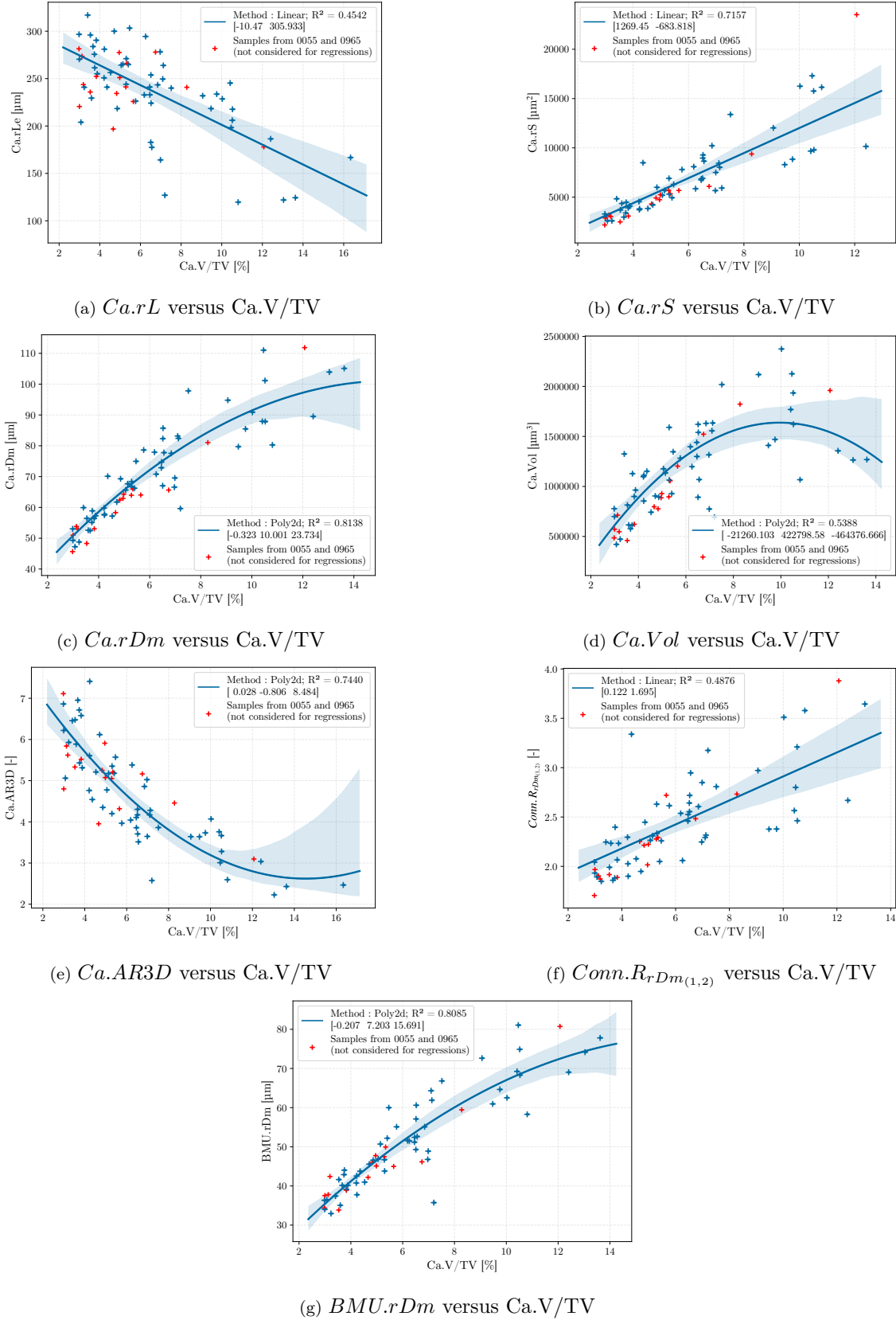


FIGURE 2.19: Polynomial regressions between architectural features (Part 1). Mean values are displayed by plus markers. Blue markers are those used for regressions. Outliers are previously removed. Red markers are those used to validate regressions ($N=16$, from 0055 and 0965 subjects). Therefore, they aren't considered to obtain regressions. Curve is the regression function. The 95 % confidence interval of the regression is displayed by the transparent coloured area.

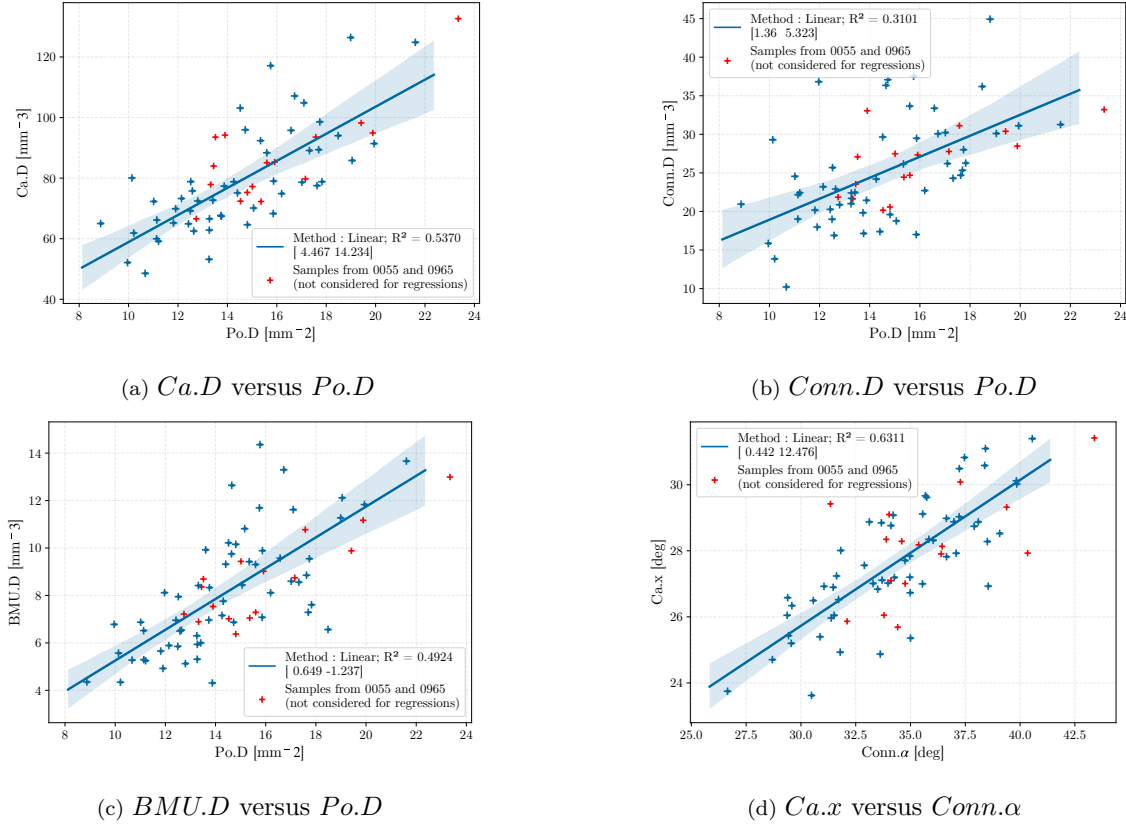


FIGURE 2.20: Polynomial regressions between architectural features (Part 2). Mean values are displayed by plus markers. Blue markers are those used for regressions. Outliers are previously removed. Red markers are those used to validate regressions (N=16, from 0055 and 0965 subjects). Therefore, they aren't considered to obtain regressions. Curve is the regression function. The 95 % confidence interval of the regression is displayed by the transparent coloured area.

$y = f(x)$	x	R^2	a_0	a_1	a_2
<i>Ca.D</i>	<i>Po.D</i>	0.54	14.23	4.47	-
<i>Conn.D</i>	<i>Po.D</i>	0.31	5.32	1.36	-
<i>BMU.D</i>	<i>Po.D</i>	0.49	-1.24	0.65	-
<i>Ca.x</i>	<i>Conn.alpha</i>	0.63	12.48	0.44	-
<i>Ca.rLe</i>	<i>Ca.V/TV</i>	0.45	305.93	-10.47	-
<i>Ca.rS</i>	<i>Ca.V/TV</i>	0.72	-683.82	1269.45	-
<i>Ca.rDm</i>	<i>Ca.V/TV</i>	0.81	23.73	10.00	-0.32
<i>Ca.Vol</i>	<i>Ca.V/TV</i>	0.54	-4.64E+05	4.23E+05	-2.13E+04
<i>Ca.AR3D</i>	<i>Ca.V/TV</i>	0.74	8.48	-0.81	0.03
<i>Conn.RrDm_(1,2)</i>	<i>Ca.V/TV</i>	0.49	1.70	0.12	-
<i>BMU.rDm</i>	<i>Ca.V/TV</i>	0.81	15.69	7.20	-0.21

TABLE 2.16: Architecture inter-parameters polynomial fitting. R^2 is the coefficient of determination of the fittings. Linear and quadratic polynomials are assessed using non-linear least-squares method. Hence, $y = a_0 + a_1x^1 + a_2x^2$ and $y = a_0 + a_1x^1$ functions are computed. To compute fittings, subjects 0055 and 0965 weren't considered.

coalescence. Interestingly, mean canal diameter and surface can be well predicted by the porosity. Indeed, a positive trend is found between both these features and porosity. It suggests that the growth of porosity mainly comes from the canals enlargement.

$y = f(x)$	x	Mean \pm std error [%]	Median error [%]
<i>Ca.D</i>	<i>Po.D</i>	8.58 ± 5.97	7.74
<i>Conn.D</i>	<i>Po.D</i>	10.08 ± 8.03	7.39
<i>BMU.D</i>	<i>Po.D</i>	11.70 ± 8.25	10.12
<i>Ca.x</i>	<i>Conn.α</i>	3.80 ± 2.85	3.06
<i>Ca.rLe</i>	Ca.V/TV	9.49 ± 8.20	8.71
<i>Ca.rS</i>	Ca.V/TV	19.79 ± 14.64	14.13
<i>Ca.rDm</i>	Ca.V/TV	6.70 ± 4.76	4.91
<i>Ca.Vol</i>	Ca.V/TV	23.05 ± 15.32	21.77
<i>Ca.AR3D</i>	Ca.V/TV	11.65 ± 9.51	10.60
<i>Conn.RrDm_(1,2)</i>	Ca.V/TV	8.14 ± 6.39	6.83
<i>BMU.rDm</i>	Ca.V/TV	6.04 ± 5.15	5.47
All features		5.51 ± 14.02	3.88

TABLE 2.17: Prediction error of architectural data. This error is computed from the 16 samples harvested from 0055 and 0965 subjects (which were, obviously, not considered to assess polynomial fits). The error is computed by dividing the absolute difference between the predicted and measured values by the measured value.

A quadratic polynomial regression is needed to correctly predict the mean canal volume from Ca.V/TV. It is somewhat surprising that this relationship isn't monotonous. Indeed, up to a 10 % volume porosity, regression is monotonically increasing. Beyond 10 %, this regression decreases. It would suggest that for extremely porous cortical cortices, canals stop enlarging. This nonsense conclusion could be induced by the lack of extremely porous samples. It would mean that the current regression isn't available for samples with more than 10 % of porosity. To compensate this lack, more highly porous sample should be considered. If outlier values aren't removed (not displayed), regression (quadratic) keeps increasing until 25 % and squared R is slightly higher (0.58). However, to maintain coherence between the different regressions, outlier values can't be considered.

Interestingly, the mean canal aspect ratio is linked with the porosity. This relationship is quite revealing in several ways. First, it means that as the porosity keeps increasing, the global shape of canals evolves. Indeed, a negative trend is found. Hence, for highly porous cortical cortices, vascular canals tend to become flattened. It makes sense with previous conclusions because, as the porosity is increasing due to trabecularisation, canals are enlarging, coalescing between themselves and, as a consequence, reducing their size and modifying their shape. Coalescence of canals is widely discussed in the literature [31, 72, 74]. However, as suggested previously, these studies are limited to planar studies. Therefore, canals length and 3D shapes aren't assessed. One of the novelties of the current

study is to prove that the global shape of the vascular canals is affected as porosity increases : canals become flatter. Second, this shows, once again, that canal shape can't be considered as very elongated as used by some Mori-Tanaka studies [111, 114]. Consequently, this feature depends on the porosity and should be correctly provided for such studies.

Regarding Figure 2.19f, it shows that shapes of interconnected canals also depends on the porosity. More porous the cortical bone is, more diameters of the two outgoing canals differ. This result would suggest that the trabecularisation isn't homogeneous in the cortical cortex. A canal can enlarge due to trabecularisation whereas a nearby canal doesn't.

In a similar way, mean diameter of BMUs also is positively correlated with the porosity (Figure 2.19g). It points out that the canal enlargement due to trabecularisation begins by a deficiency of bone creation during the remodelling process. This outcome is consistent with Lassen *et al.* [59] study where a link between BMUs geometry and cell activity is proved. Osteoporosis affects the osteoprogenitor recruitment rate that delays the bone creation and consequently BMU enlargement is more important.

As previously stated, canal, connectivity and BMU densities can't be predicted from the porosity. It highlights the poor dependency of the porosity on the densities for the benefit of pore enlargement. Similar conclusions are found by some other studies [68, 73, 74]. However, as suggested by Bala *et al.* [72], cortical porosity shouldn't be the only architectural feature to consider. Indeed, increasing of densities would lead to a reduction of spacing between canals and affects the mechanical behaviour of the bone.

Canal and BMU densities show a pretty good relationship with the pore density (Figures 2.20a and 2.20c). BMU density relationship is quite revealing because it means that denser a vascular network is, more active the bone remodelling is. This result makes sense because the bone remodelling is activated by osteocytes that detect strains/micro-damages and create Howship lacunas. Hence, if more damages are sensed, more Howship lacunas will be created.

The relationship of the density of connectivity with the pore density is more dispersive ($R^2 = 0.31$, Figure 2.20b). This dispersion shows that it is hard to predict the number of connectivity from a 2D study because, as previously proved, the canal shape is highly sensitive to the architectural changes. Indeed, canal becomes shorter as the porosity increases (Figure 2.19a). As a canal is depicted as a void between two connectivity, the density of connectivity depends on the length of canals. Nonetheless, a positive correlation between these two features is still found.

The last shown regression concerns the relationship between the mean longitudinal angle of canals and the opening angle of connectivity. Indeed, a positive trend is found. It suggests that more canals oriented are, wider the connectivity are. Hence, the orientation of the canals have an impact on the shape of connectivity.

2.4 Conclusions

The purpose of this chapter was to propose an innovative method to assess the 3D architecture of the vascular network in the cortical bone. 77 μ -CT scans were performed on the central part of dumbbell-shaped specimens harvested from 10 human subjects. Left and right humeral and femoral samples were studied. For each scan, about 2300 slices were obtained. A Python script was carried out so as to detect and quantify vascular canals in 3D. The first step of the script consists in processing each slice. Care was taken to the image processing. Indeed, many studies report a user-specified global threshold [26, 66–68, 72]. The image threshold has a great impact on the final results. Therefore, a generic image processing, which can consider different sample shapes so as to make it as robust as possible, is chosen. Each image is first filtered to reduce noise. Then, the image can be split along the brightness axis (beam hardening artefacts) where each portion is independently processed and thresholded using an Otsu threshold method. Subsequently, contours of pores are detected. Canals are 3D detected using an equivalent diameter criteria which links pores on subsequent images. Once canals are detected, and due to the tortuous network, connectivity are detected so as to obtain representative features of canals. One of the most important novelties of this work is the automatic detection of BMUs. Indeed, as they are part of the vascular network, the detection criteria consists in the use of a derivative criteria so as to identify the BMU closing cones on one-side bounded canals. From all of this, numerous 3D shape features are computed such as the orientation, diameter, length or the aspect ratio of canals. Most importantly, the new bone volume created by BMUs is estimated by detecting grooves behind the closing cones. This feature helps to quantify the bone remodelling which was never detected and measured before.

At the same time, so as to quantify errors and robustness of the algorithm, two short studies were carried out. The first one consisted in creating dummy images where within architecture geometry is known. As a matter of fact, cylindrical porosities are defined by their orientation, diameter and position in the dummy sample. The outcomes show that the error is very low (2 %) which means that the algorithm is able to correctly compute the 3D features of the within architecture. The second study consisted in quantifying the robustness of the protocol by successively scan one sample four times. In a similar way, by comparing each scan, results were poorly dispersive and the standard error

was quite low. It highlights that the entire process is poorly dependant of the protocol. From these two studies, the Python script can be considered as relevant and robust.

By comparing bearing with non-bearing bones, numerous statistically differences were found. First, samples from humeri were more porous than femoral ones. This difference is explained by the trabecularisation which more impacts humerus than femur. It thins the cortical shell. As the cortical bone is thinner in humerus than femur, trabecularisation easier impacts global porosity of the humerus. This conclusion is enforced by the significant differences between bearing and non-bearing bone found for canal diameters and lengths which affect their 3D shape. Indeed, larger and shorter canals are found in humeral samples resulting in a flattening of canals. It points out that the global shape of the canals, which has never been measured before, can't be considered as very elongated as used by some studies [111]. Using the regressions, porosity is positively and negatively correlated with mean diameters and lengths of canals, respectively. It means that during trabecularisation, canals coalesce which shortens them and makes them flatter. However, no relationships were found between the porosity and the different densities. It means that the porosity is mainly induced by canal geometry. A similar conclusion from some 2D studies was [68, 73, 74] made and can be extended to a 3D study of the cortical network thanks to the current study.

By comparing left and right limbs, no differences were found for the femur. This result makes sense because, due to their bearing functions, both left and right legs are similarly solicited. However, some differences were found by comparing left and right humeri. Indeed, left humerus seems to be more porous than the right one. Interestingly, similar trend was found for 8 subjects (10 in total). As the porosity is highly correlated with the canal shape, canals are significantly shorter in the left limb than those in the right one.

BMU features revealed some interesting results. Actually, by comparing the bearing bone with the non-bearing one, the 4 computed features revealed a significant difference between the two groups. Canals are larger and shorter in the humerus. Moreover, the mean new bone volume created by BMUs is slightly more important in the femur. However, BMUs are more efficient in the humeral cortex. As the BMU are denser in the femur, it can be explained by the fact that a homogeneous strain field occurs in the femur (due to its functions) that homogeneously activates osteocytes in the cortex. Hence, each BMU needs to create less new bone than those in humerus where the strain field is more heterogeneous.

Using the polynomial regressions, some 3D features can be predicted from planar studies. These regressions aim at estimating the global vascular network when 3D architecture can't be measured, e.g., microscopic images. It would be interesting to use this type of regression with planar studies because

micro-CT can't differentiate osteonal bone from the interstitial one whereas microscopy associated with staining method can do it. Thus, 3D vascular network could be compared to the osteonal bone and its within architecture (lacunas, canaliculi, ...).

One of the possible further studies should be to confront an equivalent study where both vascular canals and osteocytes can be seen and 3D detected (i.e. SR- μ CT as used by Gauthier [30]). Indeed, all along this chapter, BMUs are depicted as the main responsible for the bone turnover. Whereas osteocytes are the mechanosensors that activate the BMU creation. Hence, confront osteocyte features (density, shape) with BMU ones should be an interesting way to complete this study. Moreover, trabecularisation with canal enlargement have been proved to increase the porous part of the cortical bone. This pore enlargement is depicted as a bone creation deficiency that occurs in BMUs as reported by Lassen *et al.* [59] and confirmed by the positive correlation between porosity and the mean BMU diameter. By considering only this conclusion it would suggest that a denser deficient BMU network would accelerate the porosity increase. This in contrast with the fact that a more active bone creates a denser BMU network. However, osteocyte lacuna density decreases in the elderly which means that mechanosensors are less dense. As a consequence, less Howship lacunas can be initiated so as to create BMU resorption cones. It would be interesting to assess simultaneously osteocytes features and BMU features in order to understand and quantify the impact of agent in the remodelling process. Another possible study is to perform a similar study of the vascular network, and especially BMU network, on in-vivo samples. However, this kind of study requires to obtain slice images with an isotropic voxel size under 3 μ m. Currently, tomographic devices can't perform such scans due to technological limitations and radiation dose during the scan.

As described at the beginning of this chapter, samples were harvested and subsequently machined in order to obtain cylindrical dumbbell-shaped specimens. Besides the shape is optimised to fully scan the gauge length of specimens, the shape is also optimised for tensile tests. Indeed, tensile tests are subsequently performed after tomographic scans. As the vascular is 3D described, it would be interesting to understand how this micro-scale architecture impacts the macroscopic mechanical properties. Moreover, some indentations are also performed on these specimens. Indeed, the macroscopic mechanical properties of the bone is the result of lower scales phenomenons which occur due to the architecture and the mechanical properties of the bone matrix. Finally, a multi-scale correlation study is performed by confronting architectural data with micro and macro mechanics so as to predict the mechanical behaviour of the bone from a tomographic scan. These studies are described in the following chapter of this manuscript.

Highlights of Chapter 2

- An innovative technique is provided to 3D assess the vascular network of the cortical bone
 - A generic image processing is detailed (automatic threshold and image filters)
 - Pore contours are detected and used for assessment
 - Canals are clearly defined as voids that range from a connectivity to another
 - Canals, connectivity and BMUs are detected
 - Numerous geometrical features are measured
 - The robustness is quantified and remains suitable for vascular network assessment
- Left and right humeri and femurs are harvested from 10 human subjects
 - 77 dumbbell-shaped samples are scanned at a 2.94 μm resolution
- Femurs and humeri are compared so as to find significant differences
 - The humerus is more porous with a denser BMU network
 - Vascular canals are larger in the humerus
 - The trabecularisation affect more readily the humerus
 - The BMU activity is different according to the bone
- The architecture of the humerus is bias dependent
 - The left limb is more porous and canals are shorter
 - The BMU activity also differs and enhance limbs asymmetry
- Inter-parameter relationships are investigated
 - The porosity differences are mainly due to trabecularisation
 - The trabecularisation enlarges and flattens canals
 - Regressions can be used so as to extrapolate 3D features from planar studies

Chapter 3

Mechanical characterisation of human cortical bone

Contents

3.1	Introduction	93
3.2	Material and methods	94
3.2.1	Sample extraction	94
3.2.2	Macro-mechanical test : quasi-static tensile test	96
3.2.2.1	Strain rate and measurement	96
3.2.2.2	Stress measurement	96
3.2.3	Micro-mechanical test : micro-indentation test	100
3.2.3.1	Theory	102
3.2.3.2	Machine compliance	103
3.2.4	Statistics and data processing	104
3.3	Results and discussion	105
3.3.1	Bearing and non-bearing bones comparisons	105
3.3.1.1	Tensile tests	105
3.3.1.2	Indentation tests	110
3.3.2	Side comparison	112
3.3.3	Multi-scale correlation	114
3.4	Conclusions	119

3.1 Introduction

The cortical bone has a very complex micro-architecture which impacts the mechanical behaviour at upper scales. As shown in the previous chapters, vascular canal network within the cortical cortex is very tortuous and differs according to the type of bone. Indeed, different micro-architectures were found in humeral and femoral samples even in the same human subject. These differences would create different mechanical behaviour. As clarified by the first chapter of this manuscript, the cortical bone has been widely investigated so far. However, there is a large volume of published studies describing the cortical behaviour by harvesting samples from the human femur [52, 70, 84, 85, 87], or tibia and fibula [72, 84, 85, 88]. Non-bearing bones, such as humerus, are poorly investigated. Actually, as suggested by the chapter 1, this lack of studies can be explained by the fact that the sample harvest remains a challenge due to the very thin cortical shell in the humerus (mainly less than 5 mm [10, 13]). By reviewing the numerical human models, it highlights that the cortical bone is mainly considered as an isotropic elastic-plastic material. Interestingly, these models use the material data from Yamada *et al.* [105] study as inputs. For instance, HUByx model [103] uses an elastic modulus of 11 GPa and 17 GPa for humeri and femurs. However, this study uses data from different human subjects. As the bone is lifestyle dependant, it is hard to obtain a global trend by comparing different bones from different subjects. Due to their various functions, humerus and femur bones have different micro-architecture (See Chapter 2). Humeral samples are more porous than femoral ones. This difference is explained by the trabecularisation which easier occurs in the humerus by enlarging, and flattening the shape of vascular canals. Some studies report correlations between the macro-mechanical behaviour and the micro-architecture. It is widely proved that the elastic modulus is negatively correlated with the porosity [52, 70, 72, 87]. However, these studies are limited to architectural planar studies. As shown in the chapter 2, a novel method is explained and used on cortical samples. This method consists in assessing the cortical architecture in 3D that has never been reported so far. Correlating these new features with macro-mechanical features would aim at deeper explaining the phenomenons which occur during mechanical solicitations. As the bone is thoroughly remodelled during the life, different types of bone can be found in the cortex. Indeed, vascular canals are surrounded by a recent bone called osteonal bone. Older bone is found between osteons and called interstitial bone. These bone matrices have different mechanical features due to their different mineralisation rate in the collagen fibrils [52, 111]. Obviously, the bone matrix properties also impact the mechanical behaviour at upper scales.

Therefore, this chapter aims at extending the previous experimental protocol so as to perform several mechanical tests. The first one consists in testing the tensile behaviour of the previously

scanned samples. The second test consists in testing the bone matrix by performing indentation tests where the osteonal and the interstitial bones are distinguished. Then, the macro-mechanical behaviour is compared by grouping humerus and femur. Bias impact is also studied by comparing left and right limbs. Subsequently, some correlations are investigated between the macro-mechanical features and the micro-architecture and micro-mechanics.

3.2 Material and methods

3.2.1 Sample extraction

This section outlines the second part of the protocol which was previously described in the second chapter of this manuscript (Figure 3.1). To sum up this first part, parallelepiped samples are harvested from mid-diaphysis of left and right femurs and humeri of 10 human subjects (7 males, 3 females). Then, they are machined using a desktop lathe (Optimum TU 2004V) so as to obtain dumbbell-shaped samples optimised to be fully scanned along the gauge length and avoid slippage during tensile tests. Actually, some grooves are machined on the endings of samples in order to have better grips during the tensile tests.

Right after micro-CT scanning, samples are stored at 4 °C in distilled water during at least 12 h so as to fully rehydrate bone. As outlined in the previous chapter, a short deadline is established (up to 15 days after body harvest) in order to reduce the impact of the preservation method on the bone. Indeed, so far no gold-standard method exists and a little studies report the impact of different preservation methods on the mechanical behaviour of the bone [86, 93]. Whereas the fresh frozen method (−20 °C in saline solution) is suggested [86], a long-term storage impacts the material properties of the bone [93]. It highlights that the preservation method is not obvious and needs to be investigated in detail in further studies. Nevertheless, in the current work, short-term storage is chosen (up to 15 days between body harvest and mechanical test) and samples are not frozen to avoid any damage due to water freezing within the bone (pore enlargement due to water increased volume). A few hours before mechanical tests, samples are left at room temperature in distilled water.

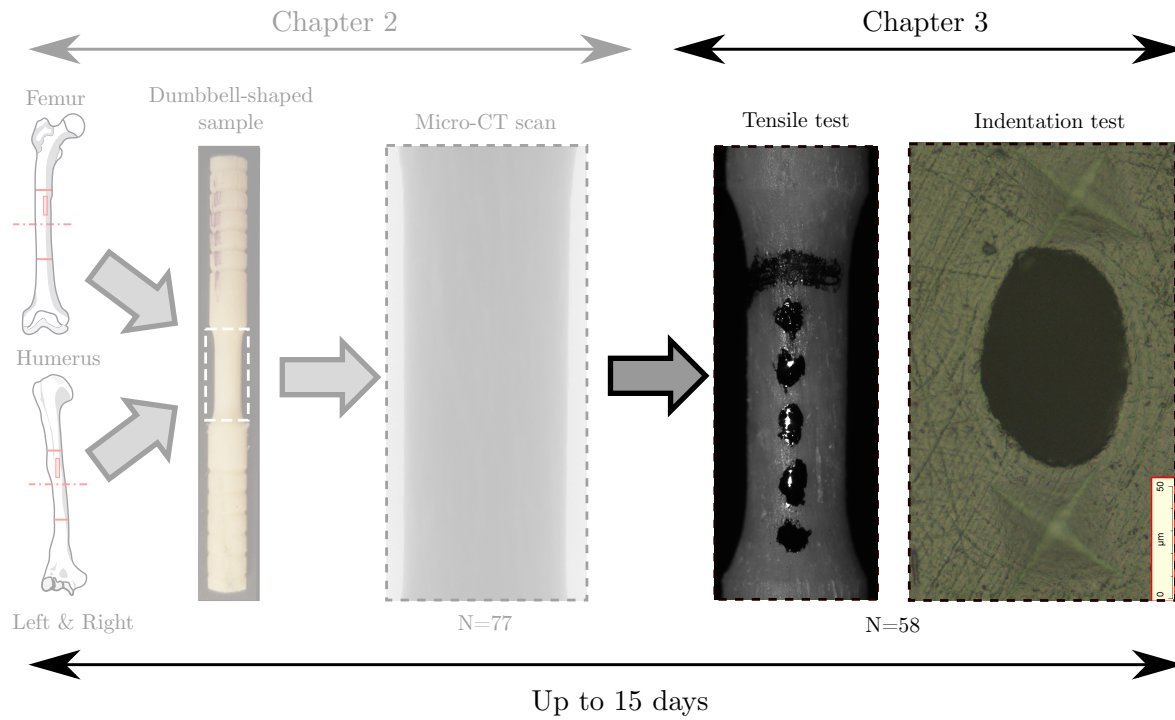


FIGURE 3.1: Shaft harvest and sample preparation scheme. The first step aims at harvesting a 100 mm piece of mid-diaphysis. Then, two parallelepipedical shape piece of cortical bone is extracted and lathed so as to obtain a dumbbell-shaped sample. Finally, the reduced section (targeted diameter = 2.5 mm, length = 6 mm) is fully scanned at a $2.94 \mu\text{m}$ isotropic resolution. Following steps (tensile and indentation tests) are described in Chapter 3. Bone samples were stored in distilled water at 4°C up to 15 days after the shaft harvest.

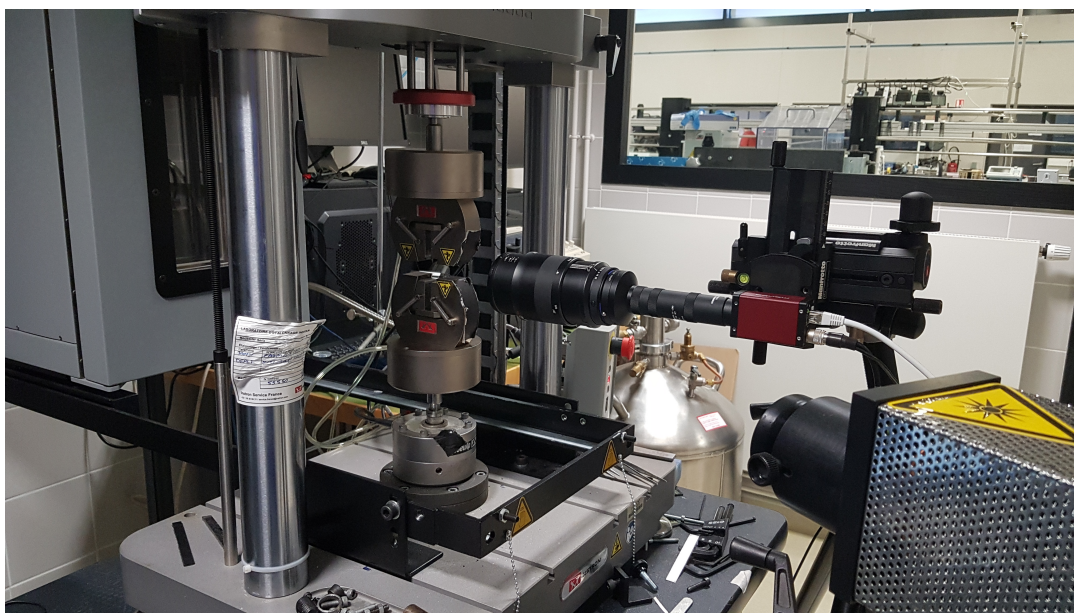


FIGURE 3.2: Set of devices used for tensile tests.

3.2.2 Macro-mechanical test : quasi-static tensile test

3.2.2.1 Strain rate and measurement

Quasi-static tensile tests until failure are performed for each sample. An ElectroPuls E3000 (INSTRON) electro-magnetic machine associated with a dynamic load capacity of 3 kN is used. Tests are conducted at a strain rate of $1.4 \times 10^{-4} \text{ s}^{-1}$. Samples are gripped using pneumatic grips so as to keep a constant gripping pressure throughout the test. Each test is carried out in a room where ambient temperature is kept at 21 °C. Due to the highly fragile mechanical behaviour of the cortical bone, displacement measurement requires a high resolution camera. Hence, strains are measured using Manta G-895 camera (4000x2000 pixels) running at 1 Hz. A 2.8 µm pixel size was obtained. Right before testing, black dots are drawn along the effective length (Figure 3.1). These black dots are used so as to create clear black and white borders which make strain measurement easier to process. Actually, images are post-processed using Digital Image Correlation and Tracking Matlab toolbox. Strain is defined as the mean displacement of all pairs of tracked points divided by the initial length (also called engineering strain). Uncertainties of displacement measurements are estimated by performing a rigid body movement. This estimation was performed right after the failure of a bone sample. Displacements are measured on the part of the sample placed in the movable jaw of the tensile machine. This short study reveals that the uncertainty is significantly lower than the pixel size and enforces that the Manta camera coupled with the tracking Matlab toolbox is well adapted for low displacement measurements as required for brittle material such as the cortical bone. This value is used for uncertainty assessment of the mechanical features.

3.2.2.2 Stress measurement

Different types of stress are computed. Indeed, the samples are designed so as to be fully scanned by micro-CT at 2.94 µm resolution. Hence, it is possible to obtain different areas and their evolution along the gauge length. As shown by Figure 3.3, on each slice, Total Area (TA) and Bone Area (BA) can be measured. The first one considers the area as it should be if the sample wasn't porous. The second area considers the within porosities by subtracting the sum of porous areas to TA.

Consequently, BA and TA are computed for all slices. Thus, the evolution of these areas is obtained (Figures 3.4 and 3.5). As the stress is the ratio between the measured load and an areal value, different stresses can be computed. Indeed, four stresses are computed and summed up in Table 3.1. Apparent and corrected stresses refer to the stresses computed from the total area and the bone area (reduced

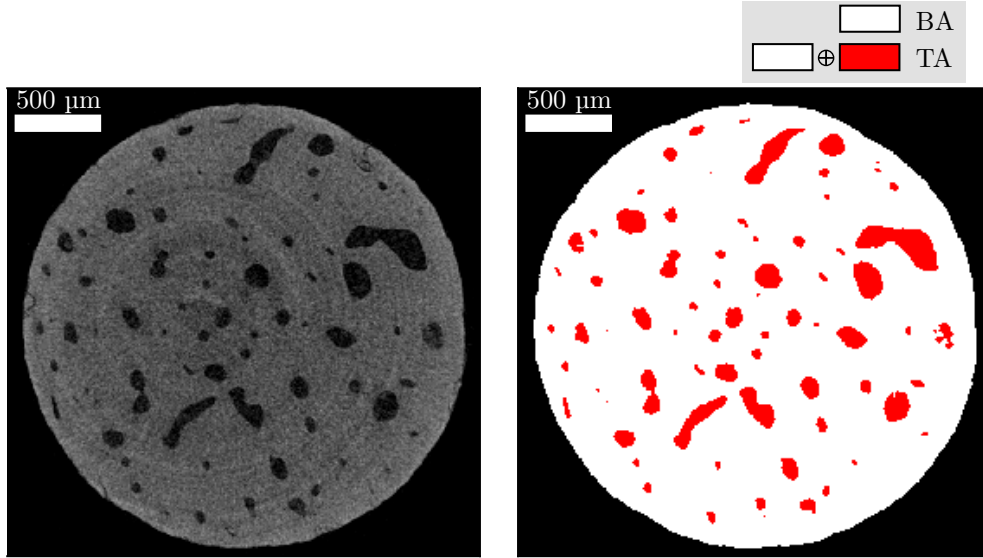


FIGURE 3.3: Definition of Bone Area (BA) and Total Area (TA). TA is the area which considers the entire area whatever the within porosity (white and red areas). BA is computed by subtracting the porous area (red area) to the total area.

by the porous part), respectively. Corrected stress is necessary so as to obtain representative value of the bone matrix and to compare them with indentation results. Likewise, the apparent stress is useful so as to correlate the respective features with the architecture ones because this type of stress depends on the within architecture.

Type of area	Area notation	Type of stress	Stress notation
Mean TA	\bar{TA}	-	σ_{TA}
Min TA	TA_{min}	Apparent stress	σ_{App}
Mean BA	\bar{BA}	-	σ_{BA}
Min BA	BA_{min}	Corrected stress	σ_{Corr}

TABLE 3.1: The different types of computed stress

It is apparent from Figure 3.5 that the porosity does not remain constant through the gauge length. Moreover, it is interesting to notice that the minimum area does not occur at the same region where the porosity is maximum. To compute average BA and TA, only values between 20 % and 80 % of the total length are considered (to avoid over-estimation due to radii).

For each type of stress, 8 mechanical features are computed and depicted in Table 3.2. To compute these features, the linear part of the mechanical behaviour of the bone needs to be detected. This linear part is equated with the elastic behaviour of the bone. Hence, yield limits have to be detected. As the boundaries between the elastic and post-elastic behaviour are not clearly exhibited, many studies use a strain offset criterion [52, 87, 92]. This major disadvantage of this criterion is that the yield limit is shifted whatever the curve shape. In the current work, elastic features are computed from a linear least-square regression of the stress-strain curve between 0 and 0.2 % of strain (Figure 3.6) If the

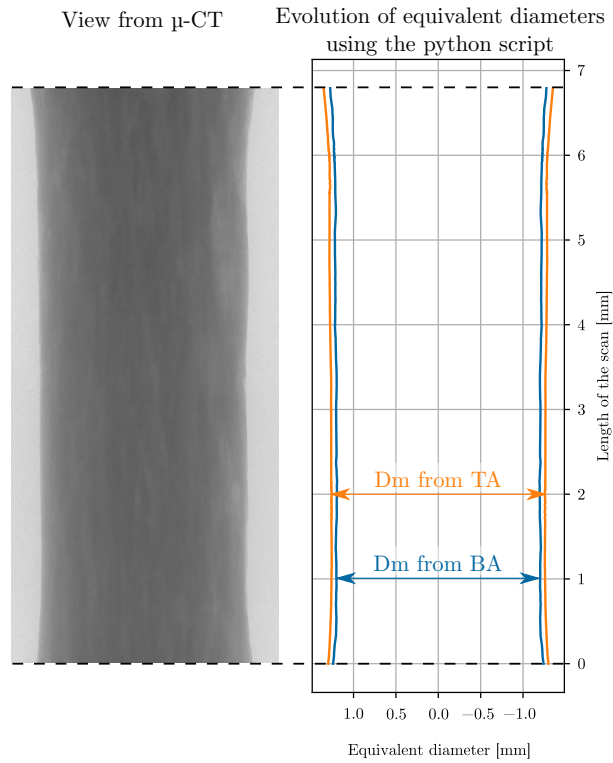


FIGURE 3.4: Side view of a typical specimen during μ -CT scanning (left). Bone and Total areas are measured for each slice. Equivalent diameter can be computed, respectively (right). It highlights that overall the transverse area remains constant along the gauge length. This figure is created from the same sample as used for Figure 3.5

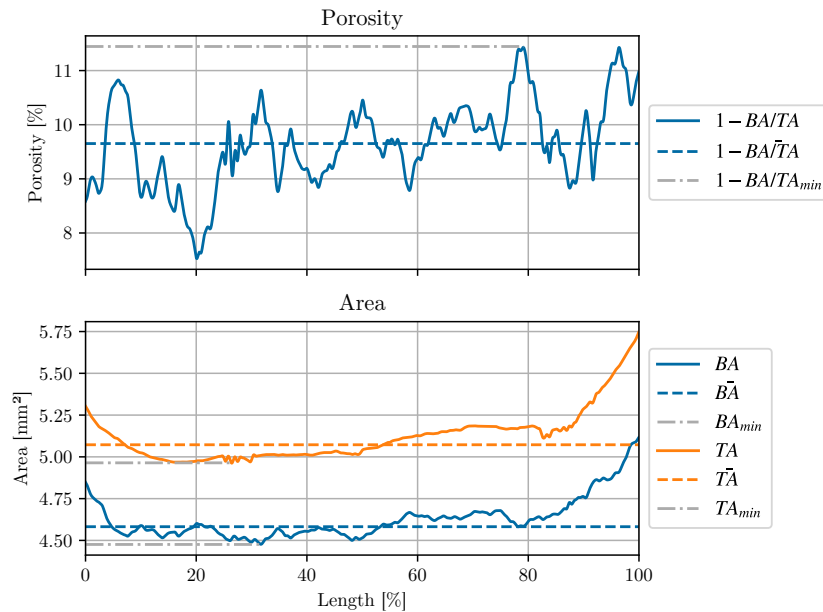


FIGURE 3.5: Porosity and area evolution along the scanned length. On the top, porosity evolution is displayed. Likewise, the mean porosity ($1 - BA/\bar{TA}$) and the maximum areal porosity are shown. On the bottom plot, BA and TA are displayed in blue and orange, respectively. Mean and minimum values are both shown in dotted lines. Areal increase on each ending comes from the beginning of scanned radii. This figure is created from the same sample as used for Figure 3.4

deviation between the linear regression and the curve exceeds 5 % then this point is considered as the yield limit. The elastic modulus is computed from the slope of this linear regression. The mechanical toughness is assessed from the area under the curve. 3 types of toughness can be measured. The linear toughness concerns the area under the curve up to the yield limit. The post-linear toughness is measured between the yield limit and the ultimate point. Total toughness is the sum of these two toughness (Figure 3.6). The ultimate point corresponds to the failure of the sample.

Mechanical features	Notation	Unit
Elastic modulus	$E_{\mathbf{X}}$	[GPa]
Yield stress limit	$\sigma_{y,\mathbf{X}}$	[MPa]
Yield strain limit	$\epsilon_{y,\mathbf{X}}$	[%]
Ultimate stress	$\sigma_{U,\mathbf{X}}$	[MPa]
Ultimate strain	$\epsilon_{U,\mathbf{X}}$	[%]
Total toughness	$U_{tot,\mathbf{X}}$	[mJ mm ⁻³]
Linear toughness	$U_{l,\mathbf{X}}$	[mJ mm ⁻³]
Post-linear toughness	$U_{pl,\mathbf{X}}$	[mJ mm ⁻³]

TABLE 3.2: Mechanical features computed for each type of stress. The \mathbf{X} suffix in bold is replaced according to the type of stress : **Corr** from corrected stress σ_{Corr} , **App** from apparent stress σ_{App} , **BA** from σ_{BA} and **TA** from σ_{TA} .

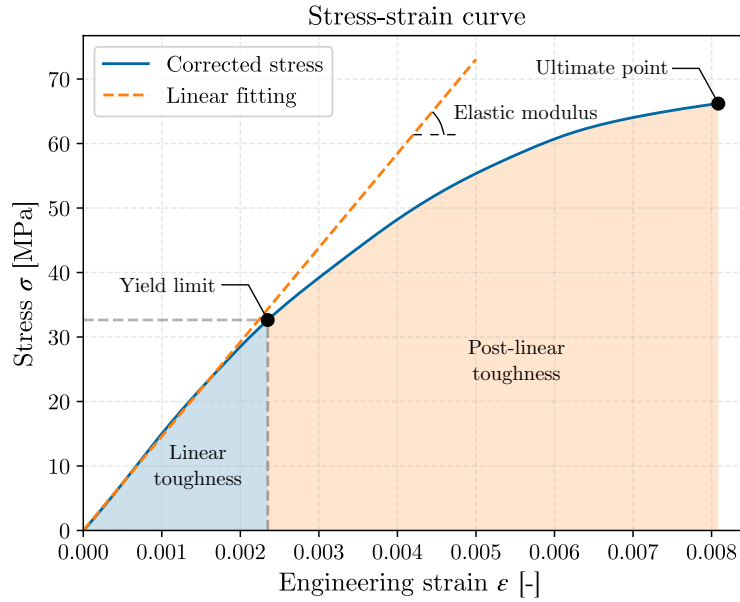


FIGURE 3.6: Typical tensile stress-strain curve. Elastic features are computed from the linear least-square regression computed between 0 and 0.2%. Due to the complex mechanical behaviour of the bone, the post-yield behaviour can not be considered only as a plastic behaviour. That is why in this manuscript this part is called "post-yield" behaviour.

3.2.3 Micro-mechanical test : micro-indentation test

As previously suggested, the macro-mechanical behaviour of the cortical bone depends on the lower scales behaviour. Indeed, the architecture was previously depicted in the chapter 2. However, the mechanical behaviour of the bone matrix needs to be assessed. The bone matrix has also a spatial arrangement which affects the mechanical behaviour of the bone matrix and consequently also affects the macroscopic one. The bone matrix has a lamellar structure formed of a stack of collagen fibrils, mineral crystals and water. The lamellae are spatially arranged. This orientation depends on the type of the osteon. This arrangement takes part to the macro-anisotropy of the cortical bone (See section 1.1.3.2 in chapter 1, page 16). As the chemical components differ between the osteonal and the interstitial bones, the mechanical behaviour is affected.

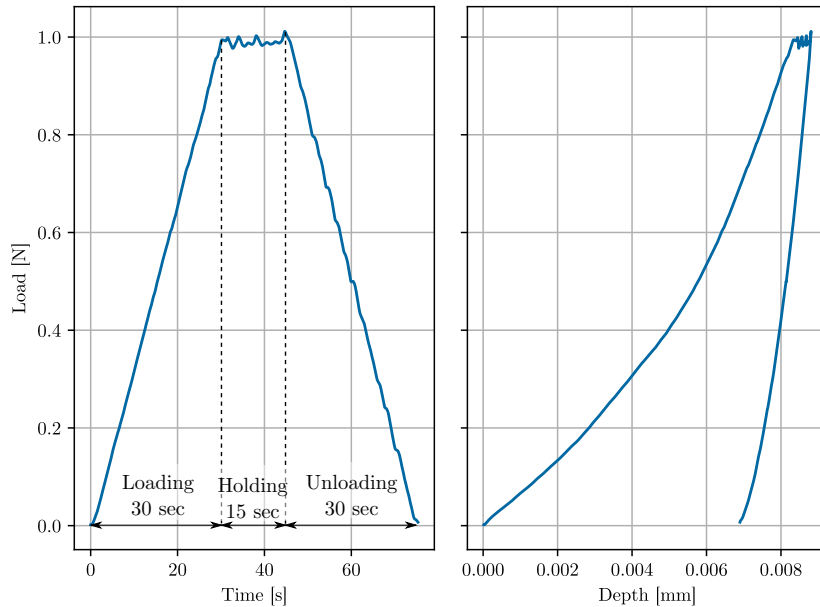


FIGURE 3.7: Indentation protocol. On the left plot, the time evolution of the loading during the indentation test. On the right plot, the typical load VS depth is displayed.

Prior to tests, two longitudinal parallelepiped bone samples are harvested from a neighbour region to the tensile ones. A cold acrylic resin is used to prepare bone samples (LevoCit, STRUERS). The low polymerisation temperature of this resin helps to prevent bone from drying. The tested surface is thoroughly polished up to obtain a surface which is suitable for micro-indentation. Care was taken during the surface grinding to ensure the parallelism between the tested surface and the holding surface in order to perform as best as possible perpendicular indentation tests. Micro-indentation tests are carried out using a vickers indentation tip coupled with a 100 N load cell (UMT Tribolab, Bruker). A trapezoidal protocol in load control up to 1 N is chosen (Figure 3.7). Loading and unloading follow a 30sec linear ramp. The maximum load is held during 15sec. So as to choose the loading value of

the test, several indentation tests have been performed from 1 to 5 N. Each test was observed using a microscope. It revealed that a 5 N test creates cracks into the bone matrix. Moreover, footprints created by indentation test above 2 N are too wide and the different types of bone can not be correctly distinguished (Figure 3.8). Therefore, 1 N is the best agreement between footprint dimensions and the load cell ability without creating cracks.

On each sample, a 3x3 array of indents is performed. Each indent is spaced 400 μm . This length is enough so as to avoid interferences between indents. Indent mapping is observed using a routine stereo microscope (M80, LEICA) so as to classify each indent (Figure 3.8). Indents which overlap a canal pore are not considered. Indents in osteons or in the interstitial bone are classified. Indents that are placed on the boundary of an osteon are reported as unknown and are only considered for pooled mean values. Hence, the hardness (H) and the elastic modulus (E) can be compared between these two types of bone. For each array of indents, the mean values are computed and used for comparisons.

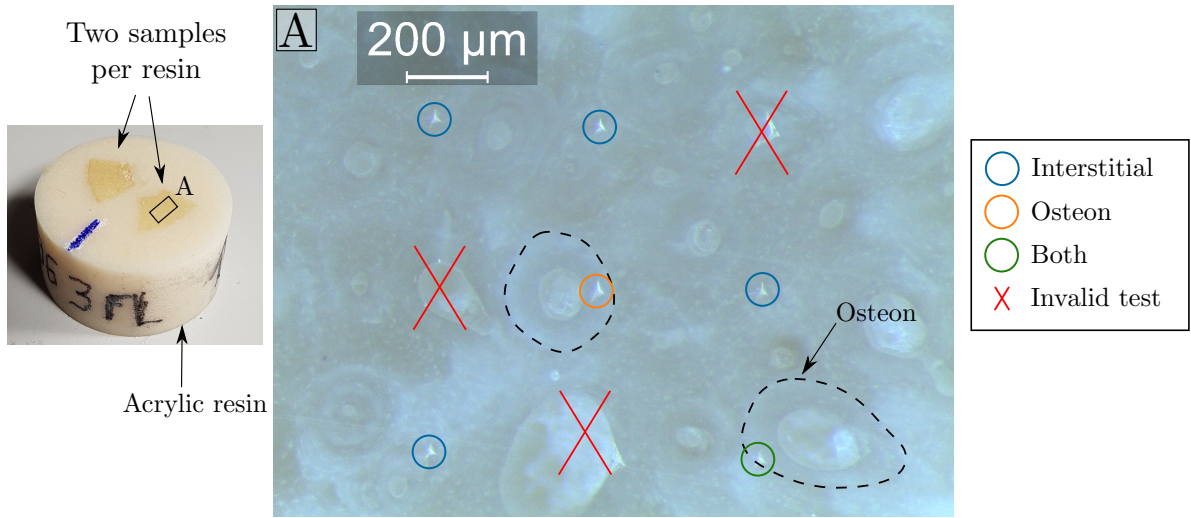


FIGURE 3.8: Snapshot of a 3x3 array of indents using the M80 (LEICA) routine stereo microscope. Each array is subsequently observed so as to identify what type of bone that was tested and remove invalid tests (pores).

Indentation features	Notation	Units	Type of bone
Mean hardness	\bar{H}_{μ}	[MPa]	Interstitial, Osteon, Both
Mean elastic modulus	\bar{E}_{μ}	[GPa]	Interstitial, Osteon, Both
Osteonal hardness	$H_{\mu, \text{osteon}}$	[MPa]	Osteon
Osteonal elastic modulus	$E_{\mu, \text{osteon}}$	[GPa]	Osteon
Interstitial hardness	$H_{\mu, \text{inter}}$	[MPa]	Interstitial
Interstitial elastic modulus	$E_{\mu, \text{inter}}$	[GPa]	Interstitial

TABLE 3.3: Indentation features computed for each type of bone.

3.2.3.1 Theory

So as to obtain some features from this kind of test, the Oliver and Pharr [120] method is used. As depicted in the first chapter of this manuscript, this method is based on the well-known Hertz contact theory. From this method two features can be computed : the elastic modulus and the hardness. This method uses the unloading part of the load-depth curve. Indeed, this part corresponds to the material spring back. This section describes how indentation curves are processed in order to obtain the mechanical features. This process is widely inspired from the Maciejak and Aubert [118] review. The whole process is carried out using a python script where constant values and the indentation tip features are specified as inputs. To compute these two features, equations 3.1 and 3.2 are used.

$$\frac{1}{E_r} = \frac{1 - \nu_f^2}{E_f} + \frac{1 - \nu_i^2}{E_i} \quad (3.1)$$

$$H = \frac{P_{max}}{A_p(h_{c_{max}})} \quad (3.2)$$

The reduced modulus, noted E_r , embodies the mechanical behaviour of both the material and the tip. To obtain the bone matrix modulus E_f , the poisson ratio needs to be known. However, regarding the current bibliography, no study provides this data. As a consequence, in this study, the poisson ratio of the bone matrix is supposed to equal to 0.33. The diamond tip has a 1141 GPa elastic modulus and a 0.07 poisson ratio. $A_p(h_{c_{max}})$ is the projected area of the footprint when the contact depth h_c is maximum. To compute the reduced modulus, equation 3.3 is used.

$$C = \frac{1}{S} = \frac{1}{\frac{dP}{dh}|_{h=h_{max}}} = C_m + \frac{\sqrt{\pi}}{2\beta\sqrt{A_p(h_{c_{max}})}} \frac{1}{E_r} \quad (3.3)$$

β is a shape indentation tip correction factor and equals to 1.012 for vickers tip. C and C_m are the global and machine compliance, respectively. The machine compliance embodies the stiffness of the machine. To reduce its impact on the final results, it needs to be assessed. The global compliance C is computed from the inverse of $S = \frac{dP}{dh}|_{h=h_{max}}$. To compute S , a power least-square regression between $P = P_{max}$ and $P = \frac{P_{max}}{2}$ is carried out (equation 3.4).

$$P = b(h - h_f)^m \quad (3.4)$$

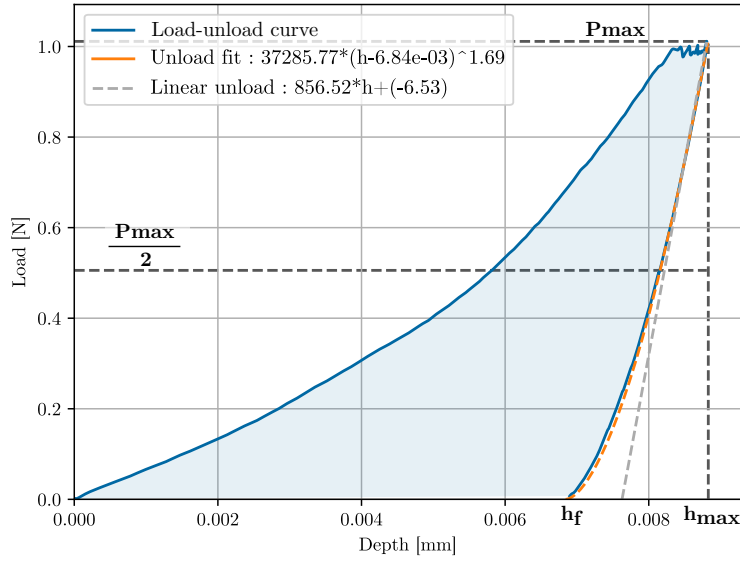


FIGURE 3.9: Indentation curve and interpretation. The unloading part between P_{max} and $\frac{P_{max}}{2}$ is considered for the power least square regression. Subsequently, $S = \frac{dP}{dh}|_{h=h_{max}}$ can be computed and is displayed by the linear function (grey dotted line). On this example, by considering the machine compliance, the reduced and material moduli equal to 23.1 GPa and 21.0 GPa, respectively. If the machine compliance is neglected, i.e. $C_m = 0$, the material modulus is reduced to 17.3 GPa.

For this regression, h_f , which is the final depth (after complete unload), is obtained from the curve (Figure 3.9). b and m are the degrees of freedom used for the power fit. Hence, S is computed from the derivative of this fit at $h = h_{max}$. Then, $A_p(h_{c_{max}})$ needs to be computed using equations 3.5 and 3.6. As a vickers indentation tip is used, ϵ and C_0 equal to 0.75 and 24.504, respectively.

$$h_{c_{max}} = h_{max} - \epsilon * \frac{P_{max}}{S} \quad (3.5)$$

$$A_p(h_{c_{max}}) = C_0 * h_{c_{max}} \quad (3.6)$$

3.2.3.2 Machine compliance

As shown by equation 3.3, the machine compliance C_m needs to be considered so as to remove the machine stiffness impact during the test. Maciejak and Aubert [118] suggest that to obtain this value, several indentation tests at various P_{max} values have to be performed. Hence, different values of global compliance C and projected areas A_p are measured. Regarding equation 3.3, the machine compliance C_m can be obtained from the intercept term of the linear regression $C = f(\frac{1}{\sqrt{A_p}})$ (Figure 3.10). Hence, 51 indentation tests are randomly performed in the bone matrix at 1, 2 and 3 N. Figure 3.10

reveals that the machine compliance equals to $2.46 \times 10^{-4} \text{ mm N}^{-1}$. This value is considered in the following sections of this manuscript. Obviously, values remain dispersive due to the heterogeneous bone matrix. However, assessing this value on the cortical bone allows to have the real stiffness which occurs during the indentation test of the cortical bone. Interestingly, the bone matrix modulus was computed by both considering the current compliance machine and neglecting it : the elastic modulus is reduced by 24 % if the compliance machine is not considered. This result highlights the machine compliance has to be considered even for soft materials such as bone.

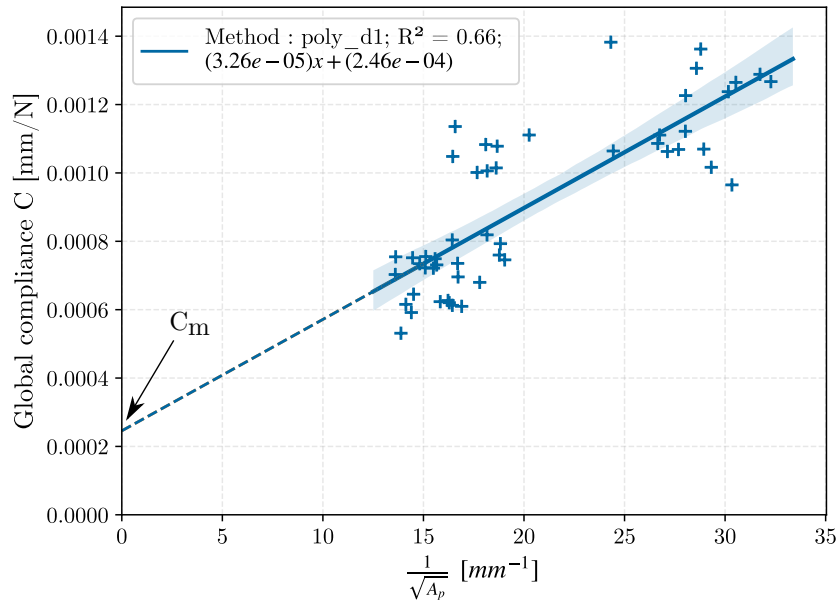


FIGURE 3.10: Machine compliance computation. To obtain the machine compliance, several indentation tests are performed with different loads. Regarding the equation 3.3, the machine compliance is the intercept term of linear regression. Values remain dispersive because of heterogeneous bone matrix. 51 indentation tests were randomly performed on a cortical bone sample. The machine compliance equals to $2.46 \times 10^{-4} \text{ mm N}^{-1}$.

3.2.4 Statistics and data processing

All the data are post-processed with Python. A database is developed so as to facilitate data processing using json ascii files to store data. DataFrame from Pandas library are used. Numpy, Scipy, StatsModels libraries are used for statistical analysis. Plots are created thanks to Matplotlib and Seaborn libraries. Data are thoroughly reported as mean \pm standard deviation. Femur and humerus were compared on the pooled population (gender, side, ...) unless other specified. Then, limbs side bias is investigated by separating the humerus and femur. A Shapiro-Wilk test reveals that many of features have not a normal distribution. Therefore, non-parametric tests were chosen. Significant differences are investigated using the non-parametric Wilcoxon Mann-Whitney (MMW) test. Two features are defined as significantly different if the p-value is below 5 %. Outlier values are defined

as 1.5 times of the inter-quartile (IQR) under the first quartile (Q_1) and below the third quartile (Q_3) ($1.5 * IQR \pm Q_i$). Spearman correlation test is performed so as to find a correlation between features. Outliers points are removed prior to correlation tests. Confidence intervals are computed from a bootstrapping method using 1000 resamples.

3.3 Results and discussion

3.3.1 Bearing and non-bearing bones comparisons

3.3.1.1 Tensile tests

Subject number	Age	Gender	Femur		Humerus		Total
			Left	Right	Left	Right	
0010	65	Male	2	2	1	1	6
0011	86	Male	2	2	1	1	6
0014	96	Female	0*	2	1	0**	3
0017	96	Female	2	2	1	1	6
0020	80	Male	2	2	2	1	7
0026	75	Male	2	2	1	2	7
0055	68	Male	2	2	2	2	8
0963	87	Female	2	2	2	1	7
0965	77	Male	1	1	1	1	4
0995	87	Male	1	1	1	1	4
Total			16	18	13	11	58

TABLE 3.4: Number of bone samples available for mechanical analysis. *No samples are available for this femur due to a hip prosthesis. **No samples are available for this humerus due to the very thin cortical layer.

58 tensile tests have successfully been performed (34 Femur, 24 Humerus). 19 samples have been lost mainly because of slippage during testing or sample crushing in grips due to high porosity. Loss percentage is more important for humeral samples (39%) due to the higher porosity than in femoral ones. Overall, at least one sample is available for each bone of the 10 human subjects. However, due to the very thin cortical layer in the right humerus of 0014, no sample is available. Obviously, no specimen is extracted from the left femur of 0014 because of a hip prosthesis in the shaft.

Figure 3.11 displays the mean stress-strain curves for each bone. So as to help to obtain the material law of each bone, a polynomial regression is performed and displayed on Figure 3.11. The polynomial coefficients are available in Table 3.5. Mean \pm standard deviation of the mechanical features are stored in Table 3.6 by highlighting each bone.

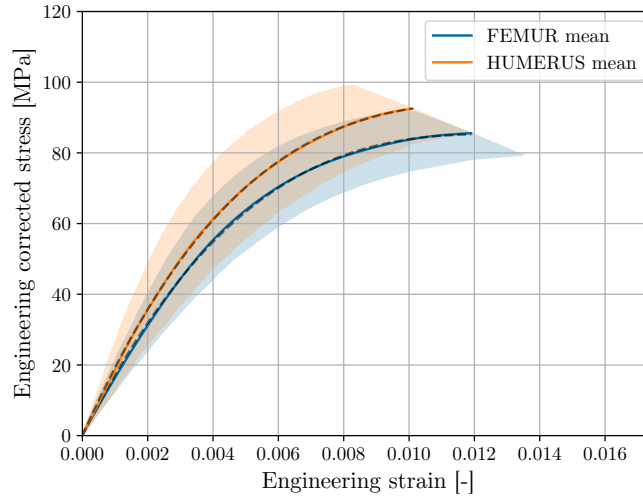


FIGURE 3.11: Mean stress-strain curves bearing and non-bearing bones. The 95 % confidence interval of the regression is displayed by the transparent colourised area. These curves were obtained from 24 and 34 samples harvested from humerus and femur, respectively. 3D polynomial regressions are displayed in grey dotted lines (see Table 3.5).

	R^2	a_3	a_2	a_1
Femur	1.00	3.0407E+07	-1.3107E+06	1.8453E+04
Humerus	1.00	3.9253E+07	-1.5509E+06	2.0826E+04

TABLE 3.5: Polynomial regressions of mean femur and humerus stress-strain curves. R^2 is the coefficient of determination of the fittings. 3rd polynomial regression is assessed using non-linear least-squares method. Hence, $y = a_3x^3 + a_2x^2 + a_1x$ function is computed. The regressions are displayed on Figure 3.11.

It is apparent from Figure 3.11 that humerus and femur have a different mechanical behaviour. Overall, even if confidence intervals overlap between themselves, the mean mechanical behaviour of the humerus remains higher in stress than femur. This mechanical behaviour is similar as depicted by Garcia [106]. Indeed, in this study, the cortical bone is described as a damageable elastic-plastic material. The first mode is the intact linear elasticity where the bone elongates with no damages. Then, the bone is gradually damaging due to crack openings (damage) and sliding (plastic) which soften the material law. In the current study, the samples are monotonically tested up to fracture. Hence, the damage and plastic part can not be individually distinguished as it is for a cyclic test. By comparing these results with Bry [10], which is the only recent study that provides mechanical data for both humeri and femurs, a similar trend is found. Mechanical features enforce this tendency. Indeed, the elastic modulus remains stiffer for humeri. By individually comparing the bearing bone with the non-bearing one, 9 human subjects have a stiffer elastic modulus for humeri. 0014 human subject shows the opposite trend. However, from this subject, only one tested sample harvested from left humerus and two tested samples harvested from right femurs have successfully been performed. As proved by the second chapter of the manuscript, this human subject is heavily impacted by trabecularisation

caused by advanced osteoporosis : a very high porosity is measured in the humeri. It proves that this subject is heavily affected by osteoporosis which leads to a softening of the cortical bone.

By analysing the mechanical features, numerous significant differences are found and enforce the conclusion that the humerus has a stiffer behaviour (Table 3.6). First, the elastic modulus is significantly higher in humerus (14 % higher). A similar trend, to a lesser extent, was found in the similar study made by Bry [10] : 23.8 ± 4.6 GPa and 15.8 ± 5.4 GPa for humerus and femur, respectively. This in contrast with the elastic moduli used to model the mechanical behaviour in some human FE models. For instance, humerus and femur have a 14 and 17 GPa elastic moduli in CHARM-70 model, respectively [104]. A possible explanation for this might be that the humerus is poorly investigated compared to the femur. As a consequence, human FE model refers to old studies where humerus and femur data come from different databases and human subjects as reported by Yamada *et al.* [105]. By comparing the femur elastic modulus, similar mean values are found by Neil Dong and Edward Guo [70] (16.6 ± 1.8 GPa) but are slightly higher in Mirzaali *et al.* [52] (18.2 ± 1.9 GPa) and Bayraktar *et al.* [87] (19.9 ± 1.8 GPa) studies. These slight differences could be explained by the different preservation methods [86, 93], the different harvest location or the stress measurement. Indeed, in the current study, different types of stress are computed thanks to the μ -CT. However, the other studies don't report the method to compute stress [52, 70, 87].

Likewise, the yield stress limit is higher in the humeri (27 ± 13 % higher). Figure 3.12b enforces this trend for all human subjects, except for 0014 human subject. This difference proves once again that the humerus remains stiffer to the femur. However, the humerus-femur ratio differs for each individual. No comparative values are found for humerus. Two other works report higher yield stress limits for human femurs [52, 87]. This difference is mainly caused by the different method to compute the yield limit. Indeed, these two studies use a strain offset criterion as commonly used for steels where yield limit isn't obvious. However, due to the brittle and dispersive behaviour of the cortical bone, the use of such a criterion shifts the limits. No differences are found concerning the yield strain limit and it is highly dispersive by comparing the different individuals (Figure 3.12c).

Interestingly, the ultimate point differs for humerus and femur. The fracture occurs at higher stress but at lower strain for humerus. Regarding strain at failure, Bry [10] found this similar trend. It contradicts the findings of Yamada *et al.* [105] where the failure is similar for both of the bones. In the literature, ultimate strain for the femur is dispersive and ranges from 1 % to 1.9 % [10, 52, 85].

Likewise, the toughness of the cortical bone is computed from the area under the curve. It highlights that about 85 % of the total toughness occurs in the post-yield behaviour. It could be explained by the fact that, in the post-yield behaviour, the cortical bone is damaging, cracks are propagating,

		Bone	Mean \pm Std	Median	Min	Max	Q1	Q3	p-value
E_{Corr}	[GPa]	Pooled	17.23 ± 2.70	17.37	10.57	23.95	15.52	18.99	0.000
		Femur	16.27 ± 1.81	16.07	12.35	19.77	15.05	17.93	
		Humerus	18.60 ± 3.13	19.15	12.92	23.95	16.92	20.92	
$\sigma_{y,Corr}$	[MPa]	Pooled	46.65 ± 15.83	42.07	21.35	77.68	35.81	55.17	0.013
		Femur	43.04 ± 14.46	39.57	21.35	73.91	30.88	51.76	
		Humerus	51.77 ± 16.26	45.55	26.04	94.57	41.41	64.38	
$\epsilon_{y,Corr}$	[%]	Pooled	0.29 ± 0.09	0.25	0.16	0.48	0.22	0.34	0.108
		Femur	0.28 ± 0.10	0.24	0.16	0.48	0.21	0.32	
		Humerus	0.29 ± 0.08	0.27	0.18	0.48	0.24	0.35	
$\sigma_{U,Corr}$	[MPa]	Pooled	88.42 ± 16.84	87.53	49.82	137.08	75.86	101.14	0.035
		Femur	85.55 ± 17.22	85.49	49.82	112.22	73.98	94.41	
		Humerus	92.49 ± 15.41	93.19	51.99	114.98	80.26	102.52	
ϵ_U	[%]	Pooled	1.12 ± 0.45	1.02	0.31	2.27	0.79	1.40	0.043
		Femur	1.20 ± 0.47	1.21	0.31	2.37	0.82	1.53	
		Humerus	1.02 ± 0.41	0.95	0.45	1.70	0.71	1.18	
$U_{tot,Corr}$	[mJ mm ⁻³]	Pooled	0.72 ± 0.44	0.62	0.08	1.65	0.35	0.92	0.166
		Femur	0.77 ± 0.44	0.74	0.08	1.96	0.36	1.08	
		Humerus	0.67 ± 0.42	0.56	0.23	1.53	0.34	0.86	
$U_{l,Corr}$	[mJ mm ⁻³]	Pooled	0.07 ± 0.05	0.05	0.02	0.18	0.04	0.10	0.042
		Femur	0.07 ± 0.05	0.05	0.02	0.15	0.03	0.08	
		Humerus	0.08 ± 0.05	0.06	0.03	0.15	0.05	0.11	
$U_{pl,Corr}$	[mJ mm ⁻³]	Pooled	0.65 ± 0.43	0.53	0.03	1.63	0.30	0.85	0.126
		Femur	0.70 ± 0.43	0.70	0.03	1.90	0.32	0.97	
		Humerus	0.58 ± 0.43	0.49	0.07	1.41	0.29	0.77	

TABLE 3.6: Mechanical features values and bearing and non-bearing comparisons. See Table 3.2 for abbreviations. Minimum and maximum values are reported without considering outliers (by groups). Q1 and Q3 are the first and third quartile, respectively. p-value is the result of significant differences, assessed by Mann-Whitney-Wilcoxon (MWW) test, between each bone. Bold values are those below 0.05 (which means that groups are significantly different).

which softens the bone and help to dissipate more mechanical energy. Slight but significant differences are found for the linear toughness : thanks to its stiffer behaviour, humeri are able to dissipate more energy. Overall, femur is somewhat tougher than humerus thanks to its higher failure strain. However, this trend is dispersive according the human subject which explains the non-significant difference for the post-yield and total toughness.

All of these features prove that the mechanical behaviours of the humerus and the femur differ. Overall, humerus is stiffer than the femur. This trend is found from the elastic part of the mechanical behaviour up to the failure. It impacts the yield and ultimate stresses. However, in the elastic part, no differences are found for the yield strain limit in spite of significant differences for the ultimate one. As the macromechanical behaviour depends on the bone matrix properties and the architecture, the differences found between the two bones are further investigated by correlating the different features so as to find explanation of the phenomenon which occurs during a mechanical loading.

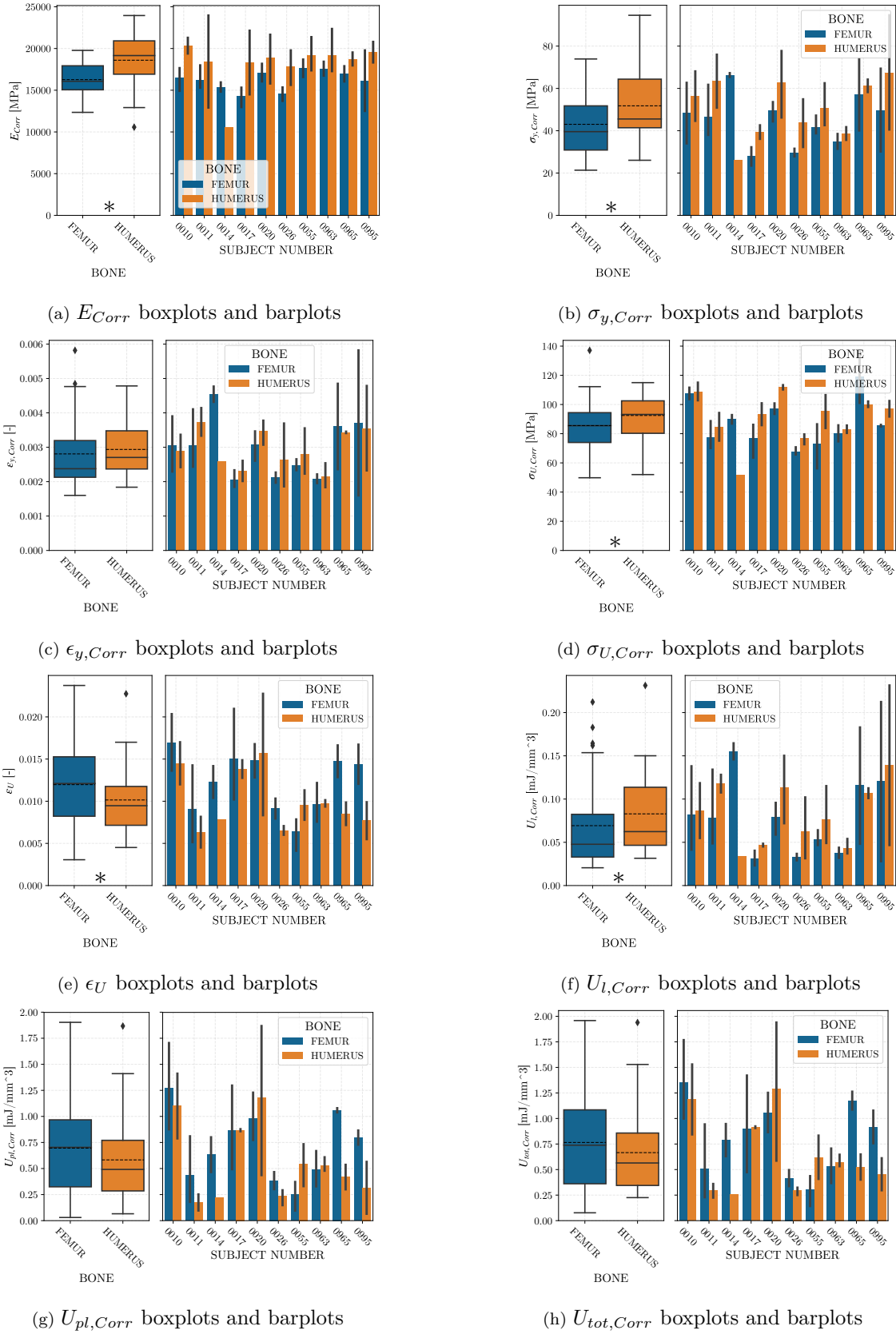


FIGURE 3.12: Mechanical features boxplots and barplots. Barplots display the mean value. The vertical black line is the 95 % confidence interval for each group. Left plot shows boxplot for all grouped left and right humeral samples. Features which are significantly different, by individually comparing the two groups, are highlighted with a star on the bottom (*). Dotted and straight horizontal lines are the mean and median values, respectively. Outliers are displayed by diamond markers. On the right, features are individually highlighted.

3.3.1.2 Indentation tests

78 3x3 arrays of indents have successfully been performed. Each bone has been tested and mean values have thoroughly been reported in the database so as to compare them with macromechanical properties. Mean \pm standard deviation values are reported in Table 3.7 and display on Figure 3.13.

	Bone	Mean \pm Std	Median	Min	Max	Q1	Q3	p-value
\bar{H}_μ [MPa]	Pooled	769.67 \pm 103.46	775.02	612.36	964.41	734.26	831.78	0.040
	Femur	745.73 \pm 97.91	741.10	649.47	860.63	712.84	806.73	
	Humerus	803.58 \pm 101.62	813.94	612.36	964.41	741.58	850.31	
\bar{E}_μ [GPa]	Pooled	21.62 \pm 4.16	21.35	12.36	29.11	18.52	24.70	0.497
	Femur	21.70 \pm 3.88	22.19	12.36	27.37	18.55	24.70	
	Humerus	21.52 \pm 4.52	21.25	13.89	29.11	17.64	24.39	
$H_{\mu,osteon}$ [MPa]	Pooled	679.80 \pm 125.17	655.04	414.91	962.82	603.47	754.55	0.117
	Femur	657.87 \pm 102.80	648.23	414.91	811.27	603.47	743.26	
	Humerus	712.23 \pm 146.44	706.93	512.84	984.37	606.89	772.93	
$E_{\mu,osteon}$ [GPa]	Pooled	19.88 \pm 4.25	20.08	11.50	29.75	16.28	22.31	0.338
	Femur	19.75 \pm 3.82	20.97	11.50	27.08	16.17	22.31	
	Humerus	20.06 \pm 4.82	18.61	12.96	29.75	16.29	23.21	
$H_{\mu,inter}$ [MPa]	Pooled	839.70 \pm 88.31	840.85	652.16	1003.14	787.88	892.50	0.459
	Femur	834.98 \pm 59.85	831.78	700.03	956.79	792.51	883.44	
	Humerus	846.27 \pm 116.58	864.59	652.16	1003.14	783.30	920.13	
$E_{\mu,inter}$ [GPa]	Pooled	23.02 \pm 4.90	22.27	13.30	31.99	20.17	27.59	0.272
	Femur	23.32 \pm 4.51	23.31	13.30	31.99	20.38	26.79	
	Humerus	22.59 \pm 5.36	22.27	14.26	30.65	18.20	27.59	

TABLE 3.7: Indentation mechanical features. Minimum and maximum values are reported without considering outliers (by groups). Q1 and Q3 are the first and third quartile, respectively. p-value is the result of significant differences, assessed by Mann-Whitney-Wilcoxon (MWW) test, between each bone. Bold values are those below 0.05 (which means that groups are significantly different).

The mean hardness, \bar{H}_μ , is the only feature which is significantly different between femur and humerus. However, this difference remains weak ($p = 0.04$) and isn't clearly found for each individual (Figure 3.13a) which makes it at least questionable. Likewise, whatever the type of bone, i.e. osteonal or interstitial, no differences or trends are found between the femur and humerus. These results are quite revealing in several ways. First, it seems possible that these results are due to heterogeneous mechanical properties of the cortical bone matrix and the very restricted volume of interest of the array of indents ($\text{Area} = 0.64 \mu\text{m}^2$). Actually, indentation remains a very local areal test and obtaining a global tendency is not obvious. The variation in the literature of indentation features seems to confirm this assumption [52, 111, 121, 122]. In accordance with these studies, the mean bone matrix modulus remains higher than 20 GPa and can reach up to 29 GPa (Figure 3.13b). Second, another possible explanation for this is that the macromechanical behaviour of the cortical bone is mainly dominated by the within architecture as supported by Mirzaali *et al.* [52]. Therefore, as the macromechanical

elastic modulus is higher in the humerus, the lack of such a difference for indentation elastic modulus would confirm that the architecture differences lead to macromechanical differences.

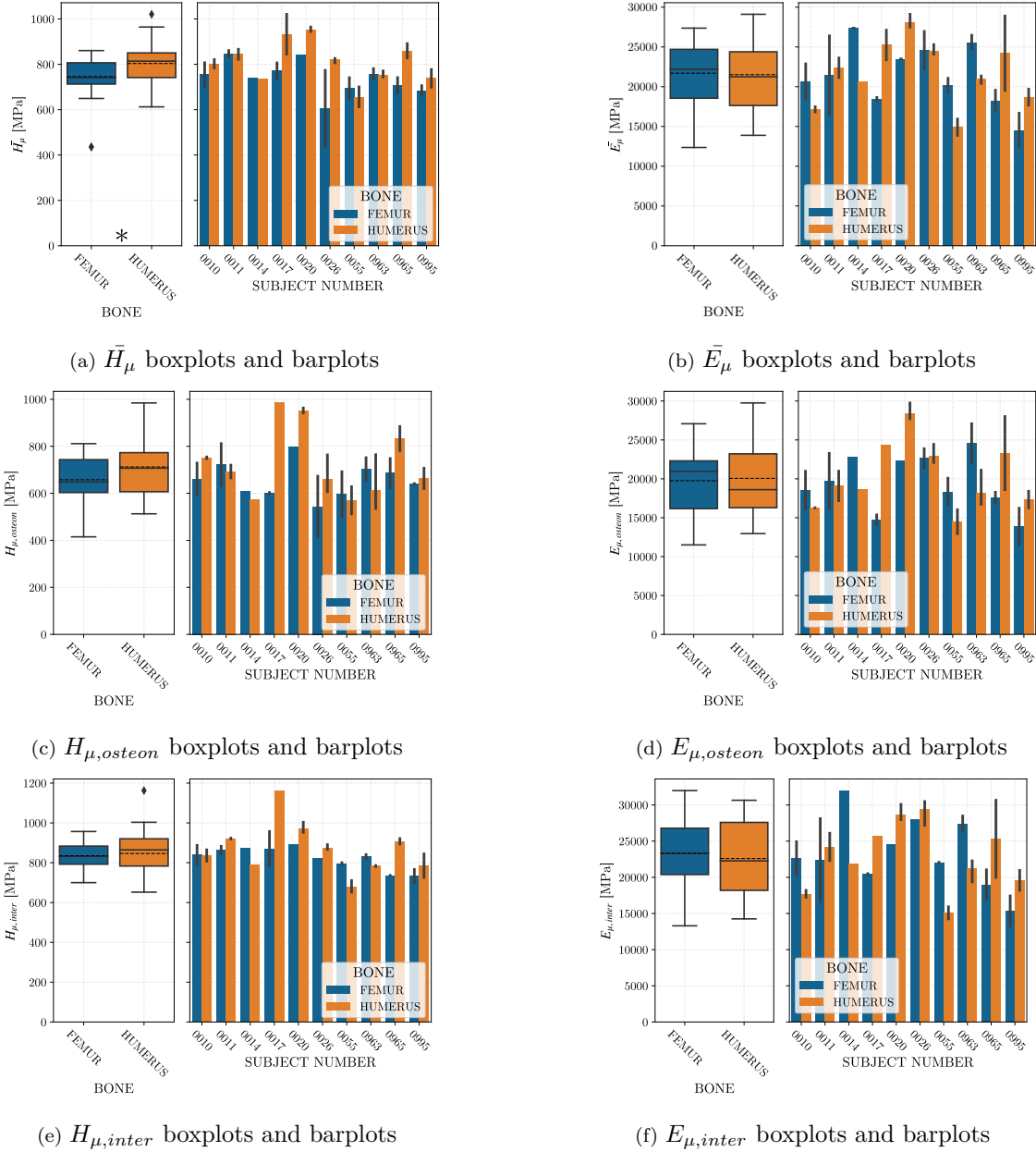


FIGURE 3.13: Indentation mechanical features boxplots and barplots. Barplots display the mean value. The vertical black line is the 95 % confidence interval for each group. Left plot shows boxplot for all grouped left and right humeral samples. Features which are significantly different, by individually comparing the two groups, are highlighted with a star on the bottom (*). Dotted and straight horizontal lines are the mean and median values, respectively. Outliers are displayed by diamond markers. On the right, features are individually highlighted.

Interestingly, both of hardness and elastic modulus are significantly higher in the interstitial bone than in the osteonal one (MWW p-value = 6.83×10^{-11} and 3.82×10^{-4} for hardness and elastic modulus, respectively). This finding is in line with other similar studies [52, 111, 121, 122]. As a matter of fact, the interstitial bone can be considered as an older bone than the osteonal one. Indeed,

during the bone remodelling, BMUs create new bone thanks to the osteoblasts. The groove of BMUs is the part of the newly created bone, called osteonal bone. The osteonal bone gradually mineralised itself up to be replaced (interstitial bone). That is why mechanical properties differ. A positive correlation between the indentation modulus and the tissue mineralisation have been reported by Kim *et al.* [146] thanks to the Raman spectroscopy.

3.3.2 Side comparison

As samples have been harvested from both left and right humeri and femurs, a similar study, as performed in the second chapter of this manuscript, is also carried out so as to study the bias impact on the mechanical behaviour of the cortical bone. 16 and 18 samples are available for left and right femurs, respectively. Likewise, 13 and 11 samples are available for left and right humeri, respectively. Figure 3.14 displays the mean mechanical behaviour and the confidence intervals of left and right limbs. A polynomial regression has been performed and coefficients are available in Table 3.8.

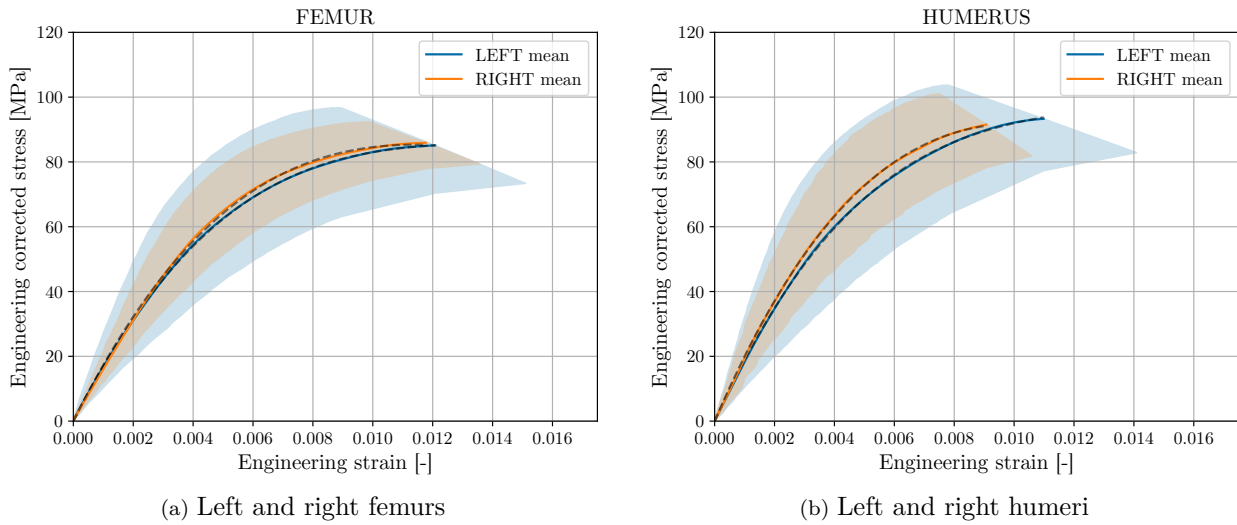


FIGURE 3.14: Mean stress-strain curves from left and right limbs. The 95 % confidence interval of the regression is displayed by the transparent colourised area. 3D polynomial regressions are displayed in grey dotted lines (see Table 3.8).

Bone	Bias	R^2	a_3	a_2	a_1
Humerus	left	1.00	4.0593E+07	-1.5185E+06	2.0322E+04
	right	1.00	3.3649E+07	-1.5744E+06	2.1563E+04
Femur	left	1.00	3.2863E+07	-1.3269E+06	1.8282E+04
	right	1.00	2.7909E+07	-1.2930E+06	1.8597E+04

TABLE 3.8: Polynomial regressions of mean left and right femurs stress-strain curves. R^2 is the coefficient of determination of the fittings. 3rd polynomial regression are assessed using non-linear least-squares method. Hence, $y = a_3x^3 + a_2x^2 + a_1x$ function is computed. Regressions are displayed on Figure 3.14.

It is apparent from Figure 3.14 that the mechanical behaviours of each bias are similar for humerus and femur. The wider confidence interval for left limbs reflects a higher variation. It is somewhat surprising that no significant differences are found between left and right humeri. However, some differences for femurs are highlighted by the MWW test. These findings are unexpected for two main reasons. The first one is that, in the chapter 2, architecture is significantly different between left and right humeri and none for femurs. Actually, samples harvested from left humeri are more porous than the right ones and this trend is confirmed by nine human subjects. The second reason, which is used to justify architectural differences in chapter 2, is the different functions between left and right upper limbs, due to bias preferences, which differently activates the bone remodelling and creates different architectures. Table 3.9 reports the differences found for femur. These differences concern the yield limit of the mechanical behaviour. Actually, the yield limit seems to appear higher in strain and stress for the right femur. By individually comparing stress-strain curves, curves with higher yield limits have a distinct slope failure which marks the beginning of the post-yield behaviour whereas the other curves, with lower yield limits, this slope failure is less obvious. It would suggest that the bone damage occurs at lower strains for samples with a lower yield limit.

		Femur side	Mean \pm Std	Median	Min	Max	Q1	Q3	p-value
$\sigma_{y,Corr}$	[MPa]	Pooled	43.04 ± 14.46	39.57	21.35	73.91	30.88	51.76	0.022
		Left	36.43 ± 7.49	35.38	26.71	52.38	30.28	40.54	
		Right	48.90 ± 16.49	45.97	21.35	73.91	37.32	66.78	
$\epsilon_{y,Corr}$	[%]	Pooled	0.28 ± 0.10	0.24	0.16	0.48	0.21	0.32	0.044
		Left	0.23 ± 0.04	0.24	0.16	0.31	0.20	0.26	
		Right	0.32 ± 0.12	0.29	0.18	0.58	0.22	0.43	
$U_{l,Corr}$	[mJ mm ⁻³]	Pooled	0.07 ± 0.05	0.05	0.02	0.15	0.03	0.08	0.020
		Left	0.04 ± 0.02	0.04	0.03	0.08	0.03	0.05	
		Right	0.09 ± 0.06	0.07	0.02	0.21	0.04	0.15	

TABLE 3.9: Mechanical features values from femurs and side comparisons. See Table 3.2 for abbreviations. Minimum and maximum values are reported without considering outliers (by groups). Q1 and Q3 are the first and third quartile, respectively. p-value is the result of significant differences, assessed by Mann-Whitney-Wilcoxon (MWW) test, between each side. Bold values are those below 0.05 (which means that groups are significantly different).

However, by analysing Figure 3.15, it appears that upper yield limit for right femurs isn't clearly exhibited for every individual. Indeed, this difference is found for 67 % of the human subjects. Moreover, for these human subjects, values for right femurs are important which would balance the mean value and subsequently the MWW test result. Consequently, the linear toughness is impacted and MWW test exhibits a significant difference.

Nevertheless, the mean mechanical behaviour of the left humeri seems to have a lower ultimate strain. Although this difference isn't statistically significant, this variation is shown by the mean

curves. However, this trend widely varies between subjects. Therefore, these discrepancies suggest that more samples harvested from more human subjects would help to clarify them.

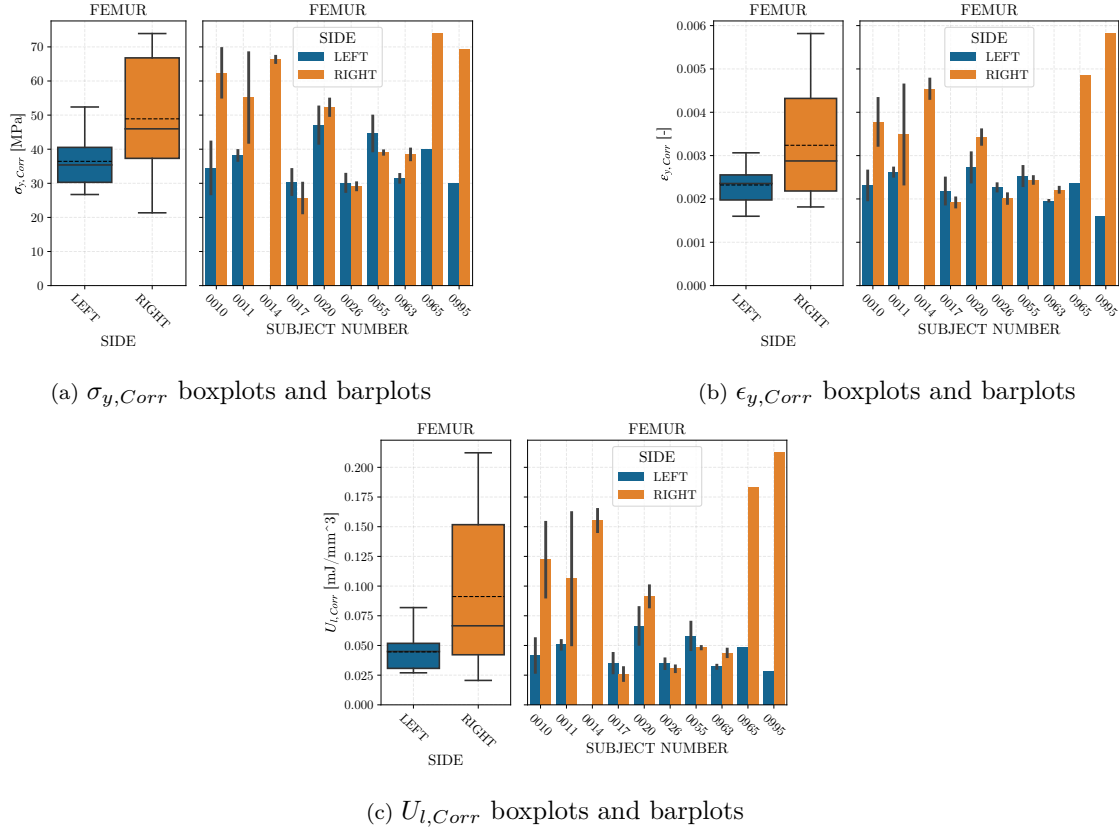


FIGURE 3.15: Mechanical features from left and right limbs boxplots and barplots. Barplots display the mean value. The vertical black line is the 95 % confidence interval for each group. Left plot shows boxplot for all grouped femoral and humeral samples. Dotted and straight horizontal lines are the mean and median values, respectively. Outliers are displayed by diamond markers. On the right, features are individually highlighted.

At the tissue level, no significant differences are found for both of the bones. A possible explanation for this might be that the bone tissue is homogeneous whatever the bias. By individually comparing indentation features, no overall trends are clarified and mean values are slightly the same for left and right limbs. Another explanation for this is that the indentation test remains slightly local and creates variations by comparing results between samples.

3.3.3 Multi-scale correlation

In the previous sections of this chapter, some trends for mechanical features are highlighted such as a stiffer elastic behaviour of humeri or higher ultimate strains for femurs. Although these trends are confirmed by statistic tests, values are highly dispersive from case to case. For instance, the elastic modulus can range from 10.57 to 23.95 GPa. However, at the tissue level, indentation results don't exhibit any similar tendency. Hence, to understand the discrepancy of the macromechanical features,

it would be interesting to confront them with the micro-architecture as depicted in the second chapter of this manuscript. In addition, this study would lead to predict the mechanical features from a tomographic scan without testing it. With the ongoing improvement of in-vivo tomographic devices, the use of such regressions would help to estimate the mechanical health of the cortical bone.

Actually, in Chapter 2, the micro-architecture of the cortical bone is depicted as a very tortuous canal network where the diameter, the length or the orientation of canals differ. These changes in the network is mainly due the bone remodelling and its defects in the elderly. Hence, as a result, the porosity of the bone cortex also differ. Some studies have previously investigated the correlation between the macromechanical and the micro-architecture [52, 72]. However, these studies are limited to planar studies of the architecture or a restricted VOI.

Therefore, a correlation study is performed. This correlation study is followed by a polynomial regression study between correlated parameters so as to predict mechanical features from architectural ones. To quantify the quality of the predictive values, 0055 and 0965 subjects aren't considered so as to find correlations and compute regressions. Moreover, outlier values are removed so as to avoid skewing results. Thus, the quality of the prediction is computed as : $|\frac{x_{predicted} - x_{measured}}{x_{measured}}|$. The quality of the regression is also evaluated by assessing R^2 for each polynomial regression. Correlations are performed only for apparent mechanical features for the simple reason that apparent features are computed from the area of the sample which considers it as non-porous (TA_{min} , see Figure 3.3, page 97). The Spearman correlation matrix is stored in Table 3.10. Spearman p-value is also computed so as to establish a significance level of $p < 0.05$. Significant correlations are highlighted in bold in this table. Subsequently, polynomial regression is investigated on the best correlation coefficient (the closest to 1 or -1). This polynomial regression is assessed up to a 4-degree polynomial function. However, to choose the degree of the polynomials, the number of coefficients, R^2 , or the interval confidence of the regression are considered. For instance, a linear regression is preferred over a quadratic or upper degrees polynomial if R^2 is slightly the same with the narrowest confidence interval. As a consequence, the regressions and predictive accuracy are performed using 46 samples (Femur = 28, Humerus = 18) and 12 samples (Femur = 6, Humerus = 6), respectively. Figure 3.16 displays the 8 mechanical features correlated with the best related architectural features. Table 3.11 stores the R^2 value of each fit, the polynomial coefficients and the predictive error.

Table 3.10 is quite revealing in several ways. First, one unanticipated finding is that the porosity (Ca.V/TV) isn't correlated with any mechanical features. Indeed, by analysing the first row of this table, no Spearman coefficients exceed more than 0.3 and, as a consequence, no significant correlations are exhibited. This finding doesn't support the previous research where porosity is negatively

	E_{App}	$\sigma_{y,App}$	$\epsilon_{y,App}$	$\sigma_{U,App}$	ϵ_U	$U_{tot,App}$	$U_{l,App}$	$U_{pl,App}$
Ca.V/TV	-0.16	-0.27	-0.27	-0.05	0.21	0.22	-0.29	0.25
Ca.D	-0.55	-0.49	-0.26	-0.46	0.02	-0.13	-0.38	-0.08
Po.D	-0.32	-0.35	-0.26	-0.38	-0.09	-0.16	-0.29	-0.12
Conn.D	-0.49	-0.52	-0.38	-0.41	0.07	-0.09	-0.47	-0.02
BMU.D	-0.37	-0.51	-0.32	-0.47	-0.12	-0.23	-0.43	-0.21
Ca.rLe	0.38	0.37	0.18	0.27	-0.09	0.07	0.32	0.02
Ca.rDm	-0.16	-0.24	-0.17	-0.10	0.18	0.15	-0.26	0.18
Ca.rS	0.09	-0.08	0.00	0.27	0.24	-0.09	-0.02	0.20
Ca.AR2D	0.04	-0.07	-0.07	-0.40	-0.42	-0.34	-0.01	-0.35
Ca.AR3D	0.24	0.29	0.15	0.20	-0.05	0.06	0.25	0.01
BMU.rDm	-0.18	-0.20	-0.12	-0.13	0.09	0.04	-0.21	0.06
BMU. $\bar{B}F$	0.52	0.40	0.10	0.27	-0.18	-0.05	0.29	-0.07
BMU.rLe	0.39	0.27	0.12	0.14	-0.18	-0.04	0.22	-0.09
BMU.BF	0.22	0.07	-0.13	-0.05	-0.18	-0.06	0.00	-0.07

TABLE 3.10: Spearman correlation matrix. Only apparent mechanical features are shown. Outlier values are removed so as to avoid impact on Spearman coefficients. 0055 and 0965 subjects aren't considered. Bold values highlight meaningful correlation (spearman p-value < 0.05).

correlated with the elastic modulus [52, 70, 85, 87]. A possible explanation for this difference is that the current architecture study analyses it in 3D. The way of computing the porosity differs with these studies : this is the ratio between the total volume of canals and the total volume of the sample. Another possible explanation might be that outlier values are removed prior to the Spearman study and regressions. Indeed, 5 samples are considered as outliers because the porosity ranges from 16.3 % up to 27.5 %. If these samples are considered for regressions, the spearman coefficient between the elastic modulus and Ca.V/TV equals to -0.33 and becomes significant at a 5 % level (0.027). Likewise, no mechanical features are correlated with the mean canal diameter, surface or the 3D aspect ratio. The lack of relationship with such architectural features reveals that the phenomenon which occurs during a mechanical loading (crack propagation, ...) is very complex and requires a no less complex architectural study as provided by a 3D assessment of the cortical bone. However, although Spearman coefficients aren't very high, they reveal several interesting correlations. Those which are mostly correlated are the different densities, that requires a 3D assessment of the vascular network.

The elastic modulus is the feature which provides the highest correlation coefficient with an architectural characteristic. Indeed, it is significantly correlated with the canal density (-0.55). As the value is negative, the polynomial regression reveals a decreasing relationship (Figure 3.16a). It means that denser the vascular network is, less stiff the bone is. This relationship makes sense because a denser canal network reduces the spacing between canals and strongly impacts the macromechanical behaviour. This accords with Bala *et al.* [72] findings. Another interesting correlation is the positive relationship between the apparent modulus and the mean bone fraction. It means that the efficiency

$y = f(x)$	x	R^2	a_0	a_1	a_2	Mean \pm std error [%]	Median error [%]
E_{App}	Ca.D	0.33	-4.43E+01	1.93E+04	-	11.04 ± 6.89	9.64
$\sigma_{y,App}$	Conn.D	0.20	-8.07E-01	6.32E+01	-	13.72 ± 12.12	8.09
$\epsilon_{y,App}$	Conn.D	0.08	-3.15E-05	3.62E-03	-	15.31 ± 13.69	11.93
$\sigma_{U,App}$	BMU.D	0.22	6.09E-01	-1.35E+01	1.46E+02	17.37 ± 15.13	15.38
ϵ_U	Ca.AR2D	0.21	1.44E+00	-1.86E+00	6.15E-01	73.39 ± 79.16	45.26
$U_{tot,App}$	Ca.AR2D	0.15	1.23E+02	-1.58E+02	5.11E+01	127.91 ± 174.31	60.92
$U_{l,App}$	Conn.D	0.10	-1.72E-03	1.11E-01	-	28.91 ± 18.46	24.89
$U_{pl,App}$	Ca.AR2D	0.14	1.26E+02	-1.60E+02	5.17E+01	210.87 ± 404.65	76.82

TABLE 3.11: Coefficients of polynomial regressions between macromechanical features and architecture. R^2 is the coefficient of determination of the fittings. Linear and quadratic polynomials are assessed using non-linear least-squares method. Hence, $y = a_0 + a_1x^1 + a_2x^2$ and $y = a_0 + a_1x^1$ functions are computed. To compute fittings, subjects 0055 and 0965 are not considered ($N = 46$). The last two columns display the prediction errors of the fittings. This error is computed from the 12 available samples of 0055 and 0965 subjects. The error is computed by dividing the absolute difference between the predicted and measured values by the measured values.

of BMUs have a positive impact on the macromechanical behaviour and ensures the fact this feature may be used to evaluate the bone health.

Likewise, yield and ultimate strengths are also correlated with connectivity and BMU densities, respectively. The yield strength is the stress limit of the elastic linear part of the mechanical behaviour. It suggests that this is the limits where bone begins to damage which creates a softening of the bone. As a consequence, the relationship between this limit and the density of connectivity makes sense. The negative correlation coefficient (-0.52) highlights that a network with more connectivity would begin to damage earlier due to the stress concentration created by the connectivity (Figure 3.16b). However, no significant correlations are found between mechanical features and the mean opening angle of connectivity. It would suggest that connectivity should be individually investigated so as understand the impact of their shape on the crack initiation and propagation. Regarding the ultimate strength, the best significant correlation is obtained with the density of BMUs (-0.47). It shows that BMUs impact the entire macromechanical behaviour of the cortical bone. This result agrees with the new bone created by BMUs. Indeed, when the new bone is created by BMUs (osteonal bone), it is less mineralised than the interstitial bone. As a consequence, its behaviour is softer and explains why this correlation is negative (Figure 3.16d).

Overall, the strain features are hard to predict from architecture (Table 3.10). Indeed, for both yield strain limit and ultimate strain, the best correlation is found with the 2D aspect ratio of canals. Although significant, these relationships haven't any physical sense and remain weak. A possible explanation might be caused by the strain measurement. Indeed, to measure displacements during tensile tests, black dots are drawn on the sample. Displacements are reported as the mean displacement

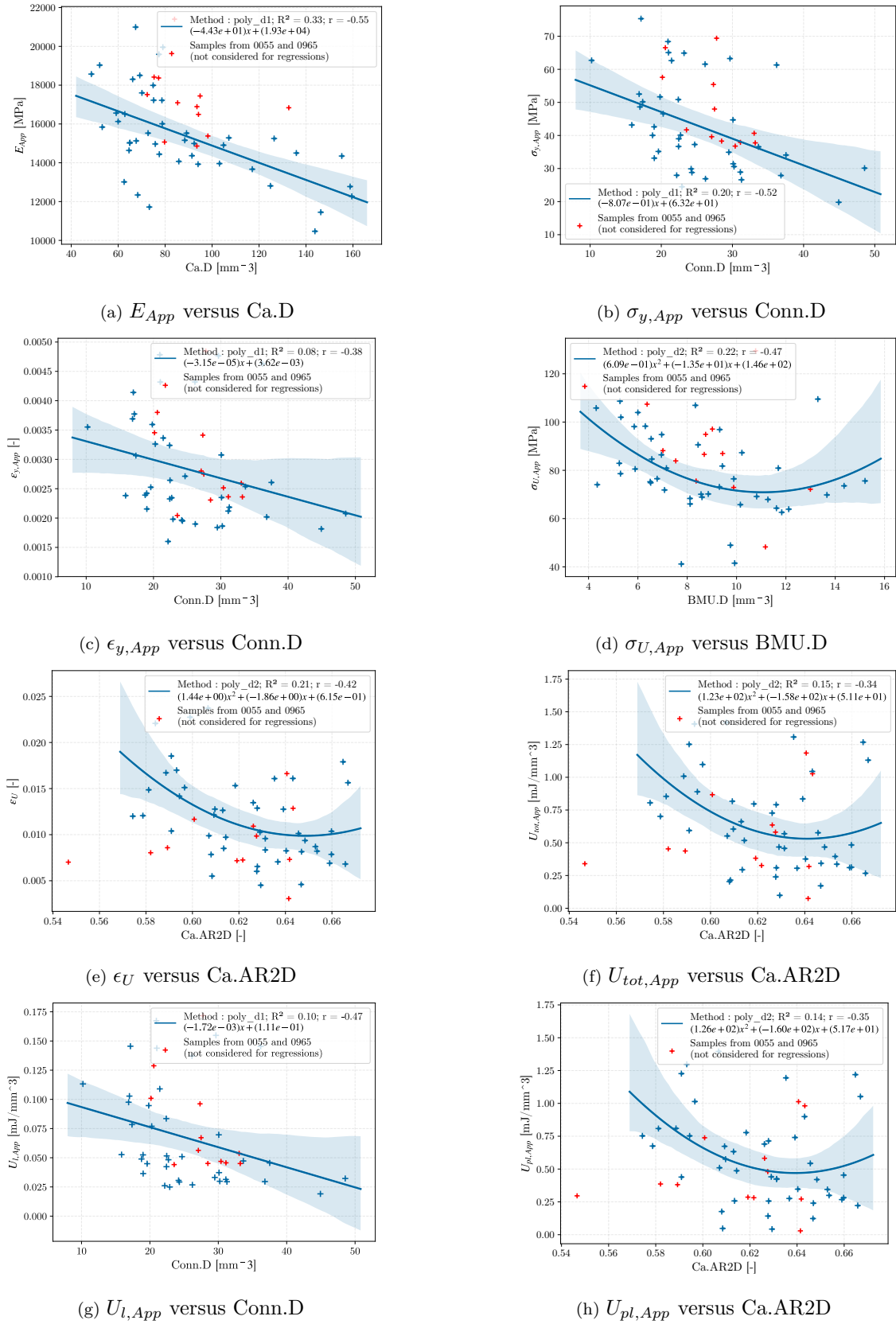


FIGURE 3.16: Polynomial regressions between macromechanical features and architecture. Mean values are displayed by plus markers. Blue markers are those used for regressions. Outliers are previously removed. Red markers are those used to validate regression (N=12, from 0055 and 0965 subjects). Therefore, they aren't considered to obtain regressions. Curve is the regression function.

The 95% confidence interval of the regression is displayed by the transparent coloured area.

on the entire length. Hence, this measure remains an external global one. However, as the bone has a within architecture, phenomena that occur during mechanical loadings are local inside the sample. A possible way to prevent this inconvenience from happening could be to perform the tensile tests under a tomographic environment. Hence, coupled with the Digital Volume Correlation method (DVC) it would be possible to obtain the strain field or the crack propagation within the sample. However, this kind of test requires heavy installations, substantially extends testing time and is currently limited to very short VOI [30].

Table 3.11 displays the prediction errors for each predicted features using the 12 samples from 0055 and 0965 subjects. Although Spearman coefficients and R^2 remain weak, the mean error is below 20 % for the elastic modulus, the yield stress and strain limit and the ultimate stress. For these features, the predictive function can be considered as admissible. However, regarding the ultimate strain and the different toughness, mean errors are very high. A possible explanation for this might be due to the way of strain measurement during the tensile test as previously explained in this section. Indeed, the predictive error for the ultimate strain is 73 %. As the toughness is computed from the area under the curve, it cumulates predictive inaccuracies for both stress and strain. Hence, as the ultimate strain is hard to predict, the toughness is highly impacted. Therefore, these predictive functions can't be used so as to quantify these features.

3.4 Conclusions

This chapter is the logical follow-up of the previous chapter on the three-dimensional assessment of the cortical bone architecture. Indeed, this study is performed on samples that have specifically designed so as to fit for a full tomographic scan but also for convenient tensile tests with recordable data. Hence, after the tomographic scan, samples are subsequently tensile tested. So as to avoid bone drying and preservation method impacts on the mechanical behaviour of the samples, all of these tests have been performed in less than 15 days after the body harvest. As the gauge length is fully scanned, four types of stress are computed from four different areas. For example, corrected stress is the ratio between the measured load and the minimum Bone Area (BA) of the gauge length from the tomographic scan. Strains are measured from post-processed images using Tracking Matlab toolbox. To understand the macromechanical behaviour of the bone, indentation tests are also performed on samples which have been harvested from a neighbour region to the tensile ones. Raw data from indentation tests require a post-process so as to obtain the hardness and elastic modulus [120]. To have the most accurate results, the machine compliance is measured and considered. So as to facilitate data processing, a kind of database is developed using Python and json files.

As a consequence, 58 monotonic quasi-static tensile tests have successfully been performed up to the failure. By comparing the 34 femoral samples with the 24 humeral ones, it highlights a stiffer behaviour of the humerus with a failure that happens at lower strains than femurs. These trends are confirmed by the MWW tests which point out numerous significant differences between the bearing and the non-bearing bone. The elastic modulus, the yield strength, and ultimate stress are higher for humeral samples. These findings are in line with Bry [10] study, which is the only recent study where humeri and femurs from same human subjects are compared. However, they are in contrast with inputs used by some human FE models which enforces the relevance of such a study. Indentation tests don't reveal any significant differences of the bone matrix modulus between humerus and femur. The evidence from this study suggests that differences found at the macroscopic scale are mainly due to the architecture differences. However, the indentation test remains a very local test (less than 1 mm^2) and the lack of differences may be due to the heterogeneity of the bone matrix and implies that the test isn't sufficiently representative of the entire bone. Nevertheless, this test reveals the significant stiffer behaviour of the interstitial bone compared to the osteonal one as proved by several similar studies [52, 111, 121, 122].

So as to investigate the impact of bias on the mechanical features, left and right limbs have been compared. Surprisingly, some differences are found for femurs and none for humeri as depicted for the architecture in the second chapter of this manuscript. However, by comparing the features which are defined as significantly different on each subject, no global trends are exhibited. It highlights that values remain dispersive and more human subjects would help to lessen the impact of variations on the results and obtain a distinct global trend.

Finally, a correlation study is performed and followed by a regression study between correlated features. The aim of this work is to understand the phenomenons which occur during a mechanical loading by investigating correlations between architecture, indentation and macromechanical features. Another aim of this study is to give some polynomial functions so as to predict the mechanical features from an architectural study. Indeed, with the ongoing improvement of in-vivo tomographic devices, these regressions would help to estimate the mechanical health of the cortical bone without testing it. In order to quantify the quality of regressions, 0055 and 0965 subjects aren't considered for correlations and regressions. Thus, the error between the predicted values and the measured values can be computed. One of the most surprisingly result is the absence of significant correlations between the mechanical features and the porosity. A possible reason for this might be due to the data processing. Indeed, outlier values are removed prior to correlations and regressions so as to avoid skewing results. If outliers are considered, some significant correlations are found with the Ca.V/TV . Moreover, it would suggest that the mechanical loading of the cortical bone creates complex phenomenons that are

hard to predict only with the porosity and requires a 3D assessment of the architecture. Regardless, many features are correlated with the different densities. First, the elastic modulus has the strongest Spearman coefficient with the canal density. This relationship makes sense because while the density of canals increases, the space between canals are reducing and soften the cortical bone. This result matches with those found by Bala *et al.* [72]. The yield stress and strain and the ultimate stress can also be predicted with an acceptable accuracy below 20 %.

This chapter has thrown up many questions in need of further investigation. Whereas some clear trends are found by comparing humeri with femurs, it is less obvious by comparing left and right limbs. Indeed, in the second chapter, significant differences between humeri left and right are found for architectural features. However, mainly due to the dispersion of the values, no similar trends are found for humerus. It points out that more human subjects would help to clarify these trends. Moreover, having additional samples would enforce the quality of predictions of the mechanical features. Likewise, only 3 female subjects are available in this study. Unfortunately, the limited number of females prevents the current study from investigating significant differences between males and females as it was done by Mirzaali *et al.* [52]. Although many macromechanical features can be predicted from the regressions, the ultimate strain and the different toughness can't be correctly computed. One possible way to enhance this might be to perform the tensile test under a tomographic environment coupled with a Digital Volume Correlation method (DVC). Indeed, the current study is limited by the fact that the stress is computed from the initial area before testing (engineering stress). However, during testing the sample shape evolves along with its minimum area. Even if the mechanical behaviour of the cortical bone remains brittle, this short upgrade would help to obtain better results and predictive functions. Similarly, this method would also improve the strain measurement. Actually, the strain is measured thanks to a camera where images are post-processed with a tracking point toolbox. Hence, an overall displacement is obtained. However, due to the within architecture, strain fields are heterogeneous. The use of the DVC method can help to obtain the spatial strain field and, as a consequence, help to describe local phenomena which occur during mechanical loading and lead to failure (crack initiation and propagation). However, this method needs heavy installations, consequent data post-processing and is very time-consuming and makes it at least questionable due to the bone drying.

Highlights of Chapter 3

- Macromechanical tensile tests are performed
 - Tests are carried out in less than 15 days after body harvest to prevent bone from drying
 - Tensile tests are performed on the samples where the gauge length were fully scanned
 - 4 types of stress are computed thanks to the previous μ -CT scan
 - 58 tests were successfully carried out
- Indentation tests are performed
 - A trapezoidal protocol in load control up to 1 N is chosen
 - A 3x3 array of indents is carried out on each sample
 - Osteonal and interstitial bones are identified so as to compare their mechanical features
 - The indentation machine compliance is considered and significantly enhances the result accuracy
- Femurs and humeri are compared so as to find significant differences
 - The humerus is significantly stiffer than the femur
 - Yield and ultimate stresses are higher for humeri
 - Strain at failure is higher for femurs
 - No significant differences are found for indentations (very local test)
- The osteonal bone is softer than the interstitial one
- Multi-scale relationships between architecture and macromechanical are investigated
 - Regressions can be useful so as to predict the mechanical health of the bone from a tomographic scan
 - The porosity is not correlated with any mechanical features
 - The different densities are correlated with several mechanical features

Conclusions and outlook

Conclusions

The purpose of the thesis was to extend the current knowledge of the cortical bone from long bones at different scales. Bone constantly adapts itself according to external factors and this process goes wrong in the elderly. Because of the population ageing, it becomes a societal goal to have a better understanding of these defects and their impacts on the mechanical behaviour of the bone.

The first chapter of this manuscript aimed at introducing the current scientific framework on cortical bone. The cortical bone is present in every part of the skeleton and especially in the long bone diaphysis. Cortical bone remains a living tissue and has a within micro-architecture that is able to adapt itself and is mechano-sensitive. Since the second part of the twentieth century, Bone Multicellular Units (BMUs) is described as the bone remodelling cradle. With the gradual enhancement of medical devices, it is widely proved that BMUs are part of the vascular architecture. The vascular network is very complex and tortuous. However, its architecture is poorly investigated in 3D and is mostly limited to planar studies and the porosity quantification. As a consequence, the macromechanical behaviour of the cortical bone is brittle with a transverse isotropy. Several types of mechanical devices can be used to assess the macromechanical bone. However, according to the type of the test, the shape of samples differs and complicates sample extraction. Therefore, most of the works, that study the human cortical bone, concern femur, which is the longest and thickest bone of the skeleton, and unbalance data for the other bones. This lack impacts the numerical human model where inputs for other bones are mainly inspired from very old and deprecated studies.

Consequently, the work done in this thesis is split into two chapters where the results are closely linked. Firstly, in the second chapter, an innovative method is provided so as to perform a 3D assessment of the vascular canals into the bone. Developed using Python, this script is based on the slices obtained from tomographic scans. The definition of the vascular canals are clearly defined as a void which ranges from a connectivity to another one. Connectivity and, especially, BMUs are also

automatically detected. As an innovative 3D method, it is able to give novel features, which have never been measured before, for canals, connectivity and BMUs. For instance, orientation, diameter or the aspect ratio (widely used by multi-scale numerical models) of the canals are performed. Likewise, new bone created by the grooves of BMUs is also estimated. This script is applied on the 77 scans of cortical bone samples harvested from left and right humeri and femur of 10 human cadavers in the elderly. These samples are dumbbell-shaped so as to fit for a full scan of the gauge length, at a $3\mu\text{m}$ resolution, and for quasi-static tensile test up to the failure.

Secondly, some micro and macromechanical tests are carried out and described in the third chapter of the manuscript. This part is followed by a multi-scale analysis that confronts 3D architectural data and indentation features with tensile results using statistics and polynomial regressions. As the gauge length was previously scanned, stresses are computed using areas obtained from tomographic scans. Strains are measured using a high-resolution camera coupled with tracking Matlab toolbox. Indentation tests are also performed on bone samples which were harvested from a neighbour region to the tensile ones. Indentation tests aim at obtaining features of the bone matrix at the tissue level. 77 mechanical tests were performed but 19 of them were lost due to sample crushing or slippage during testing. These tests were carried out in less than 15 days after the body harvest in order to reduce the impact of the preservation method and the bone drying.

In these two chapters, data are post-processed with Python. All of these data (including data from the previous chapter) are organised in a database so as to easily perform several statistic tests such as the Wilcoxon Mann-Whitney one that reveals significant differences between groups. Likewise, correlations and regressions are carried out so as to find inter-parameter relationships and understand phenomena which occur during a mechanical loading.

By comparing femur and humerus, numerous significant differences are highlighted for both architecture and mechanics. As a matter of fact, the porosity is higher in humeral samples due to the more important trabecularisation which thins the cortical shell. Vascular canals are flatter in the humeral cortical bone because they enlarge up to coalesce between themselves. This trend is enforced by BMUs that create more new bone in femur. The macromechanical behaviour is impacted by these differences. The humerus is stiffer than the femur (elastic modulus, yield and ultimate strengths) but fracture occurs higher in strain for femoral samples. These trends are mostly enforced by individual comparisons of the 10 subjects. Indentation tests don't exhibit any similar trends at the tissue level as found for the upper scale. However, it highlights that the interstitial bone is stiffer than the osteonal bone. The correlation study between architecture and mechanics shows that most of mechanical features are more linked with canal, connectivity or BMU densities than porosity as usually found in

some similar studies. Hence, it enforces the insists on the importance of the 3D assessment of the architecture to fully understand the macromechanical behaviour. No significant correlations are found between macro and micro mechanical features, surely due to the very restricted area of the indentation test. The comparison between left and right limbs also reveals some differences. Regarding to the architecture, only humerus exhibits differences. Indeed, samples from left humeri are more porous where canals are shorter and BMUs less efficient (mean new bone created). However, the only differences for the mechanical features concern the femoral samples where the yield limits are higher for the right humerus. Nonetheless, these trends aren't really confirmed by individual comparisons. More human subjects would help to enforce or contradict them.

In conclusion, several lacks revealed by the literature has been sorted out. Indeed, humeri and femurs, harvested from similar human subjects, have both been studied so as to enhance models accuracy. The vascular architecture has been assessed in 3D. This novel method automatically detects the vascular network, its connectivity and the BMUs, that have poorly been investigated before. It highlights numerous significant differences between the bearing and the non-bearing bone such as the porous volume. These results are coupled with mechanical tests at both of micro and macro-scales so as to find correlations between the architecture and the mechanical behaviour and to predict the mechanical health of the cortical bone without testing it. Likewise the architectural study, numerous differences are also found for the macromechanical features between the two types of bone such as the stiffer elastic modulus of humeri. Most of the mechanical features can be predicted from the architecture at an admissible rate.

Outlooks

Although this thesis enhances the current knowledge of the cortical bone, these results have thrown up many questions in need of further investigation. Actually, 10 human subjects are used in this study where only three females are available. Compared to the number of males, the gender dependencies can not be clearly exhibited and representative to the population. Likewise, the age impact can not be analysed due to the low number of subjects. This kind of study would be interesting to assess because a very low number of research has been reported in the first chapter and are limited on the femur. Indeed, to perform this kind of work, several dozen human subjects are required to obtain representative data. Furthermore, the use of the Python script, depicted in the second chapter, would bring novelties on the 3D shape of the vascular network that would be correlated with age or gender. In fact, Cooper *et al.* [68] show that female cortices are more porous and the bone loss is accelerated due to the trabecularisation. In contrast, Mirzaali *et al.* [52] don't report any architectural differences

between males and females. These two studies contradict each other and highlight a lack of data to exhibit a more suitable conclusion.

Similarly, as shown in the first chapter, damage of the cortical bone is investigated by some studies [10, 30, 92, 106]. One of the most common ways to assess it is the use of cyclic tests by sequentially loading and unloading the sample. This measure remains a global one because the damage is quantified from the loss of stiffness by comparing each cycle with the initial one (intact). The damage can also be visualised by carrying out the mechanical test under a tomographic environment as performed by Gauthier [30]. Hence, micro-cracks can be tracked during the test and the influence of the architecture can be directly analysed. However, this test requires heavy installation (SR μ -CT) or highly extend testing time if a conventional X-ray tubes (μ -CT) is used. An extensive testing time would lead to the bone drying and affect its mechanical properties. One of the possibilities to enhance the damage assessment would be to couple the mechanical test with ultrasonic inspections. Indeed, ultrasonic sensors are already used to assess the elastic features of the bone [72, 88]. However, some of these sensors can also be used to visualise damages [147].

The development of a device is currently under process because it requires several cares. Indeed, so as to obtain an ultrasonic scan, samples have to be placed into water and the acoustic sensors have to run all along the surface of it. As a consequence, the sensor needs to be attached on motorised bracket where displacements step should the most accurate as possible. A similar device is partially depicted in Bourse *et al.* [148] study. A feasibility assessment of the sensors have been performed on a human femoral sample and is displayed on Figure I.

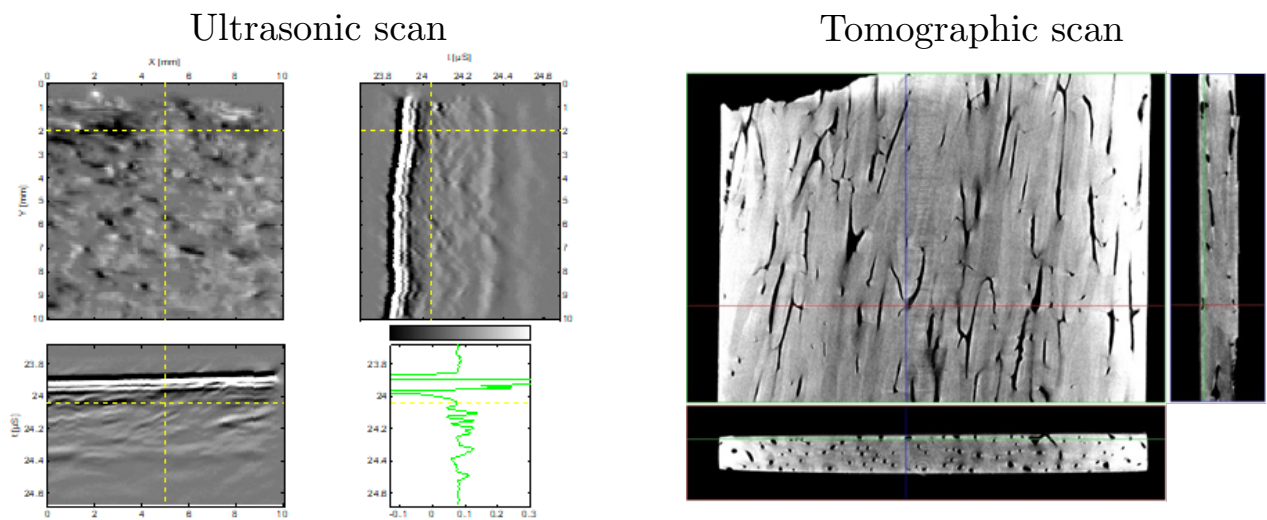


FIGURE I: Comparison of an ultrasonic scan (left) and a tomographic one (right)

From this figure, it is obvious that the ultrasonic sensor isn't as accurate as a tomographic scan. However, some of the biggest pores can be distinguished. Attention should be paid to the frequency

of the sensor. Indeed, due to the porous part of the bone, its density and the thickness of the sample, the frequency needs to be designed so as to obtain the best resolution as possible. For instance, the feasibility assessment was carried out using a 20 MHz sensor. A custom sensor is currently under process at a lower frequency so as to better detect within porosities of the sample. This sensor will be coupled with another ultrasound one in order to provide measurements of the elastic properties. Therefore, all of these require a mechanical mounting which is able to fit with the tensile machine (ElectroPuls E3000, INSTRON) and its size. Moreover, all the devices (motor, sensors, tensile machine) need to be coupled and driven by the same machine/software so as to be perfectly synchronised.

The test will be step by step performed. At each step, tensile test is stopped and sensors runs all along the surface of the sample so as to scan it. Hence, elastic properties and a similar image as shown on Figure I are obtained for each step. Motors iterate right after receiving pulse created by sensors for scanning. Thanks to this, damage can be visualised and quantified using both sensor and tensile machine. As a scan requires a couple of minutes to be performed, a tensile test up to the failure requires much less time as needed by a classical tomographic scan. Moreover, as sample is placed in water, bone drying is minimised.

Finally, due to the thesis purpose, only the cortical bone is assessed. However, bibliography reveals that the 3D architecture is poorly investigated whatever the material. As the method of the Python script remains slightly universal whatever the material, it could be performed on natural materials with architecture (wood, composite reinforced with natural fibres). Therefore a similar study by coupling mechanical and architecture can be performed. However, a great attention should be paid to the image processing and thresholding so as to obtain images with sharp contours.

Appendix A

Illustration of the common symbols

This appendix is especially made for ease of reading. Indeed, numerous novel features are defined. Therefore, many new symbols are also defined. Hence, the following page summarises the different symbols by reminding their definition with a scheme.

Entity	Notation	Features	Explanation/Scheme
Po, Ca, Conn, BMU	D	Density	$\frac{\text{Nb of entities}}{\text{Sample volume}}$
Ca	ψ	First Eulerian angle	
Ca	θ	Second Eulerian angle	
Ca	x	Longitudinal angle	
Ca	y	Transverse angle	
Ca	aLe	Apparent length	
Ca	rLe	Real length	
Ca, BMU	aS	Apparent surface	
Ca, BMU	rS	Real surface	
Ca, BMU	aDm	Apparent diameter	
Ca, BMU	rDm	Real diameter	
Ca	$AR2D$	2D aspect ratio	
Ca	$AR3D$	3D aspect ratio $\frac{Ca.aLe}{Ca.rDm}$	
Conn	α	Connectivity opening angle	
Conn	$R_{rDm(0,12)}$	$\frac{Ca_1.rDm + Ca_2.rDm}{Ca_0.rDm}$	
Conn	$R_{rDm(1,2)}$	$\frac{\max(Ca_1.rDm, Ca_2.rDm)}{\min(Ca_1.rDm, Ca_2.rDm)}$	
BMU	BF	New bone fraction	$\frac{\text{New bone created by grooves of BMUs}}{\text{Sample volume}}$
BMU	\bar{BF}	BMU efficiency	$\frac{BMU.BF}{\text{Nb of BMUs}}$

TABLE A.1: Explanations of the symbols commonly used in Chapter 2 and 3 of this manuscript.

Bibliography

- [1] KAMINA, P.. Anatomie clinique : anatomie générale, membres; vol. 1. 4ème ed.; Paris: Maloine; 2009. ISBN 978-2-224-03183-1. OCLC: 609995926.
- [2] WOLFF, J.. The Law of Bone Remodelling. Berlin, Heidelberg: Springer Berlin Heidelberg; 1986. ISBN 978-3-642-71031-5. OCLC: 851840449.
- [3] MCCORMACK, S.E., COUSMINER, D.L., CHESI, A., MITCHELL, J.A., ROY, S.M., KALKWARF, H.J., et al. Association Between Linear Growth and Bone Accrual in a Diverse Cohort of Children and Adolescents. *JAMA Pediatrics* 2017;171(9):e171769. doi:[10.1001/jamapediatrics.2017.1769](https://doi.org/10.1001/jamapediatrics.2017.1769).
- [4] VOGT, E.. Roentgen sign of plumbism: lead lines in growing bone. *Amer J Roentgenol* 1930;.
- [5] PARK, E.A., JACKSON, D., GOODWIN, T.C., KAJDI, L.. X-ray shadows in growing bones produced by lead; Their characteristics, cause, anatomical counterpart in the bone and differentiation. *The Journal of Pediatrics* 1933;3(2):265–298. doi:[10.1016/S0022-3476\(33\)80110-7](https://doi.org/10.1016/S0022-3476(33)80110-7).
- [6] KELLAM, J.F., MEINBERG, E.G., AGEL, J., KARAM, M.D., ROBERTS, C.S.. Introduction: Fracture and Dislocation Classification Compendium—2018. *Journal of Orthopaedic Trauma* 2018;32:S1–S10. doi:[10.1097/BOT.0000000000001063](https://doi.org/10.1097/BOT.0000000000001063).
- [7] CLARKE, B.. Normal Bone Anatomy and Physiology. *Clinical Journal of the American Society of Nephrology* 2008;3(Supplement 3):S131–S139. doi:[10.2215/CJN.04151206](https://doi.org/10.2215/CJN.04151206).
- [8] DWEK, J.R.. The periosteum: what is it, where is it, and what mimics it in its absence? *Skeletal Radiology* 2010;39(4):319–323. doi:[10.1007/s00256-009-0849-9](https://doi.org/10.1007/s00256-009-0849-9).
- [9] MALL, G., HUBIG, M., BÜTTNER, A., KUZNIK, J., PENNING, R., GRAW, M.. Sex determination and estimation of stature from the long bones of the arm. *Forensic Science International* 2001;117(1):23–30. doi:[10.1016/S0379-0738\(00\)00445-X](https://doi.org/10.1016/S0379-0738(00)00445-X).

- [10] BRY, R.. Contribution à l'étude de la variabilité des propriétés mécaniques de l'os cortical diaphysaire d'un os porteur (fémur) et non-porteur (humérus). Thèse de doctorat; Valenciennes; 2015.
- [11] DRAKE, R.L., DUPARC, F., DUPARC, J., MITCHELL, A., VOGL, A.W., SCOTT, J., et al. Gray's Anatomie pour les étudiants. 3ème ed.; Elsevier Health Sciences; 2015.
- [12] LEFÈVRE, Y., JOURNEAU, P., ANGELLIAUME, A., BOUTY, A., DOBREMEZ, E.. Proximal humerus fractures in children and adolescents. *Orthopaedics & Traumatology: Surgery & Research* 2014;100(1, Supplement):S149–S156. doi:[10.1016/j.otsr.2013.06.010](https://doi.org/10.1016/j.otsr.2013.06.010).
- [13] TINGART, M.J., APRELEVA, M., VON STECHOW, D., ZURAKOWSKI, D., WARNER, J.J.P.. The cortical thickness of the proximal humeral diaphysis predicts bone mineral density of the proximal humerus. *The Journal of Bone and Joint Surgery British volume* 2003;85-B(4):611–617. doi:[10.1302/0301-620X.85B4.12843](https://doi.org/10.1302/0301-620X.85B4.12843).
- [14] DIEDERICHS, G., ISSEVER, A.S., GREINER, S., LINKE, B., KORNER, J.. Three-dimensional distribution of trabecular bone density and cortical thickness in the distal humerus. *Journal of Shoulder and Elbow Surgery* 2009;18(3):399–407. doi:[10.1016/j.jse.2008.11.001](https://doi.org/10.1016/j.jse.2008.11.001).
- [15] PERCHALSKI, B., PLACKE, A., SUKHDEO, S.M., SHAW, C.N., GOSMAN, J.H., RAICHLEN, D.A., et al. Asymmetry in the Cortical and Trabecular Bone of the Human Humerus During Development. *Anatomical Record (Hoboken, NJ: 2007)* 2018;301(6):1012–1025. doi:[10.1002/ar.23705](https://doi.org/10.1002/ar.23705).
- [16] POLGUJ, M., BLIŹNIEWSKA, K., JĘDRZEJEWSKI, K., MAJOS, A., TOPOL, M.. Morphological study of linea aspera variations – proposal of classification and sexual dimorphism. *Folia Morphologica* 2013;72(1):72–77. doi:[10.5603/FM.2013.0012](https://doi.org/10.5603/FM.2013.0012).
- [17] GOSMAN, J.H., HUBBELL, Z.R., SHAW, C.N., RYAN, T.M.. Development of cortical bone geometry in the human femoral and tibial diaphysis. *Anatomical Record (Hoboken, NJ: 2007)* 2013;296(5):774–787. doi:[10.1002/ar.22688](https://doi.org/10.1002/ar.22688).
- [18] NIIMI, R., KONO, T., NISHIHARA, A., HASEGAWA, M., MATSUMINE, A., KONO, T., et al. Cortical Thickness of the Femur and Long-Term Bisphosphonate Use. *Journal of Bone and Mineral Research* 2015;30(2):225–231. doi:[10.1002/jbmr.2345](https://doi.org/10.1002/jbmr.2345).
- [19] LESZCZYŃSKI, B., SKRZAT, J., KOZERSKA, M., WRÓBEL, A., WALOCHA, J.. Three dimensional visualisation and morphometry of bone samples studied in microcomputed tomography (micro-CT). *Folia Morphologica* 2014;73(4):422–428. doi:[10.5603/FM.2014.0064](https://doi.org/10.5603/FM.2014.0064).

- [20] CHEN, H., ZHOU, X., FUJITA, H., ONOZUKA, M., KUBO, K.Y.. Age-Related Changes in Trabecular and Cortical Bone Microstructure. *International Journal of Endocrinology* 2013;2013:1–9. doi:[10.1155/2013/213234](https://doi.org/10.1155/2013/213234).
- [21] WEINKAMER, R., FRATZL, P.. Mechanical adaptation of biological materials — The examples of bone and wood. *Materials Science and Engineering: C* 2011;31(6):1164–1173. doi:[10.1016/j.msec.2010.12.002](https://doi.org/10.1016/j.msec.2010.12.002).
- [22] COOPER, D., TURINSKY, A., SENSEN, C., HALLGRÍMSSON, B.. Quantitative 3d analysis of the canal network in cortical bone by micro-computed tomography. *The Anatomical Record Part B: The New Anatomist* 2003;274B(1):169–179. doi:[10.1002/ar.b.10024](https://doi.org/10.1002/ar.b.10024).
- [23] SKEDROS, J.G., CLARK, G.C., SORENSON, S.M., TAYLOR, K.W., QIU, S.. Analysis of the Effect of Osteon Diameter on the Potential Relationship of Osteocyte Lacuna Density and Osteon Wall Thickness. *Anatomical record (Hoboken, NJ : 2007)* 2011;294(9):1472–1485. doi:[10.1002/ar.21452](https://doi.org/10.1002/ar.21452).
- [24] QIU, S., FYHRIE, D.P., PALNITKAR, S., RAO, D.S.. Histomorphometric assessment of Haversian canal and osteocyte lacunae in different-sized osteons in human rib. *The Anatomical Record* 2003;272A(2):520–525. doi:[10.1002/ar.a.10058](https://doi.org/10.1002/ar.a.10058).
- [25] JEROME, C., HOCH, B., CARLSON, C.S.. 5 - Skeletal System. Dans: TREUTING, P.M., DINTZIS, S.M., MONTINE, K.S., *éditeurs*. Comparative Anatomy and Histology (Second Edition). San Diego: Academic Press. ISBN 978-0-12-802900-8; 2018, p. 67–88. doi:[10.1016/B978-0-12-802900-8.00005-1](https://doi.org/10.1016/B978-0-12-802900-8.00005-1).
- [26] BOUSSON, V., PEYRIN, F., BERGOT, C., HAUSARD, M., SAUTET, A., LAREDO, J.D.. Cortical Bone in the Human Femoral Neck: Three-Dimensional Appearance and Porosity Using Synchrotron Radiation. *Journal of Bone and Mineral Research* 2004;19(5):794–801. doi:[10.1359/jbmr.040124](https://doi.org/10.1359/jbmr.040124).
- [27] ZHOU, X., NOVOTNY, J.E., WANG, L.. Anatomic Variations of the Lacunar-Canalicular System Influence Solute Transport in Bone. *Bone* 2009;45(4):704–710. doi:[10.1016/j.bone.2009.06.026](https://doi.org/10.1016/j.bone.2009.06.026).
- [28] YOU, L.D., WEINBAUM, S., COWIN, S.C., SCHAFFLER, M.B.. Ultrastructure of the osteocyte process and its pericellular matrix. *The Anatomical Record Part A: Discoveries in Molecular, Cellular, and Evolutionary Biology* 2004;278A(2):505–513. doi:[10.1002/ar.a.20050](https://doi.org/10.1002/ar.a.20050).

- [29] MCCREADIE, B.R., HOLLISTER, S.J., SCHAFFLER, M.B., GOLDSTEIN, S.A.. Osteocyte lacuna size and shape in women with and without osteoporotic fracture. *Journal of Biomechanics* 2004;37(4):563–572. doi:[10.1016/S0021-9290\(03\)00287-2](https://doi.org/10.1016/S0021-9290(03)00287-2).
- [30] GAUTHIER, R.. Crack propagation mechanisms in human cortical bone on different paired anatomical locations : biomechanical, tomographic and biochemical approaches. Thèse de doctorat; Université de Lyon; 2017.
- [31] COOPER, D.M.L., KAWALILAK, C.E., HARRISON, K., JOHNSTON, B.D., JOHNSTON, J.D.. Cortical Bone Porosity: What Is It, Why Is It Important, and How Can We Detect It? *Current Osteoporosis Reports* 2016;14(5):187–198. doi:[10.1007/s11914-016-0319-y](https://doi.org/10.1007/s11914-016-0319-y).
- [32] BURR, D.B., SCHAFFLER, M.B., FREDERICKSON, R.G.. Composition of the cement line and its possible mechanical role as a local interface in human compact bone. *Journal of Biomechanics* 1988;21(11):939–945. doi:[10.1016/0021-9290\(88\)90132-7](https://doi.org/10.1016/0021-9290(88)90132-7).
- [33] WANG, X., NI, Q.. Determination of cortical bone porosity and pore size distribution using a low field pulsed NMR approach. *Journal of Orthopaedic Research* 2003;21(2):312–319. doi:[10.1016/S0736-0266\(02\)00157-2](https://doi.org/10.1016/S0736-0266(02)00157-2).
- [34] GAUTHIER, R., LANGER, M., FOLLET, H., OLIVIER, C., GOUTTENOIRE, P.J., HELFEN, L., et al. 3d micro structural analysis of human cortical bone in paired femoral diaphysis, femoral neck and radial diaphysis. *Journal of Structural Biology* 2018;204(2):182–190. doi:[10.1016/j.jsb.2018.08.006](https://doi.org/10.1016/j.jsb.2018.08.006).
- [35] RHO, J.Y., KUHN-SPEARING, L., ZIOUPOS, P.. Mechanical properties and the hierarchical structure of bone. *Medical Engineering & Physics* 1998;20(2):92–102. doi:[10.1016/S1350-4533\(98\)00007-1](https://doi.org/10.1016/S1350-4533(98)00007-1).
- [36] BLACK, J., MATTSON, R., KOROSTOFF, E.. Haversian osteons: Size, distribution, internal structure, and orientation. *Journal of Biomedical Materials Research* 1974;8(5):299–319. doi:[10.1002/jbm.820080512](https://doi.org/10.1002/jbm.820080512).
- [37] TOMOIAIA, G., PASCA, R.D.. On the Collagen Mineralization. A Review. *Medicine and Pharmacy Reports* 2015;88(1):15–22. doi:[10.15386/cjmed-359](https://doi.org/10.15386/cjmed-359).
- [38] ASCENZI, A., BONUCCI, E.. THE ULTIMATE TENSILE STRENGTH OF SINGLE OSTEOONS. *Cells Tissues Organs* 1964;58(1-2):160–183. doi:[10.1159/000142580](https://doi.org/10.1159/000142580).
- [39] ASCENZI, A., BONUCCI, E.. The tensile properties of single osteons. *The Anatomical Record* 1967;158(4):375–386. doi:[10.1002/ar.1091580403](https://doi.org/10.1002/ar.1091580403).

- [40] ASCENZI, A., BONUCCI, E.. The compressive properties of single osteons. *The Anatomical Record* 1968;161(3):377–391. doi:[10.1002/ar.1091610309](https://doi.org/10.1002/ar.1091610309).
- [41] BROMAGE, T.G., GOLDMAN, H.M., MCFARLIN, S.C., WARSHAW, J., BOYDE, A., RIGGS, C.M.. Circularly polarized light standards for investigations of collagen fiber orientation in bone. *The Anatomical Record Part B: The New Anatomist* 2003;274B(1):157–168. doi:[10.1002/ar.b.10031](https://doi.org/10.1002/ar.b.10031).
- [42] WESS, T.. Collagen Fibril Form and Function. Dans: *Advances in Protein Chemistry*; vol. 70. Elsevier. ISBN 978-0-12-034270-9; 2005, p. 341–374. doi:[10.1016/S0065-3233\(05\)70010-3](https://doi.org/10.1016/S0065-3233(05)70010-3).
- [43] WEINER, S., TRAUB, W.. Organization of hydroxyapatite crystals within collagen fibrils. *FEBS Letters* 1986;206(2):262–266. doi:[10.1016/0014-5793\(86\)80993-0](https://doi.org/10.1016/0014-5793(86)80993-0).
- [44] SYKARAS, N., IACOPINO, A.M., MARKER, V.A., TRIPLETT, R.G., WOODY, R.D.. Implant Materials, Designs, and Surface Topographies: Their Effect on Osseointegration. A Literature Review 2000;:16.
- [45] MATHIEU, V., VAYRON, R., RICHARD, G., LAMBERT, G., NAILI, S., MENINGAUD, J.P., et al. Biomechanical determinants of the stability of dental implants: Influence of the bone–implant interface properties. *Journal of Biomechanics* 2014;47(1):3–13. doi:[10.1016/j.jbiomech.2013.09.021](https://doi.org/10.1016/j.jbiomech.2013.09.021).
- [46] WELTGESUNDHEITSORGANISATION, , ONIS, M.D., WELTGESUNDHEITSORGANISATION, , éditeurs. WHO child growth standards: length/height-for-age, weight-for-age, weight-for-length, weight-for-height and body mass index-for-age ; methods and development. Geneva: WHO Press; 2006. ISBN 978-92-4-154693-5. OCLC: 255763055.
- [47] DIBLEY, M.J., STAEHLING, N., NIEBURG, P., TROWBRIDGE, F.L.. Interpretation of Z-score anthropometric indicators derived from the international growth reference. *The American Journal of Clinical Nutrition* 1987;46(5):749–762. doi:[10.1093/ajcn/46.5.749](https://doi.org/10.1093/ajcn/46.5.749).
- [48] ORGANIZATION, W.H., OTHERS, . WHO scientific group on the assessment of osteoporosis at primary health care level. Dans: *Summary meeting report*. 2004, p. 5–7.
- [49] KLING, J.M., CLARKE, B.L., SANDHU, N.P.. Osteoporosis Prevention, Screening, and Treatment: A Review. *Journal of Women's Health* 2014;23(7):563–572. doi:[10.1089/jwh.2013.4611](https://doi.org/10.1089/jwh.2013.4611).
- [50] SOLTAN, N., KAWALILAK, C.E., COOPER, D.M., KONTULAINEN, S.A., JOHNSTON, J.D.. Cortical porosity assessment in the distal radius: A comparison of HR-pQCT measures

- with Synchrotron-Radiation micro-CT-based measures. *Bone* 2019;120:439–445. doi:[10.1016/j.bone.2018.12.008](https://doi.org/10.1016/j.bone.2018.12.008).
- [51] DUBOUSSET, J., CHARPAK, G., SKALLI, W., DEGUISE, J., KALIFA, G.. EOS : a new imaging system with low dose radiation in standing position for spine and bone & joint disorders. *Journal of Musculoskeletal Research* 2010;13(01):1–12. doi:[10.1142/S0218957710002430](https://doi.org/10.1142/S0218957710002430).
- [52] MIRZAALI, M.J., SCHWIEDRZIK, J.J., THAIWICHAI, S., BEST, J.P., MICHLER, J., ZYSSET, P.K., et al. Mechanical properties of cortical bone and their relationships with age, gender, composition and microindentation properties in the elderly. *Bone* 2016;93(Supplement C):196–211. doi:[10.1016/j.bone.2015.11.018](https://doi.org/10.1016/j.bone.2015.11.018).
- [53] FROST, H.M.. MEAN FORMATION TIME OF HUMAN OSTEONS. *Canadian Journal of Biochemistry and Physiology* 1963;41(5):1307–1310. doi:[10.1139/o63-146](https://doi.org/10.1139/o63-146).
- [54] FROST, H.M.. Tetracycline-based histological analysis of bone remodeling. *Calcified Tissue Research* 1969;3(3):211–237.
- [55] FROST, H.M.. Skeletal structural adaptations to mechanical usage (SATMU): 2. Redefining Wolff's Law: The remodeling problem. *The Anatomical Record* 1990;226(4):414–422. doi:[10.1002/ar.1092260403](https://doi.org/10.1002/ar.1092260403).
- [56] HADJIDAKIS, D.J., ANDROULAKIS, I.I.. Bone Remodeling. *Annals of the New York Academy of Sciences* 2006;1092(1):385–396. doi:[10.1196/annals.1365.035](https://doi.org/10.1196/annals.1365.035).
- [57] BUENZLI, P.R., PIVONKA, P., SMITH, D.W.. Bone refilling in cortical basic multicellular units: insights into tetracycline double labelling from a computational model. *Biomechanics and Modeling in Mechanobiology* 2014;13(1):185–203. doi:[10.1007/s10237-013-0495-y](https://doi.org/10.1007/s10237-013-0495-y).
- [58] ALIAS, M.A., BUENZLI, P.R.. Osteoblasts infill irregular pores under curvature and porosity controls: a hypothesis-testing analysis of cell behaviours. *Biomechanics and Modeling in Mechanobiology* 2018;17(5):1357–1371. doi:[10.1007/s10237-018-1031-x](https://doi.org/10.1007/s10237-018-1031-x).
- [59] LASSEN, N.E., ANDERSEN, T.L., PLØEN, G.G., SØE, K., HAUGE, E.M., HARVING, S., et al. Coupling of Bone Resorption and Formation in Real Time: New Knowledge Gained From Human Haversian BMUs. *Journal of Bone and Mineral Research* 2017;32(7):1395–1405. doi:[10.1002/jbmr.3091](https://doi.org/10.1002/jbmr.3091).
- [60] BURGER, E.H., KLEIN-NULEND, J.. Mechanotransduction in bone—role of the lacuno-canalicular network. *The FASEB Journal* 1999;13(9001):S101–S112. doi:[10.1096/fasebj.13.9001.s101](https://doi.org/10.1096/fasebj.13.9001.s101).

- [61] LIN, J.T., LANE, J.M.. Osteoporosis: A Review. *Clinical Orthopaedics and Related Research* 2004;425:126–134. doi:[10.1097/01.blo.0000132404.30139.f2](https://doi.org/10.1097/01.blo.0000132404.30139.f2).
- [62] SÖZEN, T., ÖZİŞİK, L., BAŞARAN, N.A.. An overview and management of osteoporosis. *European Journal of Rheumatology* 2017;4(1):46–56. doi:[10.5152/eurjrheum.2016.048](https://doi.org/10.5152/eurjrheum.2016.048).
- [63] KANIS, J.A., ODEN, A., JOHNELL, O., JOHANSSON, H., DE LAET, C., BROWN, J., et al. The use of clinical risk factors enhances the performance of BMD in the prediction of hip and osteoporotic fractures in men and women. *Osteoporosis International* 2007;18(8):1033–1046. doi:[10.1007/s00198-007-0343-y](https://doi.org/10.1007/s00198-007-0343-y).
- [64] COSMAN, F., DE BEUR, S.J., LEBOFF, M.S., LEWIECKI, E.M., TANNER, B., RANDALL, S., et al. Clinician’s Guide to Prevention and Treatment of Osteoporosis. *Osteoporosis International* 2014;25(10):2359–2381. doi:[10.1007/s00198-014-2794-2](https://doi.org/10.1007/s00198-014-2794-2).
- [65] MARIE, P., HALBOUT, P.. OPG/RANKL: Implication et cible thérapeutique dans l’ostéoporose. *médecine/sciences* 2008;24(1):105–110. doi:[10.1051/medsci/2008241105](https://doi.org/10.1051/medsci/2008241105).
- [66] ASHIQUE, A.M., HART, L.S., THOMAS, C.D.L., CLEMENT, J.G., PIVONKA, P., CARTER, Y., et al. Lacunar-canalicular network in femoral cortical bone is reduced in aged women and is predominantly due to a loss of canalicular porosity. *Bone Reports* 2017;7(Supplement C):9–16. doi:[10.1016/j.bonr.2017.06.002](https://doi.org/10.1016/j.bonr.2017.06.002).
- [67] CARTER, Y., THOMAS, C.D.L., CLEMENT, J.G., COOPER, D.M.L.. Femoral osteocyte lacunar density, volume and morphology in women across the lifespan. *Journal of Structural Biology* 2013;183(3):519–526. doi:[10.1016/j.jsb.2013.07.004](https://doi.org/10.1016/j.jsb.2013.07.004).
- [68] COOPER, D.M.L., THOMAS, C.D.L., CLEMENT, J.G., TURINSKY, A.L., SENSEN, C.W., HALLGRÍMSSON, B.. Age-dependent change in the 3d structure of cortical porosity at the human femoral midshaft. *Bone* 2007;40(4):957–965. doi:[10.1016/j.bone.2006.11.011](https://doi.org/10.1016/j.bone.2006.11.011).
- [69] HUNTER, R.L., AGNEW, A.M.. Intrasketal variation in human cortical osteocyte lacunar density: Implications for bone quality assessment. *Bone Reports* 2016;5:252–261. doi:[10.1016/j.bonr.2016.09.002](https://doi.org/10.1016/j.bonr.2016.09.002).
- [70] NEIL DONG, X., EDWARD GUO, X.. The dependence of transversely isotropic elasticity of human femoral cortical bone on porosity. *Journal of Biomechanics* 2004;37(8):1281–1287. doi:[10.1016/j.jbiomech.2003.12.011](https://doi.org/10.1016/j.jbiomech.2003.12.011).

- [71] TJONG, W., NIRODY, J., BURGHARDT, A.J., CARBALLIDO-GAMIO, J., KAZAKIA, G.J.. Structural analysis of cortical porosity applied to HR-pQCT data: HR-pQCT structural analysis of cortical porosity. *Medical Physics* 2013;41(1):013701. doi:[10.1118/1.4851575](https://doi.org/10.1118/1.4851575).
- [72] BALA, Y., LEFÈVRE, E., ROUX, J.P., BARON, C., LASAYGUES, P., PITHIOUX, M., et al. Pore network microarchitecture influences human cortical bone elasticity during growth and aging. *Journal of the Mechanical Behavior of Biomedical Materials* 2016;63:164–173. doi:[10.1016/j.jmbbm.2016.05.018](https://doi.org/10.1016/j.jmbbm.2016.05.018).
- [73] ZEBAZE, R.M., GHASEM-ZADEH, A., BOHTE, A., IULIANO-BURNS, S., MIRAMS, M., PRICE, R.I., et al. Intracortical remodelling and porosity in the distal radius and post-mortem femurs of women: a cross-sectional study. *The Lancet* 2010;375(9727):1729–1736. doi:[10.1016/S0140-6736\(10\)60320-0](https://doi.org/10.1016/S0140-6736(10)60320-0).
- [74] PERILLI, E., BALA, Y., ZEBAZE, R., REYNOLDS, K.J., SEEMAN, E.. Regional Heterogeneity in the Configuration of the Intracortical Canals of the Femoral Shaft. *Calcified Tissue International* 2015;97(4):327–335. doi:[10.1007/s00223-015-0014-5](https://doi.org/10.1007/s00223-015-0014-5).
- [75] VAN OERS, R.F.M., WANG, H., BACABAC, R.G.. Osteocyte Shape and Mechanical Loading. *Current Osteoporosis Reports* 2015;13(2):61–66. doi:[10.1007/s11914-015-0256-1](https://doi.org/10.1007/s11914-015-0256-1).
- [76] BACABAC, R.G., MIZUNO, D., SCHMIDT, C.F., MACKINTOSH, F.C., VAN LOON, J.J.W.A., KLEIN-NULEND, J., et al. Round versus flat: Bone cell morphology, elasticity, and mechanosensing. *Journal of Biomechanics* 2008;41(7):1590–1598. doi:[10.1016/j.jbiomech.2008.01.031](https://doi.org/10.1016/j.jbiomech.2008.01.031).
- [77] PRATT, I.V., COOPER, D.M.L.. A method for measuring the three-dimensional orientation of cortical canals with implications for comparative analysis of bone microstructure in vertebrates. *Micron* 2017;92:32–38. doi:[10.1016/j.micron.2016.10.006](https://doi.org/10.1016/j.micron.2016.10.006).
- [78] LAM, L., LEE, S.W., SUEN, C.Y.. Thinning Methodologies - A Comprehensive Survey. *IEEE Trans Pattern Anal Mach Intell* 1992;14:869–885. doi:[10.1109/34.161346](https://doi.org/10.1109/34.161346).
- [79] ANDREASEN, C.M., DELAISSE, J.M., EERDEN, B.C.V.D., LEEUWEN, J.P.V., DING, M., ANDERSEN, T.L.. Understanding Age-Induced Cortical Porosity in Women: The Accumulation and Coalescence of Eroded Cavities Upon Existing Intracortical Canals Is the Main Contributor. *Journal of Bone and Mineral Research* 2018;33(4):606–620. doi:[10.1002/jbmr.3354](https://doi.org/10.1002/jbmr.3354).
- [80] ANDREASEN, C.M., DELAISSE, J.M., VAN DER EERDEN, B.C.J., VAN LEEUWEN, J.P.T.M., DING, M., ANDERSEN, T.L.. Understanding age-induced cortical porosity in

- women: Is a negative BMU balance in quiescent osteons a major contributor? *Bone* 2018;117:70–82. doi:[10.1016/j.bone.2018.09.011](https://doi.org/10.1016/j.bone.2018.09.011).
- [81] GOLIATH, J.R., STEWART, M.C., STOUT, S.D.. Variation in osteon histomorphometrics and their impact on age-at-death estimation in older individuals. *Forensic Science International* 2016;262:282.e1–282.e6. doi:[10.1016/j.forsciint.2016.02.053](https://doi.org/10.1016/j.forsciint.2016.02.053).
- [82] SINGH, I.J., GUNBERG, D.L.. Estimation of age at death in human males from quantitative histology of bone fragments. *American Journal of Physical Anthropology* 1970;33(3):373–381. doi:[10.1002/ajpa.1330330311](https://doi.org/10.1002/ajpa.1330330311).
- [83] BRITZ, H.M., THOMAS, C.D.L., CLEMENT, J.G., COOPER, D.M.L.. The relation of femoral osteon geometry to age, sex, height and weight. *Bone* 2009;45(1):77–83. doi:[10.1016/j.bone.2009.03.654](https://doi.org/10.1016/j.bone.2009.03.654).
- [84] LEFEVRE, E., LASAYGUES, P., BARON, C., PAYAN, C., LAUNAY, F., FOLLET, H., et al. Analyzing the anisotropic Hooke's law for children's cortical bone. *Journal of the Mechanical Behavior of Biomedical Materials* 2015;49:370–377. doi:[10.1016/j.jmbbm.2015.05.013](https://doi.org/10.1016/j.jmbbm.2015.05.013).
- [85] EVANS, F.G.. Mechanical properties and histology of cortical bone from younger and older men. *The Anatomical Record* 1976;185(1):1–11. doi:[10.1002/ar.1091850102](https://doi.org/10.1002/ar.1091850102).
- [86] STEFAN, U., MICHAEL, B., WERNER, S.. Effects of three different preservation methods on the mechanical properties of human and bovine cortical bone. *Bone* 2010;47(6):1048–1053. doi:[10.1016/j.bone.2010.08.012](https://doi.org/10.1016/j.bone.2010.08.012).
- [87] BAYRAKTAR, H.H., MORGAN, E.F., NIEBUR, G.L., MORRIS, G.E., WONG, E.K., KEAVENY, T.M.. Comparison of the elastic and yield properties of human femoral trabecular and cortical bone tissue. *Journal of Biomechanics* 2004;37(1):27–35. doi:[10.1016/S0021-9290\(03\)00257-4](https://doi.org/10.1016/S0021-9290(03)00257-4).
- [88] SEMAAN, M., MORA, P., BERNARD, S., LAUNAY, F., PAYAN, C., LASAYGUES, P., et al. Assessment of elastic coefficients of child cortical bone using resonant ultrasound spectroscopy. *Journal of the Mechanical Behavior of Biomedical Materials* 2019;90:40–44. doi:[10.1016/j.jmbbm.2018.09.044](https://doi.org/10.1016/j.jmbbm.2018.09.044).
- [89] BAUMANN, A.P., DEUERLING, J.M., RUDY, D.J., NIEBUR, G.L., ROEDER, R.K.. The relative influence of apatite crystal orientations and intracortical porosity on the elastic anisotropy of human cortical bone. *Journal of Biomechanics* 2012;45(16):2743–2749. doi:[10.1016/j.jbiomech.2012.09.011](https://doi.org/10.1016/j.jbiomech.2012.09.011).

- [90] LI, S., DEMIRCI, E., SILBERSCHMIDT, V.V.. Variability and anisotropy of mechanical behavior of cortical bone in tension and compression. *Journal of the Mechanical Behavior of Biomedical Materials* 2013;21:109–120. doi:[10.1016/j.jmbbm.2013.02.021](https://doi.org/10.1016/j.jmbbm.2013.02.021).
- [91] NYMAN, J.S., LING, H., DONG, X., WANG, X.. Differences in the mechanical behavior of cortical bone between compression and tension when subjected to progressive loading. *Journal of the mechanical behavior of biomedical materials* 2009;2(6):613–619. doi:[10.1016/j.jmbbm.2008.11.008](https://doi.org/10.1016/j.jmbbm.2008.11.008).
- [92] MIRZAALI, M.J., BÜRKI, A., SCHWIEDRZIK, J., ZYSSET, P.K., WOLFRAM, U.. Continuum damage interactions between tension and compression in osteonal bone. *Journal of the Mechanical Behavior of Biomedical Materials* 2015;49:355–369. doi:[10.1016/j.jmbbm.2015.05.007](https://doi.org/10.1016/j.jmbbm.2015.05.007).
- [93] ZHANG, G., DENG, X., GUAN, F., BAI, Z., CAO, L., MAO, H.. The effect of storage time in saline solution on the material properties of cortical bone tissue. *Clinical Biomechanics* 2018;57:56–66. doi:[10.1016/j.clinbiomech.2018.06.003](https://doi.org/10.1016/j.clinbiomech.2018.06.003).
- [94] ALBERT, C.I., JAMESON, J., HARRIS, G.. Design and validation of bending test method for characterization of miniature pediatric cortical bone specimens. *Proceedings of the Institution of Mechanical Engineers, Part H: Journal of Engineering in Medicine* 2013;227(2):105–113. doi:[10.1177/0954411912463868](https://doi.org/10.1177/0954411912463868).
- [95] GAUTHIER, R., FOLLET, H., LANGER, M., MEILLE, S., CHEVALIER, J., RONGIÉRAS, F., et al. Strain rate influence on human cortical bone toughness: A comparative study of four paired anatomical sites. *Journal of the Mechanical Behavior of Biomedical Materials* 2017;71:223–230. doi:[10.1016/j.jmbbm.2017.03.015](https://doi.org/10.1016/j.jmbbm.2017.03.015).
- [96] BRY, R., BENNANI, B., DELILLE, R., MORVAN, H., HAULT-DUBRULLE, A., FONTAINE, C.. Mechanical characterisation under cycling loading of humerus cortical bone. *Computer Methods in Biomechanics and Biomedical Engineering* 2012;15(sup1):274–276. doi:[10.1080/10255842.2012.713616](https://doi.org/10.1080/10255842.2012.713616).
- [97] XU, T., SHENG, X., ZHANG, T., LIU, H., LIANG, X., DING, A.. Development and Validation of Dummies and Human Models Used in Crash Test. *Applied Bionics and Biomechanics* 2018;2018. doi:[10.1155/2018/3832850](https://doi.org/10.1155/2018/3832850).
- [98] IWAMOTO, M., NAKAHIRA, Y., TAMURA, A., KIMPARA, H., WATANABE, I., MIKI, K.. Development of advanced human models in THUMS 2007;:10.

- [99] IWAMOTO, M., NAKAHIRA, Y., KIMPARA, H., SUGIYAMA, T., MIN, K.. Development of a Human Body Finite Element Model with Multiple Muscles and their Controller for Estimating Occupant Motions and Impact Responses in Frontal Crash Situations. *Stapp Car Crash Journal* 2012;;38.
- [100] ROBIN, S.. HUMOS : human model for safety – a joint effort towards the development of refined human-like car occupant models. *Proceedings of 17th international technical conference on the enhanced safety of vehicles* 2001;;9.
- [101] UNTAROIU, C.D., YUE, N., SHIN, J.. A Finite Element Model of the Lower Limb for Simulating Automotive Impacts. *Annals of Biomedical Engineering* 2013;41(3):513–526. doi:[10.1007/s10439-012-0687-0](https://doi.org/10.1007/s10439-012-0687-0).
- [102] GAYZIK, F.S., MORENO, D.P., VAVALLE, N.A., RHYNE, A.C., STITZEL, J.D.. Development of the Global Human Body Models Consortium Mid- Sized Male Full Body Model 2011;;11.
- [103] ROTH, S., TORRES, F., FEUERSTEIN, P., THORAL-PIERRE, K.. Anthropometric dependence of the response of a Thorax FE model under high speed loading: Validation and real world accident replication. *Computer Methods and Programs in Biomedicine* 2013;110(2):160–170. doi:[10.1016/j.cmpb.2012.11.004](https://doi.org/10.1016/j.cmpb.2012.11.004).
- [104] JIN, X., KALRA, A., HAMMAD, A., KHANDELWAL, P., PORWAL, V., SHEN, M., et al. Development and Validation of Whole-Body Finite Element Occupant and Pedestrian Models of a 70-Year-Old Female 2018;;23.
- [105] YAMADA, H., EVANS, F.G., OTHERS, . Strength of biological materials 1970;.
- [106] GARCIA, D.. Elastic plastic damage laws for cortical bone. Thèse de doctorat; EPFL; 2006.
- [107] SEDLIN, E.D.. A Rheologic Model for Cortical Bone: A Study of the Physical Properties of Human Femoral Samples. *Acta Orthopaedica Scandinavica* 1965;36(sup83):1–77. doi:[10.3109/ort.1965.36.suppl-83.01](https://doi.org/10.3109/ort.1965.36.suppl-83.01).
- [108] MORI, T., TANAKA, K.. Average stress in matrix and average elastic energy of materials with misfitting inclusions. *Acta Metallurgica* 1973;21(5):571–574. doi:[10.1016/0001-6160\(73\)90064-3](https://doi.org/10.1016/0001-6160(73)90064-3).
- [109] ESHELBY, J.D.. The determination of the elastic field of an ellipsoidal inclusion, and related problems. *Proceedings of the Royal Society of London Series A Mathematical and Physical Sciences* 1957;241(1226):376–396. doi:[10.1098/rspa.1957.0133](https://doi.org/10.1098/rspa.1957.0133).

- [110] ESHELBY, J.D.. The elastic field outside an ellipsoidal inclusion. *Proceedings of the Royal Society of London Series A Mathematical and Physical Sciences* 1959;252(1271):561–569. doi:[10.1098/rspa.1959.0173](https://doi.org/10.1098/rspa.1959.0173).
- [111] VANDENBULCKE, F.. Caractérisation et modélisation multi-échelle du comportement mécanique à la rupture du membre scapulaire sous sollicitations dynamiques. Thèse de doctorat; Valenciennes; 2015.
- [112] RAHMOUN, J., AUPERRIN, A., DELILLE, R., NACEUR, H., DRAZETIC, P.. Characterization and micromechanical modeling of the human cranial bone elastic properties. *Mechanics Research Communications* 2014;60:7–14. doi:[10.1016/j.mechrescom.2014.04.001](https://doi.org/10.1016/j.mechrescom.2014.04.001).
- [113] HAMED, E., LEE, Y., JASIUK, I.. Multiscale modeling of elastic properties of cortical bone. *Acta Mechanica* 2010;213(1-2):131–154. doi:[10.1007/s00707-010-0326-5](https://doi.org/10.1007/s00707-010-0326-5).
- [114] GRANKE, M., GRIMAL, Q., PARNELL, W.J., SAÏED, A., PEYRIN, F., LAUGIER, P.. Elasticity and porosity in human cortical bone: models and experiments 2011;;6.
- [115] VANDENBULCKE, F., RAHMOUN, J., MORVAN, H., NACEUR, H., DRAZETIC, P., FONTAINE, C., et al. On the mechanical characterization of human humerus using multi-scale continuum finite element model. Dans: *2012 IRCOBI conference, Dublin*. 2012, p. 598–610.
- [116] CAI, X., BRENNER, R., PERALTA, L., OLIVIER, C., GOUTTENOIRE, P.J., CHAPARD, C., et al. Homogenization of cortical bone reveals that the organization and shape of pores marginally affect elasticity. *Journal of The Royal Society Interface* 2019;16(151):20180911. doi:[10.1098/rsif.2018.0911](https://doi.org/10.1098/rsif.2018.0911).
- [117] OSPALD, F.. fibergen: An introductory tool for FFT-based material homogenization. *Journal of Open Source Software* 2019;4(34):1027. doi:[10.21105/joss.01027](https://doi.org/10.21105/joss.01027).
- [118] MACIEJAK, O., AUBERT, P.. Mesure de dureté par nano-indentation. *Techniques de l'ingénieur Nanosciences : concepts, caractérisation et aspects sécurité* 2016;base documentaire : TIB194DUO.(ref. article : nm7200). Fre.
- [119] ZYSSET, P.K.. Indentation of bone tissue: a short review. *Osteoporosis International* 2009;20(6):1049–1055. doi:[10.1007/s00198-009-0854-9](https://doi.org/10.1007/s00198-009-0854-9).
- [120] OLIVER, W., PHARR, G.. An improved technique for determining hardness and elastic modulus using load and displacement sensing indentation experiments. *Journal of Materials Research* 1992;7(06):1564–1583. doi:[10.1557/JMR.1992.1564](https://doi.org/10.1557/JMR.1992.1564).

- [121] LEFEVRE, E.. Caractérisation multimodale des propriétés de l'os cortical en croissance. Thèse de doctorat; 2015.
- [122] WU, Z., OVAERT, T.C., NIEBUR, G.L.. Viscoelastic properties of human cortical bone tissue depend on gender and elastic modulus. *Journal of Orthopaedic Research* 2012;30(5):693–699. doi:[10.1002/jor.22001](https://doi.org/10.1002/jor.22001).
- [123] DEMIRTAS, A., CURRAN, E., URAL, A.. Assessment of the effect of reduced compositional heterogeneity on fracture resistance of human cortical bone using finite element modeling. *Bone* 2016;91:92–101. doi:[10.1016/j.bone.2016.07.015](https://doi.org/10.1016/j.bone.2016.07.015).
- [124] ABDEL-WAHAB, A.A., MALIGNO, A.R., SILBERSCHMIDT, V.V.. Micro-scale modelling of bovine cortical bone fracture: Analysis of crack propagation and microstructure using X-FEM. *Computational Materials Science* 2012;52(1):128–135. doi:[10.1016/j.commatsci.2011.01.021](https://doi.org/10.1016/j.commatsci.2011.01.021).
- [125] VERGANI, L., COLOMBO, C., LIBONATI, F.. Crack Propagation in Cortical Bone: A Numerical Study. *Procedia Materials Science* 2014;3:1524–1529. doi:[10.1016/j.mspro.2014.06.246](https://doi.org/10.1016/j.mspro.2014.06.246).
- [126] MULLINS, L.P., MCGARRY, J.P., BRUZZI, M.S., MCHUGH, P.E.. Micromechanical modelling of cortical bone. *Computer Methods in Biomechanics and Biomedical Engineering* 2007;10(3):159–169. doi:[10.1080/10255840601110802](https://doi.org/10.1080/10255840601110802).
- [127] ROTHAEER, X., DELILLE, R., MORVAN, H., BENNANI, B., MARKIEWICZ, E., FONTAINE, C.. A three-dimensional geometric quantification of human cortical canals using an innovative method with micro-computed tomographic data. *Micron* 2018;114:62–71. doi:[10.1016/j.micron.2018.07.006](https://doi.org/10.1016/j.micron.2018.07.006).
- [128] ROTHAEER, X., DELILLE, R., MORVAN, H., BENNANI, B., MARKIEWICZ, E., FONTAINE, C.. Quantitative method for the three-dimensional assessment of human cortical long-bone architecture based on micro-CT images. Lisbon, Portugal; 2018,.
- [129] BERTRAND, S.. In vivo 3d geometrical modeling of the human trunk using EOS X-Ray system. Theses; Arts et Métiers ParisTech; 2005.
- [130] BRADSKI, G.R., KAEHLER, A.. Learning OpenCV: computer vision with the OpenCV library. Software that sees; 1. ed., [nachdr.] ed.; Beijing: O'Reilly; 2011. ISBN 978-0-596-51613-0. OCLC: 838472784.

- [131] JONES, E., OLIPHANT, T., PETERSON, P., OTHERS, . SciPy: Open source scientific tools for Python. 2001.
- [132] VAN DER WALT, S., COLBERT, S.C., VAROQUAUX, G.. The NumPy Array: A Structure for Efficient Numerical Computation. *Computing in Science & Engineering* 2011;13(2):22–30. doi:[10.1109/MCSE.2011.37](https://doi.org/10.1109/MCSE.2011.37).
- [133] HUNTER, J.D.. Matplotlib: A 2d Graphics Environment. *Computing in Science & Engineering* 2007;9(3):90–95. doi:[10.1109/MCSE.2007.55](https://doi.org/10.1109/MCSE.2007.55).
- [134] DURAND, F., DORSEY, J.. Fast Bilateral Filtering for the Display of High-dynamic-range Images. Dans: *Proceedings of the 29th Annual Conference on Computer Graphics and Interactive Techniques*. SIGGRAPH '02; New York, NY, USA: ACM. ISBN 978-1-58113-521-3; 2002, p. 257–266. doi:[10.1145/566570.566574](https://doi.org/10.1145/566570.566574).
- [135] OTSU, N.. A Threshold Selection Method from Gray-Level Histograms. *IEEE Transactions on Systems, Man, and Cybernetics* 1979;9(1):62–66. doi:[10.1109/TSMC.1979.4310076](https://doi.org/10.1109/TSMC.1979.4310076).
- [136] GONZALEZ, R.C., WOODS, R.E.. Digital image processing. 3. ed ed.; Upper Saddle River, NJ: Pearson/Prentice Hall; 2008. ISBN 978-0-13-168728-8. OCLC: 255942782.
- [137] PARFITT, A.. Bone histomorphometry: Standardization of nomenclature, symbols and units (summary of proposed system). *Bone* 1988;9(1):67–69. doi:[10.1016/8756-3282\(88\)90029-4](https://doi.org/10.1016/8756-3282(88)90029-4).
- [138] DOGHRI, I., TINEL, L.. Micromechanics of inelastic composites with misaligned inclusions: Numerical treatment of orientation. *Computer Methods in Applied Mechanics and Engineering* 2006;195(13):1387–1406. doi:[10.1016/j.cma.2005.05.041](https://doi.org/10.1016/j.cma.2005.05.041).
- [139] REPP, F., KOLLMANNBERGER, P., ROSCHGER, A., BERZLANOVICH, A., GRUBER, G.M., ROSCHGER, P., et al. Coalignment of osteocyte canaliculi and collagen fibers in human osteonal bone. *Journal of Structural Biology* 2017;199(3):177–186. doi:[10.1016/j.jsb.2017.07.004](https://doi.org/10.1016/j.jsb.2017.07.004).
- [140] BUENZLI, P.R., THOMAS, C.D.L., CLEMENT, J.G., PIVONKA, P.. Endocortical bone loss in osteoporosis: The role of bone surface availability. *International Journal for Numerical Methods in Biomedical Engineering* 2013;29(12):1307–1322. doi:[10.1002/cnm.2567](https://doi.org/10.1002/cnm.2567); arXiv: 1206.6071.
- [141] OSTERHOFF, G., MORGAN, E.F., SHEFELBINE, S.J., KARIM, L., MCNAMARA, L.M., AUGAT, P.. Bone mechanical properties and changes with osteoporosis. *Injury* 2016;47:S11–S20. doi:[10.1016/S0020-1383\(16\)47003-8](https://doi.org/10.1016/S0020-1383(16)47003-8).

- [142] SMITH, D.W., GARDINER, B.S., DUNSTAN, C.. Bone Balance within a Cortical BMU: Local Controls of Bone Resorption and Formation. *PLoS ONE* 2012;7(7). doi:[10.1371/journal.pone.0040268](https://doi.org/10.1371/journal.pone.0040268).
- [143] DIMITRIOU, D., TSAI, T.Y., YUE, B., RUBASH, H.E., KWON, Y.M., LI, G.. Side-to-side variation in normal femoral morphology: 3d CT analysis of 122 femurs. *Orthopaedics & Traumatology: Surgery & Research* 2016;102(1):91–97. doi:[10.1016/j.otsr.2015.11.004](https://doi.org/10.1016/j.otsr.2015.11.004).
- [144] TADDEI, F., FALCINELLI, C., BALISTRERI, L., HENYS, P., BARUFFALDI, F., SIGURDSSON, S., et al. Left-right differences in proximal femur strength of post-menopausal women: a multicentric Finite Element study. *Osteoporosis international : a journal established as result of cooperation between the European Foundation for Osteoporosis and the National Osteoporosis Foundation of the USA* 2016;27(4):1519–1528. doi:[10.1007/s00198-015-3404-7](https://doi.org/10.1007/s00198-015-3404-7).
- [145] IORI, G., SCHNEIDER, J., REISINGER, A., HEYER, F., PERALTA, L., WYERS, C., et al. Large cortical bone pores in the tibia are associated with proximal femur strength. *PLoS ONE* 2019;14(4). doi:[10.1371/journal.pone.0215405](https://doi.org/10.1371/journal.pone.0215405).
- [146] KIM, G., COLE, J.H., BOSKEY, A.L., BAKER, S.P., VAN DER MEULEN, M.C.H.. Reduced Tissue-Level Stiffness and Mineralization in Osteoporotic Cancellous Bone. *Calcified Tissue International* 2014;95(2):125–131. doi:[10.1007/s00223-014-9873-4](https://doi.org/10.1007/s00223-014-9873-4).
- [147] TREUTENAERE, S.. Modélisation du comportement des composites stratifiés à préformes textiles avec prédiction du délaminage pour des simulations d'impact. Thèse de doctorat; UVHC; Valenciennes; 2016.
- [148] BOURSE, G., XÜ, W.J., MOUFTIEZ, A., VANDEVOORDE, L., OURAK, M.. Interfacial adhesion characterization of plasma coatings by V(z) inversion technique and comparison to interfacial indentation. *NDT & E International* 2012;45(1):22–31. doi:[10.1016/j.ndteint.2011.09.005](https://doi.org/10.1016/j.ndteint.2011.09.005).

List of publications

International scientific journal

Roothaer, X., Delille, R., Morvan, H., Markiewicz, E., Fontaine, C.. The Assessment of Bearing and Non-Bearing Cortical Bones: Tensile Tests and Three Dimensional Study of Vascular Architecture. *Computer Methods in Biomechanics and Biomedical Engineering* 22: 192-94, Oct. 2019.
doi:10.1080/10255842.2019.1668135.

Roothaer, X., Delille, R., Morvan, H., Bennani, B., Markiewicz, E., Fontaine, C.. A three-dimensional geometric quantification of human cortical canals using an innovative method with micro-computed tomographic data. *Micron*;114:62–71. Nov. 2018
doi:10.1016/j.micron.2018.07.006

Book Chapter

Roothaer, X., Delille, R., Morvan, H., Markiewicz, E., Fontaine, C.. A Comparison Between Bearing and Non-Bearing Human Bone: Mechanical Testing and Micro-Architecture Assessment . In *Mechanics of Biological Systems and Materials & Micro-and Nanomechanics*, Volume 4, edited by Martha E. Grady, 49-56. *Conference Proceedings of the Society for Experimental Mechanics Series*. Cham: Springer International Publishing, 2020.
doi:10.1007/978-3-030-30013-5_9

International congress

Roothaer, X., Delille, R., Morvan, H., Markiewicz, E., Fontaine, C.. The Assessment of Bearing and Non-Bearing Cortical Bones: Tensile Tests and Three Dimensional Study of Vascular Architecture.

44th congress Société de Biomécanique, Poitiers, France; 2019.

Roothaer, X., Delille, R., Morvan, H., Markiewicz, E., Fontaine, C.. A comparison between bearing and non-bearing human bone: mechanical testing and micro-architecture assessment. Society for Experimental Mechanics XIII International congress, Reno, NV, USA; 2019.

Roothaer, X., Delille, R., Morvan, H., Bennani, B., Markiewicz, E., Fontaine, C.. Quantitative method for the three-dimensional assessment of human cortical long-bone architecture based on micro-CT images. Lisbon, Portugal; 2018.

Abstract

The human skeleton aims at participating to the locomotor system, protecting and serving as brackets for the internal organs. To ensure the mechanical stiffness of the entire body, the cortical bone can be found in every part of the skeleton. A dynamic process occurs throughout the life and is named bone remodelling. This process adapts the cortical bone architecture and the shape of bones according to their functions. Due to its complexity, bone remodelling can defect in the elderly and weakens bones. This thesis studies the bearing and non-bearing long human bones by focusing on the humerus and femur. A survey of the state of the art, detailed in the first chapter, reveals several lacks. First, the femur is widely investigated compared to the other bones and this unbalance creates a lack of data for the other bones. Therefore, inputs for numerical human models come from deprecated and contradictory studies where the extra-individual differences impact the trends. Second, architectural studies are mainly limited to in-plane assessment whereas the vascular network is complex and needs more robust analyses. Thus, the second chapter describes an innovative method to 3D assess the cortical vascular network from tomographic data. This Python script automatically detects canals, connectivity and Bone Multicellular Units (BMUs), cradle of the bone remodelling activity. Then, 77 samples from left and right femurs and humeri of ten human cadavers are scanned and analysed using this method. As this method provides numerous novel features of the cortical architecture, tensile and indentation tests are also carried out in order to understand and exhibit the impact of the architecture on the mechanical behaviour. Hence, all the scanned samples are tested and available for statistical analysis. So as to identify global trends, humerus and femur are compared using different statistical tests. Likewise, the bias impact is also investigated. Finally, a correlation study followed by a regression study is described so as to provide polynomial functions in order to be used to predict the mechanical behaviour from an architectural study.

Keywords : Cortical bone, Humerus, Femur, Bearing bone, Long bone, Vascular canals, Architecture, 3D analysis, BMU, Bone remodelling, Porosity, Orientation, Length, Tomography, Micro-CT, Tensile tests, Indentation, Mechanical behaviour, Mann-Whitney-Wilcoxon, Regression, Elastic modulus, Python, Data processing

Résumé

Le squelette humain a pour fonction de protéger les organes internes tout en participant au système de locomotion. Afin d'en assurer la rigidité mécanique, l'os cortical est présent dans toutes les parties du squelette. Le remodelage osseux, processus dynamique, est actif tout au long de la vie. Il permet à l'os cortical d'adapter sa géométrie et son architecture interne en fonction des contraintes qui lui sont appliquées. Étant un processus complexe, le remodelage osseux est amené à dysfonctionner chez les personnes âgées et fragiliser leurs os. Ainsi, cette thèse étudie les os porteurs et non porteurs humains en se concentrant sur le fémur et l'humérus. La revue de la littérature, effectuée dans le chapitre 1, met en évidence plusieurs verrous scientifiques à résoudre. En effet, pour diverses raisons pratiques, le fémur est très largement étudié, délaissant l'étude des autres os. Cela a pour effet d'en impacter les données matériaux utilisées par les modèles numériques du corps humain, souvent extraites d'études très anciennes et obsolètes dont les sujets humains diffèrent. De plus, les études architecturales sont, pour la plupart, limitées à des analyses en 2D et ne sont pas adaptées par rapport à l'architecture osseuse complexe. Par conséquent, le second chapitre décrit une méthode innovante capable d'analyser et de quantifier l'architecture en 3D à partir de scans tomographiques. Les canaux, connectivités et BMUs, berceaux du remodelage osseux, sont automatiquement détectés. 77 échantillons, prélevés sur humérus et fémurs gauche et droit, sont scannés et quantifiés à partir de cette méthode. Étant donné que de nombreuses caractéristiques, jamais mesurées auparavant, sont obtenues, des essais de traction et d'indentation sont effectués afin de comprendre et de mettre en évidence l'impact de l'architecture sur le comportement mécanique. Par conséquent, l'intégralité des échantillons, précédemment scannée, est testée. Dans l'objectif d'extraire des tendances générales, les humérus et fémurs sont comparés suivant différents tests statistiques. De même, l'impact de la latéralité est aussi étudié. Pour terminer, une étude de corrélation, suivie d'une étude de régressions, est effectuée afin de fournir des fonctions polynomiales destinées à prédire le comportement mécanique à partir d'une simple étude architecturale.

Mots clés : Os cortical, Humérus, Fémur, Os porteur, Os long, Canaux vasculaires, Architecture, Analyse 3D, BMU, Remodelage osseux, Porosité, Orientation, Longueur, Tomographie, Micro-CT, Essai de traction, Essai d'indentation, Comportement mécanique, Mann-Whitney-Wilcoxon, Regression, Module élastique, Python, Traitement de données